NNT : 2019SACLX087

Thèse de doctorat

A consistent approach for coupling lumped-parameter and phase-field models for in-vessel corium to thermodynamic databases

Thèse de doctorat de l'Université Paris-Saclay
préparée à l'École Polytechnique

École doctorale n°573 Interfaces - Approches Interdisciplinaires: Fondements, Applications et Innovation
Spécialité de doctorat : Physique

Thèse présentée et soutenue à Cadarache, le 26 Novembre 2019, par

Vaishnvi TIWARI

Composition du Jury :

Yann LeBouar Directeur de Recherche, CNRS (LEM Châtillon)	Président
Jean-Marc Debierre Professeur, Aix-Marseille Université (IM2NP Marseille)	Rapporteur
Walter Villanueva Researcher, KTH Stockholm, Suède (Nuclear Power Safety Group)	Rapporteur
Florian Fichot Researcher, IRSN Cadarache (PSN-RES/SAG/LEPC)	Examinateur
Mathis Plapp Directeur de Recherche, CNRS (PMC Palaiseau)	Directeur de thèse
Romain Le Tellier Researcher, CEA Cadarache (CEA, DEN, DTN, SMTA/LMAG)	Encadrant de thèse

université PARIS-SACLAY | ÉCOLE DOCTORALE INTERFACES Approches Interdisciplinaires : Fondements, Applications et Innovation

Titre: Une approche consistante pour le couplage aux bases thermodynamiques de modèles intégraux et de champ de phase dédiés au comportement du corium en cuve.

Cette thèse de doctorat s'intéresse à la manière d'assurer une représentation thermodynamiquement consistante du corium en cuve (un mélange à haute température de matériaux fondus du cœur et des structures d'un réacteur nucléaire, décrit par le système U-O-Zr-acier) dans les modèles couplés de thermohydraulique-thermochimie mis en jeu pour l'étude des Accidents Graves (AG) des Réacteurs refroidis à l'Eau Légère (RELs), en particulier, pour la stratégie dite de rétention du corium en cuve. Dans ce contexte, l'utilisation d'une base de données thermodynamiques obtenue par la méthode CALPHAD apparait pertinente pour l'obtention des fermetures et données d'entrée des modèles de thermohydraulique et de thermochimie respectivement. Ces bases de données décrivent des modèles relatifs aux fonctions d'énergie de Gibbs des différentes phases possibles d'un système. Elles peuvent être utilisées pour évaluer les conditions possibles d'équilibre thermodynamique d'un système ainsi que ses propriétés thermodynamiques dans des conditions hors-équilibre.

Dans ce travail, une approche systématique pour l'utilisation exhaustive de ces données CALPHAD dans les modèles couplés a été proposée. Les questions soulevées ont été traitées au travers de l'étude de modèles « maquettes » décrivant une partie des phénomènes relatifs au comportement du corium en cuve à des échelles macroscopique ou mésoscopique.

Dans une première partie, la possibilité de construire les fermetures (sous la forme de relations enthalpie-température et de conditions locales d'équilibre) d'un modèle intégral à une échelle macroscopique à partir de données CALPHAD a été évaluée. En considérant le système ternaire U-O-Zr, ce modèle décrit le processus de solidification en front plan à la frontière d'un bain de corium fondu. Une seconde partie dans ce travail a été consacrée au développement d'une formulation générale pour des modèles à interface diffuse obtenus par une approche par champ de phase et s'adressant à la simulation de différents processus thermochimiques non-isothermes tels que la solidification ou la ségrégation de phase. Les questions relatives à la consistance thermodynamique du modèle ainsi qu'à la sélection de ses paramètres (en particulier, vis-à-vis de la mise à l'échelle de l'épaisseur d'interface) ont été traitées et des résultats numériques ont été discutés pour les systèmes binaires U-Zr et U-O dans des conditions isothermes.

Mots-clés: Accidents graves, corium en cuve, CALPHAD, méthode du champ de phase, modèles intégraux

université PARIS-SACLAY | ÉCOLE DOCTORALE INTERFACES Approches Interdisciplinaires : Fondements, Applications et Innovation

Title: A consistent approach for coupling lumped-parameter and phase-field models for in-vessel corium to thermodynamic databases.

This Ph.D. thesis is focused on ensuring a thermodynamically consistent representation of in-vessel corium (a high temperature mixture of molten reactor core and structural materials, described as a U-O-Zr-steel system) in the coupled thermohydraulic-thermochemical models that are used for performing Severe Accident (SA) analysis of nuclear Light Water Reactors (LWRs); in particular, the In-Vessel Melt Retention (IVMR) Strategy. In this context, the use of a thermodynamic database obtained by the CALPHAD method seems relevant by providing closures and inputs to the thermohydraulic and thermochemical models respectively. These databases consist of models for Gibbs energy functions of the possible phases for a system that can be used to obtain the equilibrium thermodynamic description for the system as well as material thermodynamic properties for out-of-equilibrium conditions.

Through this work, a systematic approach for ensuring extensive utilization of CALPHAD data in the coupled models has been developed, and the associated questions have been answered for 'mock-up' macroscopic and mesoscopic models developed for describing some of the phenomena pertaining to in-vessel corium behaviour.

As a first step, the feasibility of using CALPHAD based closures (in the form of enthalpy-temperature relations and local equilibrium conditions) has been tested on the macroscopic model developed using the lumped parameter approach. Considering the ternary U-O-Zr system, this model describes the plane front solidification process at the boundary of a molten corium pool. The second part of the work is focused on the development of a general formulation for diffuse interface models under the phase-field approach, which can be used to simulate the kinetics of various thermochemical processes under non-isothermal conditions such as solidification and phase segregation. The questions related to the thermodynamic consistency of the model as well as its parameterization (in particular with respect to the up-scaling of the interface thickness) have been addressed and the numerical results have been discussed for binary U-Zr and U-O systems under isothermal conditions.

Keywords: Severe accidents, in-vessel corium, CALPHAD, phase-field, lumped-parameter models

Acknowledgements

I would like to thank all the people who contributed to help me achieve this research. Firstly, to Dominique Pecheur, head of Service "Mesures et modélisation des Transferts et des Accidents graves (SMTA)" and Laurent Saas, head of "Laboratoire de Modélisation des Accidents Graves (LMAG)" for giving me an opportunity to carry out research at CEA Cadarache.

I am grateful to Mathis Plapp, my PhD director, without whose contribution and constant motivation, this work would not have been possible. Thank you for allowing me to pick your brain and for guiding me. I would also like to extend my deepest gratitude to Romain Le Tellier, my PhD supervisor. Your mentorship, patience and more importantly the faith you have demonstrated in my ability to overcome the obstacles during these years has been a huge source of encouragement to me.

I am indebted to all the jury members of my PhD defence: the reviewers Jean-Marc Debierre and Walter Villanueva, and the examiners Florian Fichot and Yann Le Bouar. The time invested by you all in reading my manuscript and your suggestions have not only proved to be useful in improving the manuscript but have also been enlightening.

I am grateful to all my colleagues of LMAG and LEAG for accepting me as a part of the team. A big thanks to Louis Viot for all his help and for proof-reading my manuscript. Thank you Magali for helping me stay connected to the world of reading by graciously lending me all those books, Alain for your constant worrying which never made me miss my parents and Pascal for your contagiously happy attitude. Shifali Singh, thank you for always being there for me, as a friend and a sister.

Thank you, Advait Ghate, Savneet Kaur, Zayed Parkar, Avinash Krishna, Shambhavi Nandan and Saptarshi Bhattacharjee. Three years is a long time, and I am glad to have never felt homesick because of all you wonderful people.

Above all, I thank my parents and my sister, to whom I owe all the success I have achieved in my life.

Contents

List of Figures

List of Tables

Abbreviations

AC alternating current. 5

BDBA Beyond Design Basis Accidents. 4

BWR Boiling Water Reactors. 2

CALPHAD CALculation of PHAse Diagrams. x, xv, 26–32, 37–39, 45–49, 54, 55, 59, 66, 68, 70, 72, 74, 75, 80, 93, 94, 133, 135–138, 146, 147, 164, 165, 168, 170

CEF Compound Energy Formalism . 29

CFD Computational Fluid Dynamics. 34, 39, 53, 72, 137, 138

CHF Critical Heat Flux. 12

component A component is a system-wide entity described by its thermodynamic properties such as amount, activity, or chemical potential.. 29, 38, 94, 164, 165, 167, 168

constituent A component is a system-wide entity described by its thermodynamic properties such as amount, activity, or chemical potential.. 29, 30, 32, 94, 164, 165, 167, 168

EOS Equation-Of-State. x, 36, 38, 47–49, 54, 56, 59, 60, 70, 71, 80, 135–137, 146, 147

ERVC External Reactor Vessel Cooling. 11

FCI fuel-coolant interaction. 7, 8, 12

IAEA International Atomic Energy Agency. 1

IVMR In-Vessel Melt Retention. ix, x, 11–23, 25, 38, 39, 46

LBLOCA Large-Break-Loss-Of-Coolant Accident. 5

LOCA Loss-Of-Coolant Accident. 5

LWR Light Water Reactor. 2, 4, 33

MCCI molten corium-concrete interaction. 8

OC OpenCalphad. 33, 94, 103, 130, 145, 164

PROCOR PROpagation of CORium. 23–25, 33, 35, 46–49, 71, 136, 141, 145

PWR Pressurized Water Reactor. 2, 6, 59

RIA Reactivity-Initiated Accident. 4, 5

RPV Reactor Pressure Vessel. 2, 6, 7, 11–15, 17–21, 23, 38, 46, 53, 54, 72, 147

SA Severe Accident. 24–26, 33, 34

SAM Severe Accident Management. 10

SBLOCA Small-Break-Loss-Of-Coolant Accident. 5

SBO station blackout. 5

TAF-ID Thermodynamics of Advanced Fuels-International Database. 32

List of Symbols

θ : phase of the system;

$\mathbb{S}$: species;

G_M^θ : molar Gibbs free energy for a phase θ $[J^1 mol^{-1}]$;

t : time co-ordinate $[s^1]$;

z : space co-ordinate $[m^1]$;

$\mathcal{V}$: control volume $[m^3]$;

m : mass $[kg^1]$;

$\dot{m}$: mass flow rate $[kg^1 s^{-1}]$;

$\bar{h}$: specific enthalpy $[J^1 kg^{-1} K^{-1}]$;

C_p : heat capacity $[J^1 kg^{-1} K^{-1}]$;

A : surface area $[m^2]$;

φ : heat flux $[W^1 m^{-2}]$;

$\beta_{i,j}$: interface between neighbouring zones i and j;

$\dot{q}^{mass}$: mass power density $[W^1 kg^{-1}]$;

ϕ : order parameter;

S : entropy $[J^1 K^{-1}]$;

G : Gibbs energy $[J^1]$;

Ω : grand potential $[J^1]$;

S_m : entropy production per mole of components $[J^1K^{-1}mol^{-1}]$;

G_m : Gibbs energy per mole of components $[J^1mol^{-1}]$;

Ω_m : grand potential per mole of components $[J^1mol^{-1}]$;

s_m : entropy density $[J^1K^{-1}m^{-3}]$;

g_m : Gibbs energy density $[J^1m^{-3}]$;

ω_m : grand potential density $[J^1m^{-3}]$;

ρ_j : concentration of phase j $[mol^1m^{-3}]$;

χ_j : susceptibility associated to phase j $[J^{-1}mol^2m^{-3}]$;

T : temperature $[K^1]$;

p : pressure $[J^1m^{-3}]$;

μ_i : chemical potential of component i $[J^1mol^{-1}]$;

N_i : number of moles of component i $[mol^1]$;

x_i : component mole fraction ;

y_i : constituent mole fraction ;

V_m : molar volume $[m^3mol^{-1}]$;

t : time $[s^1]$;

J_x : mass flux $[mol^1m^{-2}s^{-1}]$;

J_e : energy flux $[J^1m^{-2}s^{-1}]$;

M_{xx} : kinetic coefficient for mass transfer $[mol^2K^1J^{-1}m^{-1}s^{-1}]$;

M_{ee} : kinetic coefficient for energy transfer $[J^1K^1m^{-1}s^{-1}]$;

M_ϕ : kinetic coefficient for mobility of order parameter ϕ $[J^{-1}K^1s^{-1}m^3]$;

κ_ϕ^2 : gradient constant associated with interface energy and thickness $[J^1 m^{-1}]$;

a : positive constant related to material parameters $[J^{-1} m^3]$;

R : universal gas constant $[J^1 mol^{-1} K^{-1}]$;

δ_{kj} : Kronecker delta, *i.e.* $= 1$ when $k = j$ and 0 otherwise.

To mummy, papa, Jahnvi and all my fur babies
Feido, Lucy, Pheobe and Casper.

Chapter 1

Context and Objectives

The growth of global energy consumption has facilitated the discovery and exploitation of new resources by human-kind. Nuclear energy is one of the latest energy sources to be used at a large scale.

The first efforts to use nuclear energy for electricity generation emerged by the year 1951, with the construction of the Experimental Breeder Reactor I (EBR-I) at Idaho, United States of America. EBR-I was the world's first electricity generating nuclear power plant. From then to the present date, the IAEA reports state a total of 449 nuclear power reactors in operation all over the world, with a combined net installed capacity of 397,650 MWe[1], contributing about 11% to the global electricity production[2].

The fundamental difference between a nuclear reactor and the other power generating reactors lies in the principle of energy generation. The energy generation in nuclear reactors is a result of a controlled fission chain reaction. A fission reaction is characterized by the absorption of a neutron by a heavy nucleus (the fuel atom), causing it to split into lighter nuclei (the fission products), more neutrons and releasing energy in the form of heat and kinetic energy of the fission products [1].

Nuclear reactors can be broadly classified into two types, on the basis of the energy of the fission causing neutron. These are known as the **thermal reactors** (which use low energy neutrons to cause fission) and the **fast reactors** (that use high energy neutrons).

[1] data extracted from https://pris.iaea.org/pris/

[2] http://www.world-nuclear.org/information-library/nuclear-fuel-cycle/nuclear-power-reactors/nuclear-power-reactors.aspx

The thermal reactors can be further classified on the basis of choice of fuel and moderator material (briefly discussed in Section 1.1) to be used. Of the different types, there exist two designs that make use of light water (H_2O) as a coolant as well as a moderator:

- Pressurized Light-Water Moderated and Cooled Reactor (PWR) and;
- Boiling Light-Water Cooled and Moderated Reactor (BWR).

Together, the PWR and BWR are also known as Light Water Reactors (LWR). The present work is focused on the Pressurized Water Reactors (PWR), the most commonly used Light Water Reactor (LWR) design for civilian purposes, representing nearly 66.6% (299 out of 449) of the total operating reactors in the world[3].

1.1 Operating principle of Nuclear Reactors

Like any other power plant, a nuclear reactor has the following three components :

- **reactor core**: it is the point of energy generation. The reactor core consists of the nuclear fuel, moderator material (to slow down the neutrons released from the fission reaction for sustaining the chain reaction) and the control rods (to control the rate of fission reaction) ;
- **heat transport system**: it consists of the coolant and the heat-exchange system, to transfer the generated energy 'out' of the reactor core for electricity generation;
- **turbine generator**: for conversion of the transferred energy to electrical energy, for the purpose of distribution.

For a typical PWR, the centre of the fission reaction (*i.e.* the reactor core) consists of numerous fuel assemblies, along with control rods. Each of these fuel assemblies is composed of numerous fuel pins (consisting of uranium oxide (UO_2) fuel pellets, encased in a Zircaloy cladding) grouped together like bundles. The reactor core is situated inside the reactor pressure vessel (RPV) along with the other control and structural material (mainly composed of steel), which has a constant circulation of the coolant (water) through the

[3]extracted from https://pris.iaea.org/PRIS/WorldStatistics/OperationalReactorsByType.aspx.

core and other materials to maintain optimal temperature conditions inside the vessel.

Under normal reactor operating conditions, the heat released due to the fission of fuel atoms is collected by the coolant, causing its temperature to rise. The heated coolant exits the reactor vessel to the heat transport system, where the heat from the coolant is extracted in the heat exchangers to form steam. This steam is passed to the turbine generator, where it is finally converted to electrical energy. The exhaust steam from the turbine generators is then condensed and recycled to be fed into the reactor pressure vessel again as coolant (schematic representation given in Figure 1.1[4].

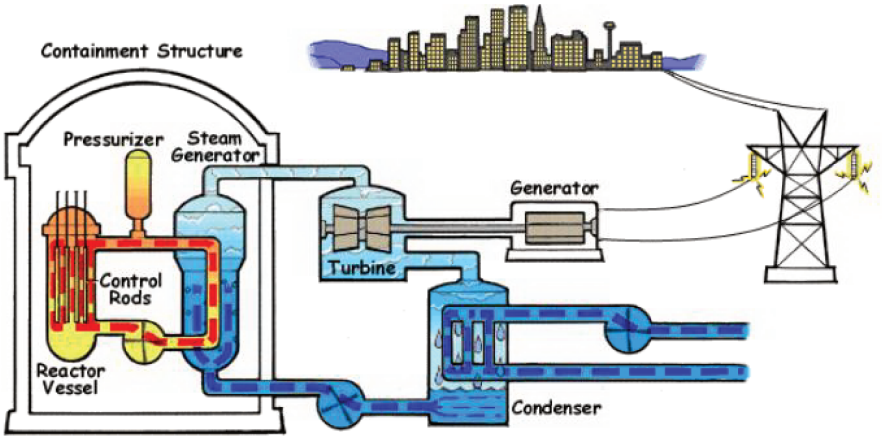

FIGURE 1.1: Operating principle of a Pressurized Water Reactor

1.2 Nuclear reactor safety and severe accidents

It is important to ensure safe operation of a nuclear power plant and to prevent and mitigate the impact of accidents that could lead to release of radiation into the environment. The approach to safe design and operation follows the concept of 'Defence-in-Depth' [2]. This approach provides a hierarchical deployment of different levels of equipment and procedures that help maintain the effectiveness of the three important physical barriers to the release of the fission products to the environment:

[4]extracted from https://www.nrc.gov/reading-rm/basic-ref/students/animated-pwr.html

- the clad on the reactor fuel (the point of generation for the fission products);
- the reactor vessel containing all the fuel elements together (to form the reactor core);
- and the leak-proof containment to prevent radioactivity release into the environment.

In line with this concept, the nuclear reactors are equipped with multiple independent and redundant safety systems apart from the basic components. These systems work in parallel to mitigate the risks associated with malfunction or operational errors during a 'design-basis accident' [5] and to prevent such situations from turning into major accidents that could lead to core meltdown.

However, the efficiency of any safety system is dependent on the accident for which it is designed and there may occur accident sequences that are not within the scope of the existing safety features. The possibility of occurrence of such 'beyond design-basis accident' (BDBA) sequences have been demonstrated by the accidents occurred at the Three Mile Island-2 (TMI-2) reactor (United States of America, 1979), the Chernobyl Reactor (Ukraine, 1986) and the most recent at the Fukushima Daiichi Nuclear Power Plants (Japan, 2011).

These accidents have stressed the need to adopt measures (in terms of safety systems for the present reactors and improved designs for future reactors) to mitigate the occurrence of accident scenarios that could lead to a core-meltdown accident (thus reducing its probability). Such accident scenarios are called 'severe accidents'.

1.2.1 Initiation and the progression of a severe accident in Pressurized Light Water Reactors

The accidents in LWRs can be classified as:

- reactivity initiated accident (RIA);
- loss of cooling accident.

[5] I.A.E.A. defines **design-basis accident** as "accident conditions against which a facility is designed according to established design criteria, and for which the damage to the fuel and the release of radioactive material are kept within authorized limits."

The first type of accident (RIA) occurs in the cases where there is an increase or insertion of reactivity in the reactor core, which could result from the malfunctioning of control rod driving mechanism. On the other hand, a cooling accident occurs when there is a malfunctioning/breakdown of the heat removal mechanisms (for maintaining the reactor core temperatures), which can result into a partial or complete meltdown of the core.

A loss of cooling accident in a nuclear reactor can be the result of a station blackout (SBO) or a loss of coolant accident (LOCA) sequence (or both). A station blackout (SBO) sequence is caused due to a complete loss of the off-site as well as the on-site alternating current (AC) electrical power[6] (as in the case of Fukushima Reactors). Such a condition has an adverse impact on the ability of the reactor to achieve safe shut-down conditions, risking the possibility of core damage. On the contrary, a loss of coolant accident (LOCA) represents the failure of the heat transport system arising from a break in the cooling circuit that can bring about core meltdown. LOCA can be characterized as a Large-Break LOCA (LBLOCA) or a Small-Break LOCA (SBLOCA), depending on the size of the break in the heat transport system, which together with the location of the break (*i.e.* in the primary or the secondary cooling circuit), determines how fast or slow the core degradation occurs. Within the spectrum of loss of cooling accidents, in terms of rate of core degradation, SBO is an intermediate case between the fast LBLOCA and the slow SBLOCA.

Further discussion is limited to the scenarios related to loss of cooling accidents that result in the meltdown of the reactor core.

1.2.1.1 Core melt initiation and the "early phase of core degradation"

Under normal operation conditions, the heat generated from fission chain reaction is constantly transferred to the flowing coolant and out of the reactor vessel by the help of the heat transport system, thus maintaining the integrity of the fuel cladding. However, a loss in the coolant flow can trigger emergency shutdown of the reactor where the fission chain reaction is brought to a halt. Despite stopping the chain reaction, heat is still being generated in the reactor core due to radioactive decay. If not managed properly, this heat can increase the fuel temperature and cause damage to the reactor core.

[6]The off-site AC power is supplied by the electrical grid to which the nuclear power plant is connected, whereas the on-site power is supplied by the emergency diesel generators. Both these alternate power sources are essential for a safe operation and accident recovery of the nuclear power plants.

Under such circumstances, the heating of the reactor core materials and their melting is strongly dependent on the composition and the configuration of the core. The following sequence of physico-chemical phenomena describes the early phase of core degradation in a PWR [2][3]:

- The increased temperature boils off the coolant present inside the core, thus lowering the overall coolant level in the RPV below the top of the active fuel region (a condition termed as "core uncovery").
- The low heat transfer properties of steam hinders the transfer of the decay heat produced from the fission products in the fuel, causing an increase in the reactor core temperature. The increasing temperatures ($\sim$ 1000 K) triggers changes to the mechanical properties of the clad, causing its deformation.
- At temperatures $\sim$ 1100 K, the control rod undergoes fusion to form molten Ag-In-Cd alloy.
- Interaction of the zircaloy clad with the steam at $\sim$ 1300 K results in its exothermic oxidation, that leads to its severe distortion and rupture. The clad rupture marks the breach of the *first* physical barrier against radiation release.
- Further increase in the temperature ($\sim 1500 - 1600$ K) facilitates the dissolution of absorber material (B_4C) into stainless steel and (as a separate event) the failure of control rods to form a eutectic melt of stainless steel-Zr and Ag-In-Cd-Zr. The melt relocates to lower (relatively cooler) regions of the core, where they tend to solidify again, blocking the flow channels between the fuel rods.
- The blockage of flow channels can cause accelerated heat up of the core, initiating dissolution of the UO_2 fuel (melting point 3100 K) in the molten Zircaloy (melting point $2030 - 2250$ K based on the degree of oxidation of the alloy) well below its melting point, to form a molten pool inside the reactor core.

This molten mixture consists of the uranium dioxide UO_2 fuel and the partially oxidized zirconium cladding ($Zr + ZrO_2$) and is known as corium.

1.2.1.2 Relocation of corium to the reactor vessel lower head - the "late phase of core degradation"

The molten corium pool eventually breaks out of the reactor core and progresses towards the lower head of the reactor vessel. As the corium is relocated from the core, it is likely to come in contact with the surrounding structural materials and the coolant (water) present in the lower head. The phenomena related to the late in-vessel phase of corium relocation depends on factors like:

- pressure of the reactor vessel;
- the amount and composition of the relocating corium;
- presence of water in lower head of the reactor vessel.

Depending on these factors, a list of possible scenarios include:

- impingement of the RPV wall (the *second* physical barrier against radiation release) by the melt jet in case of high pressure conditions;
- fuel-coolant interaction (FCI) in the 'wet' lower head (*i.e.* presence of coolant) which may or may not cause complete evaporation of the coolant. The FCI involves quenching and partial fragmentation of the corium jet[7] and a possible steam explosion. Steam explosion is a complex multi-step process, with its strength depending on factors such as the amount of relocating melt, temperature and the depth of water and the in-vessel pressure conditions. It is expected to pose a risk to the containment of radioactivity both in-vessel or ex-vessel (discussed later in the section). However, the OECD SERENA project [5] has concluded that the impact of steam explosion to induce failure of the RPV lower head can be ruled out as a possible risk to its integrity.

Assuming a complete evaporation of the coolant, the resultant debris bed at the bottom of the vessel, starts to re-heat due to the decay heat released by the fission products present in it. The re-heated debris, along with the un-quenched (or added) corium reaches a molten pool configuration which heats to a stationary state.

The contact of the heated corium pool with the reactor vessel wall results in the conduction

[7]The phenomenon of corium jet fragmentation was experimentally confirmed by the FARO tests [4].

of heat and partial ablation of the vessel wall. Inability to cool the reactor vessel wall can eventually cause its failure due to thermo-mechanical rupture or a meltout. The failure of the vessel wall denotes the breach of the second physical barrier and the beginning of the ex-vessel progression of the accident, where corium interacts with the concrete pit (also known as the reactor pit) of the reactor containment. This phase of corium progression is the last possible chance to contain the release of radioactivity in the environment.

The ex-vessel interaction of the corium pool can lead to two possible situations. On one hand, the FCI in the reactor pit could lead to a steam explosion[8]. On the other hand, corium spreads and interacts with the concrete lining of the reactor pit (molten corium-concrete interaction (MCCI)) [2], causing its ablation. At this stage, the effectiveness of preventing the escape of radioactivity into the environment depends on the thickness of the concrete lining in the reactor pit, the amount of water present in it (to cool the corium-concrete melt) and the rate at which the decay heat from the fission products in corium decreases.

The description of the various stages of corium progression (schematic representation given by Figure 1.2[9]) stresses on the importance of retention of corium within the reactor vessel in order to manage the release of radioactivity into the environment.

[8]Phase 2 of the SERENA project was focused on answering the uncertainties involved with ex-vessel FCI related to reactor containment integrity.

[9]extracted from [2].

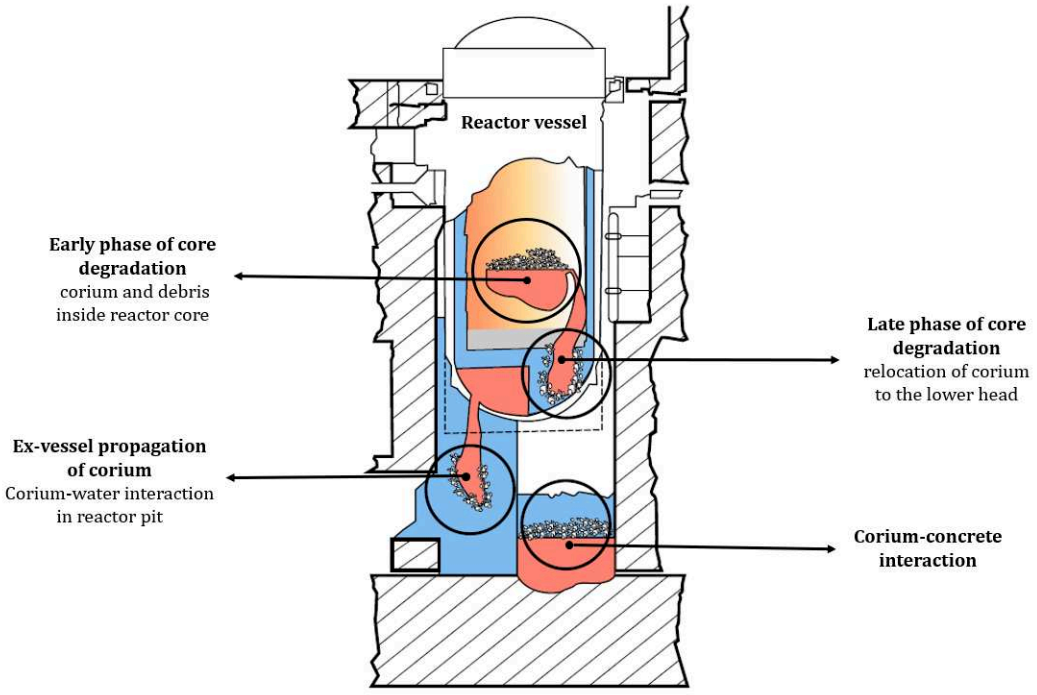

FIGURE 1.2: Different stages of corium progression during a severe accident

1.2.2 Severe accident analysis and management strategies

The phenomena associated with corium progression during a severe accident are not completely understood in the sense that there is either a lack of knowledge or the phenomena have not been modelled completely. This includes both approaches, where each phenomenon under investigation has been considered independently or in conjunction with another phenomenon. Moreover, based on how the accident progresses, the impact of these phenomena poses an uncertainty on the determination of thermal loads on the reactor containment structures. In order to predict the consequences of the phenomena and their overall impact on the integrity of the containment structure, the need for detailed studies to understand the phenomenology of these interactions was acknowledged. This marked the birth of severe accident analysis and its related management strategies.

The earliest worldwide organized efforts towards severe accidents analysis were made after the TMI-2 accident. Research projects for experimental as well as analytical development were initiated to conduct multi-disciplinary studies of the phenomena related to corium

and its interactions (based on the accident scenarios constructed from existing evidence) and to predict their consequences. The accuracy of these predictions were subject to the limitation posed by the scale at which the information was obtained. With the main focus placed on ensuring the integrity of the containment, management strategies were developed.

Reference [2] defines severe accident management (SAM) as "the use of existing and alternative resources, systems and actions to arrest and mitigate accidents that exceed the design basis of nuclear power plants". SAM strategies adopt a cyclic approach that includes:

- identifying the uncertainties related to the phenomenology associated with corium propagation and its interactions;
- identifying and prioritizing the risks related to these uncertainties with respect to the physical process under consideration;
- undertaking safety studies (numerical or experimental) to estimate the impact of these risks, and finally;
- comparison and verification of the acquired knowledge with similar other studies, to ensure complete understanding of the phenomena.

From the collective understanding of the corium behaviour, four major actions were recognized as a part of SAM strategies to ensure public safety :

- cooling of the degraded core;
- management of combustible gases;
- management of the containment temperature, pressure and integrity, and;
- management of the release of radioactivity.

As a result, two main design strategies have been employed for the coolability, stabilization and termination of severe accidents for the Gen-III reactors[10] and the future light water reactors, namely, the **in-vessel melt retention strategy** and the **ex-vessel melt retention strategy**.

[10]The Gen-III reactor designs are an improvement on the Gen-II reactor designs, with increased thermal efficiency, significantly enhanced safety systems, improved fuel technology and standardized designs for reduced maintenance and capital costs.

1.2.2.1 The In-Vessel Melt Retention (IVMR) Strategy

The IVMR strategy is based on the concept of flooding the cavity present between the reactor vessel and the containment pit with water, to submerge the vessel (either completely or partially) and to cool it from outside. The process of 'external' cooling of the vessel (ERVC) helps by ensuring that the in-vessel corium pool is cooled and stabilized thus preventing it from affecting the RPV wall integrity.

First introduced about 20 years ago ([6],[7]), the IVMR strategy was initially employed in the designing of the reactors AP600 [8] (later replaced by AP1000[9]) and as a back-fitting measure to the Loviisa VVER-440 [10]. The present day reactor designs of the Korean APR-1400 [11],[12],[13] and the Chinese HPR-1000 [14] have also been developed including IVMR concept, with an ongoing effort to study the possibilities of applying the same as a back-fitting measure for the operational Gen-II reactors[11].

1.2.2.2 The Ex-Vessel Melt Retention Strategy

The ex-vessel concept of melt retention has been adopted by the EPR design for reactors operational in Finland (and under construction at Flamanville (France) [15]) and for the Russian VVER 1000-91/99 designs constructed in Tian Wan (China) and Kudankulam (India)[16]. This strategy involves design concepts that include:

- Allowing the corium melt discharged from the reactor vessel (after RPV breach) to occupy a cavity and spread. Additionally, a layer of sacrificial concrete is installed over the cavity floor. The spreading process allows reduction of the corium pool depth to a level that can be directly cooled by a layer of water above the melt or with an indirect cooling system [17] composed of water filled channels. This concept has been adopted as a back-fitting measure to some existing Gen-II reactors [18].
- Another concept includes the presence of core-catcher that retains the molten corium flowing out of the reactor vessel [19]. The corium entering the core-catcher interacts with the sacrificial material located inside. Additionally, the core-catcher is externally cooled to transfer the heat away from the melt.

[11]Gen-II reactor refers to the design classification for nuclear reactors built until the end of 1980s. These designs include that of the PWR (Pressurized Water Reactor), CANDU (Canada Deuterium Uranium reactor, a Canadian pressurized water reactor), BWR (Boiling Water Reactor), AGR (Advanced Gas-cooled Reactor), VVER (Vodo-Vodyanoi Energetichesky Reaktor; "Water-Water Power Reactor") and the RBMK(Reaktor Bolshoy Moshchnosti Kanalnyy, "High Power Channel-type Reactor").

The success of these mentioned management strategies depends on their ability to eliminate any threats to the integrity of the containment. For the present thesis further discussions are focused on the in-vessel melt retention strategy.

1.3 Assessment of the uncertainties related to IVMR strategy

The success of the IVMR strategy depends on its ability to maintain the RPV wall integrity. Its effectiveness in ensuring vessel integrity is further related to the identification of the main processes and variables that are responsible, or pose a major threat to the RPV wall, followed by the modelling of the phenomena associated with them. Within this framework, a joint study was undertaken under the H2020 European project IVMR [20] , wherein the main risks to the safety demonstration of IVMR strategy were classified as :

- **Thermo-mechanical failure of RPV** through mechanisms like creep, plastic deformations etc.
- **Steady state heat flux values exceeding the Critical Heat Flux (CHF)**, resulting in the thermal breach of the RPV wall.
- **Transient condition interactions between in-vessel corium and the RPV wall**, leading to its excessive ablation.
- **Risk of Ex-vessel high energy steam explosion** in case the RPV fails[12].

The present thesis focuses on the risks to IVMR success that are associated with the effect of transient in-vessel corium interactions as well as steady-state conditions, that are imposed on the RPV wall, and may lead to a possible early melt-through of the wall. Thus, a detailed knowledge of the in-vessel corium behaviour is important. There are two possible approaches towards which investigations may be followed for understanding the in-vessel corium behaviour:

[12]As mentioned earlier, the risk posed by in-vessel steam explosion to the RPV integrity is not considered to be high. Nevertheless, it has an impact on the boundary conditions related to ex-vessel FCI, hence it needs to be considered.

- identification of the corium configurations that pose maximum thermal load on the RPV wall, or;
- tracking the transient conditions related to the in-vessel corium interactions to estimate their thermal impact on the RPV wall.

The following sections describe the in-vessel corium behaviour and the physical phenomena associated with it during steady state as well as transient conditions.

1.3.1 In-vessel corium behaviour : the "bounding" case approach

The in-vessel corium is a complex multi-component, multi-phase system composed of the molten fuel (UO_2), partially oxidized cladding (Zr, ZrO_2), reactor structural materials (stainless steel elements Fe, Cr, Ni) and the non-volatile fission products. Its behaviour is governed by two major phenomena :

- thermochemical interactions between the species constituting the corium pool, that can cause its separation into several liquid (immiscible) and solid phases;
- the thermal/thermal-hydraulic phenomena related to the natural convection in the pool that govern the heat flux distribution in the pool and at the pool-RPV wall interface.

The relocation of corium melt into the reactor vessel lower head, along with molten steel (from the melting of internal reactor structures) is a scenario dependent process, which also evolves with time. The high temperature molten mixture not only imposes high thermal loads onto the RPV wall, but also undergoes chemical interactions with the vessel wall material, which when coupled together can cause the RPV wall to melt. From the point of view of the IVMR strategy, the RPV wall melt-through can be prevented by an accurate estimation of the heat flux imposed by the corium pool on it for any configuration. Within this context, there is a consensus that the thermal load of an in-vessel corium configuration corresponding to an 'all liquid' state (*i.e.* all the corium and steel present in the system exists in liquid state after complete re-melting of the debris) is the maximum and that such corium configurations should be the basis of the IVMR studies.

The earliest approaches ([6], [7], [8] and [21]) were based upon considering a "bounding" case configuration, which was expected to represent the steady state configuration

that would be realized for any IVMR scenario [8]. This configuration corresponded to a completely molten oxidic pool in the lower head (corresponding to a complete melt of the debris and the structural material in the lower head), insulated from the RPV wall and the top metallic layer by an oxidic crust that is formed as a result of solidification of the corium pool layer in contact with the wall (see Figure 1.3).

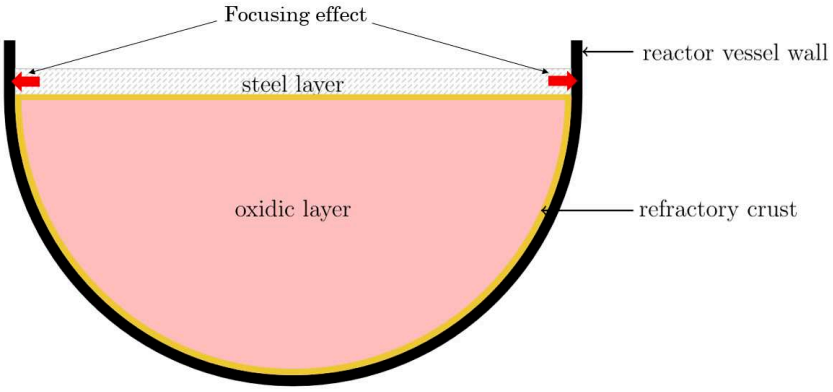

FIGURE 1.3: Two-layer configuration for in-vessel corium with a molten steel layer sitting atop the oxidic pool

In such a condition, one of the main threats to the integrity of the RPV wall is imposed by the top metallic layer. The oxidic pool transmits heat towards the vessel wall as well as its top surface through natural convection. The heat dissipated by the top surface of the oxidic pool is transmitted to the metallic layer. The high thermal conductivity of the metal layer combined with its low thickness results in high lateral heat flux being imposed on the RPV wall in contact with it. The high heat flux induces a phenomena called the "focusing effect" which could eventually cause melting of the vessel wall in contact with the metallic layer.

However, such a bounding case assumption does not take into account the thermochemical interaction between the corium-steel species and may not always exist in case of the postulated accident scenarios.

References [8] [22] have well documented the corium-steel composition (formed during the

late phase of the in-vessel progression) to lie within the domain of U-O-Zr-steel miscibility gap. The presence of a miscibility gap results in stratification of the liquid pool at thermochemical equilibrium conditions, to give two immiscible liquid phases that consists of:

- an "oxidic" phase that is rich in oxygen, and;
- a "metallic" phase rich in uranium and zirconium.

These liquid phases differ in their density, resulting in their gravity driven separation of corium to form a two-layer stratified pool. Supported by both experimental [23] as well as theoretical [24] studies, this repartitioning of the elements into two immiscible liquids is dependent on parameters like:

- the temperature (T) of the corium system;
- the atomic ratio U/Zr ($R_{U/Zr}$) and the degree of oxidation of Zr (C_n);
- the ratio between the mass of steel and corium present in the system x_{steel}.

For a given value of T, C_n and $R_{U/Zr}$, the possibility of phase segregation depends on a maximum "critical" mass of steel that corresponds to the presence of a heavy metal phase. When the amount of steel present in the system is less than this critical value (denoted by $\tilde{x}_{steel}$), the corium pool undergoes phase segregation and the heavy metal relocates to the bottom of the RPV. This relocation is a result of the redox reaction occurring in sub-oxidized corium UO_2+ Zr $\rightleftharpoons$ U + ZrO_2, with the equilibrium conditions favoring in the direction of the reduction of uranium dioxide to form metallic uranium, that is transferred along with zirconium into steel, forming the heavy metal phase. The formation of heavy metal phase is favored upto the point where the steel mass added to the system corresponds to $\tilde{x}_{steel}$.

Further addition of steel causes an inversion in the mass densities of the metallic and oxidic phases (depicted by Figure 1.4[13]), which is accompanied by the shift in the direction of the redox reaction, facilitating the oxidation of U and Zr present in the heavy metal

[13]The graph depicts the change in phase densities as a function of the amount of steel in the system. This calculation was obtained from the thermochemical equilibrium associated with the thermodynamic base NUCLEA09 [25] for the U-O-Zr-steel system and density laws implied in the codes TOLBIAC-ICB [26] and PROCOR [27].

layer. As a consequence, an inversion in the stratification occurs (explained further in Section 1.3.2).

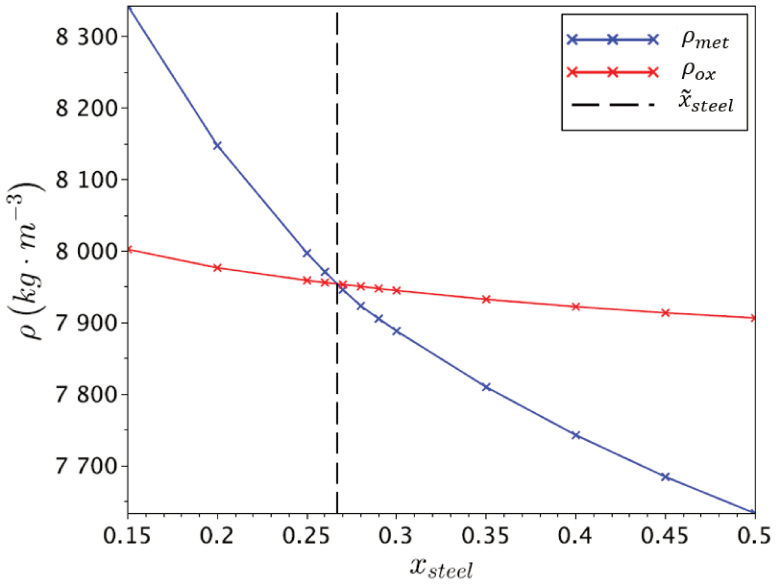

FIGURE 1.4: Evolution of densities for heavy metal (ρ_{met}) and oxidic (ρ_{ox}) phases, as a function of the amount of steel (x_{steel}) in the system for $T = 3000$ K, $R_{U/Zr} = 1.2$ and $C_n = 32\%$, where $\tilde{x}_{steel}$ denotes the critical steel mass for the present configuration

Based on the above mentioned trend, a three-layer bounding case can be defined (see Figure 1.5) to incorporate the thermochemical effects (as discussed in [22] [28] and [29]) corresponding to the critical value $\tilde{x}_{steel}$.

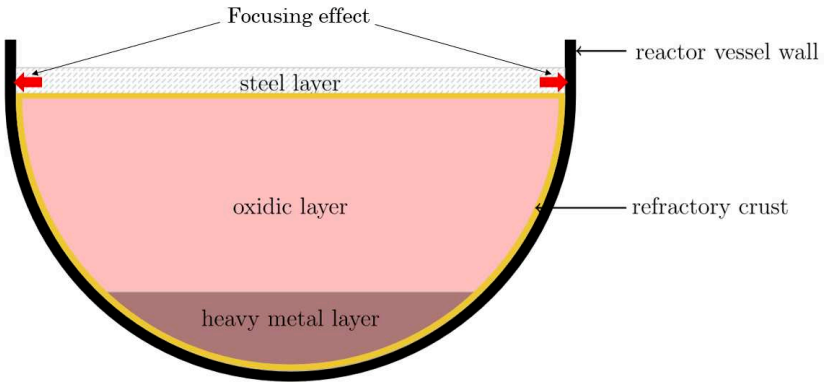

FIGURE 1.5: Three-layer configuration for in-vessel corium with a molten steel layer sitting atop the gravity separated corium pool

This configuration with the gravity separated oxidic and heavy metal phases and the upper molten steel layer, corresponds to a minimum thickness of the top steel layer. This situation poses an even greater threat to the RPV as the reduced thickness of the steel layer aggravates the problem of focusing effect, with the maximum possible heat flux being imposed on the RPV wall. For this reason, it was considered important to include the thermochemical behaviour for the modelling of in-vessel corium behaviour.

The bounding case approach, is limited in the sense that the possibility of stratification of corium pool depends, in particular, on the steel to corium mass ratio. The description of the above bounding case is given for an imposed ratio, which itself is related to both, the scenario and time dependent corium mass flow rate, as well as the steel mass introduced from the RPV wall ablation. These factors depend on the transient conditions posed by the evolution of the corium-steel system. In this context, the need for transient calculations based on these thermochemical interactions was identified as an important issue under the H2020 European IVMR project [20] for an improved knowledge of the in-vessel corium behaviour.

1.3.2 Transient conditions affecting the stratification of in-vessel corium

The study of transient corium-steel thermochemical interaction and its impact on the heat flux distribution and the transient focusing effect was conducted in the MASCA-RCW test

[30] [31] which was carried out within the framework of the OECD-MASCA experimental program [32].

As mentioned earlier in Section 1.3.1, the possibility of the presence of a three-layer stratified corium pool depends on the steel mass added to the system, which may not be even present if the initial system corresponds to a steel mass inventory that is greater than the critical mass to be present for causing stratification. Based on this parameter, two transient situations leading to the stratification of the corium pool and its inversion, can be considered. The occurrence of these transients can be explained with the help of the redox reaction occurring in the sub-oxidized corium (specific to the locations near the metal/oxide interface), and the consequent interaction with the metal layer.

For steel amount in the system being less than $\tilde{x}_{steel}$, the enrichment of the steel layer near the metal/oxide interface (as a result of the redox reaction) leads to formation of heavy metal globules in this layer. The difference in the densities of the heavy metal globules and the steel layer results in *Rayleigh-Taylor* instabilities, that eventually causes the gravity driven downward migration of the globules, to form a heavy metal layer.

Similar sequence of events are responsible for the transient conditions related to the inversion of the stratification. The formation of heavy metal is facilitated by the presence of free U and Zr in the oxidic layer near the steel/oxide interface. For the heavy metal layer present in contact with the bottom layer of the oxidic pool, an interaction between the metallic U and Zr species (from heavy metal phase) with oxygen (from the oxidic phase) results in the oxidation of the metal species and consequently, depletion of U and Zr from the heavy metal phase. This causes formation of light metal globules in the heavy metal layer and gives rise to similar *Rayleigh-Taylor* instabilities due to mass density difference. Eventually, the light metal globules rise to the top of the pool, bringing about stratification inversion.

1.3.3 Uncertainties associated with the phenomenology of in-vessel corium

The transient conditions can have a significant impact on the heat flux distribution in the corium pool, thus imposing a greater thermal load on the RPV wall than the values

estimated by the bounding cases. In addition, these transients also pose uncertainties regarding the in-vessel corium behaviour. The identification of these sources of uncertainties is of great importance from the the point of view of the success of the IVMR strategy.

The present section is focused on the description of the uncertainties specific to the two transients that have been identified in Section 1.3.2 for the mass transfer to obtain the equilibrium configurations [33]. Though these transient situations may not actually be followed in the same order during an accident scenario, they are useful in explaining all the possible uncertainties related to in-vessel corium.

1.3.3.1 Stratification of the in-vessel corium pool

The transient situations leading from a two layer corium configuration to a three-layer stratified configuration (depicted by Figure 1.6[14]) are a result of the interaction between the oxidic and the steel layers, followed by the diffusion of U and Zr species in the metal and the "ablation" of the upper molten steel layer to form an immiscible dense metal phase.

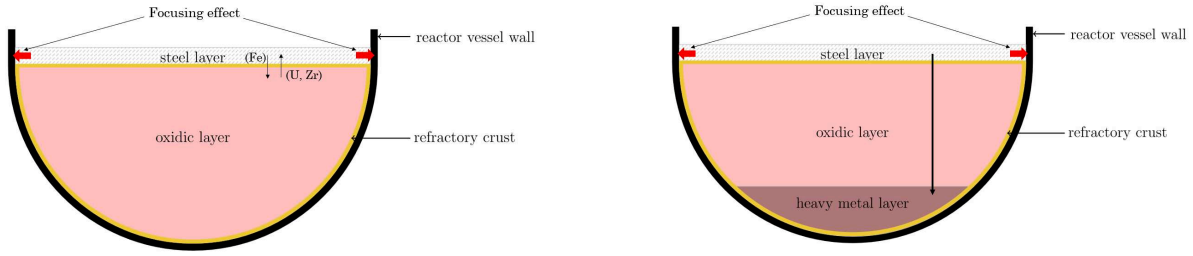

(A) Thermochemical interaction between oxide-steel layers

(B) Relocation of heavy metal layer to the bottom of the pool

FIGURE 1.6: Transient leading to the stratification of in-vessel corium pool

The initial lower head configuration (represented by Figure 1.6a) depicts the oxidic and steel layers, separated at the interface by a very thin refractory crust, which is also present along the RPV wall in the region occupied by the oxidic pool. The refractory crust along the RPV wall is formed as a result of the temperature gradient between the oxidic corium

[14]adapted from [34].

pool and the externally cooled RPV wall. It has a varying thickness that increases towards the bottom section of the wall. The crust acts as a "thermal barrier" against the heat flux transferred by the oxidic pool, thus preventing the fast ablation of the RPV wall. However, the top metal layer is not separated from the RPV wall by such a crust, which results in the vessel wall experiencing high lateral heat flux at the point of contact. This induces the focusing effect (see Section 1.3.1), which can eventually lead to vessel failure.

The thermal behaviour of the in-vessel pool for this configuration has been a subject of investigation for various experimental programs like COPO [35], ACOPO[21], BALI [36], RASPLAV-SALT, SIMECO[37] (for oxidic pool) , MELAD and BALI-metal (for the top metal layer). These experimental results have enabled defining the heat transfer correlations which can be applied to calculate the heat fluxes and the temperatures, which can be used to estimate the risk of reactor vessel melt-through. However, the correlations obtained are with respect to a steady state configuration. The use of these correlations to calculate heat fluxes under transient situations gives rise to uncertainties in the in-vessel corium description. Hence, development of improved correlations that can take into account the transient phenomena is required to ensure accuracy of the in-vessel corium description.

The horizontal refractory crust separating the oxidic pool from the steel layer (formed due to temperature gradient at the steel-corium interface) is very thin (of the order of millimeters) and probably unstable due to the mass transfer occurring between the steel and oxidic layers. Nevertheless, its presence acts as a "thermochemical barrier" against the steel-corium interactions, which has an impact on the kinetics of stratification.

As mentioned in Section 1.3.1, the transfer of species across the steel-oxide interface and the downward migration of the heavy metal phase (Figure 1.6b) poses a difficulty to the vessel wall integrity due to increased focusing effect.

1.3.3.2 Addition of steel and the inversion of corium pool stratification

The second transient (depicted by Figure 1.7[15]) is related to the inversion of the stratification.

[15] adapted from [34].

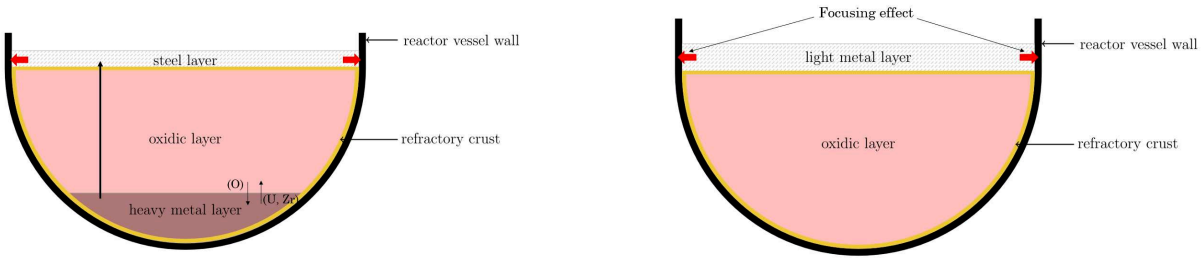

(A) Thermochemical interaction between heavy metal-oxide layers

(B) Inversion of stratification and the upward relocation of light metal layer

FIGURE 1.7: Transient leading to the inversion of stratification for in-vessel corium pool

The heavy metal layer, being deficient in oxygen, undergoes an exchange of species with the oxidic layer (schematic depicted by Figure 1.7a). This exchange of species, together with the addition of steel (from the melting of internal reactor structures) above the critical values facilitates the inversion of the stratification (as explained in Section 1.3.2) and the upward relocation of the super-heated light metal above the oxidic layer (final configuration depicted by Figure 1.7b).

This transient, leading to the upward displacement of metal, gives rise to a number of complications. Firstly, this relocation process has an impact on the stability of the horizontal crust present between the former steel-oxide layers (mentioned in Section 1.3.3.1). The interaction of molten metal with the oxidic crust can lead to its dissolution. Additionally, this relocated light metal layer also interacts with the refractory crust along the RPV wall, causing similar dissolution reactions in the lateral crust. This, combined with the thermo-mechanical phenomena such as local melting of reactor vessel wall in contact with the crust, mechanical load on the crust due to collapsing of in-vessel structures, stratification inversion process etc., has an impact on the lateral crust stability by posing a risk of its rupture. A break in the lateral crust results in the formation of localized high heat flux regions called 'hotspots' where the light metal comes in direct contact with the RPV wall. In such situations, the asymmetric thermal load experienced by the vessel wall can lead to its ablation. The problem of hotspot creation at the top of the pool is crucial as it poses greater uncertainties to the RPV integrity, that is under the influence of high heat fluxes due to focusing effect in this particular region. Consequently, such a configuration

(depicted by Figure 1.8) is more penalizing than the bounding case considered with all the molten metal sitting atop the oxidic pool (Figure 1.7b).

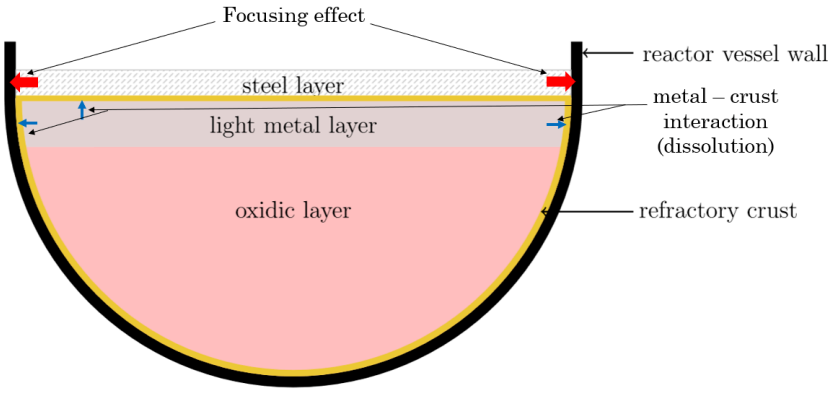

FIGURE 1.8: Transient in-vessel corium configuration with the relocated light metal on top of the oxidic pool.

It should be mentioned that the dissolution process also occurs for the crust in contact with the previously located heavy metal layer. However, the considerable threat of its complete dissolution and the formation of hotspots is less, owing to the greater thickness of the crust in contact with the heavy metal.

The impact of the steel-crust interactions on the stability of the oxidic crust has been the focus of the studies conducted under the CORDEB2 program [38]. In particular, the mechanisms involved with crust dissolution process have been determined by the VITI-CORMET experiments [39].

From the above discussions, it is evident that for a better thermodynamic description of the in-vessel corium, there is a need for detailed study of the thermochemical phenomena associated with in-vessel corium. In this respect, the two major sources of uncertainty are related to the knowledge on the:

- kinetics of the stratification process, and;
- thermochemistry of the oxidic crust, in particular the molten steel-crust interactions.

The existing analyses take into account the thermal role of the crust, which is of importance to maintain the integrity of the RPV wall. However, it is also required to understand the thermochemical phenomena (*i.e.* the dissolution process) associated with the oxidic crust as it not only impacts the kinetics of stratification, but also effects the thermo-mechanical stability of the crust itself.

1.4 Modelling of in-vessel corium: state-of-the-art and research avenues

The thermochemical-thermohydraulic phenomena related to in-vessel corium propagation evolve spatially and temporally with the changing temperature and composition of the corium pool. Under such situations, the time associated to the evolution of in-vessel corium and its postulated effect on the safety of the RPV vessel can be analyzed by the help of statistical calculations performed by the state-of-the-art numerical codes.

These numerical codes are either integral (ASTEC [40], MELCOR [41], MAAP [42], SOCRAT, ATHLET-CD) or specific to the studies related to the IVMR strategy (PROCOR [27], SIMPLE, HEFEST_URAN and IVRSYS) and have been developed by making use of the existing "shared" knowledge on the in-vessel corium behaviour, in order to estimate the heat flux distributions on the RPV wall during transient conditions. By taking into account the bounding as well as transient cases, the construction of such codes involves writing of energy and mass conservation equations for each of the defined layers, with the dependent variables averaged over space (thus being macroscopic in nature). The conservation equations are supplemented with models related to the thermochemical phenomena associated with these layers (such as models for mass transfer for the stratification) and the closures to the equation set is provided by the "closure laws" obtained from the results of the experimental studies.

The comparison of the various codes for obtaining a consolidated set of results was a part of the H2020 European project IVMR (2015-2019), wherein a step-wise approach was followed to study the impact of uncertainties related to the corium pool modelling at

different stages of in-vessel melt progression [28], first separately, and then by progressively increasing the complexity of the situation. Finally, a series of benchmark activities with sensitivity studies were conducted to assess the capability of these SA codes [43]. These studies helped in the identification of the sources for uncertainties, which need further research and developed for better performance of the SA codes. These include:

- **Uncertainties related to the kinetics of in-vessel corium stratification:** There have been efforts to develop transient thermochemical models ([29] [33]) based on the corium pool behaviour in the presence of a miscibility gap [22]. These transient models allow for an estimation of the kinetics of the stratification process. However, there is a lack of experimental data to validate these evaluations. In particular, there is no experimental information on the process of the inversion of the heavy metal layer. The experiments conducted under the MASCA program do indicate the formation of the heavy metal layer, but the characteristic time related to its inversion is unknown. Such an uncertainty can significantly alter the thermal load on the reactor vessel, and was found to be one of the major sources for large discrepancies in the results obtained during the benchmark activities of the SA codes [43].

  As a supplement to these experimental evidences, the development of numerical based simulations on a mesoscopic scale (also known as "fine" models) to study the kinetics of the responsible thermochemical processes could also be useful. The first steps in this direction were undertaken in [44], where a mesoscopic thermochemical model was developed to study the kinetics of stratification in terms of multi-component and multi-phase diffusion.

- **Lack of detailed modelling of the oxidic crust:** The present codes either do not take into presence of the oxidic crust, or it is assumed to be in quasi-static state. Such an assumption to the model has an impact only in terms of the boundary conditions specified for the solving of the conservation equations. However, the behaviour of the crust as a thermochemical barrier has a greater impact on the kinetics of the stratification process (discussed in Section 1.3.3). In addition, the interaction of the crust with the relocated light metal layer and its dissolution is of importance to its overall thermo-mechanical stability. Thus, detailed thermochemical-thermohydraulic modelling of the crust is needed which includes the interactions associated with it. A first step in this direction has been taken in context of the PROCOR platform [45].

Such models also require experimental evidences regarding crust thermochemistry, which are part of the ongoing CORDEB-2 and VITI-CORMET experiments.

An accurate description of the in-vessel corium requires not only the development of new thermochemical models, but also their coupling with the thermohydraulics models. As a consequence, such a coupling raises the issue of consistency of the thermodynamic description of the corium system. A partial or incomplete coupling between the thermochemical-thermohydraulic models could lead to erroneous calculations by the SA codes, which would have an impact on the accuracy of the IVMR strategy. One possible way to improve consistency is by using a common source for thermodynamic description (*i.e.* thermodynamic database) for deriving the inputs required by the thermochemical and thermohydraulic models. This can be achieved by coupling the thermodynamic database with the 'already coupled' thermochemical-thermohydraulics models. However, such a coupling may pose certain questions or constraints in terms of thermochemical-thermohydraulic modelling and it is imperative to answer the questions that will be associated to its feasibility.

This brings us to the objective of the present thesis work. This work aims at the development of a methodology for the coupling of the thermodynamic database to the thermochemical-thermohydraulic models for in-vessel corium description. The proposed methodology is tested on 'mock-up' macroscopic and mesoscopic models developed for studying corium progression.

The development of the macroscopic model for plane front solidification under PROCOR is focused on testing the consistency of the coupling between the thermochemical-thermohydraulics models with the thermodynamic database and is a step towards the thermochemical-thermohydraulic modelling of the crust during the solidification process. The question of thermodynamic consistency is also answered for the model developed at the mesoscopic scale, which seeks to provide a general formulation for the energy and mass balance equations that can be applied to study the kinetics of various thermochemical processes like solidification and phase separation. As a consequence, the information obtained from the mesoscopic simulations can be incorporated into the development of new thermochemical models in PROCOR.

Chapter 2

Methods and Tools

As previously mentioned, the objective of the thesis is to develop a methodology for the coupling between a thermodynamic database as a source of input and the coupled thermochemical-thermohydraulic models for obtaining a consistent description of the corium system. This consistency in the description can be achieved by making use of a single, exhaustive source for the thermodynamic representation of the system throughout all the different models and the respective closures.

The thermodynamic databases constructed from the CALPHAD method (specific to the SA studies) offer such a representation by providing information on the thermodynamic quantities. These quantities include the thermodynamic potentials like the Gibbs free energy (G) of the system and its derivatives such as entropy (S), enthalpy (H), specific heat capacity etc. In addition to these thermodynamic quantities that can be derived from CALPHAD, several thermophysical quantities (thermal conductivity, viscosity, etc.) are also required for the construction of the thermochemical models. These properties cannot be directly obtained from CALPHAD and require other sources. At the same time, the thermohydraulic models also require the thermophysical properties as inputs for providing consistent 'closures' to the conservation equations.

As various thermochemical models for studying the in-vessel corium behaviour rely on the description provided by these CALPHAD databases, it is considered to be a feasible choice for the 'single' source of thermodynamic information, which can be coupled to the thermochemical-thermohydraulic models for ensuring a consistent description.

Within the context of the present thesis, such a coupling has to be carried out for the mathematical models developed at different spatial scales (*i.e.* a macroscopic and a mesoscopic model). Regardless of the scale at which it is being implemented, a traditional mathematical model is composed of a set of governing equations (such as the mass and energy balance equations) based on underlying hypotheses, with a set of initial and boundary conditions. These set of equations can be solved analytically as well as numerically (with the help of simulations). However, the analytical approach is limited to simple cases and, in general, numerical simulations are required. The use of these models for obtaining quantitative information on the system requires correct inputs, which in this case, can be offered through the coupling with CALPHAD database.

The present chapter focuses on providing a general description of the method for the utilization of information in the thermodynamic database (Section 2.1) and for the development of the numerical models at the two scales of interest (Section 2.2).

2.1 The CALPHAD approach for thermodynamic description of in-vessel corium

For a given alloy system, its phase diagram is necessary to understand the relationship between the composition, processing conditions, the resulting micro-structure and finally the effect on material properties. The correctness of these phase diagrams (consequently the predictions made by their use) depends on the accuracy of the thermodynamic properties of the material on which they are based. However, for complex multi-component systems like in-vessel corium, this data is not readily available. Therefore, one can make use of the computational methods like CALPHAD (CALculation of PHAse Diagram) for modelling the thermodynamic properties and phase diagrams for the system.

The CALPHAD method makes use of mathematical models to describe the thermodynamic properties (e.g. Gibbs energy, entropy, enthalpy, etc.) of the possible phases for a system, as functions of the thermodynamic state variables such as temperature (T), pressure (p), composition and certain adjustable parameters [46]. The developed models

are assessed based on the collected experimental data (from techniques such as calorimetry, X-ray diffraction techniques, solubility limit studies etc.) and the results of ab initio calculations, to determine the adjustable parameters. This is followed by an optimization of the models, which results in obtaining the values for the adjustable parameters, such that they offer the best possible agreement between the experimental and theoretically calculated data.

The parameters obtained as a result of the assessment and optimization process are assembled to form the thermodynamic databases, which can be utilized for:

- obtaining equilibrium thermodynamic description and/or for producing phase diagrams of higher order multi-component systems, and ;
- extrapolation of the data to obtain material thermodynamic properties outside the range of stability for a phase.

Figure 2.1 gives a schematic representation[1] of the construction of thermodynamic databases using the CALPHAD method.

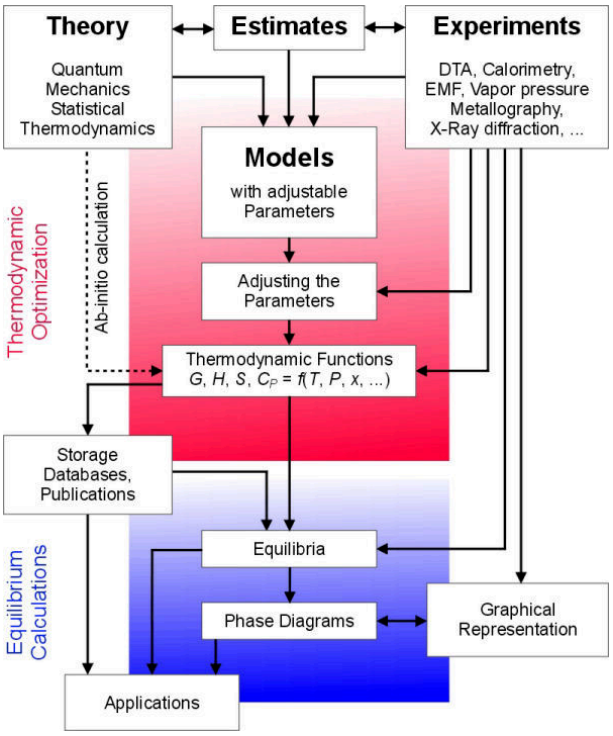

FIGURE 2.1: Schematic representation of the CALPHAD method

[1]extracted from [47].

2.1.1 Description of a system and calculation of thermodynamic equilibrium using CALPHAD method

Within the CALPHAD approach, the thermodynamic system is composed of "components"[2]. The components can combine to form "constituent" species (denoted by $\mathbb{S}$) that define the composition of a phase. It should be noted that for a thermodynamic system, the number of components and constituents may not be the same. Take for example the H-O system: The components of this thermodynamic system are the elements H and O, whereas the gas phase of the system (at low temperatures) can be composed of constituent species H_2, O_2 and H_2O.

The CALPHAD database is composed of Gibbs molar energies[3] G_M^θ for all possible phases θ that can be exhibited by the system. For a particular phase, the molar Gibbs energies ($\mathcal{G}_M^\theta$) are described as models consisting of mathematical functions dependent on the state variables such as temperature (T), pressure (p), composition $(y_i^\theta)_{i\in\mathbb{S}}$:

$$\mathcal{G}_M^\theta : T, p, (y_i^\theta)_{i\in\mathbb{S}} \rightarrow G_M^\theta \tag{2.1}$$

Keeping a general expression for the dependence of Gibbs energies on temperature and pressure, the Gibbs energy of a system is strongly dependent on the composition. This dependence on composition is affected by the strength of interactions between the constituents, which is not the same for all phases. As a result, it is not possible to have a single model for all phases and a general formalism needs to be adopted. As a consequence, the Compound Energy Formalism (CEF) [48] [49] has been adopted, which supports most of the models (based on composition dependency) such that an appropriate model for each of the existing phases can be applied.

The CEF formalism assumes the distribution of the constituents of a phase (*i.e.* ions,

[2]The components can be elements or stoichiometric compounds, depending on the way the system has been defined.

[3]In principle, all the thermodynamic properties like entropy, enthalpy etc. can be modelled in CALPHAD. However, the choice for modelling the Gibbs energy is based on two reasons: 1) all the experimental data are obtained at constant temperature and pressure conditions, and 2) the other thermodynamic properties can be easily obtained from the Gibbs energy by the use of thermodynamic relations.

neutral atoms, vacancies, etc.) into one or more sub-lattices[4] (denoted by s), where they mix according to the classical solution theory (ideal or non-ideal model). The interaction parameters related to the mixing are different in different sub-lattices. The Gibbs energy for a phase is described per mole of formula unit[5]. As a result, instead of the overall phase composition y_i^θ, Eq. 2.1 is dependent on the molar fraction of the constituent i on a sub-lattice (denoted by $y_i^{(s)}$), with $\sum_i y_i^{(s)} = 1$:

$$\mathcal{G}_M^\theta : T, p, (y_i^{(s)})_{i,s} \rightarrow G_M^\theta \tag{2.2}$$

where the molar fraction of the constituent $y_i^{(s)}$ for a sub-lattice s is expressed as the ratio between the number of sites occupied by the the constituent i on the sub-lattice s (denoted by $N_i^{(s)}$) to the total number of sites present on it (denoted by $N^{(s)}$).

$$y_i^{(s)} = \frac{N_i^{(s)}}{N^{(s)}}$$

For this sub-lattice model, the constituent composition for the phase θ can be obtained in terms of the end member fractions $y_I^{\theta,(s)}$. An "end member" represents a single constituent present in each sub-lattice of a crystal with long range order[6]. The endmember fraction $y_I^{\theta,(s)}$ for constituent i is given by the product of $y_i^{(s)}$ in each sub-lattice s :

$$y_I^{\theta,(s)} = \Pi_s y_{i\in I}^{\theta,(s)} \tag{2.3}$$

When a phase has no sub-lattices, the end member specifies a single constituent of the phase and the above fraction denotes the constituent fraction y_i^θ.

In this way, from the description of the Gibbs energy of each phase given by Eq. 2.2, the

[4]The term 'sub-lattices' can have different physical meanings in different phases. For instance, in ionic liquids, they can be used to separate anions and cations, whereas for alloys they can be identified with crystallographic sub-lattices, which represent the geometric arrangement corresponding to the first co-ordination sphere for any atom.

[5]The formula unit for a phase is defined as the sum of all the sites in all the sub-lattices of the phase ($\sum_s a^{(s)}$).

[6]A long-range ordering is present in crystals, where dislike constituents tend to be present together as clusters, such that these interactions are effective over greater distances, which is not the case for short-range ordering, where this tendency of formation of clusters exists only for the first, or in some cases second nearest-neighbours.

total Gibbs Energy for the system (G) can be obtained as :

$$G = \sum_{\theta} n^{\theta} G_M^{\theta} \tag{2.4}$$

with n^{θ} representing the amount of phase present in the system (in terms of amount of constituents per formula unit).

Each of these individual Gibbs energies (G_M^{θ}) are expressed as an addition of various contributions [50]:

$$G_M^{\theta} = {}^{srf}G_M^{\theta} + {}^{cfg}G_M^{\theta} + {}^{phy}G_M^{\theta} + {}^{E}G_M^{\theta} \tag{2.5}$$

where :

- ${}^{srf}G_M^{\theta}$ represents the Gibbs energy of a mixture of species constituting the phase θ, where each of the species is assumed to be isolated;
- ${}^{cfg}G_M^{\theta}$ is the contribution from the assumption of an ideal mixing of the species, corresponding to all the possible configurations in which they can exist;
- ${}^{phy}G_M^{\theta}$ represents the contributions to the Gibbs energy due to any particular physical phenomena that may be exhibited by the phase, such as magnetic transitions, and;
- ${}^{E}G_M^{\theta}$ describes the contribution of the excess Gibbs energy. The excess term represents the real behaviour of the phase, by taking into account the other interactions within the system (such as the effect of non-ideal mixing behaviour on the thermodynamic properties, the reactions between the species, etc.)

The thermodynamic equilibrium of the system for a fixed value of the state variables can be obtained by minimization of the total Gibbs energy (G), which can be achieved through the help of a Gibbs Energy minimizer code.

2.1.2 CALPHAD databases for in-vessel corium systems

A minimal description for the in-vessel corium can be provided by a quaternary system U-O-Zr-Fe. Particular to the application, the modelling of liquid and solid phases for corium description omits the dependency of the Gibbs energy on pressure. As a result, the pressure variable p in Eq. 2.2 is neglected (except for the modelling of the gaseous phase). There exist two databases that are widely used for obtaining corium descriptions: NUCLEA

[25] [51] and TAF-ID (Thermodynamics of Advanced Fuels-International Database) [52].

The NUCLEA database describes the Gibbs energy of a phase by making use of a non-ideal 'associate' model with a single sub-lattice, that takes into account the interactions between the elements (for e.g. elements A and B), to form associate species[7] of the form A_aB_b. Consequently, the constituents of this sub-lattice include the species A, B and the stoichiometric compound A_aB_b, which also are the end members. As there exists a single sub-lattice, the end member fraction for each species i (given by Eq. 2.3) reduces to represent the species composition y_i^θ in the phase. For such a case, a generalised relation for the concentration of the element i in terms of mole fractions (x_i), can be obtained with the help of the mole fraction of the species j (y_j) formed by it :

$$x_i = \frac{\sum_j b_{i,j} y_j}{\sum_k \sum_j b_{k,j} y_j} \tag{2.6}$$

where $b_{i,j}$ represents the stoichiometric coefficient for element i in the species j. The Gibbs energy functions for the model are written in terms of species (constituent) compositions. Introduction of the "associate species" as a new constituent for writing the Gibbs energy of formation, provides an internal degree of freedom which can be used to fit the experimental data.

The TAF-ID database, on the other hand, makes use of an ionic model (given by Eq. 2.7) to describe the liquid phase. This ionic model consists of two sub-lattices, where one sub-lattice is composed of constituents in the form of cations A, and the other sub-lattice consists of anions B, hypothetical vacancies Va (in order to model metallic liquid systems) and neutral species C_k^0 (for modelling non-metallic liquid systems). The charge on a cation (respectively on an anion) is indicated by v_i^+ (respectively v_j^-), where i, j are the specific constituents. These ions (or vacancies) occupy a number of sites (denoted by P for cations and Q for anions) on each sub-lattice, the value of which depends on the constituent fraction.

$$(A_i^{v_i^+})_P (B_j^{v_j^-}, Va, C_k^0)_Q \tag{2.7}$$

[7] Reference [47] introduces the term "associate" to denote the species formed for a shorter time duration, due to weak interactions between the atoms. Thus, the formed associate molecule is not stable in nature.

The present thesis makes use of a database that has been extracted from NUCLEA database (version 09), in combination with the Gibbs energy minimizer (see [53] for details on the algorithm) incorporated in the OpenCalphad (OC) software which is used through an interface in PROCOR for obtaining thermodynamic properties such as specific enthalpies for the system, as well as the interface temperature and composition related to local equilibrium condition.

2.2 Tools for numerical modelling

The numerical analysis includes different approaches, which can be classified into two broad categories [54] :

- lumped parameter models that consist of conservation equations integrated over large spatial zones (such as the stratified layers in a corium pool), and;
- distributed parameter models which consist of conservation equations that have been written for a spatial domain discretized by a mesh.

Within the context of SA studies, both kinds of models are useful for obtaining the relevant information. For instance, the lumped parameter models make up the integral codes such as MAAP, ASTEC etc. The purpose of these integral codes is to simulate SA conditions for a LWR. Similar to this, the integral code developed under the PROCOR platform of CEA is dedicated specifically to the study of corium progression. The platform consists of various physical models and their associated parameters for describing the various aspects associated with corium (for e.g. models related to a stratified corium pool, transient corium propagation to the lower head, corium-concrete interactions, etc.). Each of these models are constructed as a lumped parameter model to describe the evolution of corium for a spatial domain defined on a macroscopic scale (*i.e.* in the order of meters), which when combined, predicts the evolution of corium over a complete SA sequence.

On the contrary, the distributed parameter models are used to gain a better understanding of a particular set of phenomena by "zooming" into a particular part of the overall transient that takes place in an SA sequence. In this respect, the conservation

equations for these distributed parameter models have a limited scope in terms of the part of the SA sequence being studied or spatial domain described. Consequently, the system (within this domain) is represented through these distributed parameter models which are constructed on a mesoscopic scale (*i.e.* in the order of millimeters). Based on this choice of spatial scale, such models are useful for constructing detailed thermochemical models, which can be coupled with the thermohydraulic models based on Computational Fluid Dynamics (CFD) to obtain quantitative results related to these specific parts of the transient. Consequently, the information obtained from this approach can be used for improving the integral codes.

2.2.1 Lumped-Parameter models for integral codes

The lumped parameter models consist of zones or 'control volumes' (denoted by $\mathcal{V}_c$, where c represents the zone defined in the model) that are separated through interfaces (denoted by $\beta_{(i,j)_{i\neq j}}$), which may be fixed in space (with heat flux continuity) or mobile (related to a Stefan condition). Each of these zones are represented by mass averaged properties such as specific enthalpy, composition, etc. considering that the necessary closure laws for the conservation equations can be expressed in terms of these variables.

Within the context of using lumped parameter approach for modelling in-vessel corium, the determination of heat flux values for the system requires solving of the mass and energy conservation equations. The closures to the energy conservation equation depend on how the energy transfer in the system is defined. Since the corium flow is considered to be governed by natural convection under the assumption of the Boussinesq approximation, the closures for the energy conservation equations can be related to the dimensionless Rayleigh number (Ra). As a consequence, the closures do not depend on the velocity of the fluid flow, thereby excluding the need to solve the momentum conservation equation. Consequently, the mass and energy conservation equations along with their associated interface conditions, are cast into an integral form in terms of macroscopic conservation equations.

For a physical model consisting of a zone i with $N(i)$ neighboring zones, the mass and energy conservation equations for the i^{th} zone can be written according to the general

formulation of conservation equations as discussed in Appendix A:

$$\frac{dm_i(t)}{dt} + \sum_{i \in N(i)} \dot{m}_{\beta_{i,j},i}(t) + \dot{m}_{i,ext} = 0 \tag{2.8}$$

$$\frac{d}{dt}\left(\bar{h}_i m_i\right) + \sum_{j \in N(i)} \left(\bar{\varphi}_{\beta_{i,j},i} A_{\beta_{i,j}} + \bar{h}_{\beta_{i,j},i} \dot{m}_{\beta_{i,j},i}\right) + \bar{h}_{i,ext} \dot{m}_{i,ext} = \dot{q}_i^{mass} m_i \tag{2.9}$$

with the associated interface conditions formulated as:

$$\dot{m}_{\beta_{i,j},i} + \dot{m}_{\beta_{i,j},j} = 0 \tag{2.10}$$

$$\bar{h}_{\beta_{i,j},i} \dot{m}_{\beta_{i,j},i} + \bar{h}_{\beta_{i,j},j} \dot{m}_{\beta_{i,j},j} + (\bar{\varphi}_{\beta_{i,j},i} + \bar{\varphi}_{\beta_{i,j},j}) A_{\beta_{i,j}} = 0 \tag{2.11}$$

where:

- m_i represents the total mass of the zone (kg^1), which is a function of time t (s^1);
- $\beta_{i,j}, i$ (respectively $\beta_{i,ext}$) is the interface between the neighboring domains i, j (respectively between zone i and the system boundary);
- $\dot{m}_{\beta_{i,j},i}$ (respectively $\dot{m}_{i,ext}$) is the mass flow rate of i ($kg^1 s^{-1}$) associated with the interface $\beta_{i,j}, i$ (respectively the mass flow rate associated with the system boundary $\beta_{i,ext}$), which is positive for a mass flow that is directed out of the zone i and (respectively) negative for the mass flow directed towards the zone i;
- $\bar{h}_i$ is the mass-averaged specific enthalpy ($J^1 kg^{-1} K^{-1}$) of the zone i;
- $A_{\beta_{i,j},i}$ is the area (m^2) of the interface $\beta_{i,j}, i$ between the zones i and j;
- $\bar{\varphi}_{\beta_{i,j},i}$ denotes the averaged heat flux ($W^1 m^{-2}$) associated with surface $A_{\beta_{i,j},i}$, which is positive if the flux is directed out of the zone i towards the interface $\beta_{i,j}, i$ and negative if the flux is directed inside the zone i from $\beta_{i,j}, i$;
- $\dot{q}_i^{mass}$ is the mass averaged heat source associated with the zone i (represented as power density $W^1 kg^{-1}$).

The above set of equations is supplemented by equations relating the composition of the spatial zones, each of which (*i.e.* the composition) is represented by the mass fraction ($\bar{w}^k$) of the species $k \in \mathbb{S}$. This representation has been considered for the codes TOLBIAC-ICB [26] and PROCOR, where the thermophysical properties associated with the zones

are written as mixing laws applied to species density functions of temperature. Further discussion on these species conservation equations is presented in Chapter 3.

2.2.1.1 Closures to the conservation equations

For any spatial zone, the closure of the energy conservation equations Eq. 2.9 and the associated interface condition Eq. 2.11 requires appropriate enthalpy-temperature relations. For a multi-component system such as corium, these relations must take into account the dependence on the chemical composition [55] along with their dependency on temperature and pressure, for a consistent thermodynamic description of the system. In general, the dependency of the relations on pressure is neglected for studies related to corium liquid phases, which are assumed to be compatible with the Boussinesq approximation of fluid dynamics (see [56]) while modeling natural convection.

In this framework, the enthalpy-temperature relation can be described in a general way by the function:

$$\mathcal{H} : \bar{T}, \left(\bar{w}^j\right)_{j\in\mathbb{S}} \rightarrow \left(\bar{h}_\theta, \omega_\theta, \left(w_\theta^j\right)_{j\in\mathbb{S}}\right)_{\theta\in\mathbb{P}} \tag{2.12}$$

where:

- $\bar{T}$ is the average temperature (in K);
- $\left(\bar{w}^j\right)_{j\in\mathbb{S}}$ is the average composition defined in terms of mass fraction $\bar{w}^j$ for all species $j \in \mathbb{S}$;
- ω_θ is the mass fraction of phase θ, having the composition (in terms of species mass fractions) $\left(w_\theta^j\right)_{j\in\mathbb{S}}$;
- $\bar{h}_\theta$ is the specific enthalpy (J/kg) of the phase θ, and;
- $\bar{h}$ is the average specific enthalpy (J/kg) which can be obtained from the relation $\bar{h} = \sum_{\theta\in\mathbb{P}} \left[\omega_\theta \bar{h}_\theta\right]$.

Such relations are referred to as "Equation-Of-State" (EOS) and can be used to obtain a reciprocal temperature-enthalpy relation by solving the non-linear root-finding problem:

$$\text{find } \bar{T} \text{ such that } \mathcal{H}\left[\bar{T}, \left(\bar{w}^j\right)_{j\in\mathbb{S}}\right] = \bar{h}$$

2.2.1.2 Enthalpy-temperature Relations provided by CALPHAD

Recalling that the Gibbs energies are modelled per formula unit (Eq. 2.2), the Gibbs energy per mole of components $\mathcal{G}_m^\theta$ ($J^1 mol^{-1}$) can be defined from Eq. 2.2 as:

$$\mathcal{G}_m^\theta : T, p, (y_i^{(s)}) \rightarrow \mathcal{G}_M^\theta(T, p, (y_i^{(s)})_{i \in \mathbb{S}}) / \sum_i \sum_s a^{(s)} \sum_k b_i(k) y_k^{(s)} \tag{2.13}$$

where:

- $a^{(s)}$ denotes the number of sites occupied by the sub-lattice s;
- $b_i(k)$ refers to the stoichiometric coefficient of component i in the constituent species k, and;
- the denominator $\sum_i \sum_s a^{(s)} \sum_k b_i(k) y_k^{(s)}$ represents the number of mole of components per formula unit.

In the same way, one can obtain the specific Gibbs energy $\mathcal{G}^\theta$ ($J^1 kg^{-1}$) for a phase θ, by multiplying the molar masses (M_i) of each component i to their respective stoichiometric coefficients:

$$\mathcal{G}^\theta : T, p, (y_i^{(s)}) \rightarrow \mathcal{G}_M^\theta(T, p, (y_i^{(s)})_{i \in \mathbb{S}}) / \sum_i \sum_s a^{(s)} \sum_k M_i b_i(k) y_k^{(s)} \tag{2.14}$$

As a consequence, the above function can be directly used to obtain functions that describe other thermodynamic properties by making use of appropriate thermodynamic relations. For instance, keeping in mind the present requirement of evaluating specific enthalpy, the associated function can be obtained from the thermodynamic relation:

$$H = G - TS \tag{2.15}$$

$$\mathcal{H}^\theta : T, p, (y_i^{(s)})_{i,s} \rightarrow H^\theta = \mathcal{G}^\theta(T, p, (y_i^{(s)})_{i,s}) + T\mathcal{S}^\theta(T, p, (y_i^{(s)})_{i,s}) \tag{2.16}$$

where $\mathcal{S}^\theta$ is the specific entropy functional ($JK^{-1}kg^{-1}$) that is obtained from the derivative of the $\mathcal{G}^\theta$ as:

$$\mathcal{S}^\theta : T, p, (y_i^{(s)})_{i,s} \rightarrow S = -\frac{\partial \mathcal{G}^\theta}{\partial T}|_{p,(y_i^{(s)})_{i,s}} \Big(T, p, (y_i^{(s)})_{i,s}\Big) \tag{2.17}$$

Similarly, the specific heat capacity C_p can be obtained as a partial derivative of the enthalpy (given by Eq. 2.16) with respect to the temperature, for a constant pressure

condition.

Eq. 2.16 represents the general form of the enthalpy-temperature relation obtained for a phase θ from the CALPHAD database. Using such enthalpy-temperature relations to provide closures, first requires the knowledge regarding the representation of the composition at each sub-lattice. If the description of the composition is chosen to be in terms of the component mass fractions (discussed in Section 2.2.2.2), the utilization of the CALPHAD database will require additional constraints that need to be addressed. On the other hand, within the context of integral models for in-vessel corium, as the associate models used in NUCLEA database consists of a single sub-lattice with constituents as species, the representation does not change and Eq. 2.16 can be used as it is for a reduced (single sub-lattice) case to construct EOS as depicted by Eq. 2.12.

However, such a construction has two more constraints:

- The first constraint comes from the description provided by the CALPHAD database. The enthalpy-temperature relation provided by CALPHAD (Eq. 2.16) is for a single phase θ, whereas, the EOS depicted by Eq. 2.12 needs to be general in the sense that it should be able to describe a multiphasic domain. This need for general EOS is related to the system and the applications considered, which for the case of in-vessel corium is related to the description of a domain with two liquid phases and a solid phase in it.
- The second constraint is related to the validity of the EOS with respect to its dependency on composition and temperature, at a macroscopic scale.

The work presented in Chapter 3 focuses on answering these questions related to the direct utilization of CALPHAD based EOS, within the framework of macroscopic modelling.

2.2.2 Distributed parameter models for mesoscopic scales

The current knowledge on the feasibility of IVMR strategy is based on the use of integral codes for determining the heat flux distributions from the corium pool to the RPV wall. These results are obtained from the macroscopic thermohydraulic models that are based on conservative, and often invalid assumptions and heat transfer correlations. In order to obtain more accurate descriptions, these models need to be improved. This can be

achieved partly by conducting more corium-based experiments. However, owing to the limitations of corium-based experiments, an alternative tool has emerged as a viable option in the recent past due to the increasing computational power: CFD.

CFD offers a supplementary approach for gaining knowledge related to the thermal-hydraulic behaviour of the in-vessel corium. Monophasic CFD codes have been used in a number of applications, including the thermohydraulic analysis of inversion of stratification in corium pool [57], the study of natural convection in internally heated pools [58] [59], with a comparison of the results obtained from experiments. Within the framework of the H2020 IVMR project, different CFD related modelling activities have been initiated by EDF (NEPTUNE_CFD)[60], CEA (TrioCFD) [59] [61] NCBJ, NRG and UJV for studying the thermohydraulic behaviour of a homogeneous corium pool and the light metallic layer on top of it.

Such studies require modelling of the thermochemical behaviour of in-vessel corium at a spatial scale which can be coupled with the CFD based codes. In particular, the objective in this direction is to obtain a multi-phase CFD code, which can simulate the transient conditions related to the phenomena of solidification of the oxidic crust and liquid phase segregation.

The initial activities in this direction were related to the development of a thermochemical model at the mesoscopic scale for studying stratification kinetics [44]. The choice of numerical tool to be used for modelling was made according to the three important criteria:

- the model should be compatible with a Eulerian framework, which ensures a fixed mesh framework, such that no explicit tracking of the moving interface is needed;
- the model must be compatible with the CFD models, without imposing an additional constraint on the mesh size, and most importantly;
- the model should be consistent with the thermodynamic description provided by CALPHAD database (*i.e.* it should be possible to couple the model with CALPHAD database).

2.2.2.1 The diffuse interface approach and the phase-field model

The phase transformation processes (such as solidification and liquid segregation) are dependent on the evolution of the micro-structure, which is related to the dynamics of the interfaces between the different phases. The numerical modelling of such phase transformation processes can be done by either adopting a sharp-interface formulation (of the type known as "Stefan problems") or by using diffuse description of the interface. In this context, the use of a diffuse interface approach is considered to be numerically simpler compared to the sharp-interface methodology for the simple reason that the diffuse models do not need to explicitly track the motion of the interface.

Development of a detailed model that follows this phase transformation process on a mesoscopic scale (order of millimeters) requires a modelling tool that can allow the user to "up-scale" the physical thickness[8] of the interface, while conserving the physics of the system at the larger spatial scale (for eg. the conservation laws) as well as the overall motion of the interface. Consequently, the "up-scaled" interface thickness becomes a model parameter, which can be chosen in accordance with the mesoscopic scale, without changing the bulk thermodynamics, the interface energy and the bulk kinetics of the model. However, the process of up-scaling poses additional constraints on the other model parameters in order to relate them to the physical parameters associated with the system.

A diffuse-interface approach to numerical modelling relies on the continuum description of a system that is composed of two bulk phases separated by a "thick" interface of width δ (see Figure 2.2a). This concept appeared a little more than a century ago, with the model developed by van der Waals to study the liquid-gas system using a continuous density function [62]. The diffuse interface is represented by the means of variables that are functions of space (z) and time (t), that vary continuously across the interface to take constant values in the bulk regions (similar to sharp interface descriptions, see Figure 2.2). In the remainder of the thesis, these variables will be referred to as "order parameters"(ϕ). The evolution of these order parameters describes the evolution of the system.

[8]Contrary to its 'sharp' appearance on a macroscopic scale, the interface has a diffuse character on a microscopic scale, owing to a transition zone that exists between the two phases, which has a finite thickness, roughly of the order of a few atomic spacings (*i.e.* having a physical thickness of the order of 1 nanometer).

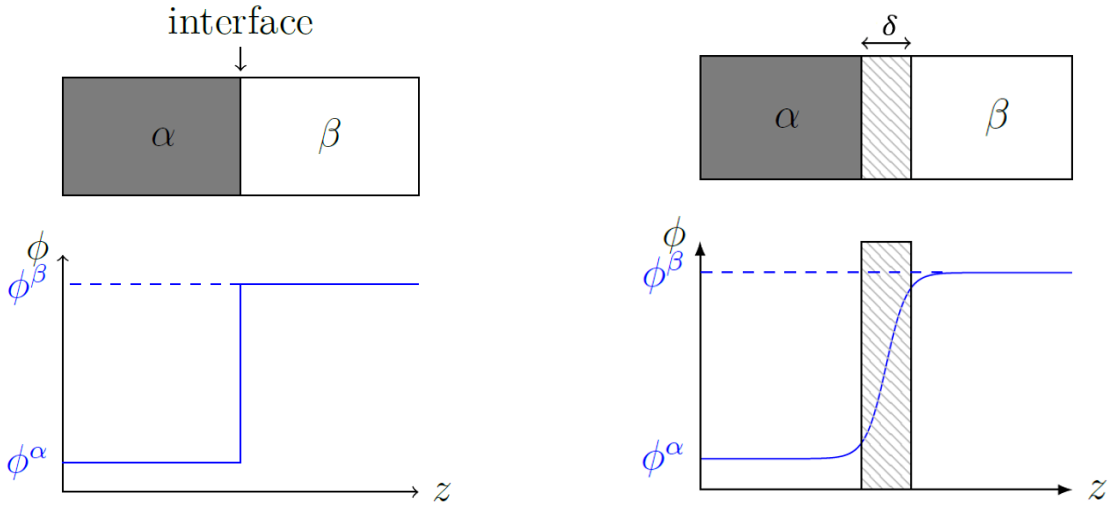

(A) Sharp interface (B) Diffuse interface

FIGURE 2.2: Diffuse vs sharp interface description

The notion of order parameters was introduced to the diffuse interface theory by Landau for describing the order-disorder phase transformations. Furthermore, the extension of this work in terms of describing the free energy of a system based on the order parameters and its gradients, was carried out by Ginzburg and Landau [63].

These works went on to become the basis of the phase-field method, which has become an important tool for simulating microstructure evolution (see for example [64], [65], [66], [67]). The phase field model allows the up-scaling of the interface thickness without affecting the bulk thermodynamics and the surface energy associated with the interface in the system. Consequently, the interface thickness is treated as a model parameter in such models. The present day applications of the phase-field method are numerous, with simulations being performed for processes ranging from solidification [68], solid-state transformations [69], crack-propagation [70], to dislocation dynamics [71] etc.

General formulation of the phase field models

As mentioned above, the main ingredients required for developing a phase-field model to depict any process, are the choice of the appropriate dynamic variables (*i.e.* order parameters) and a thermodynamic potential (like the free energy) that depends on these

order parameters for the description of the system. Most of the phase-field models found in literature are derived for constant temperature and volume conditions. In such cases, the appropriate choice for the thermodynamic potential is the Helmholtz free energy $\mathbb{F}$. This free energy potential is defined for the domain $\mathcal{V}$, as a functional of the form:

$$\mathbb{F}(\phi) = \int_{\mathcal{V}} \left(f(\phi) + \frac{{\kappa_\phi}^2}{2} |\nabla \phi|^2 \right) dV \tag{2.18}$$

where:

- $f(\phi)$ is the free energy density ($J^1 m^{-3}$).
- The gradient term $\frac{{\kappa_\phi}^2}{2} |\nabla \phi|^2$ is related to the contributions from the interactions occurring at the interface, owing to its diffuse character. This term creates a positive contribution, thus increasing the free energy of the system, which comes from the creation of an interface.
- ${\kappa_\phi}^2$ is a positive coefficient called the "gradient energy coefficient" that is related to the surface energy and the thickness associated with the interface.

The order parameters describing the system, may or may not have a physical significance, and can be distinguished as:

- **conserved:** provided the quantity depicted by the order parameter is conserved for the system (eg. local composition), or;
- **non-conserved:** provided the quantity concerning this order parameter does not remain conserved during system evolution (eg. information on phase, or local crystal structure, or magnetization etc.).

The non-conserved order parameters are assigned constant values for the two regions. For example, if we consider solidification, the non-conserved order parameter ϕ denotes the presence of the solid or liquid phase at any point in space and time, and it is assigned the values:

$$\phi = \begin{cases} 0 & \text{in the liquid} \\ 1 & \text{in the solid} \end{cases} \tag{2.19}$$

and within the diffuse interface:

$$0 < \phi < 1 \tag{2.20}$$

The system evolves with time in a manner that leads to the decrease of its free energy, such that at long times it reaches a minimum value that represents the thermodynamic equilibrium state:

$$\frac{d\mathbb{F}}{dt} \leq 0 \tag{2.21}$$

As this free energy functional is dependent on the order parameter functions, its minimum is determined w.r.t. the variations of the order parameters. This minimization can be achieved by the applicability of the Euler-Lagrange equation [64]:

$$\frac{\delta\mathbb{F}(\phi)}{\delta\phi} = 0 \tag{2.22}$$

where $\frac{\delta\mathbb{F}[\phi]}{\delta\phi}$ is the variational derivative of $\mathbb{F}[\phi]$ with respect to the field ϕ. By applying the theory of variational calculus, $\mathbb{F}[\phi]$ is calculated as:

$$\frac{\delta\mathbb{F}[\phi]}{\delta\phi} = \frac{\partial f}{\partial\phi} - \left\{\partial_x\left(\frac{\partial f}{\partial(\partial_x\phi)}\right) + \partial_y\left(\frac{\partial f}{\partial(\partial_y\phi)}\right) + \partial_z\left(\frac{\partial f}{\partial(\partial_z\phi)}\right)\right\} \tag{2.23}$$

The first term on the right hand side of Eq. 2.23 affects only the bulk part of the functional whereas the second term gives the variation of the functional with respect to gradient terms for the interface.

The kinetics of the process can be studied by tracking the evolution of the order parameters in space and time. This evolution is a result of the driving forces that tend to minimize the free energy of the system. The form of the evolution equation depends on the nature of the order parameter.

Conserved order parameters

For the order parameters (ϕ_i) related to the conserved quantities in the system, the evolution equation is derived from their respective conservation laws, which takes the form:

$$\frac{\partial\phi_i(z,t)}{\partial t} + \vec{\nabla}\vec{J}_{\phi_i} = 0 \tag{2.24}$$

where $\vec{J}_\phi$ refers to the flux associated with the order parameter. This diffusion flux can be derived in a phenomenological way from the variational derivative of the free energy

functional w.r.t. the specific order parameter (ϕ_i) as

$$\vec{J}_{\phi_i} = -M_i \vec{\nabla} \left(\frac{\delta \mathbb{F}}{\delta \phi_i} \right) \tag{2.25}$$

with M_i being the kinetic coefficient that can be a function of the local values of all the conserved order parameters. The evolution equations of the form Eq. 2.24 are referred to as *Cahn-Hilliard* equations [72], or *Model B* [73].

Non-conserved order parameters

The non-conserved order parameters, as the name suggests, do not evolve under the constraints of the conservation laws. Their evolution in space and time is described by an equation of the form:

$$\frac{\partial \phi_k(z,t)}{\partial t} = -M_k \frac{\delta \mathbb{F}}{\delta \phi_k} \tag{2.26}$$

where M_k is the kinetic parameter associated with the time scale of the relaxation of the system. The evolution equations of the form Eq. 2.26 are referred to as *Allen-Cahn* equations [74], also known as *Model A* [73]. The Allen Cahn equation simply denotes the relaxation of the system to the equilibrium condition posed by the non-conserved order parameter.

2.2.2.2 Issues related to the thermodynamic consistency of the phase field model

As mentioned earlier, the choice of thermodynamic potential for the formulation of phase-field models depends on the dynamic variables of interest. For modelling phase transformations such as solidification, these variables generally are the temperature and the composition, hence the appropriate potential is the Helmholtz free energy ($\mathbb{F}$) (as presented above). However, it should be noted, that this choice of potential is strictly valid for the studies related to constant temperature and molar volume conditions (*i.e.* isothermal systems). In the context of modelling in-vessel corium systems, as the density variation is considered to be independent of the pressure of the system, for isothermal conditions the appropriate thermodynamic potential is the Gibbs energy $\mathbb{G}$.

For cases where the variation of temperature is also taken into account *i.e.* the non-isothermal systems, incorporation of the energy equation is necessary to take into account

this temperature variation as it is associated with the energy flow across the interface. As a consequence, the thermodynamic potential that can be used to obtain a consistent description of the system changes to entropy $\mathbb{S}$. A general framework for the same is described in [75], which will be used as a starting point and is explained in detail in Chapter 4 of the thesis.

With such a formulation, the second concern is related to the coupling of the developed phase field model with the CALPHAD database for obtaining the quantities of interest. In terms of composition dependence, the evolution equation in phase field is defined in terms of the component composition, whereas the CALPHAD description is based on the composition defined in terms of constituent fractions. In such circumstances, the coupling of the phase field model with CALPHAD requires additional hypotheses which can relate the component and constituent compositions, depending on the phase which is being modelled. These questions have been addressed in detail in Chapter 4.

Chapter 3

Application of CALPHAD based closures to the lumped-parameter models for solidification of in-vessel corium

3.1 Introduction

The importance of predicting the transient thermal loads on the vessel wall for ensuring success of IVMR strategy has been discussed in length in Chapter 1. A proper understanding of the interfacial conditions between the melt and the solid crust is important as it governs the heat flux distribution on the RPV wall. In this context, ensuring thermodynamic consistency between the coupled thermochemical-thermohydraulic lumped parameter models is of prime importance. A partial or incomplete coupling between the models could lead to an erroneous results which would effectively impact the accuracy of the overall IVMR strategy.

One such example of the discrepancies involved with thermodynamic inconsistency was identified as a result of the studies involving the code cross comparison conducted by CEA and EDF [76]. The benchmark activities conducted for the models developed for different corium configurations under the PROCOR platform (CEA) and MAAP (EDF) have uncovered that an important source of disparity is related to the adopted formulation for the mass and energy conservation equations and the associated enthalpy-temperature relations. The MAAP code consists of energy conservation equations written for the

corium pool in terms of specific enthalpy, the data tabulated for which (as a function of changing temperature and composition) has been constructed under the hypothesis of 'no thermochemical interaction' between the corium and molten steel. This however, is in contradiction with the macro-segregation hypotheses (introduced in [22]) that were used for setting the boundary conditions to the system (*i.e.* the interface temperature was set equal to the liquidus temperature of the bulk molten pool). The inconsistency resulted in an erroneous calculation of the liquidus temperature for the interface between the pool-crust layer by the MAAP code. Contrarily, the PROCOR model for the corium pool consists of energy balance equations written in terms of specific enthalpies as well, but it is supplemented with explicit enthalpy-temperature relations that take into account the macro-segregation hypotheses. Consequently, the inconsistency in the calculation of interface liquidus temperature is not exhibited by the PROCOR results. However, the PROCOR model does not explicitly represent the crust. Instead, a "fictitious" quasi-stationary crust has been considered in terms of the temperature boundary condition it imposes to the liquid layers in the pool (see [77] for more details). A consistent model with an explicit description of the crust as an independent component is required in order to study its transient thermal behaviour, which is needed for the development of a complete model where additional thermochemical phenomena can be added and studied. A first initiative for the crust modelling in PROCOR has been reported in [45], and the same issue related to the thermodynamic consistency of the closures is faced in this development.

In this context, as discussed in [78], it is useful to adapt a general formulation for writing the energy conservation equations in terms of specific enthalpies and use general enthalpy-temperature relations that can be referred to as "Equation-Of-State" (EOS) to provide closures to the integral models. Additionally, from the point of view of ensuring thermodynamic consistency, the utilization of CALPHAD based enthalpy-temperature relations for constructing these general EOS is beneficial [79] [80]. However, as discussed earlier (in Chapter 2), the direct utilization of these enthalpy-temperature relations requires fulfillment of certain constraints, which is the focus of the present chapter.

3.2 Questions related to the use of CALPHAD for construction of EOS

Within the context of integral modelling in PROCOR, the constraints associated with the direct use of CALPHAD based enthalpy-temperature relations to construct the general EOS can be recalled from the discussion in Section 2.2.1.2.

The first complication is related to the use of CALPHAD based EOS for describing a multiphasic domain $\mathcal{V}$. The enthalpy-temperature relation (given by Eq. 2.16) cannot be directly used to provide closures for a multiphasic system as the description provided by Eq. 2.16 is limited to a single phase θ, whereas, the EOS depicted by Eq. 2.12 needs to take into account the possible multiphasic nature of the domain $\mathcal{V}$. Such a condition, where multiple phases may exist in a domain, is possible for in-vessel corium under two circumstances:

- if the average composition of the domain ($\bar{w}^j_{j\in\mathbb{S}}$) lies under the miscibility gap region. This results in the decomposition of the phase to give two immiscible phases within the domain (same as phase-segregation explained for in-vessel corium in Section 1.3.1), and;
- if the temperature of the domain $\bar{T}$ falls below the liquidus temperature $T_{liquidus}(\bar{w}^j_{j\in\mathbb{S}})$ that is associated with average composition of the domain. This results in solidification within the bulk liquid.

In order to address this in a general way, additional hypotheses and models must be supplemented to the CALPHAD data at the time of constructing the EOS. Additionally, it must be ensured that these hypotheses are consistent with the thermochemical models that have been coupled with the thermohydraulic model under consideration. Failure to do so could lead to errors in the prediction of the results, an issue similar to the one raised by the hypothesis used for the MAAP code, as mentioned previously.

Within this context, [81] reports the results related to the numerical tests that have been carried out in the framework of PROCOR platform for comparing the CALPHAD based general EOS that have been constructed by making use of different segregation hypothesis for the underlying thermodynamic system. These comparisons have been conducted for

a simple test case, with the aim of answering the constraint related to the treatment of a multiphasic spatial domain. It should be noted that these tests have been conducted separately and not as a part of the assessment that is presented in the following sections of this chapter. Hence, a detailed discussion of these results is not the main scope of the thesis.

The second complication arises with respect to ensuring the validity of the constructed EOS. In principle, the enthalpy evaluated from the thermodynamic function Eq. 2.16 is a local function for a given temperature and composition value, which may also be valid for a homogeneous spatial domain (in terms of both temperature and composition). Such a relation can be useful for predicting the system behaviour at a microscopic level. In case of a macroscopic spatial domain, the enthalpy is given by the relation:

$$\bar{h}_n m_n = \int_{\mathcal{V}} \rho_n h dV = \int_{\mathcal{V}} \rho_n \mathcal{H}^\theta \left[T(\vec{r}), (w^j(\vec{r}))_{j \in \mathbb{S}} \right] dV \tag{3.1}$$

where h is dependent on the state variables T and $\bar{w}^j_{j \in \mathbb{S}}$ that are functions of spatial vector $\vec{r}$. The value obtained from Eq. 3.1 depends on the inhomogeneities in the domain $\mathcal{V}_n$ related to the temperature and composition. However, this value may not be equal to the enthalpy evaluated for a macroscopic domain, based on its average composition $(m_n \mathcal{H}^\theta \left(\bar{T}, \bar{w}^j_{j \in \mathbb{S}} \right))$. This can be explained from the fact that the average of product of two quantities is not always the same as the product of the averages [55].

The evaluated enthalpy (from Eq. 3.1) can be strictly equal to $m_n \mathcal{H}^\theta \left(\bar{T}, \bar{w}^j_{j \in \mathbb{S}} \right)$ only in two cases: the spatial domain $\mathcal{V}_n$ is homogeneous, or $\mathcal{H}^\theta$ has a linear dependency on the temperature and composition variables. For these two cases mentioned, one can use the constructed EOS for evaluation of the enthalpy values.

With these constraints in mind, the feasibility of using CALPHAD database for constructing general EOS is assessed. The numerical tests related to this assessment have been conducted on a "mock-up" model developed under PROCOR platform, to describe the thermal and thermochemical evolution of the solidifying crust at the boundary of a sub-oxidized corium pool under a plane solidification front hypothesis. This mock-up model represents a minimum model that can be utilized for answering the above mentioned constraints related to the construction of EOS and any other additional questions that may need to be answered, with respect to the development of a crust model. The following

sections provide a brief description of the developed integral model, which is followed by the numerical verifications for a ternary U-O-Zr system considered for a temperature range between 1800 and 3000 K. These results (presented in Section 3.4) have been a part of a publication ([82]) for the journal *Annals of Nuclear Energy*.

3.3 Description of the corium-crust solidification model

The present model depicts a simplified configuration of a sub-oxidized corium pool with a non-eutectic[1] homogeneous composition and a fixed external boundary temperature. Figure 3.1 depicts the two-zone 1-D situation, with the liquid corium (denoted by p) undergoing solidification at its interface (denoted by β) cooled from outside (with the external boundary being denoted by α). The crust is denoted by s while the interface and external boundary areas are considered to be equal (*i.e.* $A_\beta = A_\alpha = A$). The interface is assumed at the origin ($z = z_0$) and the crust thickness (z_s) propagates with time till a steady state is achieved. The inputs related to the thermo-physical properties for both the liquid and solid phases are calculated in PROCOR using TOLBIAC-ICB code, where these properties are obtained from the mixing laws applied to species density functions of temperature (see [26]).

[1]The corium composition can be eutectic or non-eutectic, based on its composition. In general, the eutectic composition for corium is considered only in case of studies involving the Ex-vessel corium-concrete interactions.

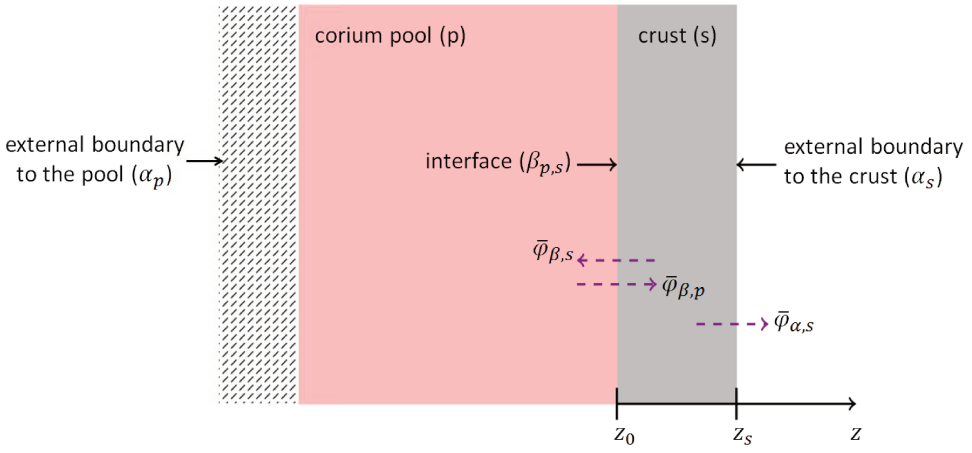

FIGURE 3.1: Corium pool - crust plane front solidification configuration, denoting the heat fluxes acting at the interface from the liquid pool ($\bar{\varphi}_{\beta,p}$) and the solid crust ($\bar{\varphi}_{\beta,s}$) sides, and the heat flux acting on the external boundary ($\bar{\varphi}_{\alpha,s}$).

3.3.1 Macroscopic conservation equations

For the two zones (denoted by subscript p and s for bulk liquid and solid phase respectively, and β, p and β, s for interfacial liquid and solid respectively), the lumped mass conservation equations and the associated interface condition is written for a closed system in terms of Eqs. 2.8 and 2.10 adapted from the general formulation discussed in Chapter 2:

$$\frac{dm_p}{dt} + \dot{m}_{\beta,p} = 0 \tag{3.2}$$

$$\frac{dm_s}{dt} - \dot{m}_{\beta,p} = 0 \tag{3.3}$$

$$\dot{m}_{\beta,p} + \dot{m}_{\beta,s} = 0 \tag{3.4}$$

where $\dot{m}_{\beta,p}$ is the solidification rate at the interface ($\dot{m}_{\beta,p} > 0$ for the mass flow occurring in the direction of the crust from the corium pool).

The external boundary for the liquid pool (α_p) is considered to be adiabatic, *i.e.* there is no transfer of heat and mass across α_p. The energy conservation equations for the two zones are written in terms of specific enthalpy $\bar{h}$ of the bulk (denoted by subscript p and s) and interfacial (denoted by subscript β, p and β, s) phases (adapted from Eq. 2.9), alongwith

the associated interface equation (adapted from Eq. 2.11) for plane front solidification :

$$\frac{d}{dt}\left(\bar{h}_p m_p\right) + \bar{\varphi}_{\beta,p} A_\beta + \bar{h}_{\beta,p}\dot{m}_{\beta,p} = \dot{q}_p^{\text{mass}} m_p \tag{3.5}$$

$$\frac{d}{dt}\left(\bar{h}_s m_s\right) + \bar{\varphi}_{\beta,s} A_\beta - \bar{h}_{\beta,s}\dot{m}_{\beta,p} + \bar{\varphi}_{\alpha,s} A_\beta = \dot{q}_s^{\text{mass}} m_s \tag{3.6}$$

$$\left(\bar{h}_{\beta,p} - \bar{h}_{\beta,s}\right)\dot{m}_{\beta,p} + \left(\bar{\varphi}_{\beta,p} + \bar{\varphi}_{\beta,s}\right) A_\beta = -\Delta h \dot{m}_{\beta,p} \tag{3.7}$$

where:

- $\bar{\varphi}_{\alpha,s}$ is the heat flux at the crust-external boundary interface (> 0), directed from the bulk solid towards the external boundary;
- $\bar{\varphi}_{\beta,s}$ is the heat flux at the crust-pool interface (< 0), directed from the bulk solid towards the interface;
- $\bar{\varphi}_{\beta,p}$ is the heat flux at the crust pool interface (> 0), directed from bulk corium pool towards the interface;
- $\Delta h \dot{m}_{\beta,p}$ is an additional interfacial term, which is discussed in Section 3.3.5.

Mass diffusion in the solid crust is neglected (*i.e.* the diffusive mass flux in the solid at the interface $\bar{J}^j_{\beta,s} = 0$). Hence, the species mass conservation and its associated interface equation for the system is given by:

$$\frac{d}{dt}\left(\bar{w}_p^j m_p\right) + \bar{J}^j_{\beta,p} A_\beta + \bar{w}^j_{\beta,p}\dot{m}_{\beta,p} = 0 \tag{3.8}$$

$$\frac{d}{dt}\left(\bar{w}_s^j m_s\right) - \bar{w}^j_{\beta,s}\dot{m}_{\beta,p} = 0 \tag{3.9}$$

$$\left(\bar{w}^j_{\beta,p} - \bar{w}^j_{\beta,s}\right)\dot{m}_{\beta,p} + \bar{J}^j_{\beta,p} A_\beta = -\Delta w^j_\beta \dot{m}_{\beta,p} \tag{3.10}$$

where:

- $\bar{w}_p^j, \bar{w}_s^j$ and $\bar{w}^j_{\beta,s}$ are the species mass fractions corresponding to the bulk liquid, bulk solid and the interfacial solid composition, respectively;
- $\Delta w^j_\beta \dot{m}_{\beta,p}$ is an additional interface term, discussed in Section 3.3.5, and;
- $\bar{J}^j_{\beta,p}$ is the diffusive mass flux for the interfacial liquid composition.

With the exception of the additional terms $\Delta h \dot{m}_{\beta,p}$ and $\Delta w^j_\beta \dot{m}_{\beta,p}$ in Eqs. 3.7 and 3.10 respectively, the model presented above is a "standard" plane front solidification model

(see, for instance, [83] for analytical solutions in the binary case with a linearized liquidus curve) that has been used in [84] for the interpretation of the LIVE-L3A test[2]

3.3.2 Modelling the fluxes in the system

The general expression for $\bar{J}^j_{\beta,p}$ is given as:

$$\bar{J}^j_{\beta,p} = -\rho_{\beta,p} \sum_{h=1}^{n-1} \left[k_m^{jh} (\bar{w}^h_{\beta,p} - \bar{w}^h_p) \right] \tag{3.11}$$

with $\rho_{\beta,p}$ as the mass density of the interface liquid and k_m^{jh} is the mass transfer coefficient for the species h with respect to species j.

For an initial assessment, the hypothesis of an infinitely fast transfer of mass in the liquid boundary layer (*i.e.* $k_m^{jh} \to \infty$) has been considered. This is a standard hypothesis for corium pool models, which comes from the consideration that all layers are well mixed. Consequently, the averaged composition of the interfacial liquid is equal to the bulk liquid phase composition (*i.e.* $\bar{w}^j_{\beta,p} = \bar{w}^j_p$). The assumption of local thermodynamic equilibrium at the interface results in the interface temperature T_β to be equal to the liquidus temperature $T_{liquidus}\left(\bar{w}^j_{\beta,p}\right)$ corresponding to the interface composition of the corium pool $\left(\bar{w}^j_{\beta,p}\right)_{j\in\mathbb{S}}$.

Continuing on a closed system analysis, the heat fluxes at each of the boundaries are modelled. For the interface, the heat transfer from the corium pool to the solid crust is a result of convection and can be expressed using Nusselt-Rayleigh correlation:

$$\bar{\varphi}_{\beta,p} = h_\Delta (\bar{T}_p - T_{\beta,p}) \tag{3.12}$$

where h_Δ denotes the heat transfer coefficient and $\bar{T}_p$ is the average temperature of the liquid pool. Out of the different heat transfer correlation available in [86], the present model makes use of the correlation for upward heat transfer that has been derived from

[2]The LIVE program headed by the Karlsruher Institute of Technology (KIT) in Germany, that aims to study the core melt phenomena during the late phase of core melt progression in the RPV both experimentally (in the form of large scale experiments with simulant materials (salt mixtures of sodium nitrate $NaNO_3$ and potassium nitrate KNO_3)) and analytically using CFD codes in order to provide a reasonable estimate of the remaining uncertainty band under the aspect of safety assessment. Within its framework, the main objective of the LIVE-L3A test was to investigate the behaviour of the molten pool and the formation of the crust at the melt/vessel wall interface influenced by the melt relocation position and initial cooling conditions [85].

the BALI experimental program (see [87]).

The heat flux across the solid at the interface $\left(\bar{\varphi}_{\beta,s}\right)$, as well as the RPV wall boundary $\left(\bar{\varphi}_{\alpha,s}\right)$ is a result of the conduction process, and can be expressed in the form of 1-D conduction:

$$\bar{\varphi}_{\alpha,s}A_{\beta} = -\lambda_s A_{\beta}\frac{\partial T_s(z_s,t)}{\partial z} \tag{3.13}$$

$$\bar{\varphi}_{\beta,s}A_{\beta} = \lambda_s A_{\beta}\frac{\partial T_s(z_0,t)}{\partial z} \tag{3.14}$$

with T_s and λ_s being the temperature distribution and thermal conductivity associated with the solid crust respectively.

A quadratic temperature profile is assumed to depict the variation across the solid at any time [54] and the boundary conditions are set for crust temperature at the interface $(T_s(z_0,t) = T_\beta)$ and the external boundary $(T_s(z_s,t) = T_{B.C.})$. Consequently, the heat flux at the two solid boundaries (*i.e.* $\bar{\varphi}_{\beta,s}$ and $\bar{\varphi}_{\alpha,s}$) are obtained in terms of T_β , $T_{B.C.}$ and the average solid temperature $\bar{T}_s$:

$$\bar{\varphi}_{\alpha,s} = \lambda_s\frac{6\bar{T}_s(t) - 2T_\beta - 4T_{B.C.}}{z_s} \tag{3.15}$$

$$\bar{\varphi}_{\beta,s} = \lambda_s\frac{6\bar{T}_s(t) - 4T_\beta - 2T_{B.C.}}{z_s} \tag{3.16}$$

3.3.3 Closures relations: CALPHAD-based EOS

The construction of the CALPHAD based EOS for providing closures to the energy conservation equations of the model will be presented in this section. For the temperature (1800 to 3000 K) and composition range of interest, only the liquid phase (`LIQUID`) and the solid face-centered cubic (U,Zr)O_{2-x} phase (`C1_FCC`) corresponding to the phase of the first appearing solid[3], have been considered. As earlier mentioned in Section 2.1.2, the Gibbs free energies for the two phases are described by a non-ideal associate model in the NUCLEA database, which is based on the following stoichiometric species as constituents: U, UO_2, Zr, ZrO_2 and O. From these Gibbs energy functions, following the procedure

[3]It has been noted that for temperatures below 2000 K, solid phases other than `C1_FCC` also appear and are stable, such as the tetragonal (Zr,U)O_{2-x} phase (`TET(OXIDE)` or `TET_OXIDE_` in the NUCLEA database) and the α-Zr(O) phase (`HCP_A3(1)` or `HCP_A3` in the NUCLEA database).

depicted by Eqs. 2.14, 2.15 and 2.16, the enthalpy-temperature relations for the two phases are obtained, which has a general form :

$$\mathcal{H}^{\theta} : \bar{T}, \bar{w}_j^{j\in\mathbb{S}} \rightarrow \bar{h} \tag{3.17}$$

In order to directly utilize these enthalpy-temperatures for providing closures, additional assumptions need to be made, such that the two constraints (discussed in detail in Section 3.2) are properly addressed. In this context, the first constraint of ensuring monophasic domains has been dealt separately for both the phases.

For the `LIQUID` phase, the mass transfer at the interface is assumed to be infinitely fast (*i.e.* $k_m^{j,h} \rightarrow \infty$) . This, in addition to the initial condition that relates the average temperature of the liquid molten pool $\bar{T}_p$ to be greater than the associated liquidus temperature $T_{liquidus}$, ensures that the liquid domain $\mathcal{V}_p$ is monophasic. Consequently the closure relations for average mass enthalpies of the bulk and interfacial liquid can be directly provided by the enthalpy-temperature relations:

$$\bar{h}_p(\bar{T}_p) = \mathcal{H}^{\texttt{LIQUID}}\left[\bar{T}_p, \left(\bar{w}_p^j\right)_{j\in\mathbb{S}}\right] \tag{3.18}$$

$$\bar{h}_{\beta,p}(T_\beta) = \mathcal{H}^{\texttt{LIQUID}}\left[T_\beta, \left(\bar{w}_{\beta,p}^j\right)_{j\in\mathbb{S}}\right] \tag{3.19}$$

In case of the crust $\mathcal{V}_s$, the problem of monophasic phase is addressed by assuming the initially formed solid to be a pure `C1_FCC` phase. Recalling that the first solid phase to be formed during the transient is `C1_FCC`, consequently, the closure relations to the energy conservation equation in solid domain can be obtained from:

$$\bar{h}_s(\bar{T}_s) = \mathcal{H}^{\texttt{C1\_FCC}}\left[\bar{T}_s, \left(\bar{w}_s^j\right)_{j\in\mathbb{S}}\right] \tag{3.20}$$

$$\bar{h}_{\beta,s}(T_\beta) = \mathcal{H}^{\texttt{C1\_FCC}}\left[T_\beta, \left(\bar{w}_{\beta,s}^j\right)_{j\in\mathbb{S}}\right] \tag{3.21}$$

In addition, CALPHAD data is exploited through equilibrium calculations that involve minimization of the Gibbs energy of the system for the given temperature and composition value, which provide the local equilibrium conditions at the interface in terms of phase transition temperature $T_{liquidus}\left(\bar{w}_{\beta,p}^j\right)_{j\in\mathbb{S}}$ (appearance of the `C1_FCC` phase) and composition $\left(\bar{w}_{\beta,s}^j\right)_{j\in\mathbb{S}}$ of the solid `C1_FCC` phase that is formed upon solidification.

With respect to the second constraint, the validity of these EOS on a macroscopic scale has been tested in the section on numerical verifications, where the dependency of the EOS (depicted by Eqs. 3.18, 3.19, 3.20 and 3.21) on temperature and composition has been studied. In this context, for the cases where this constraint is not fulfilled, the mass averaged specific enthalpy values (obtained from the EOS) can be used by adopting partial linearization of the enthalpy function in composition (as mentioned in [55]).

3.3.4 Numerical coupling scheme for time integration

The time integration of conservation equations coupled with CALPHAD related properties requires numerical discretization for solving the corium solidification transient. To do so, a macro time scale is defined with prescribed time-step Δt and a semi-explicit coupling between mass, energy conservation equations and species mass balance is considered.

Over a macro time-step $[t, t+\Delta t]$, material compositions are considered to be constant and equal to their values at t in such a way that the interface temperature along with the enthalpy-temperature relations of Eqs. 3.18, 3.19, 3.20 and 3.21 can be evaluated at t. Following this, an explicit Euler scheme is used to integrate the mass and energy conservation equations for the crust (Eqs. 3.3 and 3.6) and corium (Eqs. 3.2 and 3.5) from t to $t+\Delta t$ over a micro time-step grid (with a micro time-step δt). Finally, the updated phase compositions at $t+\Delta t$ are obtained by time integration of the species conservation equation Eqs. 3.8 and 3.9 using the explicit scheme approximation. For instance, for the solid phase, integration of Eq. 3.9 over a single time-step is given as:

$$\int_{t_i}^{t_i+\Delta t}\left(\frac{d}{dt}\left(\bar{w}_s^j m_s\right)\right)dt = \int_{t_i}^{t_i+\Delta t}\left(\bar{w}_s^j \dot{m}_{\beta,p}\right)dt \tag{3.22}$$

$$\left(\bar{w}_s^j m_s\right)|_{t+\Delta t} = \bar{w}_{\beta,s}^j|_t\left[\left(\dot{m}_{\beta,p}\right)|_{t+\Delta t} - \left(\dot{m}_{\beta,p}\right)|_t\right]\Delta t + \left(\bar{w}_s^j m_s\right)|_t \tag{3.23}$$

With previously calculated values for $\bar{w}_s^j$, $\bar{w}_{\beta,s}^j$ and m_s at time t , the updated system calculation can be obtained. These updated compositions act as inputs to the model for the next macro time-step.

3.3.5 Redox reaction at the interface

Upon updating the system composition at the end of each time step, it may be observed that the species mass conservation no longer holds true for the solid and liquid phases

of the system and there may be formation of new species in the solidified crust at the interface that were not present in the interfacial liquid. As a result, the interfacial terms $\Delta h\dot{m}_{\beta,p}$ and $\Delta w^j_\beta \dot{m}_{\beta,p}$ of Eqs. 3.7 and 3.10 respectively, have been introduced in Section 3.3.

For a study related to the solidification of a completely oxidized corium system (*i.e.* $C_{Zr} = 100\%$), the composition of the crust formed at the interface is consistent with the interface liquid in terms of the species present. For such a system, the species mass conservation equations hold true for the values of $\Delta h\dot{m}_{\beta,p}$ and $\Delta w^j_\beta \dot{m}_{\beta,p} = 0$. However, in case of the solidification of sub-oxidized corium system, the NUCLEA database predicts a difference in the composition of the solid formed at thermodynamic equilibrium at the liquidus temperature from the interfacial liquid composition. In particular, appearance of non-zero mass fraction of U species in the solid is noted. This presence may be interpreted as a result of the redox reaction ($UO_2 + Zr \rightleftharpoons U + ZrO_2$) occurring in direction of formation of U and ZrO_2 in the interfacial liquid. The extra interfacial terms $-\Delta h\dot{m}_{\beta,p}$ and $-\Delta w^j_\beta \dot{m}_{\beta,p}$ are there to correct the balance equations Eqs. 3.7 and 3.10 accordingly.

The non-zero mass fraction for U species relative to the associate model of the `C1_FCC` phase corresponds to the slight sub-stoichiometry of the (U,Zr)O_{2-x} phase. This sub-stoichiometry is to be related to vacancies in the face-centered cubic lattice and not be confused with appearance of an actual metallic U phase.

A quantity r is defined to denote the mass of interfacial liquid required for solidifying a unit mass of solid at equilibrium composition. Out of this mass r of the initial liquid at the interface $\left(\bar{w}^j_{\beta,p}\right)_{j\in\mathbb{S}}$, a unit mass of solid $\left(\bar{w}^j_{\beta,s}\right)_{j\in\mathbb{S}}$ is formed, leaving $(r-1)$ amount of "residual" liquid of composition $\left(\bar{w}^j_{\beta,p'}\right)_{j\in\mathbb{S}}$. From there, the overall species mass variation occurring at the interface gives the value of Δw^j_β as:

$$\Delta w^j_\beta = \bar{w}^j_{\beta,s} + (r-1)\,\bar{w}^j_{\beta,p'} - r\bar{w}^j_{\beta,p} \quad (j \in \mathbb{S}) \tag{3.24}$$

In practice, the value of r can be calculated from the conservation of elements, that is upheld by the system and is represented by the relation:

$$\bar{e}^i_{\beta,p} m_{\beta,p} = \bar{e}^i_{\beta,s} m_{\beta,s} + \bar{e}^i_{\beta,p'} m_{\beta,p'} \tag{3.25}$$

where $\left(\bar{e}^i_{\beta,s}\right)_{i\in\mathbb{E}}$ (respectively $\left(\bar{e}^i_{\beta,p}\right)_{i\in\mathbb{E}}$ and $\left(\bar{e}^i_{\beta,p'}\right)_{i\in\mathbb{E}}$) are the component mass fractions (for all components belonging to the element set $\mathbb{E}$) associated with the species mass fractions $\left(\bar{w}^j_{\beta,s}\right)_{j\in\mathbb{S}}$ (respectively $\left(\bar{w}^j_{\beta,p}\right)_{j\in\mathbb{S}}$ and $\left(\bar{w}^j_{\beta,p'}\right)_{j\in\mathbb{S}}$). Consequently, for a "limiting" element case corresponding to the absence of element i in the residual liquid phase (*i.e.* $\bar{e}^i_{\beta,p'}=0$), the above equation reduces to:

$$\bar{e}^i_{\beta,p} m_{\beta,p} = \bar{e}^i_{\beta,s} m_{\beta,s} \tag{3.26}$$

Recalling that r is the mass of liquid at the interface required to obtain unit mass of solid, from the above equation, it can be expressed as:

$$r = \max_{i\in\mathbb{E}} \left(\frac{\bar{e}^i_{\beta,s}}{\bar{e}^i_{\beta,p}} \right)$$

For the present case of interest, the "limiting" element for the solidifying interfacial liquid is uranium (U). Thus r is expressed as:

$$r = \frac{\bar{e}^U_{\beta,s}}{\bar{e}^U_{\beta,p}} \tag{3.27}$$

Following this, the "residual" liquid composition in terms of species mass fraction $\left(\bar{w}^j_{\beta,p'}\right)_{j\in\mathbb{S}}$ can be obtained from a simple element mass conservation and a subsequent hypothesis assuming that the "residual" liquid is obtained from a local equilibrium calculation at the interface temperature $\left(T_\beta\left(\bar{w}^j_{\beta,p}\right)_{j\in\mathbb{S}}\right)$. Note that this is the same assumption that has been used in the phase-field model of the multi-phase multi-component diffusion for in-vessel corium in [88].

In this context, Δh is interpreted as the specific enthalpy of reaction associated to the oxygen redistribution in the interfacial liquid concurrent to solidification and it is evaluated as:

$$\Delta h = r\left(\mathcal{H}^{\texttt{LIQUID}}\left[T_\beta, \left(\frac{1}{r}\bar{w}^j_{\beta,s} + \left(1-\frac{1}{r}\right)\bar{w}^j_{\beta,p'}\right)_{j\in\mathbb{S}}\right] - \bar{h}_{\beta,p}\right) \tag{3.28}$$

with $\bar{h}_{\beta,p}$ evaluated from the closure relation given by Eq. 3.19.

Such a modification of the energy and species conservation equations to ensure a thermodynamically consistent description is not common and no discussion regarding such a modification has been found in literature. It should be noted, that for a system where the composition is represented in terms of the element mass fractions, such a modification of the conservation equations will not be required. However, such a description will require additional hypotheses in order to convert the element mass fractions to the species mass fractions, which will be required for the evaluation of the thermophysical quantities.

3.4 Numerical results and analysis

The developed model was subjected to initial verification tests, with respect to global energy balance and the analysis of the heat conduction profile in the solid crust at steady state, the results of which are presented in Appendix B.

Following the initial verification, the modified thermal model with CALPHAD-based EOS inputs, has been used for evaluation of the principal variables of interest on three solidification transients for sub-oxidized and fully oxidized corium systems. These systems have a common U/Zr molar ratio $\left(R_{U/Zr}\right)$ of 1.2, which is typical of French PWRs, with different Zr molar oxidation degree C_{Zr} being 30% , 70% and 100% respectively. These varying oxidation degrees depend on the accident scenarios that lead to core degradation and the consequent corium relocation in the lower head, with $C_{Zr} = 30\%$ being the lowest possible value and $C_{Zr} = 100\%$ corresponding to the complete oxidation of corium before its relocation. For the initial system conditions of the three cases (refer to Table 3.1), the evolution of different parameters were studied for a macro (respectively micro) time-step size of $\Delta t = 100\ s$ (respectively $\delta t = 1\ s$) and have been summarized below. These conditions have been selected in such a way that a monotonic solidification transient is obtained for the corium configurations. The transient calculations are performed until steady state (defined by a criterion relative to the crust mass variation between two consecutive time-steps that should be lower than 10^{-2}kg).

Parameters	$C_{Zr} = 30\%$	$C_{Zr} = 70\%$	$C_{Zr} = 100\%$
Mass power density $\dot{q}^{mass}$ (W/kg)	100		
Solid initial mass m_s (kg)	1000		
Liquid initial mass m_p (kg)	20000		
Solid initial temperature $\bar{T}_s$ (K)	2200		
External boundary temperature $T_{B.C.}$ (K)	1800		
Interface surface area $A(m^2)$	12.56		
Liquid initial temperature $\bar{T}_p$ (K)	2700	2880	2940
Initial interface temperature $T_{liquidus}\left(\bar{w}^j_{\beta,p}(t=0)\right)$ (K)	2637.0	2818.8	2874.7

TABLE 3.1: Initial inputs to the thermal model: Case $C_{Zr} = 30\%$, $C_{Zr} = 70\%$ and $C_{Zr} = 100\%$

3.4.1 Testing the validity of using EOS

The validity of using $\mathcal{H}^{\texttt{LIQUID}}$ and $\mathcal{H}^{\texttt{C1\_FCC}}$ functions as EOS in the conservation equations is, in the general case, related to the linearity of these functions with respect to temperature and composition. As earlier mentioned in Section 3.3.3, these EOS are useful in predicting the system behaviour at a microscopic level but their validity at macroscopic levels need to be tested as well. This is because at a microscopic level, the specific enthalpy can be expressed as a function of the local temperature and composition as $\mathcal{H}^{\theta}(T, (w^j)_{j\in\mathbb{S}})$ for a given phase θ. However, this relation may not be valid for corresponding mass averaged enthalpy $\bar{h}m = \int_{\mathcal{V}} \rho h dV$ where $\mathcal{V}$ refers to the spatial zone in which volume averaging is applied and $m = \int_{\mathcal{V}} \rho dV$ is the mass of the spatial zone.

In order to test the validity of the EOS, the variation of the specific enthalpy (denoted by $\bar{h}_s$ and $\bar{h}_p$ for solid and liquid phases respectively) as a function of temperature is shown in Figure 3.3 (respectively Figure 3.2) for the solid (respectively liquid) phase at initial and steady state compositions (denoted as $\bar{w}^j_0$ and $\bar{w}^j_\infty$ respectively) over the temperature range $[T_{B.C.}, T_\beta]$ (respectively $[T_\beta, T_p]$) for the $C_{Zr} = 30\%$ and $C_{Zr} = 70\%$ cases.

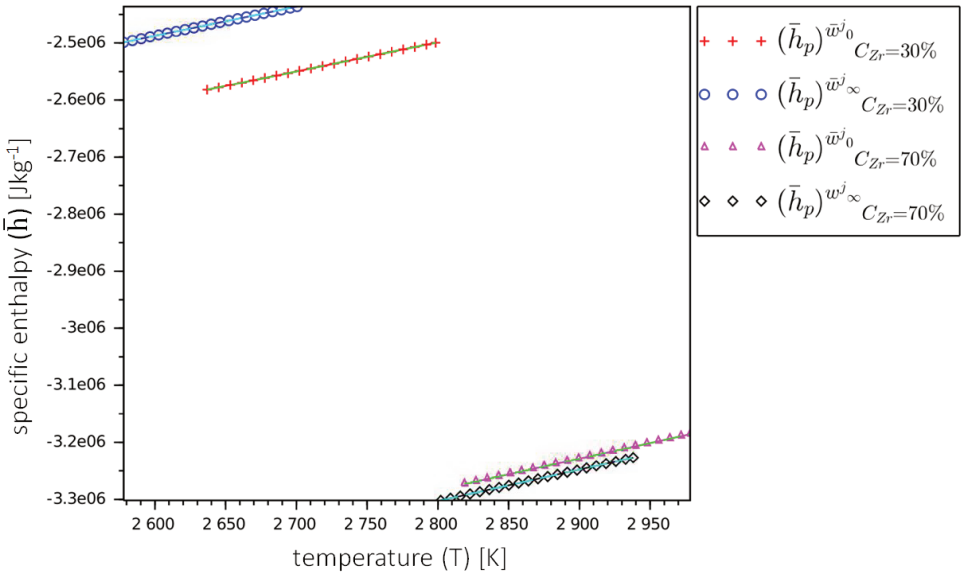

FIGURE 3.2: Verification of the linearity of $\mathcal{H}_{\texttt{LIQUID}}\left[T, (\bar{w}^j)_{j\in\mathbb{S}}\right]$: variation of the liquid enthalpy h_p with temperature T for fixed initial $(\bar{w}_0^j)$ and steady-state compositions $(\bar{w}_\infty^j)$ of the sub-oxidized corium systems with Zr oxidation degrees $C_{Zr} = 30\%$ and $C_{Zr} = 70\%$

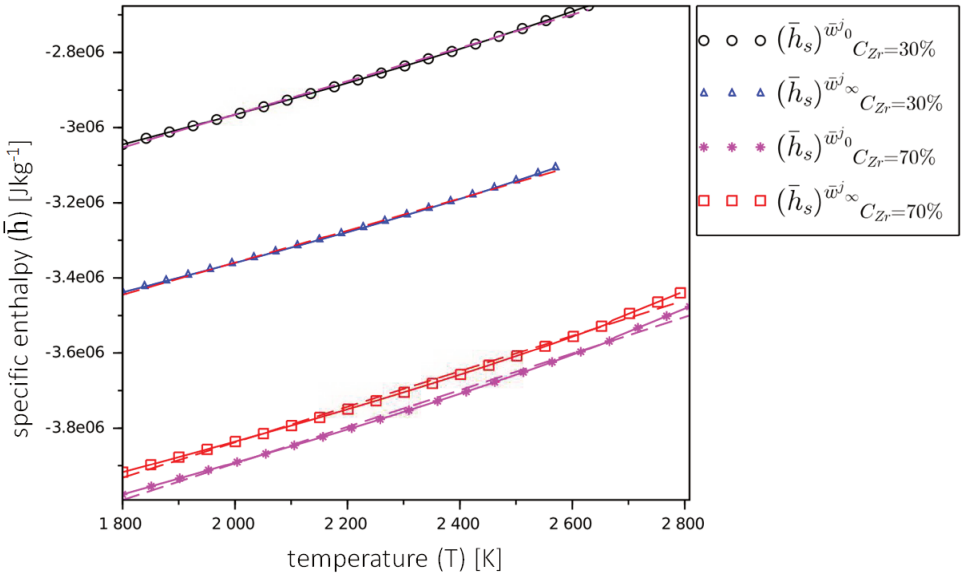

FIGURE 3.3: Verification of the linearity of $\mathcal{H}_{\texttt{C1\_FCC}}\left[T, (\bar{w}^j)_{j\in\mathbb{S}}\right]$: variation of the crust enthalpy h_s with temperature T for fixed initial $(\bar{w}_0^j)$ and steady-state compositions $(\bar{w}_\infty^j)$ of the sub-oxidized corium systems with Zr oxidation degrees $C_{Zr} = 30\%$ and $C_{Zr} = 70\%$

In addition, the dependence of both liquid and solid specific enthalpies on the phase composition at a fixed temperature was obtained (Figure 3.4). The composition was varied as a linear combination of the initial and final compositions $\left(\bar{w}_0^j \text{ and } \bar{w}_\infty^j\right)$ as $\left(\bar{w}^j\right)_{j\in\mathbb{S}} = \left(\left(1-\eta\right)\bar{w}_0^j + \eta\bar{w}_\infty^j\right)_{j\in\mathbb{S}}$ with parameter $\eta \in [0,1]$. It was verified *a posteriori* that these functions are almost linear in the range of temperatures and compositions covered by the transients. The maximum standard deviation of the residuals with respect to a linear regression is about 9076.25 J/kg ($\approx 0.2\%$) recorded for the value of $\bar{h}_s$ of $C_{Zr} = 70\%$ case for its variation with temperature at a fixed initial composition.

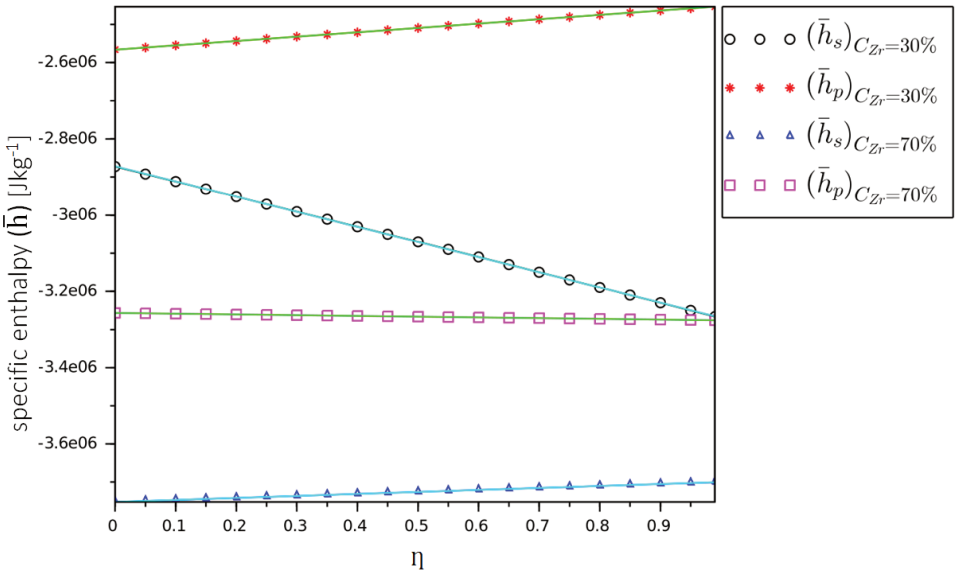

FIGURE 3.4: Verification of the linearity of $\mathcal{H}\left[T, \left(\bar{w}^j\right)_{j\in\mathbb{S}}\right]$: variation of the liquid and solid phase enthalpies (h_p and h_s respectively) with changing composition, for sub-oxidized corium systems with Zr oxidation degrees $C_{Zr} = 30\%$ and $C_{Zr} = 70\%$ at a fixed temperature T

3.4.2 Time evolution of temperature and enthalpy variables

The incorporation of composition changes has a significant effect on the evaluation of the temperatures for the solid and liquid (bulk as well as at the interface) phases. For the two systems (*i.e.* the sub-oxidized and completely oxidized corium systems), it can be seen

from Figure 3.5 (respectively Figure 3.6) that the time-evolution of the liquid (respectively solid) phase temperature is different, with the change in the liquidus temperature being small for the completely oxidized corium system ($C_{Zr} = 100\%$) compared to that for the sub-oxidized corium systems with $C_{Zr} = 30\%$ and $C_{Zr} = 70\%$ respectively.

This difference in trends is due to the dependence of the liquidus temperature on the interface composition. The variations in the composition are seen to directly effect the liquidus temperature. For a completely oxidized system, the change in composition is observed to be small, with the maximum variation being recorded for the mass fraction of ZrO_2 in the solid crust ($\approx -9.5\%$) as well as in the bulk liquid ($\approx 0.92\%$), resulting in almost no variation of the liquidus temperature ($< -2^{\circ}$). In comparison, the sub-oxidized systems of corium undergo larger changes in their composition. For system $C_{Zr} = 30\%$, the highest being recorded for the amount of Zr present in the solid crust ($\approx -64\%$) (respectively $\approx -59^{\%}$ for $C_{Zr} = 70\%$) and the appearance of species U in the solid ($\bar{w}_s^U = 0.062$) (respectively $\bar{w}_s^U = 0.031$ for $C_{Zr} = 70\%$) (see Section 3.3.5). The larger changes in the system composition result in a more significant variation of the liquidus temperature ($\approx -59^{\circ}$ for $C_{Zr} = 30\%$) (respectively for $C_{Zr} = 70\%$, $\approx -17^{\circ}$) as can be seen in Figure 3.5. This dependence affects the overall system by altering the associated thermo-physical properties, and consequently the solidification transient.

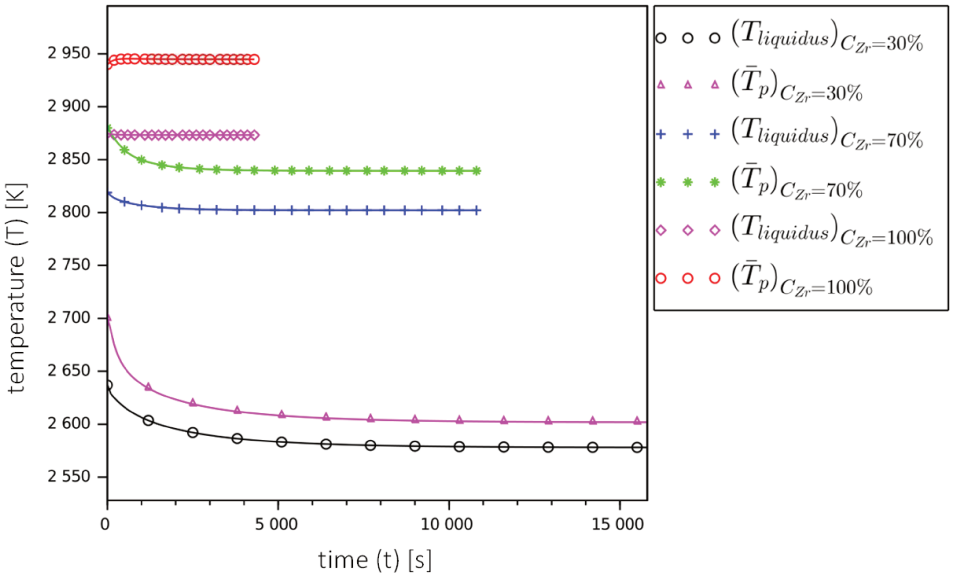

FIGURE 3.5: Evolution of bulk liquid and interface temperatures ($\bar{T}_p$ and $T_{liquidus}$ respectively) with time. Comparing three corium systems with Zr oxidation degrees $C_{Zr} = 30\%$, $C_{Zr} = 70\%$ and $C_{Zr} = 100\%$

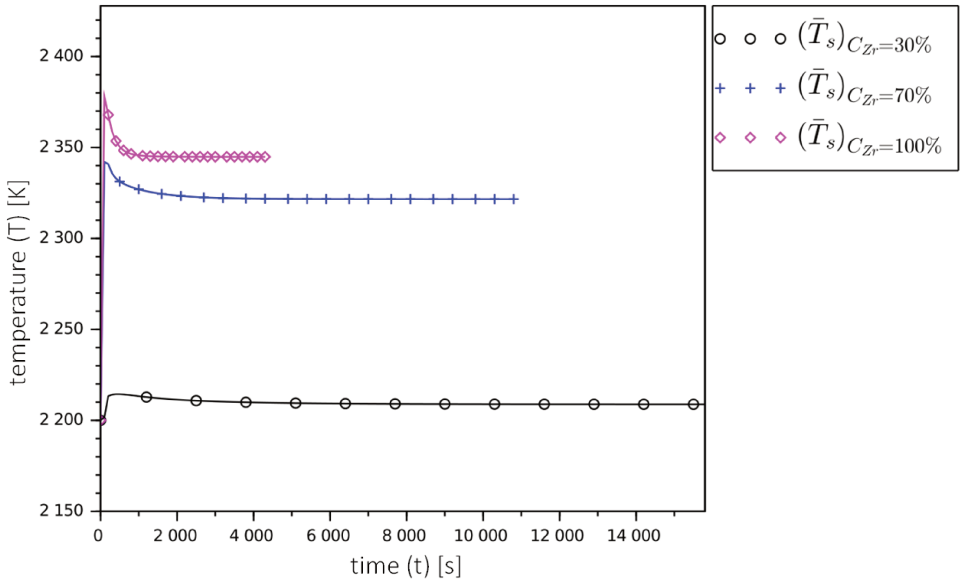

FIGURE 3.6: Evolution of bulk solid temperature ($\bar{T}_s$) with time. Comparing three corium systems with Zr oxidation degrees $C_{Zr} = 30\%$, $C_{Zr} = 70\%$ and $C_{Zr} = 100\%$

Apart from the changes in the temperature and composition of the phases, the redox reaction also has an impact on the phase change enthalpy values for the corium composition. As shown in Section 3.3.5, the redox reaction results in addition of a term (Δh) in the interface energy balance equation. The value of Δh was computed at every macro time-step and it was observed to be small compared to the phase change enthalpy values $\left(\bar{h}_{\beta,p} - \bar{h}_{\beta,s}\right)$ to cause any significant changes on the solidification transient as shown in Figure 3.7. Note that the value of Δh for the completely oxidized corium is not strictly zero (at $t = 0\ s$, $\Delta h \approx 0.5\% \left(\bar{h}_{\beta,p} - \bar{h}_{\beta,s}\right)$); this is related to the solid composition calculated by Open-Calphad that exhibits very small amounts of U ($\approx 10^{-5}$) and O ($\approx 10^{-6}$) for $C_{Zr} = 100\%$, which can be attributed to the numerical convergence of the minimization process and has no impact on the overall transient.

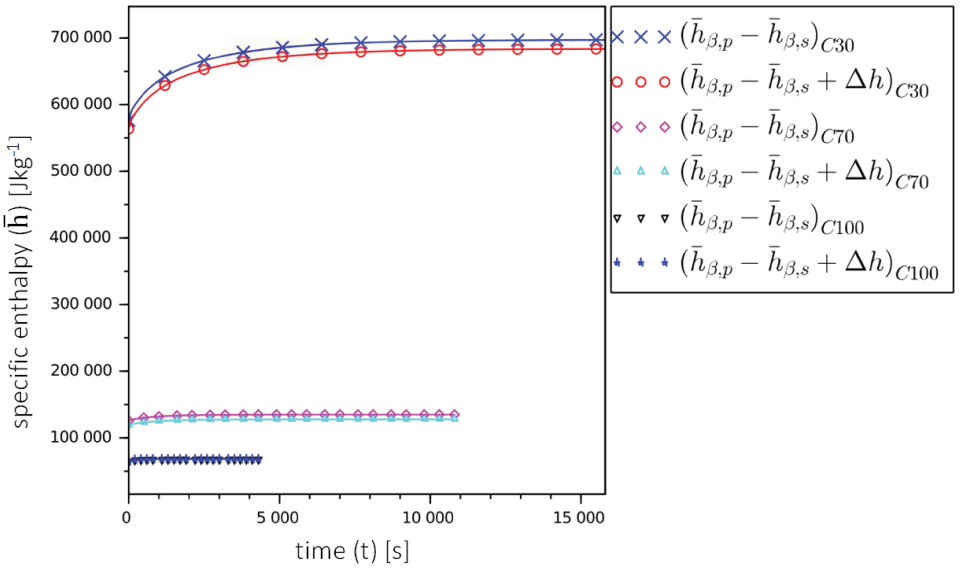

FIGURE 3.7: Evolution of the phase change enthalpies for the solid ($h_{\beta,s}$) and liquid ($h_{\beta,p}$) phases present at the interface with time. Comparing three corium systems with Zr oxidation degrees $C_{Zr} = 30\%$, $C_{Zr} = 70\%$and $C_{Zr} = 100\%$

A large difference in the phase change enthalpy values (neglecting the additional interface term) for $C_{Zr} = 30\%$ is seen when compared to $C_{Zr} = 70\%$ and $C_{Zr} = 100\%$ cases. At $t = 0\ s$, $\left(\bar{h}_{\beta,p} - \bar{h}_{\beta,s}\right)$ for $C_{Zr} = 30\%$ is approximately 5 times the value of $\left(\bar{h}_{\beta,p} - \bar{h}_{\beta,s}\right)$ for $C_{Zr} = 70\%$, whereas it is nearly 9 times the value of $\left(\bar{h}_{\beta,p} - \bar{h}_{\beta,s}\right)$ for $C_{Zr} = 100\%$ (refer

to Figure 3.7). This is mainly related to the modification in the enthalpy value for the liquid phase. At $t = 0\ s$, $C_{Zr} = 30\%$ value for $\bar{h}_{\beta,p}$ is 21% higher than $C_{Zr} = 70\%$ value (respectively 32% higher than $C_{Zr} = 100\%$) while for the solid this increase is limited to 7% (respectively 14% for $C_{Zr} = 100\%$). This important variation is attributed to the large dependence of the enthalpy as a function of the oxygen content. Note that for pure compounds such as UO_2 and ZrO_2, it has been verified that this dispersion of specific latent heat of solidification is largely reduced and values are consistent with published data as shown in Table 3.2.

compound	NUCLEA'09	[89]	[90]
UO_2	276	277	259±15
ZrO_2	730	706	n/a

TABLE 3.2: Latent heat of fusion in kJ/kg for UO_2 and ZrO_2 from different sources

The liquid enthalpy values computed from CALPHAD data are likely to have a large uncertainty because of the scarcity of associated experimental data and measurements of latent heat of solidification for such ternary systems at high temperature are not available [91]. Because of the considerable difference in the values of phase change enthalpies $\left(\bar{h}_{\beta,p} - \bar{h}_{\beta,s} + \Delta h\right)$ between the $C_{Zr} = 30\%$, $C_{Zr} = 70\%$ and $C_{Zr} = 100\%$ cases, an important difference in the corium solidification rate is observed. This difference increases with time, resulting in a slower solidification rate for $C_{Zr} = 30\%$ compared to $C_{Zr} = 70\%$ and $C_{Zr} = 100\%$. Figure 3.8 gives the time evolution of crust mass for the three cases. It can be observed that the degree of oxidation of the corium determines the rate of heat transfer and consequently the solidification rate for the system. Lesser Zr oxidation in a system leads to a longer transient time before reaching steady state, owing to its decreasing solidification rate.

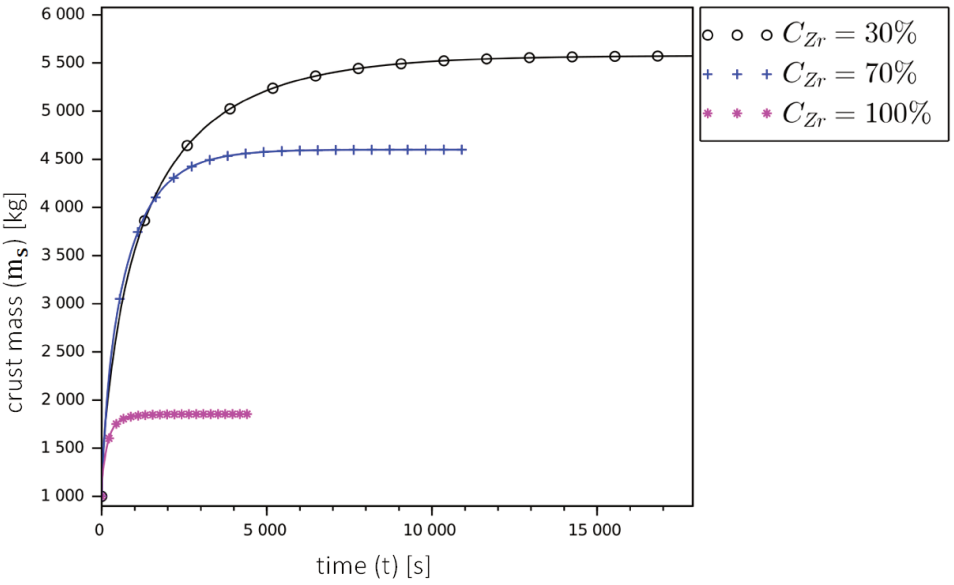

FIGURE 3.8: Evolution of solid crust mass m_s with time. Comparing the trend for three corium systems with Zr oxidation degrees $C_{Zr} = 30\%$, $C_{Zr} = 70\%$ and $C_{Zr} = 100\%$

3.4.3 Stability of the explicit coupling scheme

A parametric study on the explicit time-step integration was performed for the $C_{Zr} = 30\%$ case to check the accuracy and stability of the integration scheme used. The results obtained with a step-size value smaller (i.e. $\Delta t = 10\ s$) than the initially chosen value of $\Delta t = 100\ s$ were very similar to each other. For a larger time-step ($\Delta t = 1000\ s$), limited damped oscillations are observed on the crust mass with the maximum amplitude observed at the end of first macro time-step (updated crust mass value at $t = 1000^{+}s$ being approximately 2.5% less than the crust mass evaluated at $t = 1000^{-}s$) and the differences decreasing for subsequent time-steps (trend depicted by Figure 3.9). This can be explained as it was observed that for a larger time-step, the value of heat fluxes at the interface $\bar{\varphi}_{\beta,p}$ and $\bar{\varphi}_{\beta,s}$ underwent oscillations due to the interface temperature discontinuities (due to the composition update at the end of each macro time-step) that lead to changes of sign of $\left(\bar{\varphi}_{\beta,p} + \bar{\varphi}_{\beta,s}\right)$ before and after the composition updates.

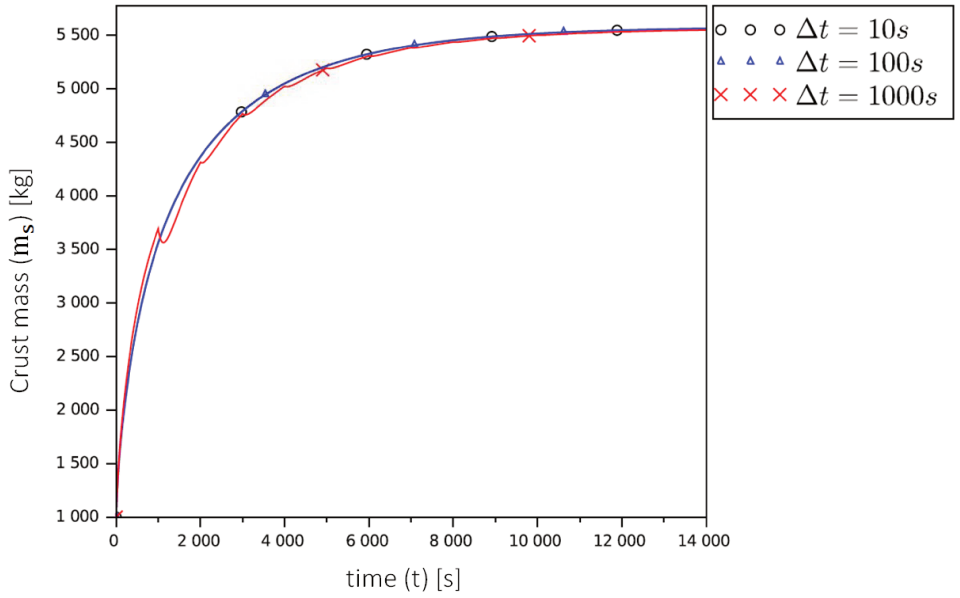

FIGURE 3.9: Evolution of solid crust mass m_s with time. Comparing the stability of the explicit coupling time scheme for a corium system with Zr oxidation degree $C_{Zr} = 30\%$, for three different micro time-step values of $\Delta t = 10$ s, $\Delta t = 100$ s and $\Delta t = 1000$ s

3.5 Modelling of finite mass transfer in liquid boundary layer

It should be recalled that the results discussed in Section 3.4 with respect to the thermodynamic consistency of coupling, are specific to a model description based on the hypothesis of infinitely fast mass transfer in the liquid boundary layer at the interface. Considering a finite mass transfer in the liquid boundary, this condition of $\bar{w}^j_{\beta,p} = \bar{w}^j_p$ will no longer hold true. For such a case, a generalized expression for the mass averaged composition of the interfacial liquid ($\bar{w}^j_{\beta,p}$) can be derived from Eqs. 3.10 and 3.11:

$$(r-1)\dot{m}_{\beta,p}\ \bar{w}^j_{\beta,p} = (r-1)\dot{m}_{\beta,p}\ \bar{w}^j_{\beta,p'} - \rho A_\beta \sum_{h=1}^{n-1} k_m^{jh}\left(\bar{w}^h_{\beta,p} - \bar{w}^h_p\right) \tag{3.29}$$

From the point of view of ensuring thermodynamic consistency, writing the species conservation equations for this finite mass transfer case involves coupling with CALPHAD

as solving the above equation, requires calculation of the mass transfer coefficients k_m^{jh} before-hand. These coefficients can be deduced from analysis based on heat and mass transfer correlations for natural convection (as obtained in [92]), and are related to the diffusion coefficient D for binary systems (see [93]) through the relation:

$$k_m = D^{2/3}\left(\frac{Nu}{H}\mu^{1/3}Gr^{1/12}Pr^{\mathrm{r}}\right) \tag{3.30}$$

where:

- Nu is the Nusselt number, which represents the ratio of convective to conductive heat transfer at the boundary in a fluid;
- Gr is the Grashof's number, which represents the correlation of heat and mass transfer due to thermally induced natural convection;
- Pr^{r} is the Prandtl number, which represents the ratio of momentum diffusivity to thermal diffusivity, and r is the exponent which is equal to $-1/2$ and $-1/3$ for $Pr \leq 1$ and $Pr \gg 1$ respectively;
- μ refers to the momentum diffusivity ($m^2 s^{-1}$), and;
- H represents the height of the fluid layer (m).

However, for an n component system (which is of interest for the present case), there exist $n-1$ independent inter-diffusion coefficients[4] D_{kj}^n [94]. As a result, the diffusion coefficients can be conveniently represented in an $n-1$ dimensional matrix notation called the Fick matrix $[D]$, where each element of the matrix denotes a diffusion coefficient D_{kj}^n (evaluated by eliminating the composition dependence of n^{th} element):

$$D_{kj}^n = D_{kj} - D_{kn} \tag{3.31}$$

These D_{kj} (which are dependent on the mobility value ς_k for the component k) can be calculated by adopting a linearized theory for mass fluxes, which is discussed in Appendix D. In case of a n-component system, a diagonalization of $[D]$ can be performed in order to apply Eq. 3.30 for its different eigenvalues in order to calculate the mass transfer coefficient k_m^{jh}

[4]The derivations for the expressions of these inter-diffusion coefficients is one of the focuses of Chapter 4, with an exception that the final expression for diffusion coefficients are required to be in terms of mass fractions (to ensure consistency with the description adopted for the macroscopic model) instead of molar concentrations.

Having ensured a consistent evaluation of the mass transfer coefficient values, the species equations need to be solved so as to obtain a physical solution related to the evolution of liquid composition with time. However, the dependency of $\bar{w}^j_{\beta,p}$, $\bar{w}^j_{\beta,p'}$ and r values on the bulk liquid composition $\bar{w}^j_p$, results into a non-linear system of equations. In order to solve for the interface liquid composition $\bar{w}^j_{\beta,p}$, a fixed point iteration scheme with relaxation was used. With this updated modeling of the interface condition in species mass fractions, different numerical simulations were performed for the system conditions described in Section 3.4. In all cases, convergence issues were faced with $\bar{w}^{j^{(n+1)}}_{\beta,p}$ going rapidly out of the allowed range [0,1] during iterations in such a way that these simulations could not be completed. The analysis made through additional tests (by direct evaluation of the function associated with this non-linear problem over its input variable space) showed that the existence of a solution to this non-linear system in the general case is questionable. Further analysis is needed but it was considered out of main scope of this Ph.D. thesis and thus, was not undertaken.

3.6 Conclusions

The work presented in this chapter has allowed for a detailed discussion on exploring the possibility of using CALPHAD database for constructing general EOS to be used as closures in corium-related thermal models associated with phase segregation. In particular, it was shown that the consistent use of CALPHAD data for evaluating interface quantities related to the local equilibrium assumption requires a modification of the species conservation equations for the case of a sub-oxidized corium. Although the testing of these CALPHAD based EOS has been done on a mock-up model, the feasibility of using them to obtain thermodynamically consistent closures (as reported by the obtained results) also addresses the issue of thermodynamic consistency for the coupled thermochemical-thermohydraulic models for in-vessel corium description.

Moreover, the numerical study related to the adoption of different segregation hypotheses during the EOS construction [81] further confirms the applicability of such an approach where a general EOS, supplemented by appropriate hypotheses, can be used for providing

closures to the models for depicting different cases, such as treating the liquid miscibility gap. The next step in this direction is to actually construct a complete EOS and verify its use for in-vessel corium modeling in the PROCOR.

Chapter 4

Consistent formulation of a mesoscopic model for in-vessel corium through phase-field

This chapter presents a thermodynamically consistent formulation of a non-isothermal phase-field model which can be used to simulate the kinetics of thermochemical processes associated with in-vessel corium behaviour. In principle, this formulation can be used for a wide range of applications, two of which have been discussed in the chapter; namely the process of corium solidification at the RPV boundary and the inter-liquid transfer associated to a miscibility gap in the case of transient stratification of in-vessel corium. Furthermore, the questions related to the use of CALPHAD-based description for mesoscopic models are addressed. In addition, the constraints posed on the model due to the upscaling of the interface have been studied for isothermal conditions in simple binary systems.

As mentioned earlier in Chapter 2, a phase-field model is useful as it can be introduced in the frame of CFD based codes, which can be used to gain knowledge regarding the thermohydraulic behaviour for in-vessel corium.

4.1 Thermodynamic representation of an n-component system

Recalling the discussion in Section 2.2.2.2, it is known that the formulation of a phase-field model requires the choice of an appropriate thermodynamic potential, which can be used for the consistent derivation of the evolution equations of the dynamic variables of interest. For an n-ary system (*i.e.* composed of n components) to be studied in isothermal conditions with a fixed volume, the appropriate thermodynamic potential for description is the Helmholtz free energy $\mathbb{F}$, which can be derived from the molar internal energy of the system ($\tilde{E}_m$) through a Legendre transformation. This molar internal energy is represented as a state function[1] of variables $\tilde{S}_m$, V_m and x_i as:

$$\tilde{E}_m = T\tilde{S}_m - pV_m + \sum_{i=1}^{n} \tilde{\mu}_i x_i \tag{4.1}$$

where:

- $\tilde{S}_m$ is the molar entropy for the system;
- V_m represents the molar volume of the system;
- x_i is the mole fraction of the i^{th} component, expressed as $x_i = \frac{N_i}{N}$, where N_i is the number of moles of component i and N is the total number of moles in the system, and;
- $\tilde{\mu}_i$ is the chemical potential associated with the i^{th} component, and it is expressed as $\tilde{\mu}_i = \frac{\partial \tilde{E}}{\partial N_i}$.

The above system description can be reduced by defining $n-1$ 'independent' component concentrations (in terms of mole fractions), with the n^{th} component concentration expressed in terms of these independent concentrations as $x_n = 1 - \sum_{i=1}^{n-1} x_i$. Substituting the relation in the above equation, the molar internal energy for the reduced system (denoted by E_m) is expressed as:

$$E_m = TS_m - pV_m + \sum_{i=1}^{n-1} \mu_i x_i + \tilde{\mu}_n \tag{4.2}$$

[1]It should be noted that the tilde notation introduced above is only to distinguish the thermodynamic representation of an n-ary system from that for a reduced system composed of $n-1$ constituents.

with :

$$\mu_i = (\tilde{\mu}_i - \tilde{\mu}_n) \tag{4.3}$$

If the system is defined for a constant pressure condition, with the internal energy density e_m (expressed as E_m/V_m) expressed as a function of the variables $s_m, (x_i/V_m)$ and a non-conserved parameter ϕ that denotes the phase of the system, de_m is obtained from Eq. 4.2 as:

$$de_m = Tds_m + \sum_{i=1}^{n-1} \mu_i d\left(\frac{x_i}{V_m}\right) + \frac{\partial e_m}{\partial \phi} d\phi \tag{4.4}$$

where:

- T is defined as the partial derivative of e_m with respect to the entropy density s_m (expressed as S_m/V_m): $T = \frac{\partial e_m}{\partial s_m}$, and;
- μ_i is defined as the partial derivative of e_m with respect to the component molar concentration x_i/V_m : $\mu_i = \frac{\partial e_m}{\partial (x_i/V_m)}$.

In order to utilize the thermodynamic description provided by CALPHAD, a Legendre transformation of the internal energy to the Gibbs energy of the system is required. This has been discussed in detail in Appendix C, which gives the thermodynamic relation between the Gibbs energy density g_m and the internal energy density of a reduced system as:

$$\begin{aligned} dg_m &= de_m - Tds_m - s_m dT \\ &= \sum_{i=1}^{n-1} \mu_i d\left(\frac{x_i}{V_m}\right) + \frac{\partial e_m}{\partial \phi} d\phi - s_m dT \end{aligned} \tag{4.5}$$

For a binary system (*i.e.* $n = 2$), the thermodynamic representation for the system can be achieved in terms of a single component concentration as:

$$E_m = TS_m - pV_m + \mu x \tag{4.6}$$

With $\mu = (\tilde{\mu}_1 - \tilde{\mu}_2)$. For constant pressure condition, dividing by the molar volume V_m yields the expression for the internal energy density $e_m(s_m, (x/V_m), \phi)$:

$$de_m = Tds_m + \mu d\frac{x}{V_m} + \frac{\partial e_m}{\partial \phi} d\phi \tag{4.7}$$

The Legendre transformation of the internal energy density for the reduced binary system to the Gibbs energy density gives the final form as:

$$dg_m = \mu d\frac{x}{V_m} + \frac{\partial e_m}{\partial \phi} d\phi - s_m dT \tag{4.8}$$

For a system composed of materials whose density is not dependent on pressure, the thermodynamic description can be obtained by making use of the Gibbs free energy as the thermodynamic potential. Furthermore, assuming that the molar volume V_m for such systems is constant, the Helmholtz free energy functional ($\mathbb{F}$) is equivalent to the Gibbs free energy functional ($\mathbb{G}$) and so the evolution equations for the phase-field model can be derived in a consistent manner. In terms of coupling the phase-field model with CALPHAD to obtain the thermodynamic properties, recalling that the NUCLEA database consists of Gibbs energies that are functions of the constituent composition y_i, there exists an additional question of the relating the system composition (which is defined in terms of component x_i) to y_i. Consequently, just having the information on the element compositions is not sufficient, but the relation between the elements and the species mole fractions must also be known, which depends on the system which is being treated. For instance, for a U-O-Zr system, it is necessary to know about the state of oxygen (*i.e.* if it exists as a free element or is combined with other elements) in relation to the formation of oxide compounds. The solution to this question is addressed later in the chapter.

However, for the phase-field model to take into account the effect of temperature variation in the system, the appropriate potential to describe the system is entropy (as proposed by [75]). The following section discusses the formulation of a generalized phase-field model that was developed for studying the thermochemical processes associated with the in-vessel corium. It should be noted that although the presentation of equations has been made in terms of the solid liquid phases, this model can be used to study both, the solidification as well as the phase-segregation in liquid systems. Furthermore, for the sake of clarification, the formulation has been given for binary systems, but it can be applied to the treatment of an n-ary system as the evolution equations for the binary system can be converted for multi-component system by replacing the terms dependent on the reduced system composition (x), with the terms dependent on x_i $\forall i \in n-1$, for the reduced $n-1$ component system.

4.2 Consistent formulation of evolution equations from the entropy functional

The formulations based on Gibbs (or Helmholtz) free energy functional are applicable strictly to the study of isothermal systems, and are extended to some non-isothermal cases by 'patching in' an energy equation [95]. In order to treat non-isothermal cases, incorporation of the energy equation is necessary since it takes into account the temperature variation associated with the energy flow across the moving phase boundary. As a result of the addition of the energy conservation equation, the dependent variable changes from temperature to energy and consequently the thermodynamic potential changes from the Gibbs free energy to the entropy $\mathbb{S}$.

This approach of using an entropy functional for the formulation of phase field models, first introduced by Penrose and Fife [75], is useful for obtaining thermodynamically-consistent equations for non-isothermal systems, with the possibility to obtain isothermal situations as a special case. Writing the entropy density as a function of e_m, $\frac{x}{V_m}$ and ϕ, the entropy functional for a constant volume V system [96] is given as:

$$\mathbb{S} = \int_V \left(s_m(e_m, \frac{x}{V_m}, \phi) - \frac{1}{Ta} f_{dw}(\phi) - \frac{1}{T} \frac{{\kappa_\phi}^2}{2} |\nabla \phi|^2 \right) dV \tag{4.9}$$

where :

- s_m refers to the local molar entropy density;
- ϕ is the non-conserved phase field variable or the order parameter, which indicates the phase of the material. ϕ is defined as a continuous spatial function, where it is assumed that at any instant in time, it takes a value of 1 and 0 in the bulk solid and liquid phase regions, whereas it varies continuously between these two values across the interface;
- $f_{dw}(\phi)$ is a double-well function given by:

  $$f_{dw}(\phi) = \frac{1}{4} \left[\phi^2 (1 - \phi)^2 \right]$$

  which has mimina at $\phi = 0$ and $\phi = 1$. Together $s_m(e_m, \frac{x}{V_m}, \phi) - \frac{1}{Ta} f_{dw}(\phi)$ denote the local entropy density of the system;

- a is a pre-factor that is used for the up-scaling of the interface thickness, and;
- κ_ϕ is the positive gradient coefficient for ϕ. This constant parameter is associated with the formation of the interface and accounts for the energy "cost" to the system associated with it.

In a general formulation, there also exist gradient terms κ_e^2, κ_x^2 that are associated with gradients in energy and composition within the interface. The physical significance of these gradient coefficients and how to obtain them depends on the spatial scale of the problem being studied. On a microscopic scale, these coefficients will result from the interactions that occur at this scale, and they can be typically be obtained from mean field approximations to microscopic models, in a manner similar to [97]. On a macroscopic scale, the gradient coefficients will be obtained from the macroscopic properties of the interface, in particular the surface tension and the interface thickness (for example, see [65] [98] and [99]). However, for most phase field models, the effect of these gradients is not taken into account. In this respect, by taking into account the phase-field ϕ, a simplest choice for the modelling can be made, where only the gradient coefficient associated with ϕ is retained as it allows for a direct control on the parameters associated with the interface (such as the interface energy and thickness). This choice has been adopted for the development of the present model. Consequently, for the entropy functional given by Eq. 4.9, the time derivative is given as:

$$\frac{d\mathbb{S}}{dt} = \int_V \left[\left(\frac{\partial s_m}{\partial e_m} \right) \dot{e}_m + \left(\frac{\partial s_m}{\partial x/V_m} \right) \dot{x}/V_m + \left(\frac{\partial s_m}{\partial \phi} - \frac{1}{Ta} f'_{dw}(\phi) + \frac{{\kappa_\phi}^2}{T} \nabla^2 \phi \right) \dot{\phi} \right] dV \quad (4.10)$$

The driving forces for overall phase transformation can be obtained by calculating the variational derivative of the entropy functional (*i.e.* Eq. 4.10):

$$\left(\frac{\delta \mathbb{S}}{\delta e_m} \right) = \left(\frac{\partial s_m}{\partial e_m} \right) \quad (4.11)$$

$$\left(\frac{\delta \mathbb{S}}{\delta (x/V_m)} \right) = \left(\frac{\partial s_m}{\partial (x/V_m)} \right) \quad (4.12)$$

$$\left(\frac{\delta \mathbb{S}}{\delta \phi} \right) = \left(\frac{\partial s_m}{\partial \phi} - \frac{1}{Ta} f'_{dw}(\phi) + \frac{1}{T} {\kappa_\phi}^2 \nabla^2 \phi \right) \quad (4.13)$$

4.2.1 Derivation of the kinetic equations for the conserved and non-conserved variables

To discuss the kinetics of a model, time evolution equations are required for the fields which control the evolution of the entropy functional. For the energy and concentration fields, since they are conserved quantities, their evolution is governed by the local energy and mass conservation laws:

$$\dot{e}_m = -\nabla J_e \tag{4.14}$$

$$\frac{\dot{x}}{V_m} = -\nabla J_x \tag{4.15}$$

To ensure consistency with the second law of thermodynamics, the local entropy production must be non-negative. This can be achieved by adopting the linear phenomenological equations for coupled heat and mass transfer given by the gradients corresponding to variation in entropy with respect to changing energy and concentration:

$$J_e = M_{ee}\nabla\left(\frac{\delta\mathbb{S}}{\delta e_m}\right) + M_{ex}\nabla\left(\frac{\delta\mathbb{S}}{\delta(x/V_m)}\right) \tag{4.16}$$

$$J_x = M_{xe}\nabla\left(\frac{\delta\mathbb{S}}{\delta e_m}\right) + M_{xx}\nabla\left(\frac{\delta\mathbb{S}}{\delta(x/V_m)}\right) \tag{4.17}$$

where M_{xx} and M_{ee} are related to the inter-diffusion coefficients for the components and the heat conduction, respectively. The coefficients M_{ex} and M_{xe} describe the coupled effect of the heat and mass transfer which can be related to the Soret and Dufour effects[2]. These coefficients are considered to be equal to each other according to Onsager's reciprocal relations. The second law of thermodynamics requires these coefficients to be positive[3]. If the contribution of the cross-terms is ignored, Eqs. 4.16 and 4.17 can be simplified as:

$$J_e = M_{ee}\nabla\left(\frac{\delta\mathbb{S}}{\delta e_m}\right) = M_{ee}\nabla\left(\frac{\partial s_m}{\partial e_m}\right) \tag{4.18}$$

$$J_x = M_{xx}\nabla\left(\frac{\delta\mathbb{S}}{\delta(x/V_m)}\right) = M_{xx}\nabla\left(\frac{\partial s_m}{\partial(x/V_m)}\right) \tag{4.19}$$

[2]The Soret effect refers to the presence of mass diffusion fluxes that arise due to spatial variations in the temperature of a system. On the other hand, the Dufour effect refers to the presence of an energy flux due to a concentration gradient.

[3]For a general case where the cross terms M_{xe} and M_{ex} are considered, from the second law of thermodynamics, it is required that the matrix M composed of these coefficients M_{ee}, M_{xx}, M_{xe} and M_{ex} must be positive. Only in the specific case where the cross terms are taken to be zero, does it imply that the diagonal terms M_{ee} and M_{xx} are positive.

It should be noted that by neglecting the effect of the cross terms does not change any of the discussions that are related to the point of answering the thermodynamic closures. The time evolution of the order parameter ϕ, which is a non-conserved quantity, is given by the Allen-Cahn equation:

$$\frac{\partial \phi}{\partial t} = M_\phi \frac{\delta \mathbb{S}}{\delta \phi} = M_\phi \left(\frac{\partial s_m}{\partial \phi} - \frac{1}{Ta} f'_{dw}(\phi) + \frac{1}{T} {\kappa_\phi}^2 \nabla^2 \phi \right) \tag{4.20}$$

where M_ϕ is a positive kinetic parameter related to the mobility of the interface. The application of the evolution equations Eqs. 4.14, 4.15 and 4.20 to determine the kinetics of the model requires the evaluation of the driving forces for the phase transformation [66].

The driving forces for the evolution equations (denoted by the gradients of the partial derivatives given on the R.H.S. of Eqs. 4.18, 4.19 and 4.20) can be obtained from the thermodynamic relations detailed in Appendix C.

For the energy conservation equation, starting from the first principle of thermodynamics and using Eq. C.4 of Appendix C:

$$\nabla \left(\frac{\partial s_m}{\partial e_m} \right) = \nabla \left(\frac{1}{T} \right) = -\frac{1}{T^2} \nabla T \tag{4.21}$$

In a similar manner, for the mass conservation equation, the derivative $\frac{\partial s_m}{\partial (x/V_m)}$ can be obtained from Maxwell's equations Eq. C.29 from Appendix C and the driving force is given as:

$$\nabla \left(\frac{\partial s_m}{\partial (x/V_m)} \right) = \nabla \left(-\frac{\mu}{T} \right) \tag{4.22}$$

For the non-conserved order parameter ϕ, the driving force is given by the expression for $\frac{\delta \mathbb{S}}{\delta \phi}$ in Eq. 4.20, where $\frac{\partial s_m}{\partial \phi}$ is given by Eq. C.28 of Appendix C :

$$\frac{\partial s_m}{\partial \phi} = -\frac{1}{T} \left(\frac{\partial e_m}{\partial \phi} \right)_{s_m, \frac{x}{V_m}} = -\frac{1}{T} \left(\frac{\partial g_m}{\partial \phi} \right)_{T, \frac{x}{V_m}} \tag{4.23}$$

where $\frac{\partial g_m}{\partial \phi}$ is obtained from the Gibbs energy density written for the system by introducing an interpolation function $p(\phi)$ between Gibbs energy densities of homogeneous phases g_m^s and g_m^l:

$$g_m(T, \frac{x}{V_m}, \phi) = p(\phi) g_m^s(T, \frac{x^s}{V_m}) + (1 - p(\phi)) g_m^l(T, \frac{x^l}{V_m}) \tag{4.24}$$

where $x_s = 0$ and $x_l = x$ if $\phi = 0$, $x_s = x$ and $x_l = 0$ if $\phi = 1$ and, when $\phi \in]0,1[$, x_s and x_l are the compositions of the solid and liquid phases at equilibrium for an overall composition given by x as explained in more details in the next section.

$$p(\phi) = \phi^3(10 - 15\phi + 6\phi^2) = \begin{cases} 0 & \phi = 0 \\ 1 & \phi = 1 \end{cases} \tag{4.25}$$

$$p'(\phi) = 30\phi^2(1-\phi)^2 = 0 \;\forall\; \phi \in \{0,1\} \tag{4.26}$$

Substituting Eqs. 4.21 and 4.22, the fluxes for energy and mass (*i.e.* Eqs. 4.18 and 4.19) can be expressed as :

$$J_e = M_{ee}\nabla\left(\frac{1}{T}\right) = -\frac{M_{ee}}{T^2}\nabla T \tag{4.27}$$

$$J_x = M_{xx}\nabla\left(-\frac{\mu}{T}\right) = -M_{xx}\nabla\left(\frac{\mu}{T}\right) \tag{4.28}$$

Eqs. 4.27 and 4.28 can be substituted in Eqs. 4.14 and 4.15 to get the final forms for the evolution equations for the variables e_m and x/V_m :

$$\dot{e}_m = -\nabla.\left[-\frac{M_{ee}}{T^2}\nabla T\right] \tag{4.29}$$

$$\frac{\dot{x}}{V_m} = -\nabla.\left[-M_{xx}\nabla\left(\frac{\mu}{T}\right)\right] \tag{4.30}$$

It should be noted that under the constant molar volume assumption, the energy equation given by Eq. 4.29 can be equivalently written in terms of the specific enthalpy h.

In the above formulation, if the dependency on the phase marker ϕ is dropped and instead the gradient coefficient in composition (κ_x^2) is considered, the evolution equations given by Eq. 4.29 (when written in the form of enthalpy) and Eq. 4.30 present a non-isothermal extension to the Cahn-Hilliard model developed in [44] for studying the kinetics of inter-layer mass transfer in the liquid miscibility gap of in-vessel corium. In order to solve the system of evolution equations (*i.e.* Eqs. 4.29 and 4.30 for enthalpy and composition respectively), the energy conservation equation requires closures in terms of enthalpy-temperature relations. From the point of view of thermodynamic consistency, this system is very similar to the case discussed in Chapter 3 and the closure relations can be obtained by using an EOS (constructed from CALPHAD) of the form $\mathcal{H}^\theta : T, x \rightarrow h^\theta$.

4.2.2 Limitations to the formulation in entropy approach

The use of the phase-field model developed from the entropy functional approach for studying a two-phase binary (or n-ary) system has certain limitations. Contrary to the case of a pure substance, the energy (or enthalpy) as well as the composition of the binary system varies across the interface. In order to achieve the condition of local equilibrium, both phases must follow the conditions that:

- the chemical potentials of the two phases must be equal, *i.e.* $\mu_s(x_s/V_m) = \mu_l(x_l/V_m)$, where x_s/V_m (respectively x_l/V_m) refer to the component composition in phase θ ($\theta = s, l$), and;
- the grand potential density (denoted as $\omega_m = g_m - \mu x/V_m$) must be equal for the two phases.

As a result, the bulk and the interface quantities cannot be decoupled and a non-linear system of equations needs to be solved in order to obtain the composition at the interface. Several alternate solutions have been proposed to solve this problem of non-linearity, which includes the option of defining separate fields for the composition of each of the phases (as proposed in [99]).

However, it should be noted that for the system defined in terms of enthalpy, composition and ϕ, the corresponding intensive variables to the conserved quantities (i.e. temperature T and chemical potential μ) remain constant across the interface at equilibrium. Thus, these variables can be used as dependent variables for deriving the phase-field model [100]. Consequently, the corresponding thermodynamic potential must be changed to the grand potential functional (denoted by $\breve{\Omega}$) from entropy.

4.3 Equivalent formulation of phase-field model from the grand potential

Following the Legendre transformation from Gibbs energy to the grand potential (discussed in Appendix C) the thermodynamic relation between grand potential density (ω_m) and

entropy density (s_m) is obtained by Eq. C.20 as:

$$\left(\frac{\partial \omega_m}{\partial T}\right)_{\mu,\phi} = -s_m \tag{4.31}$$

Thus, by making use of this thermodynamic relation, the entropy functional given by Eq. 4.9 can be re-written in a thermodynamically consistent way (see for example [101]) as:

$$\breve{\Omega} = \int_V \left(\omega_m(T,\mu,\phi) + \frac{1}{a} f_{dw}(\phi) + \frac{\kappa_\phi^2}{2}|\nabla\phi|^2\right) dV \tag{4.32}$$

with ω_m expressed as an interpolation (given by uni-variate function $p(\phi)$ in Eq. 4.25) between the homogeneous grand potential densities for the phases $\theta = s$ and l :

$$\omega_m = p(\phi)\omega_m^s(T,\mu) + (1-p(\phi))\omega_m^l(T,\mu) \tag{4.33}$$

The variational derivatives for $\breve{\Omega}$ can be obtained as (details in Appendix C):

$$\frac{\delta\breve{\Omega}}{\delta T} = \left(\frac{\partial \omega_m}{\partial T}\right) = -s_m \tag{4.34}$$

$$\frac{\delta\breve{\Omega}}{\delta \mu} = \left(\frac{\partial \omega_m}{\partial \mu}\right) = -\frac{x}{V_m} \tag{4.35}$$

$$\frac{\delta\breve{\Omega}}{\delta \phi} = \left(\frac{\partial \omega_m}{\partial \phi} + \frac{1}{a} f'_{dw}(\phi) - \kappa_\phi^2 \nabla^2\phi\right) = -T\frac{\delta \mathbb{S}}{\delta\phi} \tag{4.36}$$

Similarly, the partial derivative of the grand potential density with respect to the dependent variables T, μ and ϕ can be obtained from Eq. 4.33.

4.3.1 Evolution equations for the conserved and non-conserved order parameters

The coupled equations for the evolution of the conserved variables μ and T from the grand potential functional (Eq. 4.32), are obtained by making use of the mass and energy conservation equations, and the time-evolution of the non-conserved order parameter ϕ:

4.3.1.1 Conserved order parameters T and μ:

4.3.1.1.1 Mass conservation equation

In the expression for the mass conservation equation given by Eq. 4.30, the substitution of Eq. C.21 (from Appendix C) for $\frac{x}{V_m}$ gives:

$$\frac{\partial}{\partial t}\left(\frac{\partial \omega_m}{\partial \mu}\right) = \nabla\left[-M_{xx}\nabla\left(\frac{\mu}{T}\right)\right] \tag{4.37}$$

By making use of Eq. C.24 from Appendix C and re-arranging the terms, the mass conservation equation is written in terms of the derivative of the molar grand potential (denoted by Ω_m) with respect to the variables T, μ and ϕ:

$$\left(\frac{\partial^2 \Omega_m}{\partial T \partial \mu}\right)\frac{\partial T}{\partial t} + \left(\frac{\partial^2 \Omega_m}{\partial \mu^2}\right)\frac{\partial \mu}{\partial t} = V_m \nabla\left[-M_{xx}\nabla\left(\frac{\mu}{T}\right)\right] - \left(\frac{\partial^2 \Omega_m}{\partial \mu \partial \phi}\right)\frac{\partial \phi}{\partial t} \tag{4.38}$$

4.3.1.1.2 Energy conservation equation

In Eq. 4.29 for conservation of energy, the time derivative of the molar internal energy density $e_m(s_m, x/V_m, \phi)$ can be expressed as derivative of the grand potential density (from Eqs. C.20, C.21 and C.22 of Appendix C) as:

$$\begin{aligned}\frac{\partial e_m}{\partial t} &= T\frac{\partial s_m}{\partial t} + \mu\frac{\partial}{\partial t}\left(\frac{x}{V_m}\right) + \left(\frac{\partial e_m}{\partial \phi}\right)\frac{\partial \phi}{\partial t} \\ &= -T\frac{\partial}{\partial t}\left(\frac{\partial \omega_m}{\partial T}\right) - \mu\frac{\partial}{\partial t}\left(\frac{\partial \omega_m}{\partial \mu}\right) + \left(\frac{\partial \omega_m}{\partial \phi}\right)\frac{\partial \phi}{\partial t}\end{aligned} \tag{4.39}$$

Substituting Eq. 4.37 for $\frac{\partial}{\partial t}\left(\frac{\partial \omega_m}{\partial \mu}\right)$ and Eq. C.25 for $\frac{\partial}{\partial t}\left(\frac{\partial \omega_m}{\partial T}\right)$ in Eq. 4.39, the final form of the energy conservation equation (in Ω_m) can be obtained by equating Eqs. 4.29 and 4.39:

$$\begin{aligned}\left(\frac{\partial^2 \Omega_m}{\partial T^2}\right)\frac{\partial T}{\partial t} + \left(\frac{\partial^2 \Omega_m}{\partial \mu \partial T}\right)\frac{\partial \mu}{\partial t} = \frac{V_m}{T}\nabla\left[-\frac{M_{ee}}{T}\nabla T\right] - \frac{V_m \mu}{T}\nabla\left[-M_{xx}\nabla\left(\frac{\mu}{T}\right)\right] \\ + \frac{1}{T}\left(\frac{\partial \Omega_m}{\partial \phi} - T\frac{\partial^2 \Omega_m}{\partial T \partial \phi}\right)\frac{\partial \phi}{\partial t}\end{aligned} \tag{4.40}$$

Thus, Eqs. 4.38 and 4.40 represent the coupled equations in the evolution of the variables μ and T.

4.3.1.2 Non-conserved order parameter ϕ

As mentioned earlier in Section 2.2.2.1 of Chapter 2, the evolution of the non-conserved order parameter is governed by the Allen-Cahn equation, which is given by Eq. 4.20. From Eq. C.28 of Appendix C this equation can be modified as:

$$\frac{\partial \phi}{\partial t} = M_\phi \left[-\frac{1}{T}\frac{\partial \omega_m}{\partial \phi} - \frac{1}{Ta} f'_{dw}(\phi) + \frac{1}{T}{\kappa_\phi}^2 \nabla^2 \phi \right] \tag{4.41}$$

The partial derivative of ω_m with respect to ϕ can be evaluated from Eq. 4.33, which upon substitution in the above equation gives a final expression for the time evolution of ϕ (in terms of Ω_m):

$$\frac{\partial \phi}{\partial t} = \left(\frac{M_\phi \kappa_\phi^2}{T} \right) \nabla^2 \phi - \left(\frac{M_\phi}{aT} \right) f'_{dw}(\phi) - \left(\frac{M_\phi \left(\Omega_m^s - \Omega_m^l \right)}{V_m T} \right) p'(\phi) \tag{4.42}$$

The derivation of the evolution equations for the dependent variables (Eqs. 4.38, 4.40 and 4.42) together give the phase-field model in the grand potential formulation. As mentioned earlier, in the context of the present thesis, this model has been used to study the kinetics of solidification and phase segregation in liquid system, the numerical results for which will be presented in Section 4.5.

4.3.2 Parameters of the phase-field model

The present section is dedicated to the derivation of the parameters related to the diffuse interface description and those related to the evolution of the dependent variables T, μ and ϕ.

4.3.2.1 The diffuse-interface parameters

The diffuse interface shows interaction of the phases. The gradient terms in the functional take into account these interactions, which in turn depend on variation of the order parameter through the interface thickness. This is the region where ϕ undergoes a relevant change, as it is constant in the bulk phases. This is dependent on the evolution equation for ϕ.

The surface energy per unit area σ_β can be obtained as the difference between the value

of the grand potential functional for the system with interface $\breve{\Omega}_{T_\beta}$ and the homogeneous phases (*i.e.* without contribution of the terms related to interface) $\breve{\Omega}^{hom}_{T_\beta}$ for the system at equilibrium temperature T_β and chemical potential μ:

$$\sigma_\beta = \frac{\breve{\Omega}_{T_\beta} - \breve{\Omega}^{hom}_{T_\beta}}{\text{Interface area}} \tag{4.43}$$

where $\breve{\Omega}^{hom}_{T_\beta}$ is expressed as :

$$\breve{\Omega}^{hom}_{T_\beta} = \int \omega_m(T_\beta, \mu) d^3r \tag{4.44}$$

and $\breve{\Omega}_{T_\beta}$ is given by Eq. 4.32 taken at $T = T_\beta$. For the system at equilibrium, the phase-field order parameter ϕ attains the values 1 and 0 at the boundaries of the system (corresponding to $z = 0$ and $z = L$ respectively). Therefore, without loss of generality it can be considered that $\phi(0) = 0$ and $\phi(L) = 1$. Thus σ_β can be written for a 1-D domain as :

$$\sigma_\beta = \int_0^L \left[\frac{1}{a} f_{dw} + \frac{\kappa_\phi^2}{2} \left(\frac{d\phi(z)}{dz} \right)^2 \right] dz \tag{4.45}$$

For a system under equilibrium, the grand potential densities for the solid and liquid phases follow the condition:

$$\omega^s_m(T_\beta, \mu) = \omega^l_m(T_\beta, \mu) \tag{4.46}$$

$\therefore$ the equilibrium profile for the order parameter ϕ is given by Eq. 4.42 at steady state:

$$\frac{1}{a} f'_{dw}(\phi) = \kappa_\phi^2 \frac{d^2\phi(z)}{dz^2} \tag{4.47}$$

The multiplication of the L.H.S. and R.H.S. of the above equation with $\frac{d\phi}{dz}$ gives:

$$\kappa_\phi^2 \left(\frac{d^2\phi(z)}{dz^2} \right) \left(\frac{d\phi(z)}{dz} \right) = \frac{1}{a} \left(\frac{df_{dw}}{d\phi(z)} \right) \left(\frac{d\phi(z)}{dz} \right) \tag{4.48}$$

This can be integrated with respect to z within the domain $[0, z]$ to obtain:

$$\frac{\kappa_\phi^2}{2} \left(\frac{d\phi(z)}{dz} \right)^2 = \frac{1}{a} \left[f_{dw}(\phi(z)) - \underbrace{f_{dw}(\phi(0))}_{=0} \right] = \frac{1}{a} f_{dw}(\phi(z)) \tag{4.49}$$

where Eq. 4.45 can be substituted for the R.H.S. and the relation for σ_β can be obtained as:

$$\sigma_\beta = \int_0^L \kappa_\phi^2 \left(\frac{d\phi(z)}{dz}\right)^2 dz \tag{4.50}$$

Eq. 4.50 can be written as an integration with respect to ϕ, with a change of variables that is given as :

$$\sigma_\beta = \int_0^L \kappa_\phi^2 \left(\frac{d\phi(z)}{dz}\right)^2 dz = \int_{\phi(0)}^{\phi(L)} \kappa_\phi^2 \left(\frac{d\phi(z)}{dz}\right) d\phi \tag{4.51}$$

For an analytical solution to σ_β, an expression is required for the term $\frac{d\phi(z)}{dz}$ in the above equation. This can be done by re-visiting the Eq. 4.49:

$$\frac{d\phi(z)}{dz} = \frac{\sqrt{2}}{\kappa_\phi}\sqrt{\frac{1}{a} f_{dw}(\phi(z))} \tag{4.52}$$

The above relation can be substituted in Eq. 4.51 to obtain the surface energy as:

$$\begin{aligned}
\sigma_\beta &= \sqrt{\frac{2}{a}}\kappa_\phi \int_{\phi(0)}^{\phi(L)} \sqrt{f_{dw}(\phi(z))} d\phi \\
&= \sqrt{\frac{2}{a}}\kappa_\phi \int_{\phi(0)}^{\phi(L)} \frac{1}{2}\phi(1-\phi) d\phi \\
&= \frac{\kappa_\phi}{\sqrt{2a}} \left[\frac{\phi^2}{2} - \frac{\phi^3}{3}\right]_{\phi(0)}^{\phi(L)}
\end{aligned} \tag{4.53}$$

As $\phi(0) = 0$ and $\phi(L) = 1$, the final expression for the interface energy is obtained as :

$$\sigma_\beta = \frac{\kappa_\phi}{6\sqrt{2a}} \tag{4.54}$$

The interface thickness δ_β is defined as:

$$\delta_\beta = \frac{\phi(L) - \phi(0)}{max\left(\frac{d\phi(z)}{dz}\right)} \tag{4.55}$$

with $\phi(L) - \phi(0) = 1$ and the maximum for $\frac{d\phi(z)}{dz}$ calculated to be $\frac{1}{4\sqrt{2a}\kappa_\phi}$ for $\phi(z) = 0.5$. Substituting the max value for Eq. 4.52 in Eq. 4.55, the interface thickness can be calculated as:

$$\delta_\beta = 4\sqrt{2a}\kappa_\phi \tag{4.56}$$

As a consequence, the values for the parameters κ_ϕ^2 and a can be calculated directly from the interface parameters σ_β and δ_β, by using the relations :

$$\kappa_\phi^2 = \frac{3}{2}\sigma_\beta\delta_\beta \tag{4.57}$$

$$a = \frac{\delta_\beta}{48\sigma_\beta} \tag{4.58}$$

4.3.2.2 The kinetic parameters

The evolution of the variables T and μ is given by the energy and mass conservation equations given by Eqs. 4.40 and 4.38, respectively. The linear phenomenological equations (Eqs. 4.27 and 4.28) can be recalled from Section 4.2.1 for relating the fluxes for energy (J_e) and mass transfer (J_x):

$$J_e = -\frac{M_{ee}}{T^2}\nabla T \tag{4.59}$$

$$J_x = -M_{xx}\nabla\left(\frac{\mu}{T}\right) \tag{4.60}$$

The expressions for the kinetic coefficients M_{ee} and M_{xx} can be derived from Fourier's law of heat conduction and Fick's law of diffusion respectively.

4.3.2.2.1 Kinetic coefficients for energy and mass conservation equations

Fourier's law of heat conduction relates the heat flux J_e to be proportional to the negative gradient in temperature:

$$J_e = -\lambda\nabla T \tag{4.61}$$

where the coefficient of proportionality λ is the thermal conductivity ($Wm^{-1}K^{-1}$) of the material. Equating Eqs. 4.59 and 4.61, the kinetic coefficient M_{ee} is obtained as:

$$M_{ee} = \lambda T^2 \tag{4.62}$$

where λ is dependent on the phase (hence on ϕ), and can be expressed as an interpolation between the homogeneous phase thermal conductivities λ_s and λ_l.

For a single phase, the diffusive mass flux J_x for a reduced system with independent driving

forces (given by $\nabla\mu_i$) is represented as (detailed derivation presented in Appendix D):

$$J_k = \sum_{i=1}^{n}\left[\sum_{j=1}^{n}\left[\delta_{ij}-x_i\right]\left[\delta_{jk}-x_k\right]\frac{x_j D_j}{V_m R}\nabla\frac{\mu_i}{T}\right] \tag{4.63}$$

where R is the universal gas constant ($JK^{-1}mol^{-1}$) and δ_{jk} is the Kronecker delta function which is equal to 1 for $j=k$ and equal to 0 for $j\neq k$. Comparing Eqs. 4.60 and 4.63, the kinetic coefficients of diffusion can be obtained for the bulk phase θ (denoted by M^{θ}_{xx}, $\theta = s$ and l for solid and liquid phase respectively), which for a binary system is reduced to:

$$M^{\theta}_{xx} = \frac{x(1-x)}{V_m R}\left[(1-x)D^{\theta}_1 + xD^{\theta}_2\right] \tag{4.64}$$

with D^{θ}_1 and D^{θ}_2 being the self diffusion coefficients for the two components in phase θ. Within the interface, where the two phases co-exist, this kinetic coefficient can be determined by applying an interpolation function $h_{mixing}(\phi)$ between the two-phases of the form:

$$M_{xx} = \left[h_{mixing}(\phi)M^{s}_{kj} + (1-h_{mixing}(\phi))M^{l}_{kj}\right] \tag{4.65}$$

It should be noted that unlike the interpolation function $p(\phi)$ introduced in Section 4.2.1, the function $h_{mixing}(\phi)$ does not have to follow the same constraints as mentioned in Eq. 4.25. For the sake of convenience, the numerical analysis carried out in Section 4.5 makes use of the same function (as $p(\phi)$) for defining this interpolation function $h_{mixing}(\phi)$.

4.3.2.2.2 Choice of kinetic coefficient M_ϕ

For a system to achieve thermodynamic equilibrium, the condition $\Omega^{s}_{m}(T,\mu,\phi) = \Omega^{l}_{m}(T,\mu,\phi)$ must be satisfied. For the isothermal case, this corresponds to finding the solution of the evolution equations Eqs. 4.38 and 4.42 of the model simplified under the constant temperature assumption (*i.e.* $\dot{T}=0$), which are given as:

$$\left(\frac{\partial^2\Omega_m}{\partial\mu^2}\right)\frac{\partial\mu}{\partial t} = -V_m\nabla(M_{xx}\nabla\frac{\mu}{T}) - \left(\frac{\partial^2\Omega_m}{\partial\mu\partial\phi}\right)\dot{\phi} \tag{4.66}$$

$$\frac{\partial\phi}{\partial t} = \underbrace{\left(\frac{M_\phi\kappa^2_\phi}{T}\right)\nabla^2\phi}_{I} - \underbrace{\left(\frac{M_\phi}{aT}\right)f'_{dw}(\phi)}_{II} - \underbrace{\left(\frac{M_\phi\left(\Omega^{s}_{m}-\Omega^{l}_{m}\right)}{V_m T}\right)p'(\phi)}_{III} \tag{4.67}$$

In the absence of a phase field parameter, the kinetics of the system depends only on the characteristic time τ associated to diffusion (discussed below), which is governed by the chemical potential gradient imposed by the initial state of the system. However, upon introducing the phase field parameter, the driving force for the phase transformation is governed by the coupled effect of the two phenomena. In this case, the evolution of the system towards equilibrium is associated to the relaxation of the phase field as well as the chemical potential gradient. Thus, the kinetics of the system depends on the choice of the phase field mobility M_ϕ as well as the initial composition of the system.

In order to ensure that the model depicts the kinetics of the thermochemical process correctly (with the phase field order parameter ϕ being used as a 'marker' for the interface position), it is important to choose an appropriate value for the mobility coefficient M_ϕ. This can be achieved by following the procedure of non-dimensionalizing the evolution equations Eqs. 4.66 and 4.67 for the dependent variables. The dimensionless quantities are introduced as:

$$t^* = \frac{t}{\tau} \tag{4.68}$$

$$z^* = \frac{z}{L} \tag{4.69}$$

$$\mu^* = \frac{\mu}{\mu_0} \tag{4.70}$$

$$\Omega_m^* = \frac{\Omega_m}{\Omega_0} \tag{4.71}$$

$$\Delta\Omega_m^* = \frac{\Omega_m^s - \Omega_m^l}{\Delta\Omega_0} \tag{4.72}$$

$$M_{xx}^* = \frac{M_{xx}}{M_0} \tag{4.73}$$

where:

- τ is the characteristic time associated the evolution of the variable μ, which represents the time taken for the diffusion process to occur in the system of a given length scale L, and;
- μ_0 , Ω_0, $\Delta\Omega_0$ and M_0 are the characteristic values associated to the order of magnitudes of μ , Ω_m, $\Omega_m^s - \Omega_m^l$ and M_{xx} respectively.

The characteristic time for the evolution of ϕ, depends on the magnitudes of the contributing terms. As a result, a characteristic time associated to each of these terms can be defined. The terms I and II of Eq. 4.67 correspond to the capillary force, which are related to the intrinsic properties of the interface defined by the parameters of interface energy σ_β and interface thickness δ_β (see Eqs. 4.54 and 4.56). Whereas, term III couples the evolution of ϕ to the chemical potential μ. The magnitude of this term is not known *a priori*, but depends on the thermodynamic driving force $(\Omega_m^s - \Omega_m^l)/V_m$ for the interface, which is an external parameter related to the choice of initial state of the system.

It can be recalled from Section 4.3.2 that at equilibrium, terms I and II balance one another to give the equilibrium profile for ϕ. Since these two terms dependent on one another, the characteristic times associated to them are proportional to one another (the proof for the same is presented in Appendix F). Hence they should not be considered separately. Instead, two characteristic time scales are defined for the evolution of ϕ, where:

- the first time scale is associated to the interface properties (*i.e.* the terms I and II), and is expressed as:
$$\frac{1}{\tau_\phi} = \frac{M_\phi}{aT} \tag{4.74}$$
- the second time scale is associated to the thermodynamic driving force that is set externally (term III):
$$\frac{1}{\tau_3} = \frac{M_\phi \Delta\Omega_0}{V_m T} \tag{4.75}$$

If the interface motion is considered to be slow so as to ensure that the hypothesis of local equilibrium at the interface is followed (*i.e.* the intensive properties like temperature (T) and the chemical potential (μ) are equal for the co-existing phases), it is imperative for the heat and species transfer **across the interface** to occur rapidly compared to the 'relaxation' of the interface. This implies that the characteristic times for the evolution of ϕ (τ_ϕ and τ_3) must be greater than the diffusion time associated with species transfer across the interface (denoted by t_{diff}), which is defined as:

$$t_{diff} = \frac{\delta_\beta^2}{D_x} \tag{4.76}$$

where D_x is the species diffusion coefficient, that is related to the kinetic coefficient M_{xx} by Eq. D.40 of Appendix D. At the same time, for the entire process to be **'diffusion**

controlled'[4], τ_ϕ and τ_3 must be smaller than τ, which is expressed from Eq. F.10 of Appendix F as:

$$\tau = \frac{L^2}{D_x} \tag{4.77}$$

From the above mentioned conditions, it is clear that the two characteristic time scales associated to Eq. 4.67 must follow the conditions:

$$\frac{\delta_\beta^2}{D_x} \ll \tau_\phi \ll \frac{L^2}{D_x} \tag{4.78}$$

$$\frac{\delta_\beta^2}{D_x} \ll \tau_3 \ll \frac{L^2}{D_x} \tag{4.79}$$

Thus, by substituting Eqs. 4.74 and 4.75 in the above relations for τ_ϕ and τ_3 respectively, a maximum and minimum bound for the choice of M_ϕ value can be obtained.

As mentioned in the beginning of this section, the characteristic time scales τ, τ_ϕ and τ_3 can be obtained through the non-dimensionalization of Eqs. 4.66 and 4.67. To do so, two approaches were followed (which are discussed in Appendix F), which yielded two sets of bounding values for M_ϕ by using the Eqs. F.18 and F.19 and Eqs. F.47 and F.48 of Appendix F respectively. Both of these approaches bounds have been used to discuss the numerical results presented in Section 4.5.

Further, the combination of Eqs. 4.78 and 4.79 yields a maximum value condition on the choice of interface thickness δ_β :

$$\left(\frac{\delta_\beta}{L}\right)^2 \left(\frac{a\Delta\Omega_0}{V_m}\right) \ll 1 \tag{4.80}$$

$$\delta_\beta \ll \left(\frac{48L^2\sigma_\beta V_m}{\Delta\Omega_0}\right)^{1/3} \tag{4.81}$$

However, it must be recalled that above mentioned constraints on the choice of M_ϕ (and also δ_β) are valid only for the cases where the interface motion is assumed to be slow, which is the case for most physical situations (and has also been considered for the present study). For a case corresponding to fast motion of the interface (such as the case of rapid

[4]This condition for the process to be diffusion controlled is chosen as the main interest of using the model is to study the overall evolution of the system that takes place at a much larger scale compared to the kinetics of the interface.

solidification, discussed in [101]), there may exist additional conditions which have an influence on the choice of phase-field mobility. The discussion related to these conditions has not been included in the present thesis work.

4.3.3 Conditions for application of the grand potential approach

The idea of formulating a phase-field model in grand potential functional requires the elimination of the extensive variables of enthalpy h and composition x in favor of the intensive variables T and μ, both of which depend on space and time. This elimination is simple if the extensive variables are related to their corresponding intensive variables by simple invertible functions. Moreover, if the functions for the Gibbs free energies are convex in x and h, a monotonous relation between these variables (*i.e.* the extensive and intensive variables) exists, which makes it possible to switch to T and μ as the dynamic variables. Consequently, the enthalpy (respectively the composition) of the system can be obtained as a partial derivative of the grand potential functional with respect to the temperature (respectively the chemical potential).

4.4 Numerical scheme for time integration

The numerical solution to the model can be obtained by making use of the Euler explicit or the semi-implicit time integration schemes. This requires numerical discretization of the evolution equations in space and time. The spatial discretization in 1-D for the evolution equations was achieved by using the finite differences method in a manner similar to Appendix B of [44], where a thicker mesh size was adopted for the discretization of the bulk regions and a relatively thinner mesh was used for the interface such that at least 10 spatial nodes lie within the interface of thickness δ_β. The temporal discretization of the evolution equations was achieved by making use of a theta-scheme, which has been referred to in Appendix G.

In principle, any of the two time integration schemes can be utilized to solve the evolution

equations for the system. However for the case of the explicit time scheme, the choice of spatial mesh size (*i.e* Δz value) poses a condition related to the 'maximum' allowable time-step Δt for which the numerical scheme is stable. In particular, for the present phase-field model this criterion for the stability depends on behaviour of the non-linear source terms present in the evolution equations (detailed in Section G.2 of Appendix G). As a consequence, depending on the maximum Δt value obtained, the choice between the use of explicit or the semi-implicit time scheme has been made for solving the transients discussed in the following Section 4.5 on the numerical results.

4.5 Numerical results and analysis

For the developed phase-field model simplified under the constant temperature assumption, the validity of the coupled evolution equations in chemical potential and the phase-field order parameter (given by Eqs. 4.66 and 4.67) was tested for studying the processes of solidification and phase segregation in the binary U-Zr and U-O systems respectively. The purpose of these numerical simulations was limited to addressing the constraints associated with the coupling of the the model with CALPHAD, and to answer the questions related to the up-scaling of the interface and its effect on the choice of the phase-field mobility M_ϕ.

The initial condition of the system is set by defining initial spatial profiles for the non-conserved order parameter ϕ (which takes constant values of 0 and 1 in the regions corresponding to the bulk phases and varies smoothly between these values within the interface defined by a thickness δ_β (m)) and the mole fraction of the component U (denoted by x_U), which is expressed as interpolation of the compositions in bulk phases (denoted by $x_U^{\theta^{\phi=0}}$ $\forall$ $\phi \in \{0,1\}$) in ϕ:

$$x_U = p(\phi) x_U^{\theta^{\phi=1}} + (1 - p(\phi)) x_U^{\theta^{\phi=0}} \tag{4.82}$$

The conversion of this initial x_U profile to a profile in chemical potential μ, requires solving the non-linear equation within the interface region, where a solution for phase compositions $x_U^{\theta^\phi}$ must be found, such that the condition of local equilibrium in the interface

$\mu_{\phi=1}(x_U^{\theta^{\phi=1}}) = \mu_{\phi=0}(x_U^{\theta^{\phi=0}})$ is satisfied. Contrary to the entropy approach, this non-linear system is to be solved only at the time of initializing the system.

The transient calculations were performed until the steady state condition for the system was obtained, which corresponds to the thermodynamic equilibrium condition for the system defined by the equilibrium chemical potential value μ_{eq} (the numerical steady state condition is defined by a criterion relative to the chemical potential variation between two consecutive time-steps that should be lower than $10^{-1}\ Jmol^{-1}$).

4.5.1 Testing the model for solidification of U-Zr system under isothermal conditions

4.5.1.1 Thermodynamic description of the U-Zr system

The binary U-Zr system is composed of pure elements U and Zr, which also are the constituent species for the system. Consequently, the component and constituent compositions are related to each other as:

$$x_U = y_U \tag{4.83}$$

$$x_{Zr} = y_{Zr} \tag{4.84}$$

The conservation of mass gives the relation between the component composition (respectively the constituent composition from Eqs. 4.83 and 4.84) as:

$$x_U + x_{Zr} = 1 \tag{4.85}$$

In terms of coupling the grand potential model with the CALPHAD description given for the phases from the NUCLEA database, the equivalence of the compositions makes it easy for directly obtaining the required thermodynamic quantities (details in Appendix E) without the need for applying additional hypotheses.

For this system, the equilibrium calculations performed by OC at temperature $T = 1500$ K showed the presence of a single solid phase (denoted by `BCC_A2A` in NUCLEA database), and for $T = 1800$ K, the presence of both solid (`BCC_A2A`) and liquid phases (denoted by `LIQUID` in NUCLEA database) was noted. The variation in the Gibbs free energy as a

function of the molar composition of the element U (x_U) was studied for the phases of interest (*i.e.* the `BCC_A2A` and `LIQUID` phases) at a constant temperatures of 1500 and 1800 K. From the Figures 4.1 and 4.2, it can be observed that the Gibbs energy curves for the two temperatures are convex in x_U.

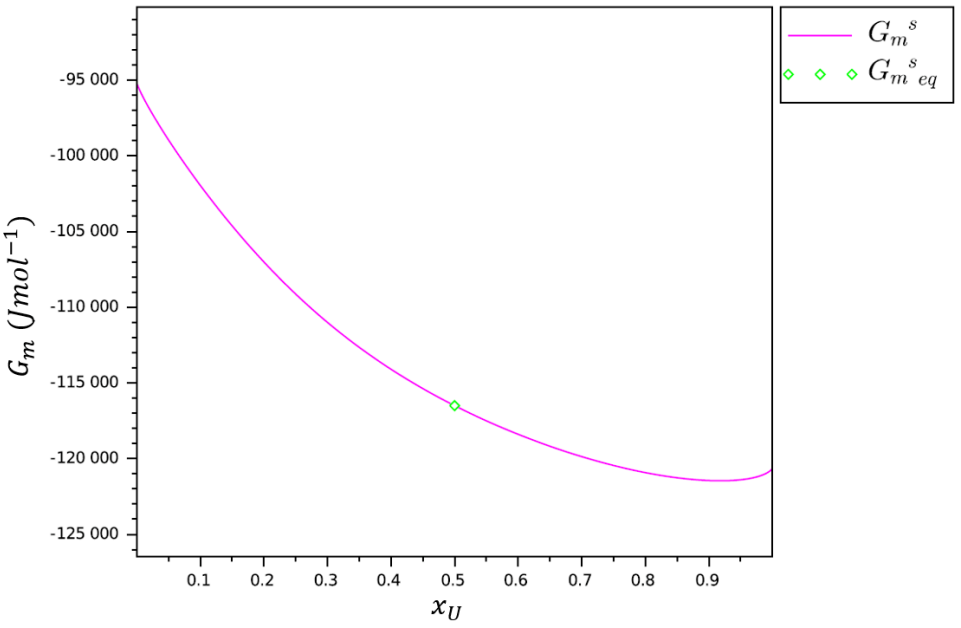

FIGURE 4.1: Variation of the molar Gibbs free energy G_m with the mole fraction of U x_U and the equilibrium molar Gibbs energy $G_{m\ eq}$ for the `BCC_A2A` phase of binary U-Zr system at $T = 1500$ K.

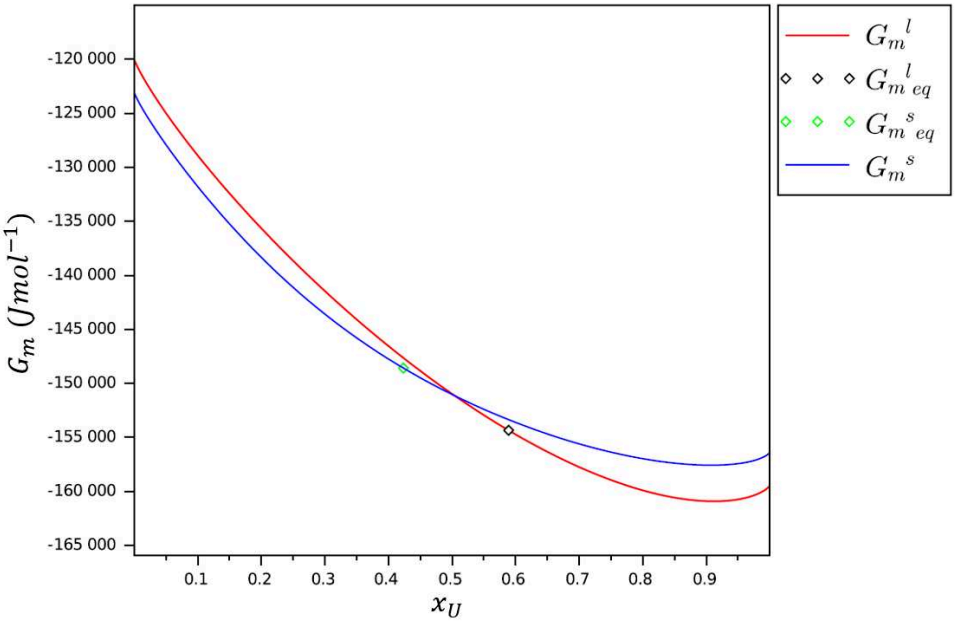

FIGURE 4.2: Variation of the molar Gibbs free energy G_m with the mole fraction of U x_U and the equilibrium molar Gibbs energy $G_{m\ eq}$ for the `LIQUID` and `BCC_A2A` phases of binary U-Zr system at $T = 1800$ K.

Upon plotting the chemical potential values as a function of composition (for the two temperatures), the Figures 4.3 and 4.4 show that a monotonous relation between μ and x_U exists for the U-Zr system (with the exception of the cases when the composition tends towards a unary system *i.e.* $x_U \to 0$ or $x_U \to 1$). Hence, it is possible to invert the Gibbs energy functions to be dependent on μ for the composition range (excluding the unary system cases).

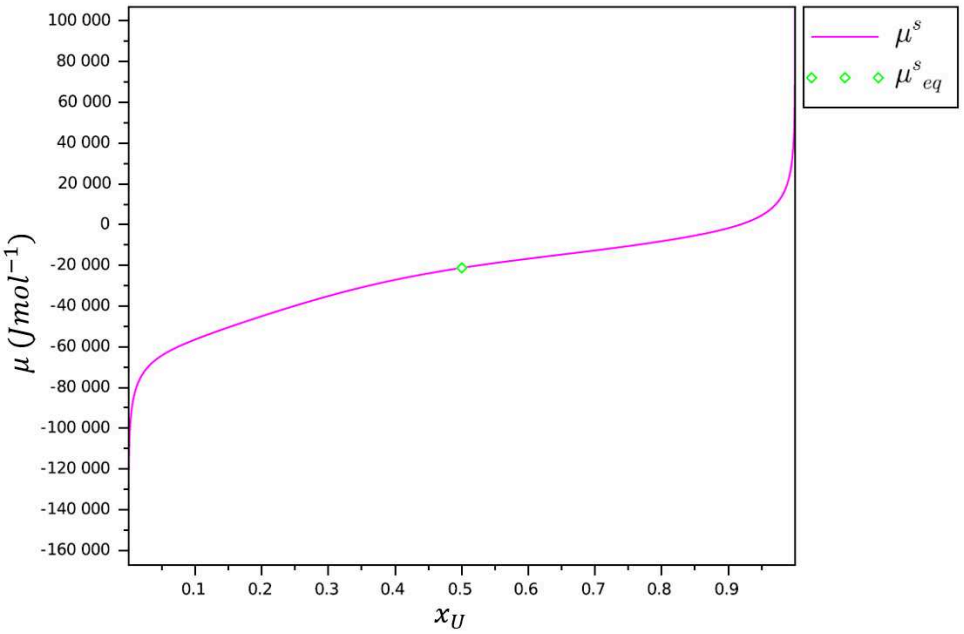

FIGURE 4.3: Variation of the chemical potential μ with the mole fraction of element U and the equilibrium chemical potential μ_{eq} for the `BCC_A2A` phase in a binary U-Zr system at $T = 1500$ K.

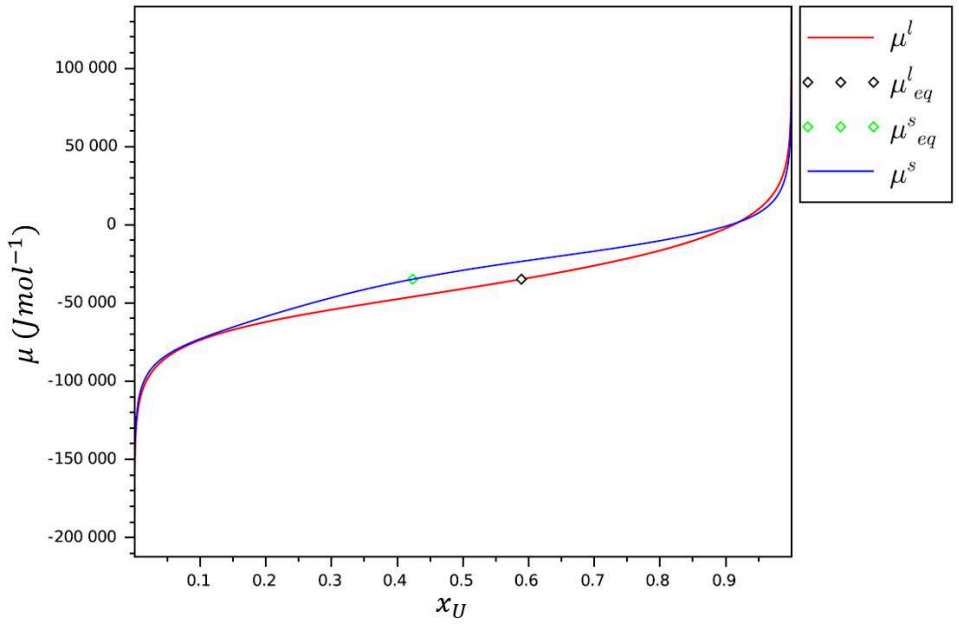

FIGURE 4.4: Variation of the chemical potential μ with the mole fraction of element U and the equilibrium chemical potential μ_{eq} for the `LIQUID` and `BCC_A2A` phases in a binary U-Zr system at $T = 1800$ K.

4.5.1.2 Initialization of the system and inputs to the model

The initial condition proposed for the solidification model is related to the initial spatial profiles constructed in terms of μ and ϕ. The developed model was tested for three cases:

- Case 1: a (`BCC_A2A`) phase for the temperature $T = 1500$ K, with an initial homogeneous composition $x_U = 0.5$;
- Case 2: a (`BCC_A2A`) phase at $T = 1500$ K with a non-homogeneous initial composition, and;
- Case 3: a two phase system composed of (`BCC_A2A`) and `LIQUID` phases at 1800 K, with the average initial composition $x_U = 0.5$.

The inputs for the model parameters have been described for this system under consideration in Table 4.1.

Input parameters	U-Zr system	
	Single-phase	Two-phase
Length scale for the system L (m)	0.5	
Interface thickness δ_β (m)	5.0×10^{-4}	
Temperature T (K)	1500	1800
Molar volume V_m $(m^3 mol^{-1})$	1.79×10^{-5}	
a $(J^{-1}m^3)$	1.04×10^{-4}	
Gradient coefficient κ_ϕ^2 (Jm^{-1})	7.50×10^{-5}	
Kinetic coefficient M_{xx} $(mol^2 K J^{-1} m^{-1} s^{-1})$	8.38×10^{-5}	
Interface energy σ_β (Jm^{-2})	0.1	
Average initial composition x_U	0.5	

TABLE 4.1: Initial inputs to the phase-field model for testing solidification in binary U-Zr system under isothermal conditions

For the present analysis, since the main focus is on answering the questions associated with thermodynamic consistency, the input for kinetic coefficient for diffusion M_{xx} (see

Table 4.1) is assumed to be equal for both phases (*i.e.* $M_{kj}^{s} = M_{kj}^{l}$), even though this is not physically possible in the case of solidification.

4.5.1.3 Initial verification of the model on a single phase system

The initial verification of the model was performed for the cases associated with single phase-system, corresponding to (first) a homogeneous and (second) a non-homogeneous initial composition. Upon recalling the system of coupled evolution equations in μ (Eq. 4.66) and ϕ (Eq. 4.67), for a pure solid phase, the initial spatial profile for the phase-field order parameter corresponds to:

$$\phi(z) = 1 \ \forall \ z \in [0, L] \tag{4.86}$$

For a constant value of ϕ, the term corresponding to $\dot{\phi}$ is 0. As a result, contribution of this term to Eq. 4.66 is 0 and Eq. 4.66 reduces to a diffusion equation of the form:

$$\left(\frac{\partial^2 \Omega_m}{\partial \mu^2}\right) \dot{\mu} = -\frac{V_m}{T} \nabla (M_{xx} \nabla \mu) \tag{4.87}$$

In terms of the presence of a single phase, this diffusion is equivalent to re-distribution of mass within the phase to obtain a homogeneous composition at steady state. The solution to the above equation can be obtained by applying the Euler explicit scheme (see Section G.1 of Appendix G for details on the discretization of the evolution equations), with a time-step value $\Delta t = 100$s. This value of Δt corresponds to the maximum value that can be obtained from the CFL condition on $\dot{\mu}$ equation for the explicit scheme (see Section G.2 of Appendix G for details).

As a first step, the model was tested for a first case of the homogeneous initial composition of the solid. As there exist no gradients in the chemical potential (*i.e.* $\nabla \mu = 0$) for this system, the initial and steady state compositions are expected to be the same. This was verified by the model (depicted by Figure 4.5).

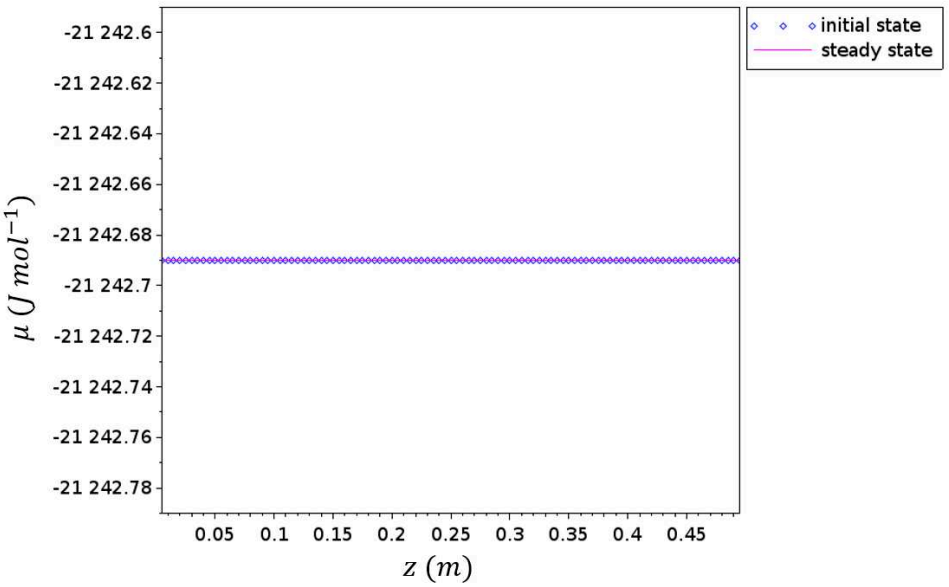

FIGURE 4.5: Initial and steady state profiles for chemical potential μ in space z, for transient calculations performed for the `BCC_A2A` phase in U-Zr binary system with a homogeneous initial composition $x_U(t = 0) = 0.5$.

The model was then tested for a non-homogeneous initial composition of the solid. For this initial state of the system, there exists a gradient in the chemical potential (as shown in Figure 4.6) which corresponds to the non-homogeneous distribution of composition in space. The transient simulations verified the expected behaviour which corresponds to the reduction of chemical potential gradient with time. Also, the steady state composition for the system was found to be consistent with the expected homogeneous system composition $\bar{x}_U^{ss} = 0.5$ that is associated with the mass conservation (see Figure 4.7).

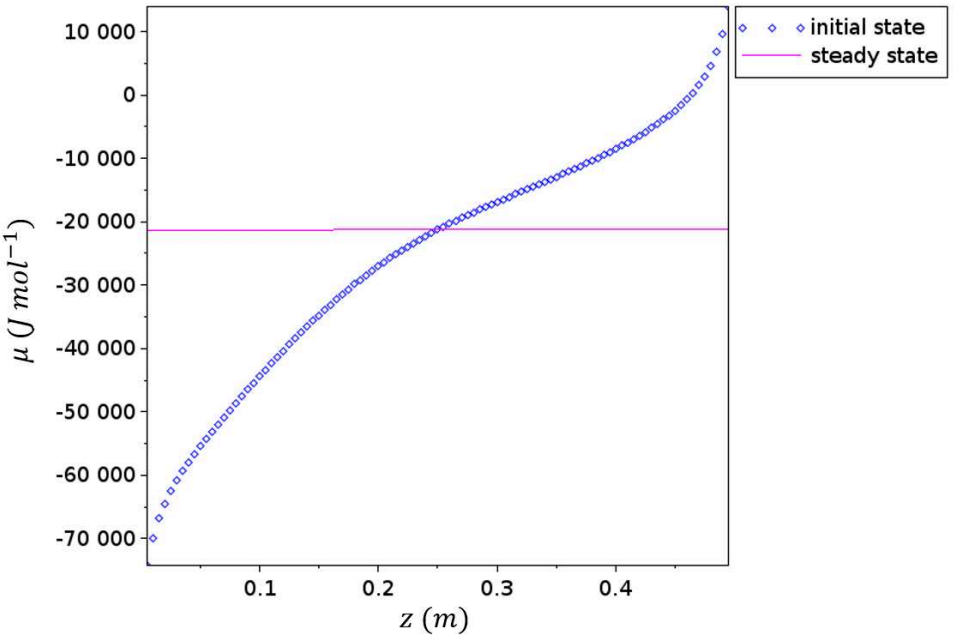

FIGURE 4.6: Initial and steady state profiles for chemical potential μ in space z, for transient calculations performed for the `BCC_A2A` phase in U-Zr binary system with a non-homogeneous initial composition.

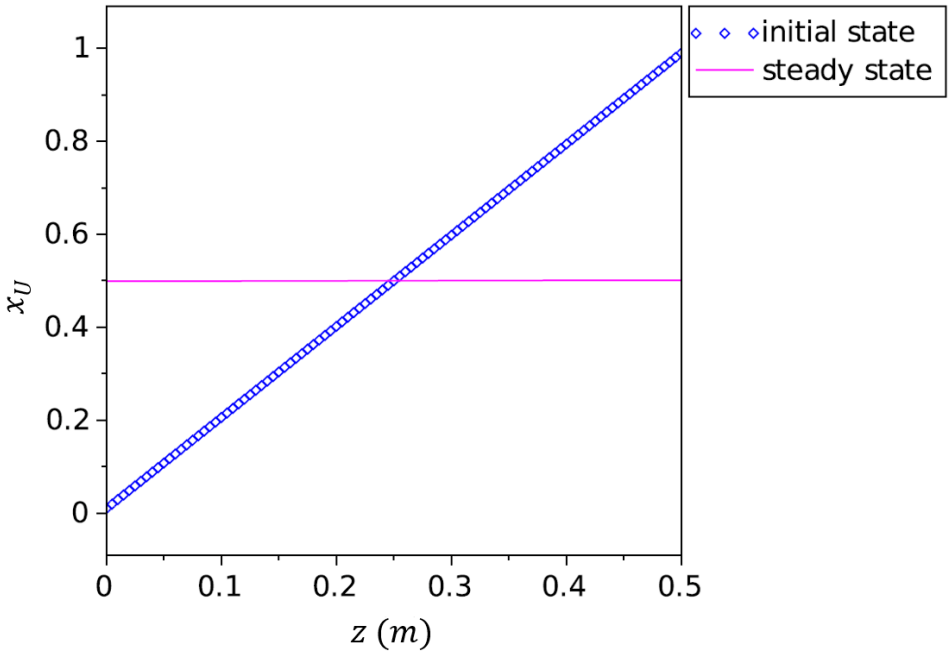

FIGURE 4.7: Initial and steady state profiles for composition x_U in space z, for transient calculations performed for the `BCC_A2A` phase in U-Zr binary system with a non-homogeneous initial composition.

Moreover, the ϕ profile does not undergo any change during the transient (see Figure 4.8), which is expected since the initial and final conditions for the single phase system remain the same (*i.e.* $\phi(z) = 1 \; \forall z \in [0, L]$ at the steady state).

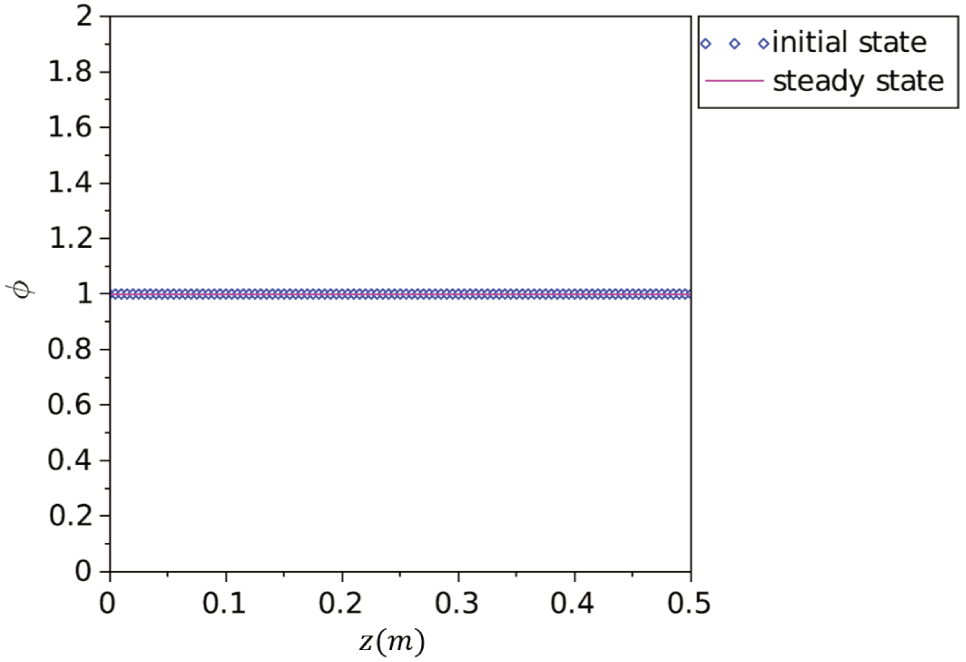

FIGURE 4.8: Initial and steady state profiles for phase field ϕ in space z, for transient calculations performed for the `BCC_A2A` phase in U-Zr binary system.

4.5.1.4 Results for a two phase system

Following the initial set of verifications on the single phase system, the model was tested on a two phase system. Apart from the verification of the solidification transient, the tests on the two phase system was also performed for determining an appropriate value for kinetic parameter M_ϕ, for which the model best depicts the expected transient conditions.

Due to the initial homogeneous composition of the system, the coupling of grand potential values of the two phases with the interpolation function $p(\phi)$ results in an initial condition for the intensive variable μ with the existence of a sharp gradient between the values for the initial solid and liquid phase, across the interface (see Figure 4.9).

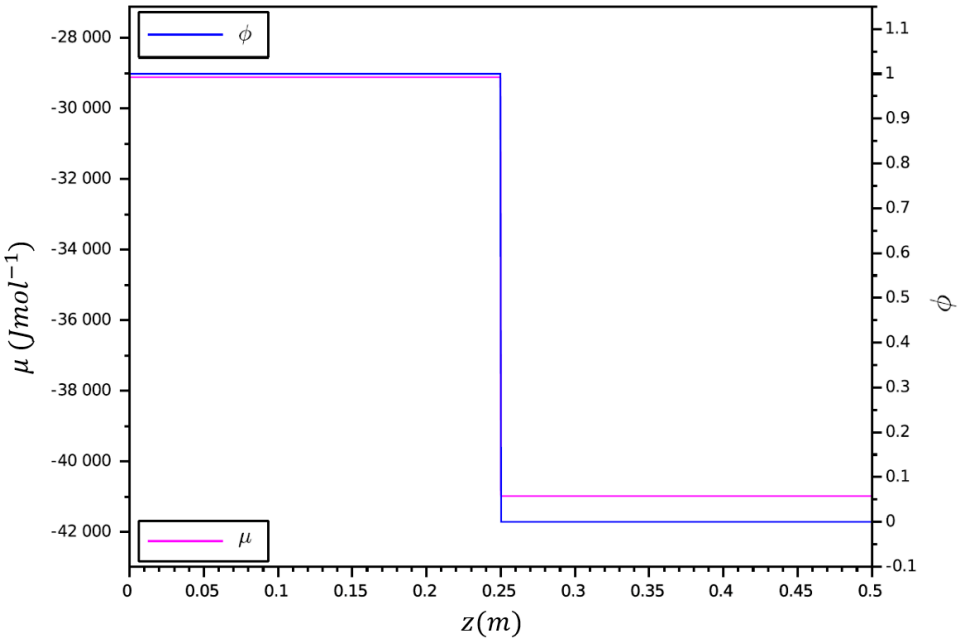

FIGURE 4.9: Initialization of the two phase U-Zr system with a homogeneous composition : profiles for chemical potential μ and phase-field order parameter ϕ in space z.

The initial profile for ϕ is represented by a continuous function that takes up constant values of 1 and 0 in bulk solid and liquid phase respectively and varies smoothly between these values across the interface (see Figure 4.9) with the initial position of the interface $z_\beta^0 = 2.5 \times 10^{-1}$ m. For this choice of initial system, the model behaviour was studied and the results related to the choice of the phase-field mobility M_ϕ value and the scale separation for the interface have been discussed in the following Sections 4.5.1.4.1 and 4.5.1.4.2. These tests determine the appropriate model kinetic parameter value for which the transient achieves a steady state configuration corresponding to a spatial profile with $\mu = \mu_{eq}$ (obtained as $-34833.4\ Jmol^{-1}$ from the equilibrium calculation performed by OC) and the steady state position of the interface (denoted by z_β^{ss}, also determined with the help of an equilibrium calculation, by making use of the lever rule). This position denotes the fraction of the solid and liquid phase present in the system at equilibrium. For the present system configuration, $z_\beta^{ss} = 2.688 \times 10^{-1}$ m. Further, the validity of M_ϕ parameter was tested for a system with different initial conditions (in Section 4.5.1.4.3).

4.5.1.4.1 Comparison among the choices for phase-field mobility M_ϕ

In the present section, the initial tests are carried out for a set of M_ϕ values that were taken from the range presented by the minimum and maximum bounds based on the conditions posed by Eqs. F.18 and F.19 (obtained from the non-dimensionalization of the evolution equations, discussed in Appendix F). As a second part, the obtained results will be analysed with respect to the alternate bounds on M_ϕ, that were obtained from Eqs. F.47 and F.48 (based on the alternate approach to non-dimensionalization presented in Appendix F).

From the conditions posed by Eqs. F.18 and F.19, an upper and lower bound value for M_ϕ common to the two inequalities was obtained:

$$6.26 \times 10^{-8}\ J^{-1}K^{1}s^{-1}m^{3} \ll M_\phi \ll 1.08 \times 10^{-5}\ J^{-1}K^{1}s^{-1}m^{3} \tag{4.88}$$

The choice of M_ϕ must be made within the range presented by these bounds, such that the above condition is followed. Three different values of M_ϕ were chosen ($M_\phi = 1.0 \times 10^{-5}$, 1.0×10^{-6} and $1.0 \times 10^{-7}\ J^{-1}K^{1}s^{-1}m^{3}$) and the effect of each choice on the behaviour of the model was studied. For each of these simulations, the transient calculations were performed until the final time for the transient was equal to twice the characteristic time for diffusion ($t_f = 2\tau$). At the end of the complete simulation, the final values for the chemical potential were compared to μ_{eq} (comparison between the values was made up to the order of 10^{-1}).

Case: $M_\phi = 1.0 \times 10^{-5}\ J^{-1}K^{1}s^{-1}m^{3}$

For $M_\phi = 1.0 \times 10^{-5}\ J^{-1}K^{1}s^{-1}m^{3}$ (close to the upper bound for M_ϕ), the evolution of the solidification transient is tested by using the semi-implicit scheme for time discretization, with a time step $\Delta t = 10^{-3}\ s$.

The results obtained from the transient calculations show that the choice of M_ϕ value as 10^{-5} causes the phase field to react very rapidly, compared to the effect of the chemical potential gradient. Consequently, the process is entirely governed by the adjustment of the phase field order parameter and the model reacts to the local driving force first. For the given initial condition, the driving force is composed of two opposite phenomena acting on the either side of the interface. This results in "creation" of a new interface (depicted by

the steady state spatial profiles for composition and order parameter ϕ in Figures 4.10 and 4.11 respectively) because the condition that the interface exists in local equilibrium, is violated.

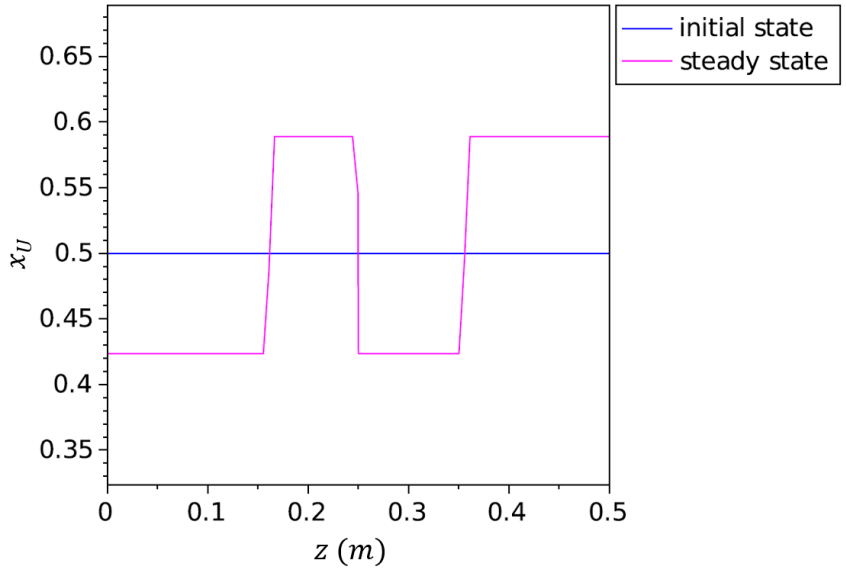

FIGURE 4.10: Initial and steady state profiles for composition x_U in space z for transient calculations performed with $M_\phi = 1.0 \times 10^{-5}\ J^{-1}K^1s^{-1}m^3$, for a fixed scale separation and initial condition on a two phase U-Zr system.

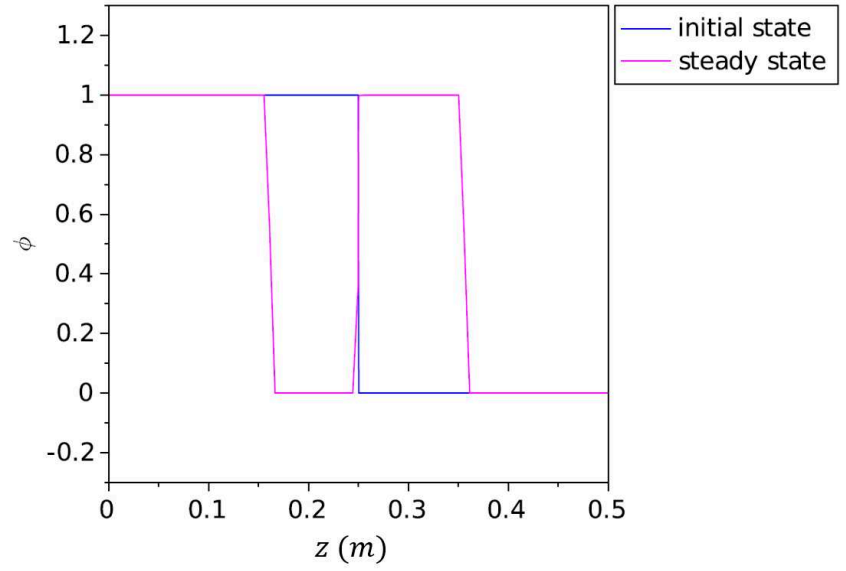

FIGURE 4.11: Initial and steady state profiles for phase-field order parameter ϕ in space z for transient calculations performed with $M_\phi = 1.0 \times 10^{-5}\ J^{-1}K^1s^{-1}m^3$, for a fixed scale separation and initial condition on a two-phase U-Zr system.

Case: $M_\phi = 1.0 \times 10^{-6}\ J^{-1}K^1s^{-1}m^3$

For $M_\phi = 1.0 \times 10^{-6}\ J^{-1}K^1s^{-1}m^3$ (close to the logarithmic mean of the range for M_ϕ presented by Eq. 4.88), the evolution of the solidification transient is tested by using the semi-implicit scheme for time discretization, with a time step $\Delta t = 1\ s$.

The results obtained from the transient calculations depict that the model behaviour is in accordance with the kinetics of the solidification process (*i.e.* the time taken for the ϕ, μ and x_U profiles to reach their steady state configuration corresponds to the macroscopic characteristic time associated to diffusion τ), with the final position of the interface (z_β^f) being equal to (z_β^{ss}) (see Figures 4.13 and 4.12).

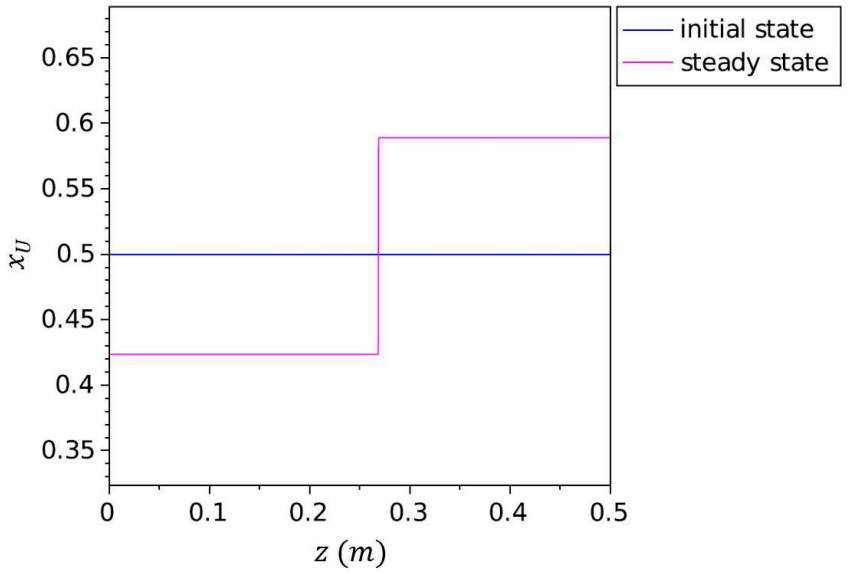

FIGURE 4.12: Initial and steady state profiles for composition x_U in space z for transient calculations performed with $M_\phi = 1.0 \times 10^{-6}\ J^{-1}K^1s^{-1}m^3$, for a fixed scale separation and initial condition on a two phase U-Zr system.

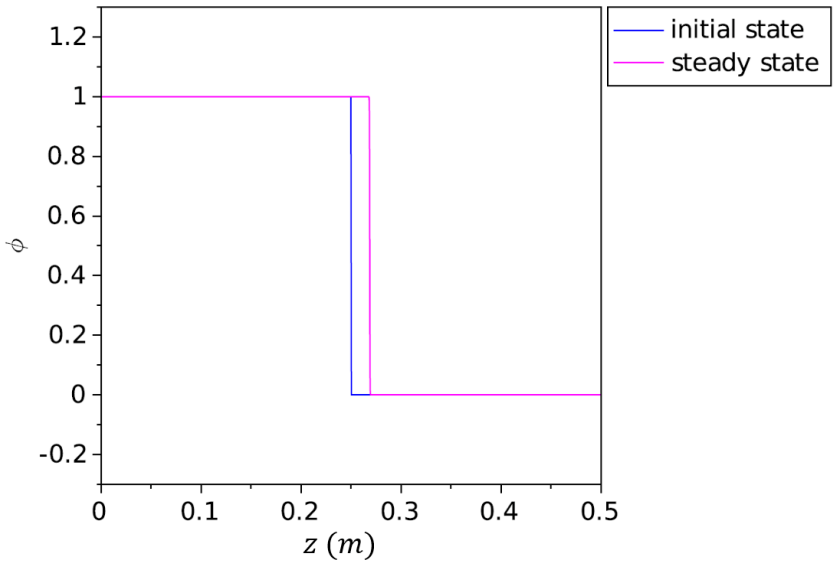

FIGURE 4.13: Initial and steady state profiles for phase-field order parameter ϕ in space z for transient calculations performed with $M_\phi = 1.0 \times 10^{-6}\ J^{-1}K^1s^{-1}m^3$, for a fixed scale separation and initial condition on a two phase U-Zr system.

Another way to verify the transient behaviour of the model, is to compute the interface energy for steady state by making use of the integral represented by Eq. 4.50 and verify that it is equal to the initially set value (given in Table 4.1). For the present case, the error in the interface energy calculated from Eq. 4.50 $\left(\sigma_\beta^f = 0.099\right)$ with respect to the initially imposed interface energy (σ_β) is 1.0%.

Case: $M_\phi = 1.0 \times 10^{-7}\ J^{-1}K^1s^{-1}m^3$

For $M_\phi = 1.0 \times 10^{-7}\ J^{-1}K^1s^{-1}m^3$ (close to the lower bound for M_ϕ), the evolution of the solidification transient is tested by using the semi-implicit scheme for time discretization, with a time step $\Delta t = 10\ s$. The initial and steady state spatial profiles for the variables x_U, ϕ and μ are depicted by Figures 4.14, 4.15 and 4.16.

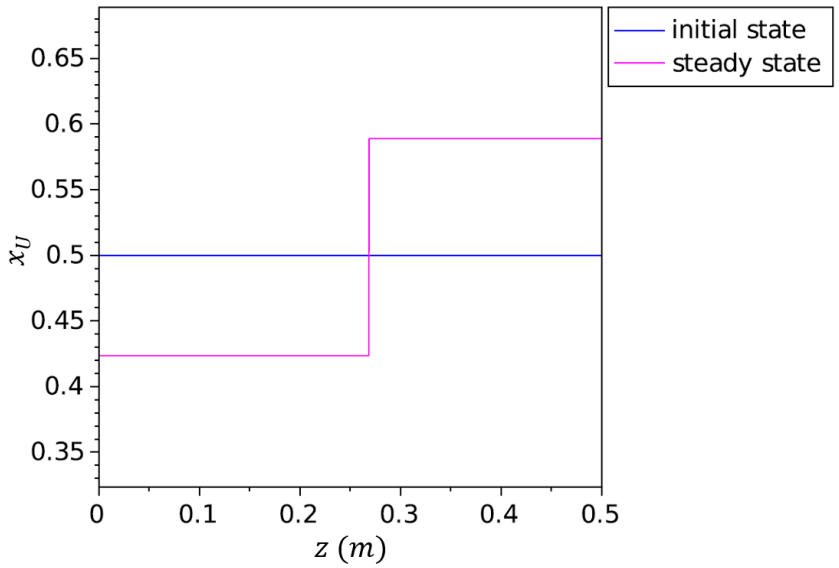

FIGURE 4.14: Initial and steady state profiles for composition x_U in space z for transient calculations performed with $M_\phi = 1.0 \times 10^{-7}\ J^{-1}K^1s^{-1}m^3$, for a fixed scale separation and initial condition on a two phase U-Zr system.

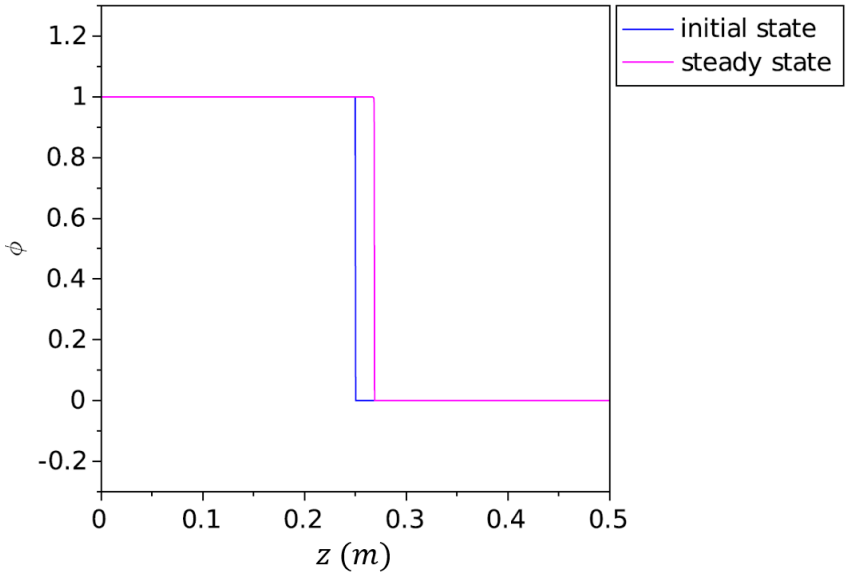

FIGURE 4.15: Initial and steady state profiles for phase-field order parameter ϕ in space z for transient calculations performed with $M_\phi = 1.0 \times 10^{-7}\ J^{-1}K^1s^{-1}m^3$, for a fixed scale separation and initial condition on a two phase U-Zr system.

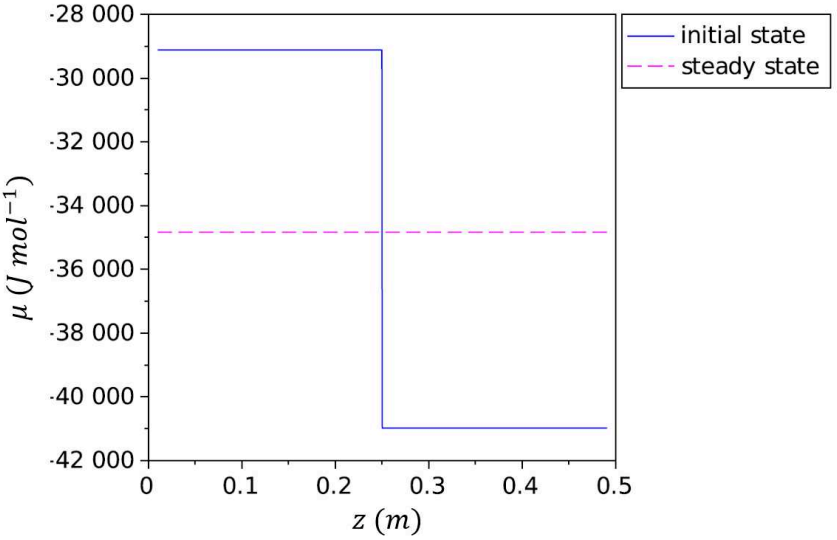

FIGURE 4.16: Initial and steady state profiles for chemical potential μ in space z for transient calculations performed with $M_\phi = 1.0 \times 10^{-7}\ J^{-1}K^1s^{-1}m^3$, for a fixed scale separation and initial condition on a two phase U-Zr system.

The evolution of variables x_U, ϕ and μ was observed to be according to the expected movement of the interface. The final position of the interface z_β^f was also found to be $\approx z_\beta^{ss}$. However, the transient time (t_f) corresponding to this steady state position and composition is greater than the characteristic time related to diffusion. This suggests that the process is not controlled by the species diffusion.

The transient calculations performed with phase field mobility values of as 10^{-6} and 10^{-7} exhibit similar transients with different time values corresponding to their steady states. For a lower value of the phase field mobility (*i.e.* $M_\phi = 1.0 \times 10^{-7}\ J^{-1}K^1s^{-1}m^3$), the condition for the process to be diffusion controlled is violated as the macroscopic characteristic time corresponding to the steady state is not conserved. This is evident in Figures 4.17 and 4.18, where the system is unable to reach the steady state values for composition and chemical potential at the time corresponding to τ.

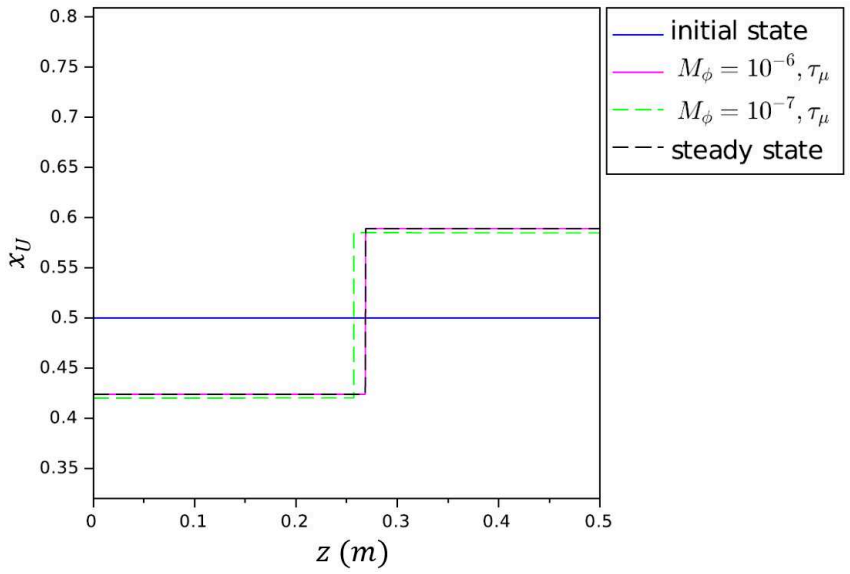

FIGURE 4.17: Comparison of composition x_U profiles for different phase field mobility values

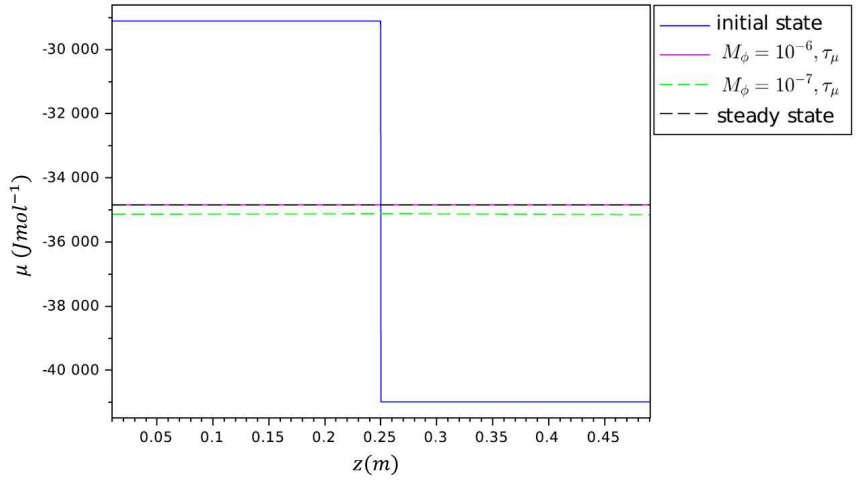

FIGURE 4.18: Comparison of chemical potential μ profiles for different phase field mobility values

On tracking the interface position (*i.e.* the spatial co-ordinate z corresponding to the value $\phi(z) = 0.5$) during the transient, it was observed that only for case when $M_\phi = 1.0 \times 10^{-6}\ J^{-1}K^1s^{-1}m^3$, the time taken by the interface to achieve the expected steady state position is consistent with the characteristic macroscopic time for diffusion, whereas,

for the case of $M_\phi = 1.0 \times 10^{-7}\ J^{-1}K^1s^{-1}m^3$ the interface takes a longer time to reach the steady state position (see Figure 4.19).

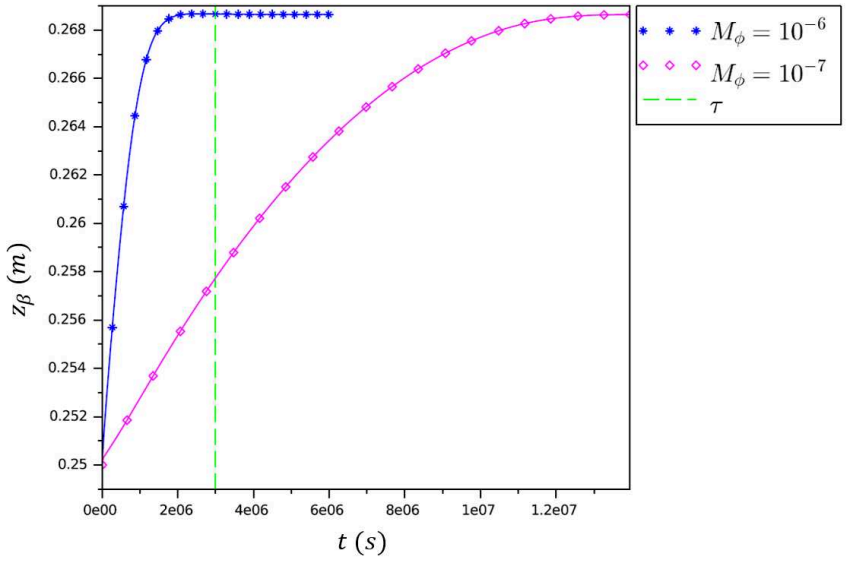

FIGURE 4.19: Tracking interface position z_β: comparison of profiles for different phase field mobility values

This can be related to the approach followed for non-dimensionalization of the evolution equations (detailed in Appendix F). The range for M_ϕ value given by Eqs. F.18 and F.19 is rather large and does not offer a clear indication of the appropriate choice. Consequently, an alternate approach was followed, through which new maximum and minimum bounds for M_ϕ values were evaluated from the conditions given by Eqs. F.47 and F.48. These conditions provide a narrower range for M_ϕ compared to Eq. 4.88:

$$3.49 \times 10^{-7}\ J^{-1}K^1s^{-1}m^3 \ll M_\phi \ll 3.94 \times 10^{-6}\ J^{-1}K^1s^{-1}m^3 \tag{4.89}$$

The logarithmic mean evaluated from these maximum and minimum bounds corresponds to the value $1.17 \times 10^{-6}\ J^{-1}K^1s^{-1}m^3$, which is close to the choice of $M_\phi = 1.0 \times 10^{-6}\ J^{-1}K^1s^{-1}m^3$.

4.5.1.4.2 Comparison between the choice of scale separation

As a next step, the model behaviour was studied for a reduced interface thickness δ_β, while keeping the M_ϕ value fixed to $1.0 \times 10^{-6}\ J^{-1}K^1s^{-1}m^3$ (as obtained from the previous section). To do so, a different ratio for scale separation (δ_β/L) was chosen and the transient calculations were performed by using the semi-implicit scheme for time discretization, with a time step of $\Delta t = 1\ s$. As a consequence of changing the interface thickness, the parameters a, κ_β^2 are modified (mentioned in Table 4.2).

Model Parameters	Input values
Scale separation δ_β/L	10^{-4}
Interface thickness $\delta_\beta\ (m)$	5.0×10^{-5}
$a = \delta_\beta/48\sigma_\beta\ (J^{-1}m^3)$	1.04×10^{-5}
Gradient coefficient $\kappa_\phi^2 = 1.5\sigma_\beta\delta_\beta\ (Jm^{-1})$	7.50×10^{-6}

TABLE 4.2: Model parameters calculated for a scale separation $\delta_\beta/L = 10^{-4}$.

The evolution of the variables x_U, ϕ and μ was observed to be according to the expected behaviour, with the composition of the phases and the chemical potential profiles depicting the expected steady state values (depicted in Figures 4.20 and 4.22 respectively). The motion of the ϕ profile was also observed to be in accordance with the expected behaviour, with the final interface position z_β^f equal to z_β^{ss}. Also, the time taken for the transient to reach steady state configuration (in x_U, μ and ϕ) is also in accordance with the characteristic time associated with the diffusion (τ).

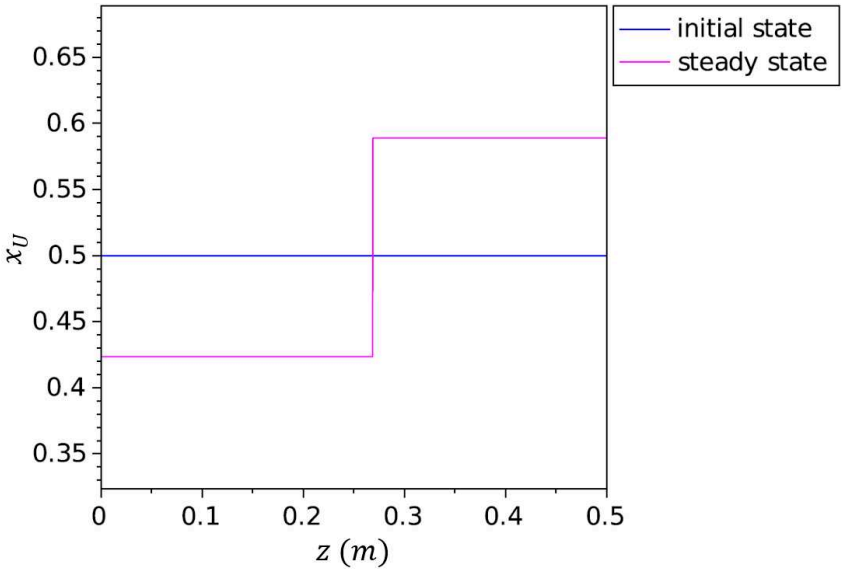

FIGURE 4.20: Initial and steady state profiles for composition x_U in space z for transient calculations performed with $M_\phi = 1.0 \times 10^{-6}\ J^{-1}K^1s^{-1}m^3$, for a reduced scale separation ratio $\delta_\beta/L = 10^{-4}$ on a two phase U-Zr system.

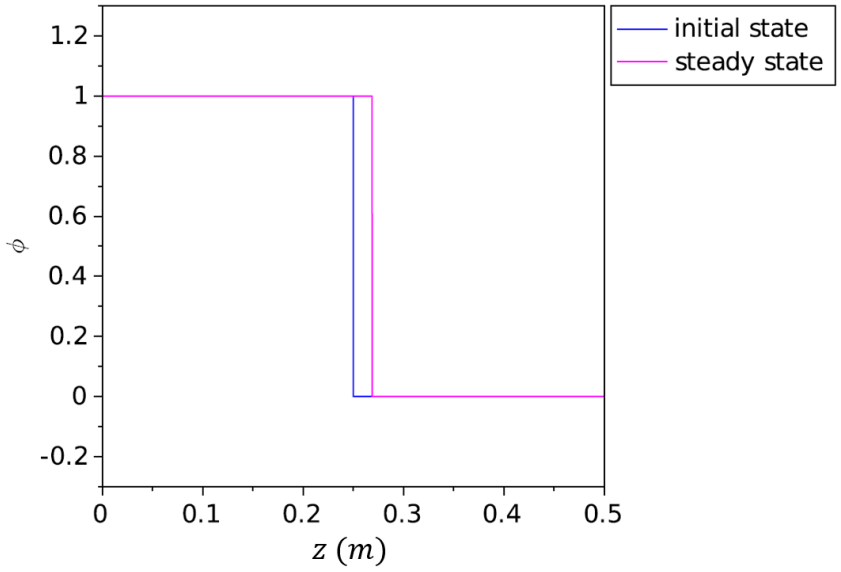

FIGURE 4.21: Initial and steady state profiles for phase-field order paramter ϕ in space z for transient calculations performed with $M_\phi = 1.0 \times 10^{-6}\ J^{-1}K^1s^{-1}m^3$, for a reduced scale separation ratio $\delta_\beta/L = 10^{-4}$ on a two phase U-Zr system.

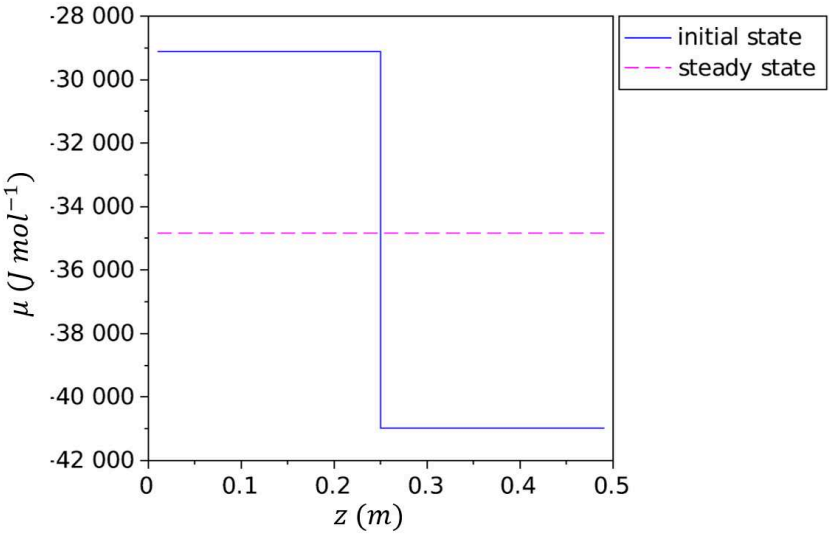

FIGURE 4.22: Initial and steady state profiles for chemical potential μ in space z for transient calculations performed with $M_\phi = 1.0 \times 10^{-6}\ J^{-1}K^1s^{-1}m^3$, for a reduced scale separation ratio $\delta_\beta/L = 10^{-4}$ on a two phase U-Zr system.

The error in the final interface energy (from Eq. 4.50) with respect to the initially imposed interface energy (*i.e.* σ_β^f and σ_β respectively) is about 1.0%. The final calculated interface thickness (δ_β^f) was found to be in agreement with the initially imposed interface thickness (δ_β^i).

In order to compare the behaviour of the model for the different choices for scale separation, three spatial co-ordinates were chosen, out of which two co-ordinates represented the bulk phase regions ($z_1 = 0.109$ m for solid and $z_3 = 0.408$ m for liquid phase) far away from the interface. The third co-ordinate ($z_2 = 0.249$) m is chosen such that it is very close to the interface for the case $\delta/L = 10^{-4}$ and inside the interface for $\delta/L = 10^{-3}$ (depicted by Figure 4.24).

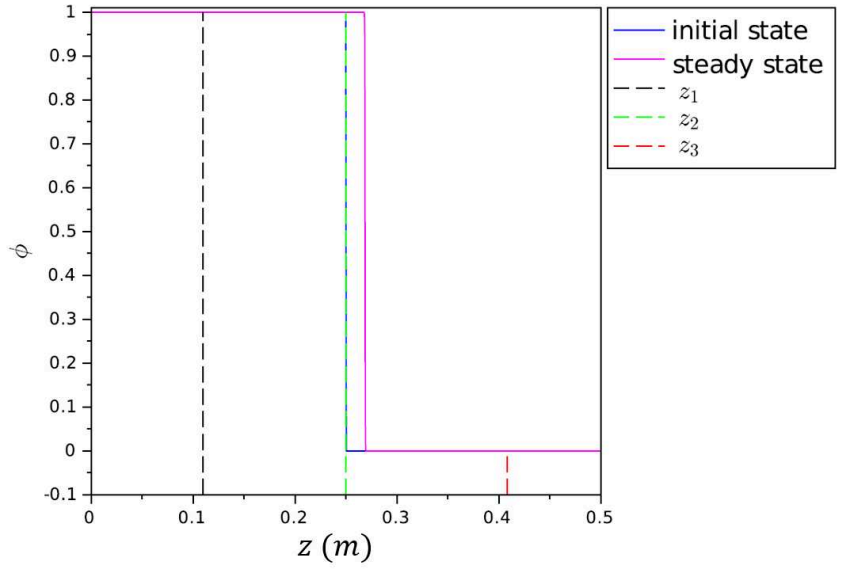

FIGURE 4.23: Positions z_1, z_2 and z_3

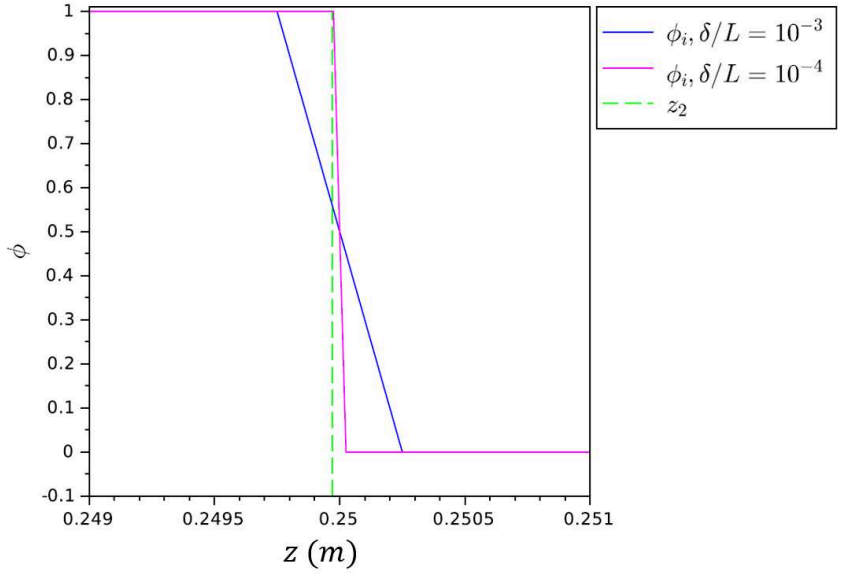

FIGURE 4.24: Position z_2 relative to the two cases of scale separation ratio : $\delta/L = 10^{-3}$ and $\delta/L = 10^{-4}$.

For these positions, the evolution of the mole fraction x_U was plotted with respect to time (see Figures 4.25, 4.27 and 4.26). For the two points z_1 and z_3 lying far away from

the interface (*i.e.* Figures 4.25 and 4.26) , the evolution of the transients for x_U are in accordance with the steady state conditions for these regions.

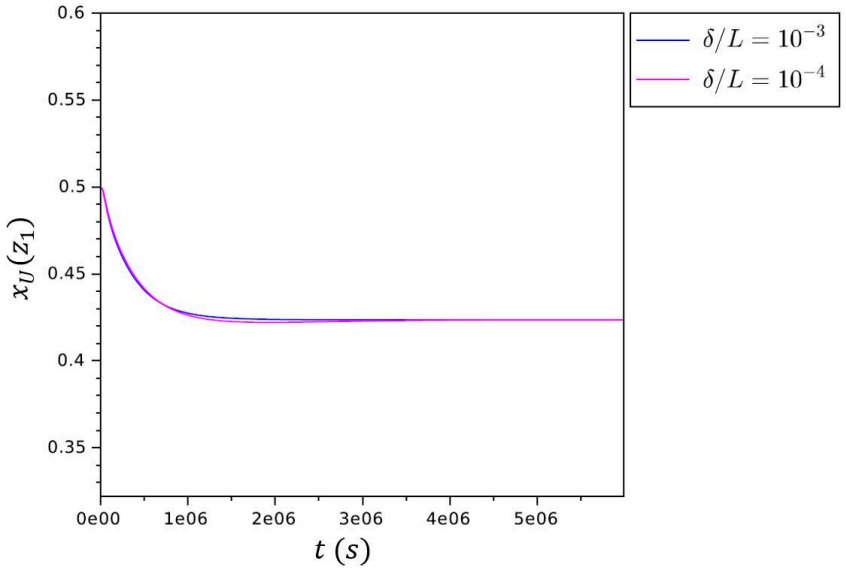

FIGURE 4.25: Variation of composition x_U with time t at position z_1

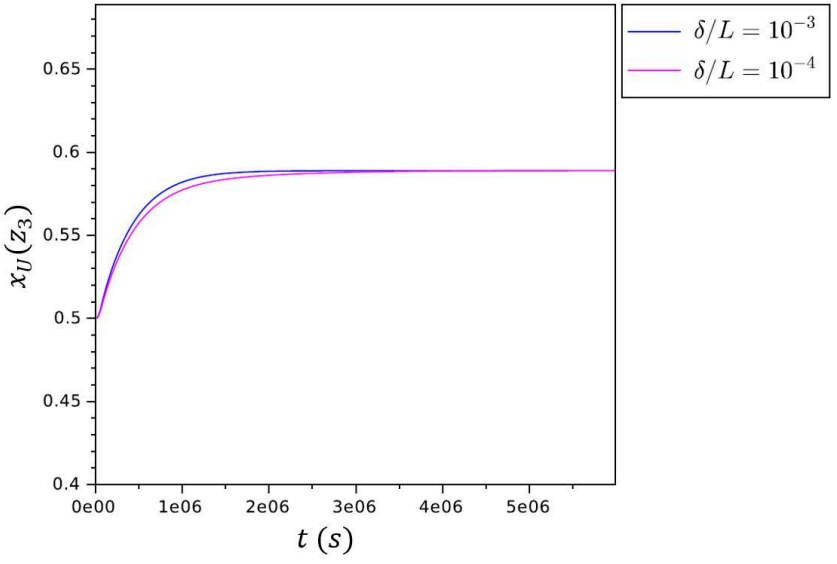

FIGURE 4.26: Variation of composition x_U with time t at position z_3

As stated earlier, for the case $\delta/L = 10^{-4}$, z_2 corresponds to a position just outside the diffuse interface (in the bulk solid region). On the contrary, for the case $\delta/L = 10^{-3}$, z_2 corresponds to a position within the diffuse interface. The steady state ϕ profile for both cases denotes z_2 to have the equilibrium concentration of the solid phase (see Figure 4.27), which is in accordance with the expected behaviour. The sharp drop in composition x_U during the initial time values can be explained from the fact that the description provided for the spatial point z_2 (in terms of its relative position with respect to the diffuse interface) corresponds to the initial position of the interface. As the interface position is adjusted during the transient, after a few thousands of seconds, this spatial point z_2 corresponds to the bulk solid region. Thus, the composition value at this point corresponds to the bulk solid phase composition.

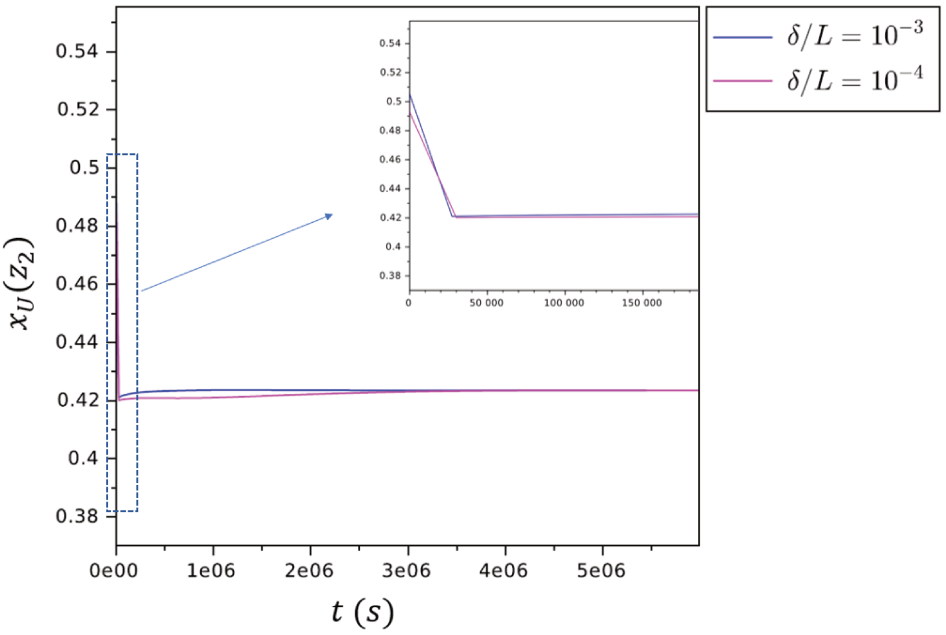

FIGURE 4.27: Variation of composition x_U with time t at position z_2

However, it should be noted (from Figure 4.28) that for a constant value M_ϕ, the rate at which the composition evolves for the two scale separations is not the same. This can be explained from the fact that the evolution equation for ϕ (Eq. 4.42) depicts that the rate of change of phase is proportional to the driving force $\frac{\delta\check{\Omega}}{\delta\phi}$ which, for the present case, is set

by the gradient of chemical potential across the interface. The proportionality constant for this relation is given by the phase field mobility M_ϕ, which itself is not a fixed parameter, but is dependent on the macroscopic diffusion characteristic time as well as on the diffusion time for species across the interface (discussed in Section 4.3.2.2.2). As a consequence, alteration in the interface thickness will cause a change in the magnitude of the driving force. A decrease in the interface thickness causes the driving force to increase. If the rate of phase change is assumed to be a constant, the increase in the magnitude of the driving force must be accompanied by an increase in the magnitude of the phase field mobility. For the case depicted by Figure 4.28, the choice for $M_\phi = 1.0 \times 10^{-6}\ J^{-1}K^1s^{-1}m^3$ results in a 'slower' motion of the interface for a finer choice of interface thickness (corresponding to the scale separation $\delta/L = 10^{-4}$).

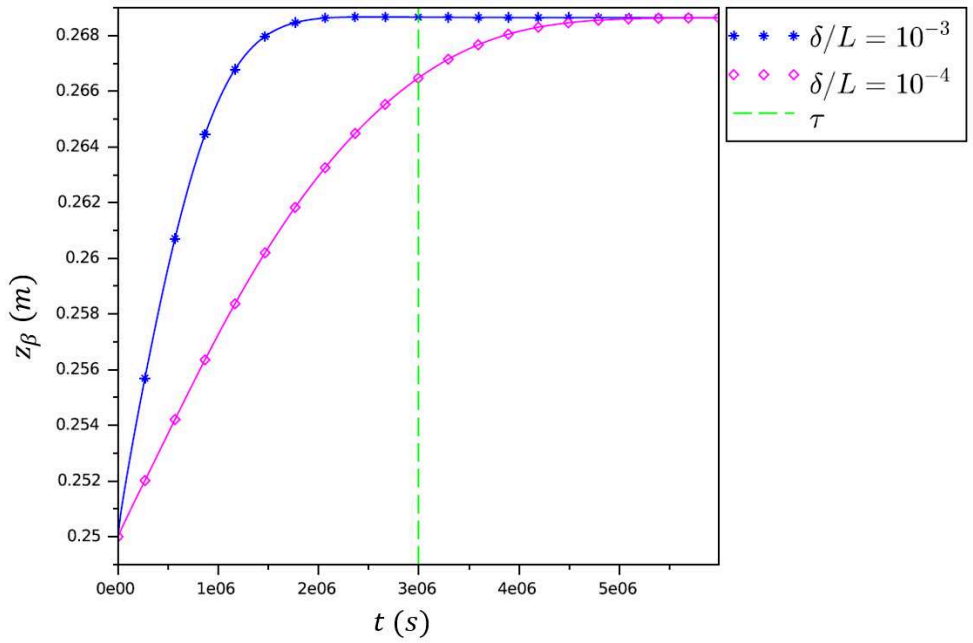

FIGURE 4.28: Tracking interface position z_β: comparison of profiles obtained from transient simulations performed for a fixed value of $M_\phi = 1.0 \times 10^{-6}\ J^{-1}K^1s^{-1}m^3$ and two different scale separation ratios δ/L.

Consequently, if the rate of phase change is to be kept the same as it was depicted for case corresponding to $\delta_\beta/L = 10^{-3}$ and $M_\phi = 1.0 \times 10^{-6}\ J^{-1}K^1s^{-1}m^3$, a 'higher' value

for M_ϕ must be chosen. This can be justified, as the allowed range for M_ϕ obtained by Eqs. F.47 and F.48 is:

$$3.49 \times 10^{-8}\ J^{-1}K^1s^{-1}m^3 \ \ll M_\phi \ll\ 3.94 \times 10^{-4}\ J^{-1}K^1s^{-1}m^3 \tag{4.90}$$

which implies that for a choice of M_ϕ that is comparable to the logarithmic mean $M_\phi = 3.7 \times 10^{-6}\ J^{-1}K^1s^{-1}m^3$ (obtained from the bounds of the above condition), the transient behaviour should be comparable to the transient discussed for $M_\phi = 1.0{\times}10^{-6}\ J^{-1}K^1s^{-1}m^3$ in Section 4.5.1.4.1. This is confirmed by Figure 4.29 where, for the simulations performed with $M_\phi = 4.0 \times 10^{-6}\ J^{-1}K^1s^{-1}m^3$, $\delta_\beta/L = 10^{-4}$, the characteristic time associated with the system to reach steady state is close to the calculation performed for the case of a thicker interface (*i.e.* $\delta_\beta/L = 10^{-3}$).

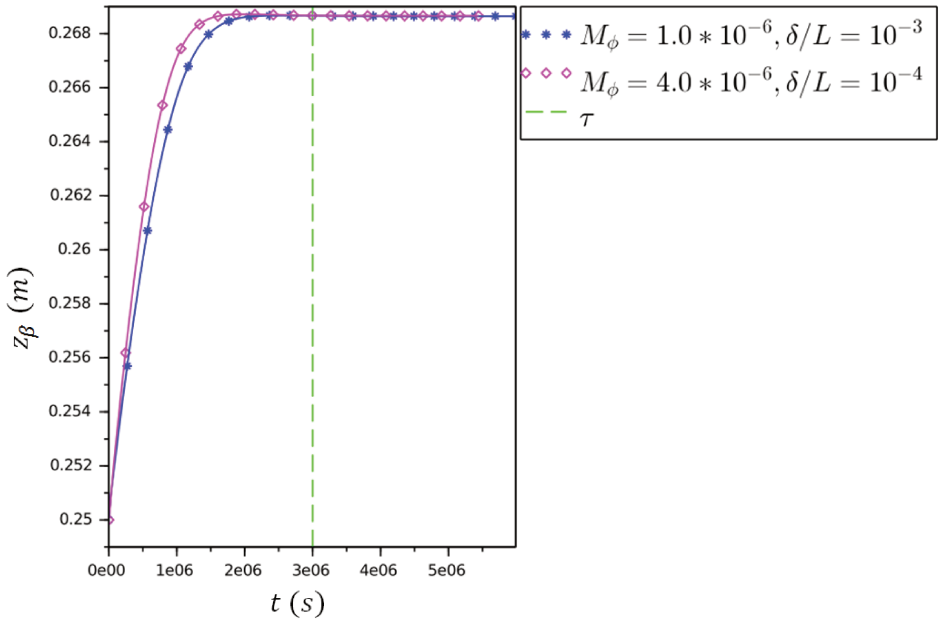

FIGURE 4.29: Tracking interface position z_β with respect to time t: comparison between the transient evolution of system for different initial parameters related to the scale separation ratios δ/L and the phase-field mobility M_ϕ.

4.5.1.4.3 Comparison between different choices for the initial condition of the system

Recalling Section 4.3.2.2.2, it can be seen that for Eq. 4.80 to be valid, the ratio between the thermodynamic driving force and the capillary force (given by $a\Delta\Omega_0/V_m$) must be very small. However, the results demonstrated in Sections 4.5.1.4.1 and 4.5.1.4.2 are related to simulations performed on a system for which the initial state corresponded to a sharp gradient in μ across the interface, as depicted by Figure 4.9). Due to such an extreme initial condition posed by μ, the thermodynamic driving force (given by $(\Delta\Omega_0)/V_m$) acting on the system is high within the interface. Consequently, for a fixed capillary force (defined by $1/a$) the condition of $(a\Delta\Omega_0/V_m) \ll 1$ is violated at the initial time-step, which could have an effect on the model behaviour. To ensure that the condition $(a\Delta\Omega_0/V_m) \ll 1$ holds true even for the initial state, an alternate approach for system initialization was followed, where the chemical potential in the diffuse interface region was set to the equilibrium chemical potential value, whereas the chemical potential values for the bulk regions corresponded to the homogeneous composition with $x_U = 0.5$ (corresponding initial spatial profiles for μ and x_U are depicted by Figures 4.30 and 4.31 respectively).

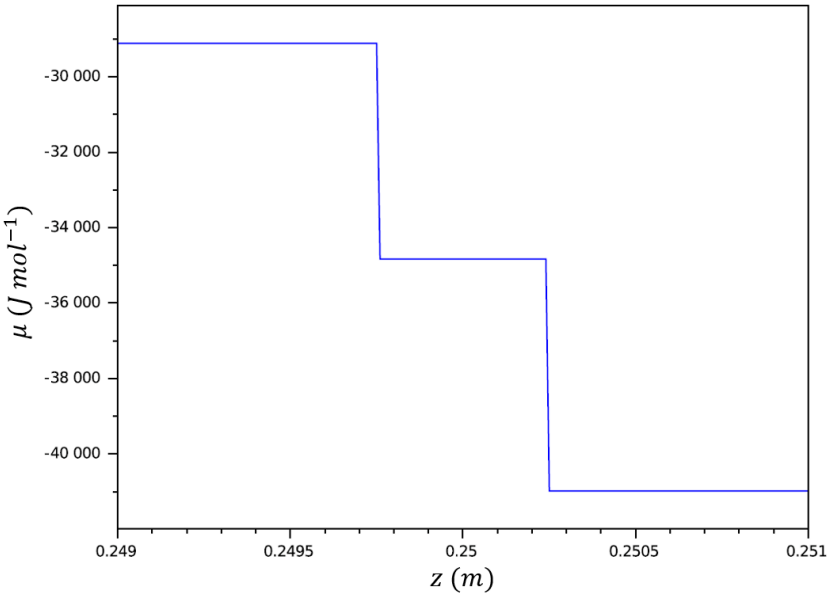

FIGURE 4.30: Initial μ profile vs z corresponding to the two-phase binary U-Zr system initialized with $\mu = \mu_{eq}$ within the interface.

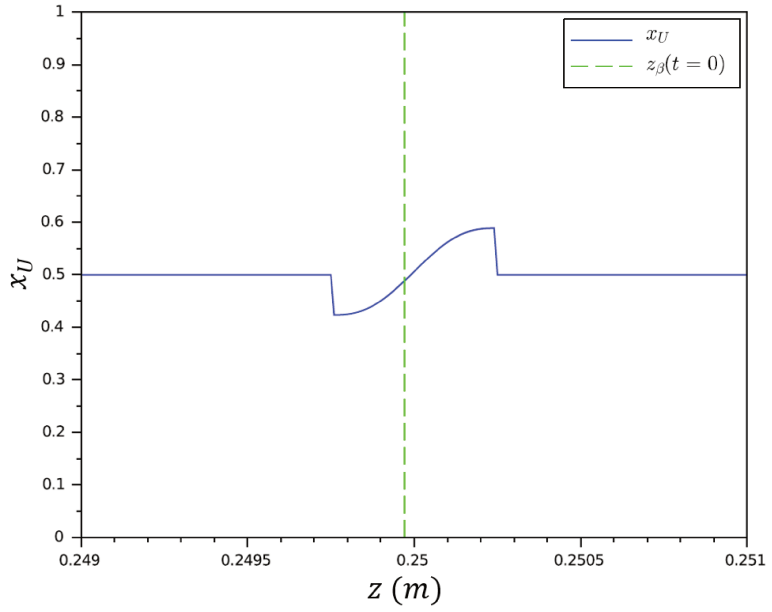

FIGURE 4.31: Initial x_U profile vs z corresponding to the two-phase binary U-Zr system initialized with $\mu = \mu_{eq}$ within the interface.

For this initial state, it was observed that the condition on the ratio of thermodynamic driving force to the capillary force is followed ($a\Delta\Omega_m/V_m \approx 0.1$). With this adopted configuration, the upper and lower bounds for the choice of M_ϕ were evaluated from Eqs. F.47 and F.48 (corresponding to the alternate approach of non-dimensionalization), which was found to be equal to the range presented by Eq. 4.89. As a consequence, the logarithmic mean value is the same ($1.17 \times 10^{-6}\ J^{-1}K^1s^{-1}m^3$), and the choice of $M_\phi = 1.0 \times 10^{-6}\ J^{-1}K^1s^{-1}m^3$ can be retained. The transient was solved for a semi-implicit scheme in time discretization, with a time-step value of $\Delta t = 1\ s$ and it was observed that the evolution of the system was exactly comparable to that of the homogeneous initial condition (depicted by Figure 4.32, which compares the evolution of the interface position with time for the two cases represented by **modified x** and **homogeneous x** respectively) and the time taken by the system to reach steady-state was consistent with the macroscopic characteristic time for diffusion (τ).

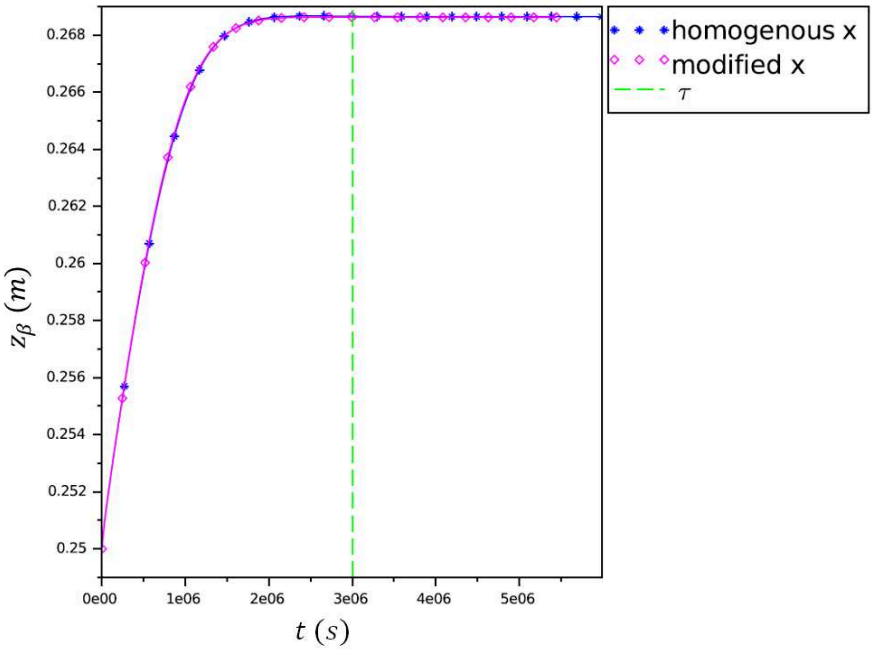

FIGURE 4.32: Tracking interface position z_β: comparison of profiles for different initial conditions imposed on the system and fixed values for parameter M_ϕ and the scale separation ratio δ_β/L.

Above all, the results based on the discussions in Sections 4.5.1.4.1, 4.5.1.4.2 and 4.5.1.4.3, all confirm the robustness of the conditions that are posed by Eqs. F.47 and F.48 (corresponding to the alternate non-dimensionalization approach in Appendix F) on the choice of the phase-field mobility value M_ϕ. This is further proven from the discussion above, which shows that despite the choice of a different initial state for the system, the use of these conditions resulted in the same upper and lower bounds.

4.5.2 Testing the model for liquid phase segregation in U-O system under isothermal conditions

4.5.2.1 Thermodynamic description of the U-O system

The binary U-O system is different from the binary U-Zr system in the sense that it exhibits a liquid miscibility gap, for a large range of temperature and composition. For a fixed temperature of $T = 3200$ K , two phases are seen to co-exist: an oxygen-rich "oxidic" phase and another uranium-rich "metallic" phase. Within the context of in-vessel corium behaviour, it can be recalled from Chapter 1 that a similar situation has been documented for the U-O-Zr-steel system in [8] and [22], which is related to the transient stratification of the corium pool.

For the present system composed of U-O that is considered here, the thermodynamic description obtained from CALPHAD in terms of the constituent molar fractions y depicts the presence of three species UO_2, U and O at equilibrium, with the overall sum of the constituent mole fraction given as $y_U + y_O + y_{UO_2} = 1$ and the relation between the component (element) molar fractions and the constituent molar fractions as :

$$x_U = \frac{y_O + 2y_{UO_2}}{1 + 2y_{UO_2}} \tag{4.91}$$

$$x_O = \frac{1 - y_O}{1 + 2y_{UO_2}} \tag{4.92}$$

In order to ensure that the reduction of the system can be applied to this U-O system, an additional hypothesis is required. Going back to the initial choice of temperature, an equilibrium calculation for the system at 3200 K highlighted the absence of "free" oxygen in the system (*i.e.* $y_O = 0$). If the assumption of no "free" oxygen is applied to the initial state of the system, the equality in the number of constituents and components can be obtained, ensuring direct use of the thermodynamic data from CALPHAD (see Appendix E for details). Consequently, this ensures the absence of free oxygen in system during the transient and the system can then be determined in terms of a single component molar fraction. This approach is consistent with the general hypothesis proposed in [44] for systems of interest for application to in-vessel corium, where the redox reactions are supposed to be at local equilibrium at all times.

Recalling Section 4.3.3, for the conditions on the use of Grand Potential model, a monotonous invertible relation between the chemical potential μ and the component molar fraction x must be ensured. From Figure 4.33, it can be seen that this condition does not hold true for the U-O liquid, where the chemical potential exhibits a non-monotonous trend for a large range of composition, which represents the composition range of U for the presence of miscibility gap. However, on considering the regions close to the extremes of the composition range and encompassing the equilibrium points, monotonous μ functions of x_U can be constructed. Consequently, these two regions can be selected to denote the "oxidic" and the "metallic" liquid phases respectively (see Figure 4.34) and the functions can be used to obtain the thermodynamic properties for these two liquid phases.

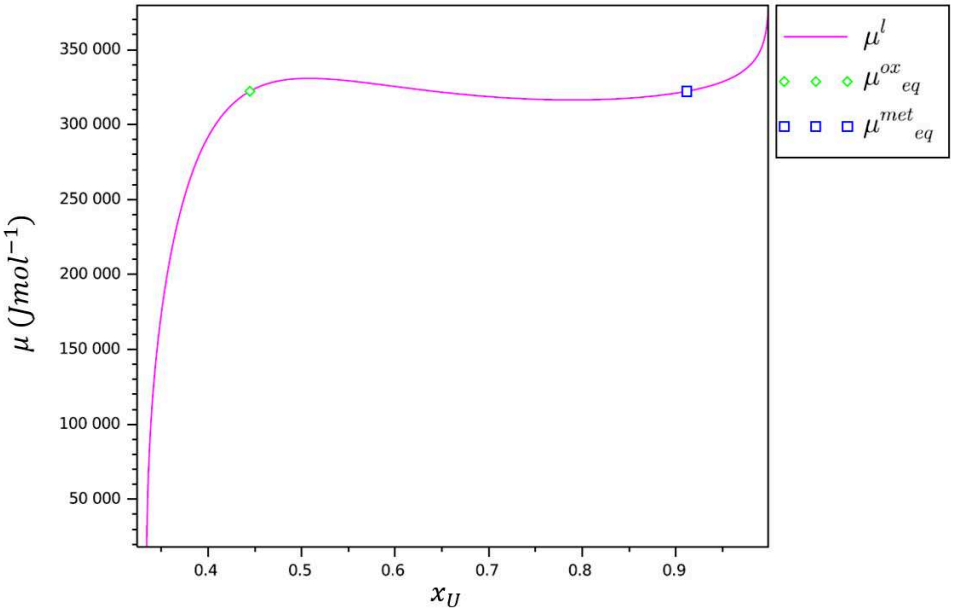

FIGURE 4.33: Variation of chemical potential μ with respect to the component composition x_U, evaluated at a fixed temperature $T = 3200$ K for U-O binary liquid system.

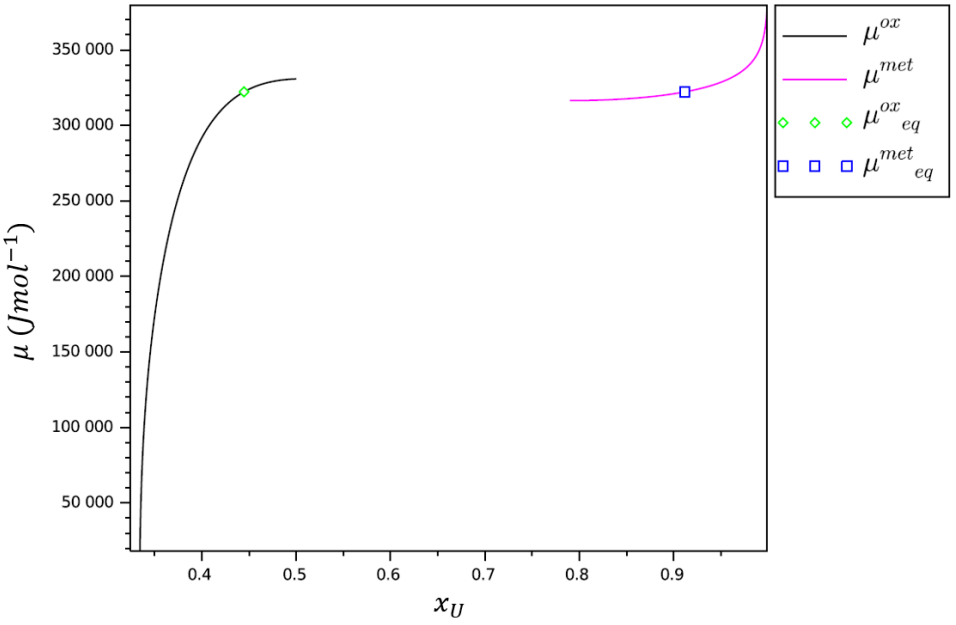

FIGURE 4.34: Variation of chemical potential μ with respect to the component composition x_U, corresponding to the oxidic (ox) and metallic (met) liquid domains, evaluated at a fixed temperature $T = 3200$ K for U-O binary liquid system.

4.5.2.2 Initialization of the system

The assumption $y_O = 0$ for the initial system imposes a constraint on the range for x_U $\left(x_U \in \left[\frac{1}{3}, 1\right]\right)$. Moreover, the choice of separate phase domains for the oxidic and metallic liquids imposes an additional constraint on the range of x_U for these domains, such that the composition ranges corresponding to these separate domains are given as:

$$x_U \in [(1/3 + \epsilon), 0.5] \text{ in oxidic phase} \tag{4.93}$$

$$x_U \in [0.79, (1.0 - \epsilon)] \text{ in metallic phase} \tag{4.94}$$

where ϵ is an arbitrary small value (set to 10^{-3}). These two factors were taken into consideration for defining two initial states for the system, which are mentioned as:

- Case 1, where the initial condition in μ corresponds to values for pure oxidic and metallic composition in the bulk regions and the μ values in the interface have been obtained under the hypothesis of local equilibrium, and;

- Case 2, which corresponds to the initial condition with $\mu = \mu_{eq}$ value within the interface, while keeping μ corresponding to pure phases in the bulk.

The construction of an initial condition (in terms of μ) corresponding to Case 1 requires a careful construction of the initial x_U profile within the interface region. This is because there exists a very narrow range in μ, for which both liquid phases co-exist (see Figure 4.35).

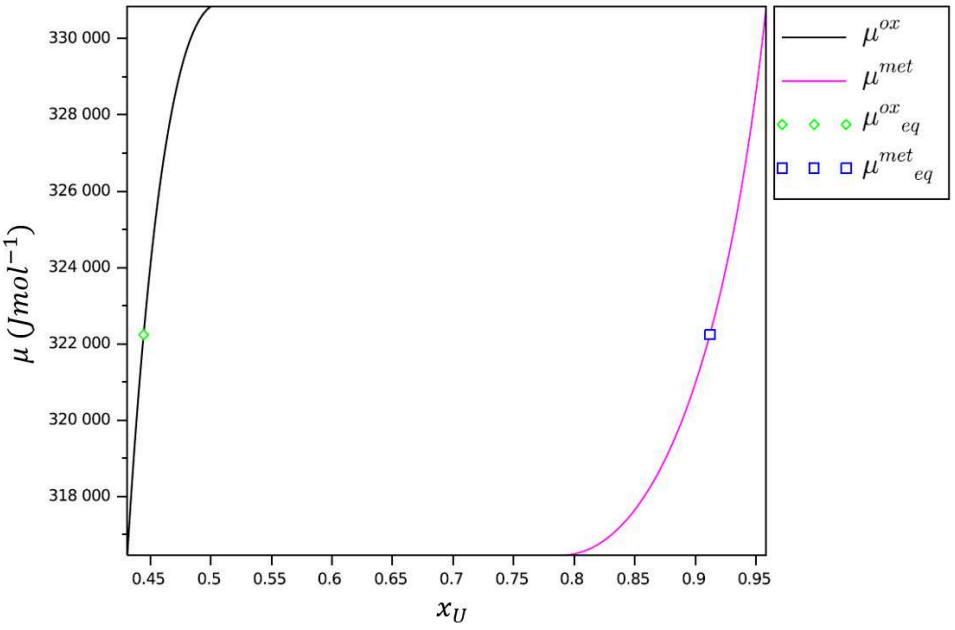

FIGURE 4.35: Variation of chemical potential μ with respect to the component composition x_U, corresponding to the common range of μ where both oxidic (ox) and metallic (met) liquid domains co-exist, evaluated at a fixed temperature $T = 3200$ K for U-O binary liquid system.

This common range also provides an "allowed" range for x_U in the two phases which is given as :

$$x_U^{ox} \in [0.43115, 0.5] \tag{4.95}$$

$$x_U^{met} \in [0.79, 0.95840] \tag{4.96}$$

With these allowed composition ranges, the initial component molar fraction x_U for the interface region can be determined by using the relation:

$$x_U = p(\phi)x_U^{ox} + (1 - p(\phi))x_U^{met} \tag{4.97}$$

Consequently, a map for the allowed range of x_U was obtained (depicted by Figure 4.36) for varying values of ϕ in Eq. 4.97, which gives a confined range for x_U as a function of ϕ which can be used to set the initial condition, such that the conversion of this profile from x_U to μ is possible (*i.e.* x_U^{ox} and x_U^{met} values can be found, such that the condition $\mu_{ox}(x_U^{ox}) = \mu_{met}(x_U^{met})$ is satisfied).

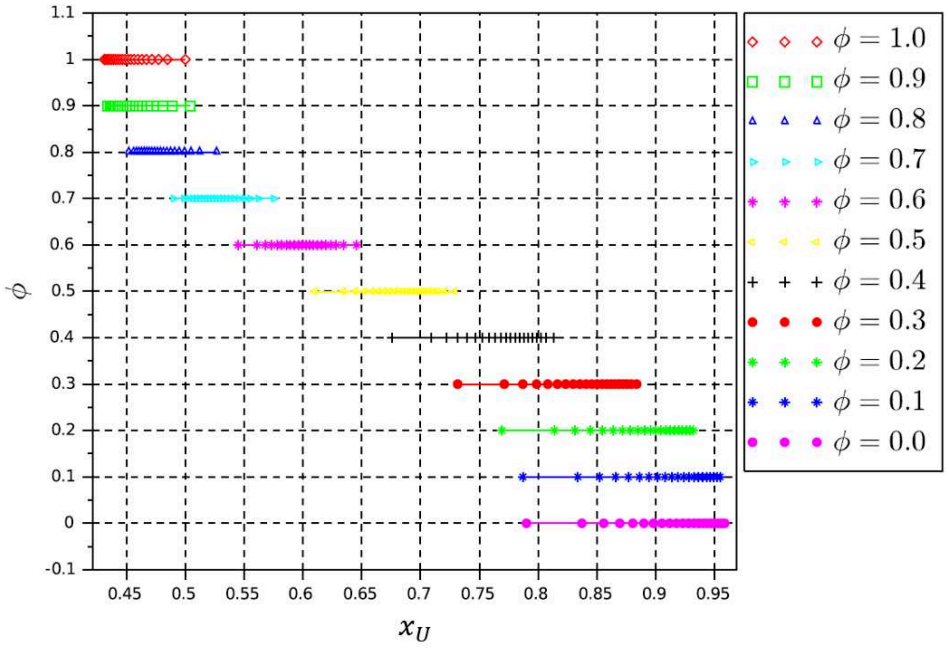

FIGURE 4.36: Possible range for composition x_U within the interface, for different values of ϕ.

The alternative way of initializing the system with equilibrium μ value within the interface is similar to Section 4.5.1.4.3. With these two initial profiles as input conditions, the model was subjected to verifications. As mentioned before, the initialization of the system affects the choice of scale separation and the appropriate phase field mobility value. This effect is

discussed in detail in the following section.

4.5.2.3 Results for U-O liquid case

With the two initial conditions on the system mentioned in Section 4.5.2.2, the model was used to study the evolution of the transient for the phase segregation process. The input parameters to the model have been mentioned in Table 4.3 and the transient simulations were performed until the steady state conditions associated with the chemical potential of the system ($\mu = \mu_{eq}$), and the expected position of the interface z_β^{ss} were achieved.

Input parameters	U-O system	
System initialization	Case 1	Case 2
Length scale for the system L (m)	0.1	
Interface thickness δ_β (m)	1.0×10^{-4}	
Temperature T (K)	3200	
Molar volume V_m $(m^3 mol^{-1})$	1.18×10^{-5}	
a $(J^{-1}m^3)$	2.09×10^{-5}	
Gradient coefficient κ_ϕ^2 (Jm^{-1})	1.56×10^{-5}	
Interface energy σ_β (Jm^{-2})	0.1	
Kinetic coefficient M_{xx} $(mol^2 K J^{-1} m^{-1} s^{-1})$	7.35×10^{-6}	7.21×10^{-6}
Average initial composition $\bar{x}_U^i$	0.67737	0.67465

TABLE 4.3: Initial inputs to the phase-field model for testing phase segregation in binary U-O system under isothermal conditions

For the two initial conditions considered for the present case of U-O system, it was observed that the different initial states have slightly different initial mass inventories (see Table 4.3). This difference in mass is due to the fact that the profile within the interface is not symmetric in Case 1, while it is in Case 2. As a consequence, the equilibrium calculations performed with these $\bar{x}_U^i$ compositions yield different expected steady state positions for the interface, which are mentioned in Table 4.4.

Initial state	z_β^{ss} (m)
Case 1	0.05142
Case 2	0.05201

TABLE 4.4: Expected steady state evaluated from the average mass inventories for the two initial systems defined for the U-O system.

Based on the choice made for the scale separation (*i.e.* $\delta_\beta/L = 10^{-3}$) for the numerical simulations, the minimum and maximum bounds on the M_ϕ value were obtained for the two systems from the relations Eqs. F.47 and F.48 as:

Initial system	M_ϕ $(J^{-1}K^1s^{-1}m^3)$ from Eqs. F.47 and F.48
Case 1	$1.47 \times 10^{-7} \ll M_\phi \ll 4.45 \times 10^{-7}$
Case 2	$1.44 \times 10^{-7} \ll M_\phi \ll 4.36 \times 10^{-7}$

TABLE 4.5: Maximum and minimum bound values obtained for the choice of phase-field mobility M_ϕ for two initial U-O systems.

Contrary to the discussion in case of the U-Zr system, where the bounds obtained from Eqs. F.47 and F.48 were independent of the choice of initial state, for the present case a slight difference is observed in the values mentioned in Table 4.5. This difference can be explained from the fact that these bounds are evaluated by taking the averaged value for the kinetic coefficient M_{xx}, which is related to the average initial composition x_U^i. However, the maximum value condition on the choice of δ_β, when evaluated from Eqs. F.47 and F.48, gives the same value for both systems:

$$\delta_\beta \ll 1.45 \times 10^{-4}\ m \tag{4.98}$$

From the above relation, it is evident that the choice of $\delta_\beta = 1.0 \times 10^{-4}\ m$ is very close to the maximum allowed limit. As a consequence, a finer interface thickness value should be chosen. However, this would mean that for the numerical simulations, the space discretization mesh defined for the system should be of the order of micrometers ($10^{-6}\ m$),

which is unfavorable due to the strict conditions posed by it on the choice of time-step to be applied for the time integration of the evolution equations.

Without changing the scale separation, an attempt was made to study the evolution of the two systems with $M_\phi = 1.0 \times 10^{-7}\ J^{-1}K^1s^{-1}m^3$, (which is consistent with the order of magnitude for the logarithmic mean value obtained from the bounds given by Eqs. F.47 and F.48) in order to verify the capability of the model to reach a consistent steady-state. The time-step value was chosen as $\Delta t = 1\ s$ and the calculations were performed by using a semi-implicit numerical scheme for a final time corresponding to 2τ.

From the transient calculations it was observed that the conservation of initial mass inventory is violated, resulting in a difference between the steady state and the expected average composition (denoted by $\bar{x}_U^{ss,exp} = 0.68384$ corresponding to μ_{eq}). This default in mass also affects the steady state interface position, the percentage error associated to which is depicted in Table 4.6, along with the percentage error in the average steady state composition $\bar{x}_U^{ss}$ calculated with respect to the initial average composition $\bar{x}_U^i$.

Initial system	$\bar{x}_U^i$	calculated $\bar{x}_U^{ss}$	error % (w.r.t. $\bar{x}_U^{ss,exp}$)	error % (w.r.t. $z_\beta^{ss,exp}$)
Case 1	0.67737	0.68769	1.52	−4.41
Case 2	0.67465	0.68582	1.65	−4.71

TABLE 4.6: Calculated initial and steady state average mass composition for the two systems and the error percentages with respect to the expected values of steady state average composition $\bar{x}_U^{ss,exp}$ and the interface positions $z_\beta^{ss,exp}$ (given in Table 4.4).

In order to verify the source of error for such a behaviour, different analyses were performed. As a first step, since the spatial profile in μ is obtained through an interpolation in x_U, the error associated with use of this interpolation function to calculate μ_{eq} from the equilibrium phase compositions, and its effect on the calculation of the expected steady state position was studied. The direct calculation of μ_{eq} from OC showed a slight variation in comparison to the μ_{eq} value obtained from the interpolated μ value for the equilibrium mass fractions x_U^{ox} and x_U^{met} for the two phases. However, the impact of this difference in μ_{eq} value on the expected steady state position of the interface was found to be negligible (the

percentage error in the calculation of the expected steady-state value was less than 0.001%).

The second analysis was performed to verify the evolution for ϕ. For this, the transient simulations were performed for a case where the initial condition on the system was set corresponding to μ_{eq}. In addition to this, the choice of M_ϕ value close to the lower bound results in a condition where the evolution of the transient is no longer governed by diffusion of species through the bulk phases (*i.e.* the characteristic time of evolution is governed by τ_ϕ). Instead, the adjustment of the ϕ spatial profile is required to reach thermodynamic equilibrium. Since the expected steady state position of the interface is related to the average composition of the system at equilibrium (*i.e.* $\bar{x}_U^{ss}$), for an initial system corresponding to μ_{eq}, this z_β^{ss} is very close to the initial interface position. The transient simulations verified that for such an initial state of the system, the adjustment of the ϕ profile was as per the expected steady state, with the $z_\beta^f \rightarrow z_\beta^{ss}$.

At this point, it is useful to recall the discussion on the consideration of separate 'oxidic' and 'metallic' domains for construction of the thermodynamic function in μ (from Section 4.5.2.1). This approach was followed in order to obtain monotonous relation between μ and x_U (within the confined regions), which could be used for switching the thermodynamic representation of the system in terms of the intensive variable - a condition that is necessary for the application of the grand potential formulation (see Section 4.3.3). Consequently, it was determined that for the local equilibrium hypothesis to uphold at all times within the interface, the chemical potential values must lie within the common range $\mu \in [316460.3, 330840.1]$ at all times.

Having said this, in order to develop a generalized model that is not bound by such system specific conditions, a prolongation of the thermodynamic functions for the two liquid phases was carried out, based on the universal maximum and minimum values for μ in the system. In principle, if the condition for μ within the interface is satisfied, this prolongation should have no effect on the behaviour of the model. This can be explained by recalling Eq. 4.67:

$$\frac{\partial \phi}{\partial t} = \left(\frac{M_\phi \kappa_\phi^2}{T}\right) \nabla^2 \phi - \left(\frac{M_\phi}{aT}\right) f'_{dw}(\phi) - \left(\frac{M_\phi \left(\Omega_m^s - \Omega_m^l\right)}{V_m T}\right) p'(\phi) \tag{4.99}$$

In the above equation, only the third term on L.H.S. is coupled to μ (in terms of $\Omega_m(\mu, \phi)$),

which is multiplied by the function $p'(\phi)$. As the $p'(\phi)$ function varies only within the interface and is 0 for the bulk phases (see Eq. 4.26), this implies that the evolution of ϕ is not dependent on the value of μ outside the interface, which gives a theoretical support to the approach of using prolonged thermodynamic functions.

However, for the transient calculations performed on the system represented by Case 2, it was observed that this condition on μ is violated during the initial time-steps in the transient (see Figure 4.37), where for $t = 1$ s and $t = 250$ s, μ does not lie in the common range (denoted by horizontal dashed red lines in the same figure) within the interface.

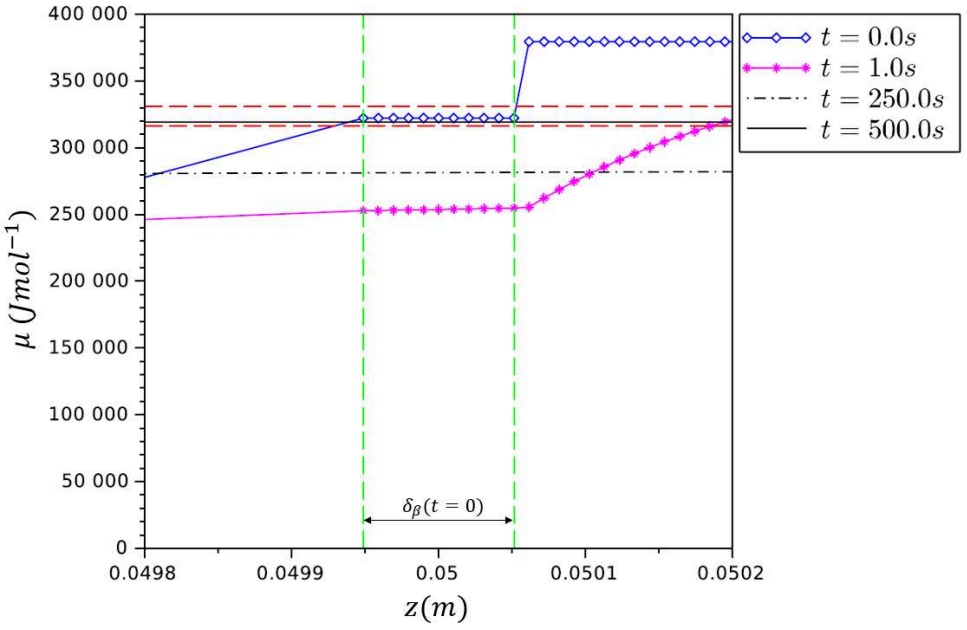

FIGURE 4.37: Variation of chemical potential μ in space z during the initial transient time-steps, depicting the violation of the condition on μ values within the interface (represented by the horizontal dashed red lines corresponding to the μ range associated with the co-existence of the oxidic and metallic phase). Case: initial condition corresponding to μ_{eq} in the interface.

Although the violation of the condition for μ was resolved after few initial time-steps, its effect on the default in the mass inventory $\bar{x}_U$ was not resolved. This deviation in $\bar{x}_U$ had a significant impact on the determining the expected steady state position of the

interface, which was verified upon comparing the steady state position exhibited by the transient (*i.e.* z_β^{ss} of Table 4.4) to the value for z_β^{ss} that was calculated for the altered average composition (see Table 4.7).

Initial system	calculated $\bar{x}_U^{ss}$	calculated z_β^{ss} (m)	z_β^f (m)
Case 2	0.68582	0.04956	0.04972

TABLE 4.7: Comparing the equilibrium interface position z_β^{ss} to the interface position depicted by the transient, for the system (Case 2) exhibiting the violation of mass balance.

In order to address this issue of non-conservation, an alternate approach was adopted, wherein an initial condition similar to Case 2 was defined, with the exception that the interface thickness for the initial μ profile (denoted by δ^μ) was taken to be twice the interface thickness(*i.e.* $\delta^\mu = 2 \times \delta_\beta$). Although the violation of the condition on μ was resolved faster, the impact of this violation on the mass balance was similar to that for Case 2. Thus, in order to utilize the phase-field model for studying phase segregation kinetics, the question related to an alternate initial condition for the system must be answered so as to ensure that the interface condition for μ is not violated during the transient evolution.

4.6 Conclusions

Through this chapter, a general formulation for a phase-field model to study thermochemical processes related to in-vessel corium has been proposed. For this phase-field model, the questions associated to its coupling with CALPHAD data have been answered. In particular, it was shown that for the model to be used for studying phase segregation process, an alternative method must be developed to initialize the system so as to ensure conservation of mass during the transient. Furthermore, the effect of 'up-scaling' the interface thickness (in order to ensure that the model can be used to describe thermochemical phenomena at a

mesoscopic scale) on the kinetics of the phase-field model have been studied. In particular, the constraints related to the maximum choice of interface thickness, and consequently its impact on the choice of the phase-field mobility parameter M_ϕ were discussed.

Although these studies have been performed for simplified models at isothermal conditions and for binary systems, from the point of view of consistent thermodynamic description, the findings can be applied to an n-component system. The next steps in this direction would be related to the verification of the complete non-isothermal model with respect to the effect of temperature variation on the the model kinetics.

Chapter 5

General conclusions and future perspectives

This thesis work was focused on answering some of the questions related to the thermodynamic consistency of the coupled thermochemical-thermohydraulic models for the description of in-vessel corium. To do so, a systematic approach was followed to ensure an extensive utilization of the thermodynamic description for in-vessel corium that is provided by the CALPHAD method, in the coupled models that have been developed at macroscopic and mesoscopic scales.

As a first step in this direction, the feasibility of using CALPHAD was tested on a 'mock-up' model developed at the macroscopic scale for studying the plane front solidification process at the boundary of a molten corium pool. This model was developed for the ternary U-O-Zr system, where a general formulation for writing the energy conservation equations in terms of specific enthalpies was adopted.

For such a formulation, the questions related to the use of CALPHAD-based enthalpy-temperature relations (referred to as "Equation-Of-State" - EOS) for providing closures to the model were answered. These EOS were subjected to verification for the transient simulations (discussed in Chapter 3), where the validity of these EOS related to the linearity of these functions with respect to temperature and composition changes was confirmed. The obtained numerical results confirmed the feasibility of using these EOS to provide closures to the conservation equations in corium-related thermal models, and to address the issue of thermodynamic consistency for the coupled in-vessel corium models

developed on a macroscopic scale. Moreover, the numerical study carried out in [81] further confirmed the applicability of using a general EOS, supplemented by appropriate hypotheses, for providing closures to the models for depicting different cases, such as treating the liquid miscibility gap.

This work has also touched to a general question associated with the formulation of the conservation equation related to composition in the frame of multi-component multi-phase transport models. Here, these conservation equations were formulated in terms of stoichiometric species mass fractions (because the considered thermophysical properties laws are formulated with these variables) and it was shown that, in this case, the evaluation of the interface quantities related to the local equilibrium assumption required non-standard modification of the interface conservation equations to take into account the redox process concurrent to solidification of sub-oxidized corium.

This initial success of using CALPHAD-based closures for the macroscopic in-vessel corium models has proved to be encouraging for undertaking the next step in this ongoing work, where a complete EOS can be constructed and verified for the in-vessel corium modelling of the PROCOR code. Additionally, the information obtained through this work is useful for the ongoing work discussed in [45], which focuses on the development of a model that describes the thermochemical coupling of the solid crust with the corium pool at the boundary of the reactor pressure vessel.

The second part of the work was based on the encouraging results obtained during Clément Cardon's thesis [44], which proposes a Cahn-Hilliard model for studying the kinetics of inter-layer mass transfer in the liquid miscibility gap of in-vessel corium. The initial objective in this framework was to study the conditions of extension of such a model to non-isothermal conditions and investigate the questions related to its thermodynamic consistency. For this, a phase-field model (including non-conserved phase-field variable ϕ as a phase marker) was developed by adopting a rather general formulation in grand potential that can be used to simulate the kinetics of the solidification and phase segregation processes under non-isothermal conditions. This choice of using the grand potential is favorable in terms of performing numerical simulations as the bulk and interface properties can be adjusted independently. Although the presentation of the evolution equations for the dependent variables (in Chapter 4) was made for the description of

a binary system, they can be applied to an n-component system without a loss of generality.

The closures for this non-isothermal model were studied in details, in particular, the constraints associated with the use of CALPHAD data. It was observed that for a non-isothermal extension of the model developed in [44] (where only conserved variables associated with element molar fractions are involved), the question of thermodynamic consistency can be answered in a similar way as for the macroscopic model by making use of CALPHAD-based EOS. In the case where a non-conserved phase-field variable is considered as a phase marker, the additional issue associated with the effect of an 'up-scaling' of the interface thickness on the kinetics of the phase-field model was discussed. In particular, the conditions related to the maximum choice of interface thickness, and its impact on the choice of the phase-field mobility parameter M_ϕ were discussed.

Numerical studies were performed for the analysis of solidification and phase-segregation in binary U-Zr and U-O systems respectively under isothermal conditions. For these systems it was observed (and verified with the help of numerical results in the U-Zr case) that in order to use this model for simulating processes with a broadened interface, the choice of the phase-field mobility parameter M_ϕ needs to be made from within a range that is posed by the characteristic times associated with the diffusion of mass across the system and the interface separately. Also, it was noted that the maximum possible choice for the scale separation in the system was rather constraining (considering the use of such a model in the frame of CFD) and was dependent on the system under consideration. In particular, for the case of studying the liquid miscibility gap in the U-O system, the condition imposed on the maximum 'allowed' interface thickness is such that using this model to simulate this process on a mesoscopic scale is probably impractical.

Moreover, due to the presence of a liquid miscibility gap in the U-O system, the exploitation of the CALPHAD data to provide closures to this model was not straightforward as the model condition related to the need of convex Gibbs energy functions was not fulfilled for this system. An alternate approach was proposed to solve this problem where two separate phase domains with monotonic Gibbs energy variations were selected from within the system. With this approach, it was observed that for the model to behave correctly, the chemical potential values within the interface region must always

lie within a common 'allowed' range of values which is obtained from the overlapping region where both the phase domains co-exist. Consequently, the initial condition for the system was constructed accordingly. However, the transient simulations performed with such an initial condition were not successful and a violation of the mass conservation was observed as the constraint on the chemical potential range within the interface was not fulfilled at all times. In this context, the question of initializing correctly the model in this U-O case so as to ensure conservation of mass over the transient has been left opened.

Although from the initial results related to the up-scaling of the interface, the integration of this model into the CFD based codes may not be entirely favourable for studying the evolution of in-vessel corium on a large scale (*i.e.* the order of meters) due to the strong conditions posed on the resolution of the interface, it seems promising to apply the model on a finer spatial scale. One such example where this model could be useful is to study the dissolution process related to the interaction between the crust and liquid metal phase, as studied in the context of the VITI-CORMET experiments [39]. Furthermore, the verification of the model for non-isothermal conditions is still required in order to determine if the variation of temperature has any further constraints on the kinetics of the model.

Apart from these near future perspectives, there lies the scope of achieving a stronger coupling of the phase-field models to the CALPHAD description. This is because at present, not all the physical quantities that are of interest to the model are derived in a thermodynamically consistent way. One such example is the interfacial energies used in the model description. As these values are very difficult to measure experimentally for the corium system (as, generally speaking, for all solid-liquid interfaces), the closures related to them for the model are restricted to the use of constant parameters. In this context, an extension of CALPHAD to model these interfacial energies by making use of the Butler equation [102] seems promising.

Appendices

Appendix A

General formulation of conservation equations for the Lumped Parameter models

This appendix presents the formulation of the conservation equations for the lumped-parameter models implemented in PROCOR, based on the local conservation equations. The further details are mentioned in Appendices A & B of [103].

For a spatial domain split into different sub domains (or zones) $\mathcal{V}_n$, the boundary of the region $\mathcal{V}_n$, denoted by $\partial\mathcal{V}_n$ is split as $\partial\mathcal{V}_n = \cup_{m\in N(n)}\beta_{n,m} \cup \beta_{n,ext}$ where $\beta_{n,m} = \beta_{m,n}$ is the interface between the neighboring domains n and m and $\beta_{n,ext}$ is the part of $\partial\mathcal{V}_n$ that lies on the boundary of the system. $N(n)$ represents the number of neighboring regions to $\mathcal{V}_n$.

For this spatial region $\mathcal{V}_n$, the local conservation equation can be written for any mass intensive property p with units $([p]\, kg^{-1})$:

$$\frac{\partial \rho_n p_n}{\partial t} + \vec{\nabla}.\rho_n \vec{v}_n p_n + \vec{\nabla}.\vec{\varphi}_n^p = \rho_n \dot{s}_n^p \tag{A.1}$$

with ρ_n being the mass density, $\vec{v}_n$ is the fluid velocity, $\vec{\varphi}_n^p$ is the flux associated with the property p $([p]\, m^{-2}s^{-1})$ and $\dot{s}_n^p$ is the source mass density associated with p $([p]\, kg^{-1}s^{-1})$. Integrating over $\mathcal{V}_n$ and using Reynolds and Gauss theorems, the macroscopic conservation

equation for $\mathcal{V}_n$ is obtained as:

$$\frac{d}{dt}\left(\int_{\mathcal{V}_n} \rho_n p_n dV\right) + \int_{\mathcal{V}_n} \left(\vec{\varphi}_n^p + \rho_n p_n(\vec{v}_n - \vec{u}_{\partial\mathcal{V}_n})\right).a\vec{A} = \int_{\mathcal{V}_n} \rho_n \dot{s}_n^p \tag{A.2}$$

where $\vec{u}_{\partial\mathcal{V}_n}$ is the velocity of the domain boundary $\partial\mathcal{V}_n$. Defining $\bar{p}_n$ and $\bar{\dot{S}}_n^p$ as:

$$\bar{p}_n m_n = \int_{\mathcal{V}_n} \rho_n p_n dV \tag{A.3}$$

$$\bar{\dot{S}}_n^p = \int_{\mathcal{V}_n} \rho_n \dot{s}_n^p dV \tag{A.4}$$

where $m_n = \int_{\mathcal{V}_n} \rho_n dV$ is the mass of the domain n. With this Eq. A.2 can be re-written as:

$$\frac{d}{dt}\left(\bar{p}_n m_n\right) + \int_{\mathcal{V}_n} \left(\vec{\varphi}_n^p + \rho_n p_n(\vec{v}_n - \vec{u}_{\partial\mathcal{V}_n})\right).d\vec{A}_n = \bar{\dot{S}}_n^p m_n \tag{A.5}$$

with $d\vec{A}_n$ is $\vec{n}_n dA$ with $\vec{n}_n$ the normal vector to $\beta_{n,m}$ pointing outwards of $\mathcal{V}_n$. For an interface $\beta_{n,m}$, the interface condition equations are obtained by integration of Eq. A.1 over a control volume that collapses on the interface as depicted on Figure A.1. In this integration process, similar to the previous one for obtaining Eq. A.2, as the volumes on both sides of the interfaces tend towards zero $\epsilon \to 0$, the volume terms become zero while the surface terms are restricted to terms evaluated on both sides of the interface $\beta_{n,m}$ *i.e.*

$$\int_{\beta_{n,m}} \left(\vec{\varphi}_n^p + \rho_n p_n(\vec{v}_n - \vec{u}_{\partial\mathcal{V}_n})\right).d\vec{A}_m + \int_{\beta_{n,m}} \left(\vec{\varphi}_m^p + \rho_n p_m(\vec{v}_m - \vec{u}_{\partial\mathcal{V}_n})\right).d\vec{A}_m = 0 \tag{A.6}$$

Eq. A.6 is sometimes referred to as Kotchine's theorem and is valid only when there is no accumulation, generation or transport of property p on the interface (refer to [104] for an example). In particular, surface tension is not taken into account here.

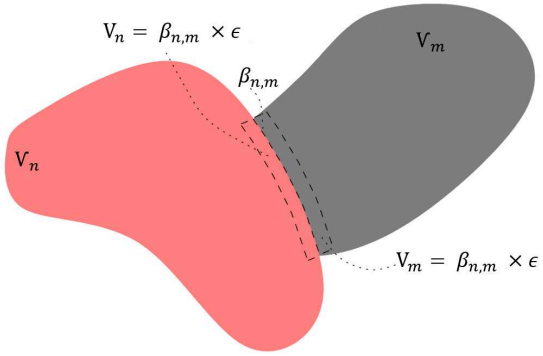

FIGURE A.1: Control volume for interface equations

For $p = 1$, the mass conservation equation is obtained. In particular, denoting:

$$\dot{m}_{\beta_{n,m},n} = \int_{\beta_{n,m}} \rho_n(\vec{v}_n - \vec{u}_{\partial\mathcal{V}_n}).d\vec{A}_n \tag{A.7}$$

$$\dot{m}_{n,ext} = \int_{\beta_{n,ext}} \rho_n(\vec{v}_n - \vec{u}_{\partial\mathcal{V}_n}).d\vec{A}_n \tag{A.8}$$

the mass fluxes through $\beta_{n,m}$ and $\beta_{n,ext}$ respectively, the mass conservation equation for $\mathcal{V}_n$ is written (from Eq. A.5) is simply:

$$\frac{dm_n}{dt} + \sum_{m \in N(n)} \dot{m}_{\beta_{n,m},n} = 0 \tag{A.9}$$

and, the associated interface conditions on $\beta_{n,m}$ (obtained from from Eq. A.6) is given as:

$$\dot{m}_{\beta_{n,m},n} + \dot{m}_{\beta_{n,m},m} = 0 \tag{A.10}$$

$\bar{p}_{\beta_{n,m},n}$, $\bar{p}_{n,ext}$, $\vec{\varphi}_{\beta_{n,m},n}$ and $\vec{\varphi}_{n,ext}$ are defined as:

$$\bar{p}_{\beta_{n,m},n}\dot{m}_{\beta_{n,m},n} = \int_{\beta_{n,m}} \rho_n p_n(\vec{v}_m - \vec{u}_{\partial\mathcal{V}_n}).d\vec{A}_n \tag{A.11}$$

$$\bar{p}_{n,ext}\dot{m}_{n,ext} = \int_{\beta_{n,ext}} \rho_n p_n(\vec{v}_m - \vec{u}_{\partial\mathcal{V}_n}).d\vec{A}_n \tag{A.12}$$

$$\bar{\varphi}^p_{\beta_{n,m},n} A_{\beta_{n,m}} = \int_{\beta_{n,m}} \vec{\varphi}^p_n.d\vec{A}_n \tag{A.13}$$

$$\bar{\varphi}^p_{n,ext} A_{\beta_{n,ext}} = \int_{\beta_{n,ext}} \vec{\varphi}^p_n.d\vec{A}_n \tag{A.14}$$

where $A_{\beta_{n,m}}$ (resp. $A_{\beta_{n,ext}}$) is the area of $\beta_{n,m}$ (resp. $\beta_{n,ext}$). Eq. A.5 can be written as:

$$\frac{d}{dt}\left(\bar{p}_n m_n\right) + \sum_{m \in N(n)} \left(\bar{\varphi}^p_{\beta_{n,m},n} A_{\beta_{n,m}} + \bar{p}_{\beta_{n,m},n} \dot{m}_{\beta_{n,m},n}\right) + \bar{p}_{n,ext} \dot{m}_{n,ext} = \bar{\dot{S}}^p_n m_n \tag{A.15}$$

The overall system is considered to be closed (in terms of mass), the interface conditions of Eq. A.6 can be formulated as:

$$\bar{p}_{\beta_{n,m},n} \dot{m}_{\beta_{n,m},n} + \bar{p}_{\beta_{n,m},m} \dot{m}_{\beta_{n,m},m} + \left(\bar{\varphi}^p_{\beta_{n,m},n} + \bar{\varphi}^p_{\beta_{n,m},m}\right) A_{\beta_{n,m}} = 0 \tag{A.16}$$

For $p = w^j$, the mass fraction of species j, the species mass conservation for $\mathcal{V}_n$ is obtained from Eq. A.15 as:

$$\frac{d}{dt}\left(\bar{w}^j_n m_n\right) + \sum_{m \in N(n)} \left(\bar{J}^j_{\beta_{n,m},n} A_{\beta_{n,m}} + \bar{w}^j_{\beta_{n,m},n} \dot{m}_{\beta_{n,m},n}\right) + \bar{w}^j_{n,ext} \dot{m}_{n,ext} = 0 \tag{A.17}$$

where $\bar{J}^j$ is the diffusive mass flux associated to species j and the interface conditions for $\beta_{n,m}$ given by Eq. A.16 are:

$$\bar{w}^j_{\beta_{n,m},n} \dot{m}_{\beta_{n,m},n} + \bar{w}^j_{\beta_{n,m},m} \dot{m}_{\beta_{n,m},m} + \left(\bar{J}^j_{\beta_{n,m},n} + \bar{J}^j_{\beta_{n,m},m}\right) A_{\beta_{n,m}} = 0 \tag{A.18}$$

For $p = h$ the mass enthalpy, neglecting viscous dissipation and the effect of the pressure material derivative, the energy conservation equation is obtained from Eq. A.15 as:

$$\frac{d}{dt}\left(\bar{h}_n m_n\right) + \sum_{m \in N(n)} \left(\bar{\varphi}_{\beta_{n,m},n} A_{\beta_{n,m}} + \bar{h}_{\beta_{n,m},n} \dot{m}_{\beta_{n,m},n}\right) + \bar{h}_{n,ext} \dot{m}_{n,ext} = \dot{q}^{mass}_n m_n \tag{A.19}$$

where $\bar{\varphi}$ is the heat flux and $\dot{q}^{mass}_n$ is the mass power density. The interface condition can be obtained similar to Eq. A.16 as:

$$\bar{h}_{\beta_{n,m},n} \dot{m}_{\beta_{n,m},n} + \bar{h}_{\beta_{n,m},m} \dot{m}_{\beta_{n,m},m} + \left(\bar{\varphi}_{\beta_{n,m},n} + \bar{\varphi}_{\beta_{n,m},m}\right) A_{\beta_{n,m}} = 0 \tag{A.20}$$

Appendix B

Initial verification tests on the developed macroscopic 1-D plane front solidification model

This appendix presents the initial verification tests performed on the 'mock-up' 1-D model for plane-front solidification, developed in PROCOR. The model was subjected to verification with respect to global energy balance and the analysis of the heat conduction profile in the solid crust at steady state.

For a sub-oxidized corium composition defined by its U/Zr molar ratio, Zr oxidation degree $C_{Zr} = 30\%$ and the initial temperature conditions, the input values for the solid and liquid masses were chosen accordingly in order to observe a pure solidification front for the transient till a steady state is achieved. These initial inputs have been given in Table B.1. Additionally, it has been assumed that both solid and liquid phases have same initial composition (denoted by $(\bar{w}_0^j)_{j\in\mathbb{S}}$) and internal mass power density ($\dot{q}^{mass}$), which is taken to be a constant. For the initial composition $\bar{w}_0^j$, the liquidus temperature $T_{liquidus}$ was calculated by an equilibrium calculation in OC.

Container dimensions (radius, height) $[m]$	2, 1
Solid initial mass m_s^0 $[kg]$	1000
Liquid initial mass m_p^0 $[kg]$	20000
Mass power density $\dot{q}^{mass}$ $[W/kg]$	100
Molar U/Zr ratio	1.2
Zr oxidation degree C_{Zr}	30%
Solid initial temperature $\bar{T}_s$ $[K]$	2200
Liquid initial temperature $\bar{T}_p$ $[K]$	2700
Initial interface temperature $T_{liquidus}\left(\bar{w}^j_{\beta,p}(t=0)\right)$ $[K]$	2637
External boundary temperature $T_{B.C.}$ $[K]$	1800

TABLE B.1: Initial inputs: verification of the thermal model for a sub-oxidized corium system $C_{Zr} = 30\%$

As first step of verification, the thermal model is tested with an EOS (referred to as "manufactured" EOS) of the type $h_p(T) = C_p^p T - h^*$ for the liquid phase (p) and $h_s(T) = C_p^s T$ for the solid phase (s), where C_p^θ refers to the specific heat capacity of the phase θ ($\theta = p$ for liquid and $= s$ for solid phase respectively) and h^* is the reference enthalpy of the liquid in the stable state. As a consequence, the calculations performed from the thermal model based on such a manufactured EOS (with the reference enthalpy value set to $h^* = \Delta h - (C_p^p - C_p^s)T_{liquidus}$) yielded same results as that obtained from a thermal model formulated explicitly in terms of temperature with constant values for heat capacity (C_p^s and C_p^p for solid and liquid phases respectively) and the enthalpy for phase change Δh.

At the end of the first verification, the "manufactured" EOS used in the thermal model was replaced by the EOS obtained from CALPHAD (*i.e.* Eqs. 3.18, 3.19, 3.20 and 3.21 from Chapter 3) and the model was tested for the verifications related to global heat balance and steady state conduction profiles. It should be noted that for this initial verification, the dependency of the CALPHAD based EOS on the compositions has not been taken into account. Instead, the initial composition $\bar{w}_0^j$ is used for the bulk as well as interfacial liquid and solid phases.

B.1 Global energy balance at steady state

The energy conservation equation for the entire system can be written by adding the Eqs. 3.5 and 3.6 and substituting Eq. 3.7 for the heat fluxes :

$$\frac{d}{dt}\left(\bar{h}_p m_p\right) + \frac{d}{dt}\left(\bar{h}_s m_s\right) - \Delta h \dot{m_{\beta,p}} + \bar{\varphi}_{\alpha,s} A_\beta = \dot{q}_p^{\text{mass}} m_p + \dot{q}_s^{\text{mass}} m_s \tag{B.1}$$

Under steady state conditions, the above equation reduces to:

$$\bar{\varphi}_{\alpha,s} A_\beta = \dot{q}_p^{\text{mass}} m_p + \dot{q}_s^{\text{mass}} m_s \tag{B.2}$$

Eq. B.2 represents the global energy balance for the system at steady state.

The conductive heat flux at the external boundary $\bar{\varphi}_{\alpha,s}$ is a function of the thickness of the solid crust. At initial time steps, due to negligible thickness of the solid layer, the heat flow outwards to the RPV wall is high. However, with the increasing crust thickness, the rate at which heat is transferred to the RPV wall, decreases. The internal powers (denoted by $\dot{q}_p^{\text{mass}} m_p$ and $\dot{q}_s^{\text{mass}} m_s$ for the liquid corium and solid crust respectively), on the other hand, change according to the evolving liquid and solid masses respectively. With the progression of the interface in the direction of solidification, the crust mass increases and the liquid mass decreases, up to the time when a steady-state is achieved. At this steady state, the rate of heat transferred to the vessel wall by conduction is equal to the total heat generated in the crust and the pool.

The above behaviour was observed in the calculations performed by the CALPHAD-EOS based thermal model. Figure B.1 depicts the evolution of the internal powers of the solid and liquid phases with time such that their summation reaches a constant value which is equal to the conductive heat flux at steady state.

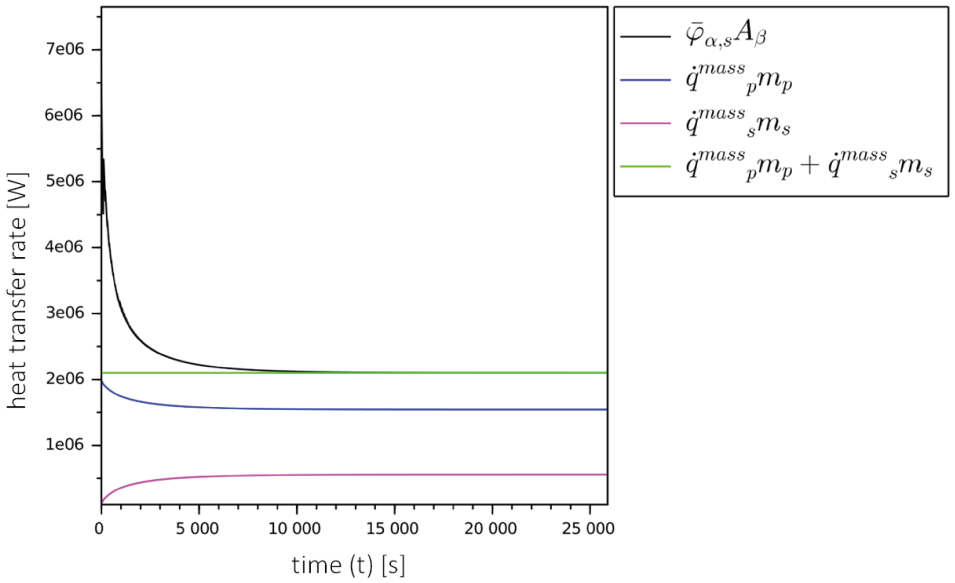

FIGURE B.1: Evolution of heat transfer rate (W) at the system boundaries with time (t) : verifying the global heat balance for the system.

B.2 Analysis of the heat conduction profile in the solid crust at steady state

Recalling that the choice of a "quadratic" temperature profile to depict the spatial variation of the crust temperature is an assumption made for the present model, it is necessary that for steady state conditions, this profile should match exactly with the solution of the 1-D heat conduction problem which, is obtained by solving the macroscopic heat balance equation for the solid crust (Eq. 3.6) at steady state.

Upon comparing the spatial variation of the crust temperature evaluated by the model (denoted by $T_{numerical}$ in Figure B.2), to the analytical steady state solution for the crust temperature profile (denoted by $T_{analytical}$ in Figure B.2), it was observed that $T_{numerical}$ and $T_{analytical}$ values are very close to each other, with the difference between the two being of the order of 10^{-6}, thus verifying the accuracy of the developed model in

terms of producing results (*i.e.* the developed model works within the numerical accuracy limits and has no bugs).

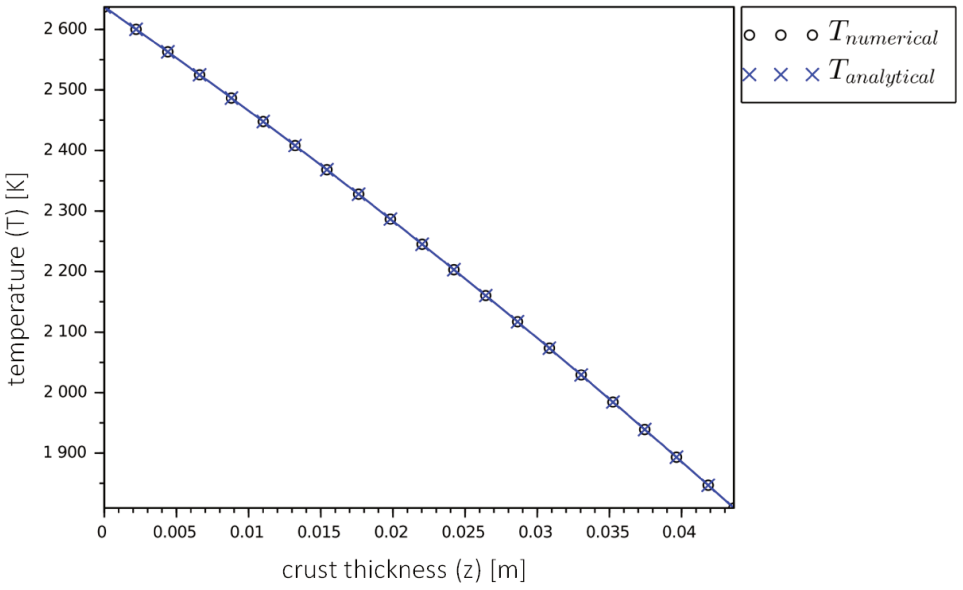

FIGURE B.2: Spatial variation of steady state temperature in the solidified crust: comparing the numerical solution for crust temperature ($T_{numerical}$) with the analytical solution ($T_{analytical}$).

Appendix C

Legendre transformation of Thermodynamic potentials

The present appendix deals with the transformations between the thermodynamic potentials by making use of the Legendre transformation. A Legendre transformation is a variable transformation that enables conversion of a function of one set of variables to another function of conjugate set of variables. Consider a function $f(x_1, x_2, ...x_n)$, the complete differential of f is given as:

$$df = \sum_{i=1}^{n} \left(\frac{\partial f}{\partial x_i} \right)_{x_j (j \neq i)} dx_i \tag{C.1}$$

The Legendre transformation of f w.r.t. x_i is given by another function g, which is expressed as:

$$g = f - \sum_{i=p+1}^{n} \left(\frac{\partial f}{\partial x_i} \right)_{x_j (j \neq i)} x_i \tag{C.2}$$

where $n - (p + 1)$ denotes the number of variables which we want to change to their corresponding conjugates.

In the context of thermodynamics, an equation of state corresponding to a thermodynamic potential can be converted to the equation of state corresponding to another thermodynamic potential by altering any one of the variables with its conjugate. The following section demonstrates in detail, the Legendre transformation from internal energy to the grand potential.

Legendre transformation from internal energy to grand potential

The thermodynamic state of an isolated system can be defined by using an 'equation of state', which relates the molar internal energy E_m of the system to its molar entropy S_m, molar volume V_m and mass fraction x : $E_m(S_m, V_m, x)$. The differential of this equation of state gives:

$$\begin{aligned} dE_m &= \left(\frac{\partial E_m}{\partial S_m}\right)_{V_m,x} dS_m + \left(\frac{\partial E_m}{\partial V_m}\right)_{S_m,x} dV_m + \left(\frac{\partial E_m}{\partial x}\right)_{S_m,V_m,} dx \\ &= TdS_m - pdV_m + \mu dx \end{aligned} \tag{C.3}$$

With T and p defined as:

$$T \equiv \left(\frac{\partial E_m}{\partial S_m}\right)_{V_m,x} \tag{C.4}$$

$$p \equiv -\left(\frac{\partial E_m}{\partial V_m}\right)_{S_m,x} \tag{C.5}$$

For a constant molar volume, the internal energy density e_m can be obtained as :

$$de_m = Tds_m + \mu d\left(\frac{x}{V_m}\right) \tag{C.6}$$

The choice of internal energy $E_m(S_m, V_m, x)$ as an equation of state is not convenient to work with. This is because in practice, experiments are performed in isothermal conditions (*i.e.* $dT = 0$) rather than adiabatic conditions (dQ = 0). A Legendre transformation allows working with another equation of state by changing the variable S_m to its conjugate variable T. Thus, the transformation is taken for $e_m(s_m, x/V_m, \phi)$ w.r.t. s and it is given as:

$$f_m = e_m - Ts_m \tag{C.7}$$

where f_m is the Helmholtz free energy density $f_m(T, x/V_m, \phi)$. Using the thermodynamic relation

$$df_m = de_m - Tds_m - s_m dT \tag{C.8}$$

If the system is assumed to have a constant molar volume, the Helmholtz free energy density becomes equivalent to the Gibbs free energy density which is a suitable

thermodynamic potential for a system defined for a constant temperature as well as pressure conditions.

This Gibbs energy can be expressed as a Legendre transformation : $G = H - TS$, with $H = E + pV$. For a constant volume system it is given by the form:

$$\begin{aligned} G_m &= E_m - TS_m + pV_m && \text{(C.9)} \\ g_m &= e_m - Ts_m + p && \text{(C.10)} \\ dg_m &= de_m - Tds_m - s_m dT && \text{(C.11)} \end{aligned}$$

where de_m is given by Eq. C.6. Substituting this expression for de_m in Eq. C.11:

$$dg_m = \mu d\left(\frac{x}{V_m}\right) - s_m dT + \frac{\partial e_m}{\partial \phi} d\phi \tag{C.12}$$

For Gibbs energy density defined as $g_m(T, \frac{x}{V_m}, \phi)$, following relations are obtained:

$$\begin{aligned} \left(\frac{\partial g_m}{\partial T}\right)_{\frac{x}{V_m},\phi} &= -s_m && \text{(C.13)} \\ \left(\frac{\partial g_m}{\partial x/V_m}\right)_{T,\phi} &= \mu && \text{(C.14)} \\ \left(\frac{\partial g_m}{\partial \phi}\right)_{T,\frac{x}{V_m}} &= \left(\frac{\partial e_m}{\partial \phi}\right)_{s_m,\frac{x}{V_m}} && \text{(C.15)} \end{aligned}$$

For a system that allows interchanging of particles with a reservoir, the chemical potential is constant. To describe such a system, the grand potential (per mole) $\Omega_m(T, V_m, \mu)$ is defined as the Legendre transform of the molar Gibbs free energy. Consequently, the thermodynamic relation between grand potential density and Gibbs energy density is given as:

$$\begin{aligned} \omega_m &= g_m - \mu\frac{x}{V_m} \\ &= e_m - Ts_m + p - \mu\frac{x}{V_m} \end{aligned} \tag{C.16}$$

$\therefore$ the complete differential for the grand potential density ω_m is given as:

$$d\omega_m = de_m - Tds_m - s_m dT - \mu d\left(\frac{x}{V_m}\right) - \frac{x}{V_m}d\mu \tag{C.17}$$

Substituting Eq. C.6 for de_m, Eq. C.17 can be written as:

$$d\omega_m = -s_m dT - \frac{x}{V_m}d\mu + \frac{\partial e_m}{\partial \phi} \tag{C.18}$$

Thus, grand potential density is obtained as a function of the conserved variables T, μ and the non conserved variable ϕ:

$$d\omega_m = \left(\frac{\partial \omega_m}{\partial T}\right)_{\mu,\phi} dT + \left(\frac{\partial \omega_m}{\partial \mu}\right)_{T,\phi} d\mu + \left(\frac{\partial \omega_m}{\partial \phi}\right)_{T,\mu} d\phi \tag{C.19}$$

with the relations:

$$\left(\frac{\partial \omega_m}{\partial T}\right)_{\mu,\phi} = -s_m \tag{C.20}$$

$$\left(\frac{\partial \omega_m}{\partial \mu}\right)_{T,\phi} = -\frac{x}{V_m} \tag{C.21}$$

$$\left(\frac{\partial \omega_m}{\partial \phi}\right)_{T,\mu} = \left(\frac{\partial e_m}{\partial \phi}\right)_{s_m, \frac{x}{V_m}} \tag{C.22}$$

and $\dot{\omega}_m$ as :

$$\begin{aligned}\frac{\partial \omega_m}{\partial t} &= \left(\frac{\partial \omega_m}{\partial T}\right)_{\mu,\phi}\frac{\partial T}{\partial t} + \left(\frac{\partial \omega_m}{\partial \mu}\right)_{T,\phi}\frac{\partial \mu}{\partial t} + \left(\frac{\partial \omega_m}{\partial \phi}\right)_{T,\mu}\frac{\partial \phi}{\partial t} \\ &= -(s_m)\frac{\partial T}{\partial t} - \left(\frac{x}{V_m}\right)\frac{\partial \mu}{\partial t} + \left(\frac{\partial \omega_m}{\partial \phi}\right)_{T,\mu}\frac{\partial \phi}{\partial t}\end{aligned} \tag{C.23}$$

where:

$$\frac{\partial}{\partial t}\left(\frac{\partial \omega_m}{\partial \mu}\right)_{T,\phi} = \left(\frac{\partial^2 \omega_m}{\partial T \partial \mu}\right)_{\phi}\frac{\partial T}{\partial t} + \left(\frac{\partial^2 \omega_m}{\partial \mu^2}\right)_{T,\phi}\frac{\partial \mu}{\partial t} + \left(\frac{\partial^2 \omega_m}{\partial \mu \partial \phi}\right)_{T}\frac{\partial \phi}{\partial t} \tag{C.24}$$

$$\frac{\partial}{\partial t}\left(\frac{\partial \omega_m}{\partial T}\right)_{\mu,\phi} = \left(\frac{\partial^2 \omega_m}{\partial T^2}\right)_{\mu,\phi}\frac{\partial T}{\partial t} + \left(\frac{\partial^2 \omega_m}{\partial \mu \partial T}\right)_{\phi}\frac{\partial \mu}{\partial t} + \left(\frac{\partial^2 \omega_m}{\partial T \partial \phi}\right)_{\mu}\frac{\partial \phi}{\partial t} \tag{C.25}$$

The derivatives of the grand potential density with respect to T and ϕ can be obtained by comparing the Maxwell's relations for g_m and ω_m as:

$$\left(\frac{\partial \omega_m}{\partial T}\right)_{\mu,\phi} = \left(\frac{\partial g_m}{\partial T}\right)_{\frac{x}{V_m},\phi} = -s_m \tag{C.26}$$

$$\left(\frac{\partial \omega_m}{\partial \phi}\right)_{T,\mu} = \left(\frac{\partial g_m}{\partial \phi}\right)_{T,\frac{x}{V_m}} = \left(\frac{\partial e_m}{\partial \phi}\right)_{s_m,\frac{x}{V_m}} \tag{C.27}$$

Finally, the expression for $s_m(e_m, x/V_m, \phi)$ can be obtained in terms of the derivatives of ω_m by using the mathematical identity $\left(\frac{\partial x}{\partial y}\right)_z = -\left(\frac{\partial x}{\partial z}\right)_y \left(\frac{\partial z}{\partial y}\right)_x$, while keeping the variables x/V_m and ϕ fixed one at a time:

$$\begin{aligned}\left(\frac{\partial s_m}{\partial \phi}\right)_{e_m,\frac{x}{V_m}} &= -\left(\frac{\partial s_m}{\partial e_m}\right)_{\phi,\frac{x}{V_m}} \left(\frac{\partial e_m}{\partial \phi}\right)_{s_m,\frac{x}{V_m}} = -\frac{1}{T}\left(\frac{\partial e_m}{\partial \phi}\right)_{s_m,\frac{x}{V_m}} \\ &= -\frac{1}{T}\left(\frac{\partial g_m}{\partial \phi}\right)_{T,\frac{x}{V_m}} = -\frac{1}{T}\left(\frac{\partial \omega_m}{\partial \phi}\right)_{T,\mu}\end{aligned} \tag{C.28}$$

$$\begin{aligned}\left(\frac{\partial s_m}{\partial (x/V_m)}\right)_{e_m,\phi} &= -\left(\frac{\partial s_m}{\partial e_m}\right)_{\phi,\frac{x}{V_m}} \left(\frac{\partial e_m}{\partial (x/V_m)}\right)_{s_m,\phi} = -\frac{1}{T}\left(\frac{\partial e_m}{\partial (x/V_m)}\right)_{s_m,\phi} \\ &= -\frac{1}{T}\left(\frac{\partial g_m}{\partial (x/V_m)}\right)_{T,\phi} = -\frac{\mu}{T}\end{aligned} \tag{C.29}$$

Appendix D

Evaluating diffusion coefficients and chemical mobilities for multi-component mass transfer

The present appendix focuses on deriving suitable expressions for the multi-component diffusion coefficients (D_{kj}) and the kinetic coefficient for mass transfer (M_{xx}), which are required in Chapters 3 and 4 respectively.

The solutions to the equations of mass transfer in multi-component systems are limited to some very special situations. Thus, the only option remaining is to rely on simplified models for deducing the solution. The Linearized theory developed by Toor is an approach towards solving these multi-component diffusion problems. In this approach, the fluxes in a multi-component system are described by a linear combination of appropriate driving forces, with proportionality constants which depend on the multi-component diffusion coefficients and appropriate binary mass transfer coefficients.

For an n-component system, the general expression for the fluxes J_k is given as:

$$J_k = -\sum_{k=1}^{n} L_{ki} F_i \tag{D.1}$$

Where L_{ki} are the phenomenological parameters that relate the flux of component k to all the driving forces F_k. The driving forces are defined in a way such that under isothermal conditions, the rate of entropy production per unit volume (invariant under Gallilean

transformations [105]) is given by:

$$\sigma = \frac{\partial S}{\partial t} = \frac{1}{T}\sum_{k=1}^{n} J_k F_k \tag{D.2}$$

The Onsager's reciprocal relation for the phenomenological coefficients is given by:

$$L_{ki} = L_{ik} \tag{D.3}$$

It should be noted that the mass flux value evaluated from Eq. D.1 depends on the choice of reference frame. A linear expression for fluxes in the lattice-fixed frame of reference (denoted by $\tilde{J}_k$) is given by taking the driving forces equal to the gradient of the chemical potentials (denoted by $\tilde{\mu}_j$ for a non-reduced system composed of n interdependent driving forces):

$$\tilde{J}_k = -\sum_{j=1}^{n} L_{kj} \nabla \tilde{\mu}_j \tag{D.4}$$

which follows the relation:

$$\sum_{k=1}^{n} \tilde{J}_k = 0 \tag{D.5}$$

Transformation of Eq. D.4 to obtain mass fluxes (denoted by J_k) for a volume fixed frame of reference (*i.e.* for a reference frame defined such that there is no net flow of volume) :

$$J_k = -\sum_{j=1}^{n} L'_{kj} \nabla \tilde{\mu}_j \tag{D.6}$$

with the phenomenological coefficient L'_{kj} expressed as:

$$L'_{kj} = \sum_{i=1}^{n} \left[\delta_{ki} - x_k \left(\frac{V_i}{V_m}\right)\right] L_{ij} \tag{D.7}$$

where:

- δ_{ki} is the Kronecker delta , *i.e.* = 1 when i=k and 0 otherwise;
- x_k is the mole fraction of the component k;
- V_i is the partial molar volume $V_i = \left(\frac{\partial V}{\partial N_k}\right)_{P,T,N_j}$ with N_k being the number of moles of component k;
- V_m is the molar volume given by $V_m = \sum_{j=1}^{n} x_j V_j$.

The above transformation is applicable as it does not change the value of the fluxes as they satisfy the relation:

$$\sum_{k=1}^{n} J_k V_k = 0 \tag{D.8}$$

The phenomenological coefficient L_{ki} can be evaluated by making use a model similar to the 'vacancy exchange mechanism' model for Crystalline phases[1] [105], the phenomenological coefficients are identified as:

$$L_{kj} = \begin{cases} 0 & \forall k \neq j \\ c_k \varsigma_k & \forall k = j \end{cases} \tag{D.9}$$

where c_k denotes the molar concentration ($mol^1 m^{-3}$) for component k and ς_k is the mobility of the component k.

The Eqs. D.6 and D.7 serve as a common point for further discussion, where these equations can be manipulated to obtain the quantities of interest, as per the requirements of the study performed in the present thesis.

D.1 Evaluation of diffusion coefficients

In order to treat the problem of finite mass transfer for the mock-up plane front solidification model discussed in Chapter 3, the relation derived for the mass transfer coefficient k_m from Eq. 3.30 requires diffusion coefficient values as inputs.

Starting from Eq. D.6 for the mass fluxes in a volume fixed frame, the driving force is given by the gradient of the chemical potentials $\tilde{\mu}$, which are functions of the compositions. In principle, these $\tilde{\mu}$ can be expressed as:

$$\tilde{\mu}_i = \tilde{\mu}_i \left(c_1, c_2, ..., c_n\right) \tag{D.10}$$

[1] In the vacancy exchange mechanism, it is assumed that the process of diffusion occurs by the jumping of atoms into their neighboring vacant lattice sites. Additionally, it's assumed that the distribution of these vacant sites is random for any given instance.

where the condition on the concentrations is given by $\sum_i^n c_i V_i = 1$. By applying the chain rule of derivation, Eq. D.6 can be written as:

$$J_k = -\sum_i^n L'_{ki} \sum_{j=1}^n \frac{\partial \tilde{\mu}_i}{\partial c_j} \nabla c_j \tag{D.11}$$

which can be re-written as:

$$J_k = -\sum_{j=1}^n D_{kj} \nabla c_j \tag{D.12}$$

The term D_{kj} is introduced as the diffusivity (or diffusion coefficient) and is expressed as:

$$D_{kj} = \sum L'_{ki} \frac{\partial \tilde{\mu}_i}{\partial c_j} \tag{D.13}$$

With L'_{ki} being calculated using Eqs. D.7 and D.9, for the relation $c_k = \frac{x_k}{V_m}$, a final expression is obtained for the diffusion coefficients associated with the mass fluxes under a volume fixed frame of reference:

$$D_{kj} = \sum_i \left(\delta_{ik} - x_k \left(\frac{V_i}{V_m} \right) \right) x_i \varsigma_i \frac{\partial \mu_i}{\partial x_j} \tag{D.14}$$

In the above expression, the quantity $\frac{\partial \mu_i}{\partial x_j}$ is purely thermodynamic and can be evaluated from the thermodynamic description of the system. In order to do so, it is required that the chemical potentials of each component must be expressed in terms of mole fractions to obtain a correct result.

However, from the point of interest of the macroscopic model developed in Chapter 3 which is developed under a 'mass fixed' frame of reference, a change of reference frame is required in order to obtain appropriate values for mass fluxes. Consequently, the expression for the diffusion coefficients given by Eq. D.14 will not hold true for a system represented under a mass fixed frame of reference. The section below, presents the derivation of the appropriate diffusion coefficients under the transformation of the system.

Reference Frame Transformations and Calculation of Multicomponent diffusion coefficients

For molar fluxes expressed in the volume fixed frame, recalling the equations Eq. D.12 and Eq. D.8, with the driving force equal to the gradient of molar concentration c_i that

obey $\sum_k c_k V_k = 1$. On the other hand, in a mass fixed frame of reference, the mass flux (denoted by $J_k^{\mathtt{m}}$) holds the relation:

$$\sum J_k^{\mathtt{m}} = 0 \tag{D.15}$$

This mass flux is related to molar flux ($J_k^{\mathtt{M}}$) as:

$$J_k^{\mathtt{M}} = \frac{J_k^{\mathtt{m}}}{M_k} \tag{D.16}$$

Where M_k refers to the molar mass of the component k. The molar flux obeys the relation:

$$\sum J_k^{\mathtt{M}} M_k = 0 \tag{D.17}$$

Using the linear theory, the mass flux can be expressed as:

$$J_k^{\mathtt{m}} = -\rho \sum_i D_{k,i}^{\mathtt{m}} \nabla w_i \tag{D.18}$$

with the driving force represented by the gradient of mass fraction w_i, and $D_{k,i}^{\mathtt{m}}$ being the diffusion coefficient evaluated under mass fixed reference frame.

When the fluxes in one reference frame (P) are to be measured in a different frame of reference (R) that is moving with an average relative velocity of v_{PR} with respect to reference frame P, the relation between quantities is given by the equation [106]:

$$J_k^{\mathtt{R}} = J_k^{\mathtt{P}} + c_k v_{PR} \tag{D.19}$$

Thus, using the above relation, the molar flux value for the mass-fixed frame can be expressed in terms of molar flux in volume fixed reference frame as:

$$J_k^{\mathtt{M}} = J_k^{\mathtt{V}} + c_k v_{VM} \tag{D.20}$$

Using equations Eq. D.16 and Eq. D.15, an expression for v_{Vm} instead, is obtained as:

$$v_{Vm} = -\frac{1}{\rho} \sum_i M_i J_i^{\mathtt{V}} \tag{D.21}$$

Eq. D.20 can be expressed in terms of $J_k^{\mathtt{m}}$ and $J_k^{\mathtt{v}}$ as:

$$J_k^{\mathtt{m}} = \sum_i \left(\delta_{ki} M_k - \frac{c_k M_k M_i}{\rho} \right) J_i^{\mathtt{v}} \tag{D.22}$$

Substitution of the expressions for fluxes in linear theory (*i.e.* Eq. D.18 and Eq. D.12) to the above relation gives us:

$$-\rho D_{k,j}^{\mathtt{m}} \nabla w_j = -\left(\sum_i \left(\delta_{ki} M_k - \frac{c_k M_k M_i}{\rho} \right) D_{i,j} \right) \nabla c_j \tag{D.23}$$

The mass fraction w_i can be expressed in terms of the molar concentration values c_i from the relation:

$$w_i = \frac{M_i}{\rho} c_i \tag{D.24}$$

$$\nabla c_i = \frac{1}{M_i} \left(w_i \nabla \rho + \rho \nabla w_i \right) \tag{D.25}$$

A linear relation between the diffusion coefficients $D_{k,j}^{\mathtt{m}}$ and $D_{i,j}$ can be obtained by neglecting the term $\nabla\rho$ and using Eq. D.25 in conjunction with Eq. D.23, which is given as:

$$D_{k,j}^{\mathtt{m}} = \sum_i \left(\frac{\delta_{ki} M_k}{M_j} - \frac{w_k M_i}{M_j} \right) D_{i,j} \tag{D.26}$$

Thus, substituting the value obtained from Eq. D.14 into the above relation, an appropriate expression for evaluating the diffusion coefficients associated to fluxes in a mass fixed frame of reference can be obtained.

D.2 Evaluating the Kinetic coefficients for mass transfer

It can be recalled from Chapter 4 that the expression for mass flux J_x for the system is expressed by the linear phenomenological equation Eq. 4.19 as:

$$J_x = \mathcal{M}_{xx} \nabla \left(\frac{\delta \mathbb{S}}{\delta (x/V_m)} \right) \tag{D.27}$$

Where $\mathcal{M}_{xx}$ is the kinetic coefficient related to the mass diffusion. In order to evaluate this mass flux, the diffusion mobilities (denoted by $\mathcal{M}_{xx}$) need to be calculated. The following steps can be applied for manipulating Eqs. D.6 and D.7 to obtain these kinetic coefficient value.

In general, the relation for the phenomenological coefficients L_{ik} given by Eq. D.3 is valid only for the conditions where the set of driving forces are independent of each other. If the F_k are identified with the chemical potential gradients $\nabla \mu_k$, the invariance of the entropy production term upon the change of reference frame is ensured by application of the Gibbs-Duhem relation. However, the Gibbs-Duhem relation imposes an interdependence of the driving forces, causing a violation of Eq. D.3. As a result, it is preferred to work with a set of $n-1$ independent forces $\nabla \Phi_k$ where Φ_k are the appropriate potentials. By introducing these appropriate expressions for the independent forces, the sum $\sum_{k=1}^{n-1} J_k \Phi_k$ can give the correct entropy production.

Starting from Eq. D.6 for the mass flux of component k for isothermal diffusion under a volume fixed frame of reference, the phenomenological coefficient L'_{kj} is expressed by Eq. D.7. For working with $n-1$ independent set of driving forces $\nabla \Phi_i$, Eq. D.6 modifies to:

$$J_k = -\sum_{i=1}^{n} L''_{ki} \nabla \Phi_i \tag{D.28}$$

where:

$$\nabla \Phi_i = \nabla \tilde{\mu}_i - \frac{V_i}{V_n} \nabla \tilde{\mu}_n \tag{D.29}$$

$$L''_{ki} = \sum_{j=1}^{n} \sum_{r=1}^{n} \left[\delta_{ir} - x_i \frac{V_r}{V_m} \right] \left[\delta_{jk} - x_k \frac{V_j}{V_m} \right] L_{jr} \tag{D.30}$$

For the case where $\frac{V_j}{V_m} = 1$ the above expressions reduces to (for chemical potential in the reduced system (μ) linked to chemical potentials of the non-reduced system ($\tilde{\mu}$) as $\mu = \tilde{\mu}_i - \tilde{\mu}_n$):

$$\nabla\Phi_i = \nabla\tilde{\mu}_i - \nabla\tilde{\mu}_n = \nabla\mu_i \tag{D.31}$$

$$L''_{ki} = \sum_{j=1}^{n}\sum_{r=1}^{n}\left[\delta_{ir} - x_i\right]\left[\delta_{jk} - x_k\right]L_{jr} \tag{D.32}$$

It should be noted that the Eq. D.28 depends on the choice of n which will correspond to the dependent potential. The phenomenological coefficient L_{kj} can be expressed by using the similar approach of applying a model similar to the 'vacancy exchange mechanism' model (*i.e.* Eq. D.9 as mentioned before). Following the condition, the expression for L''_{ki} is obtained as :

$$L''_{ki} = \sum_{j=1}^{n}\left[\delta_{ij} - x_i\right]\left[\delta_{jk} - x_k\right]L_{jj} \tag{D.33}$$

The diffusion mobility ς_k is related to the tracer diffusion coefficient D^*_k through the Einstein relation as:

$$\varsigma_k = \frac{D^*_k}{RT} \tag{D.34}$$

The tracer diffusion coefficient D^*_k can be assimilated to the self diffusion coefficient D_k under the assumption of no isotopic effect (*i.e.* it is considered that two atoms of different masses do not have different diffusion coefficients), which are calculated from the Arrhenius law:

$$D_k(T) = D^*_{k_0} exp^{(-E_d/kT)} \tag{D.35}$$

Substitution of Eq. D.34 into Eq. D.9, the phenomenological coefficient L_{kj} can be expressed as:

$$L_{kk} = c_k\frac{D_k}{RT} \tag{D.36}$$

The above expression can be substituted in Eq. D.33 to get the final expression for the coefficient L''_{ki}:

$$L''_{ki} = \sum_{j=1}^{n}\left[\delta_{ij} - x_i\right]\left[\delta_{jk} - x_k\right]\frac{x_j D_j}{V_m RT} \tag{D.37}$$

from which a final expression for the mass flux J_k can be obtained :

$$J_k = \sum_{i=1}^{n}\left[\sum_{j=1}^{n}\left[\delta_{ij} - x_i\right]\left[\delta_{jk} - x_k\right]\frac{x_j D_j}{V_m RT}\nabla\Phi\right] \tag{D.38}$$

For isothermal conditions, the phenomenological equation given by Eq. 4.28 reduces to :

$$J_x = -\frac{\mathcal{M}_{xx}}{T}(\nabla\mu) \tag{D.39}$$

Upon comparing Eq. D.39 with Eq. D.38, an expression for $\mathcal{M}_{xx}$ can be obtained:

$$\mathcal{M}_{xx} = TL''_{k1} = \sum_{j=1}^{n} [\delta_{ij} - x_i] [\delta_{jk} - x_k] \frac{x_j D_j}{V_m R} \tag{D.40}$$

Specific to the case of binary systems, Eq. D.28 can be re-written by using Eqs. D.31 and D.37 (with $n = 2$ corresponding to the dependent potential) :

$$J_1 = -L''_{11}\nabla\mu_1 = -\frac{x(1-x)}{V_m RT} [(1-x)D_1 + xD_2] \nabla\mu_1 \tag{D.41}$$

where $x = x_1$. Thus, using the relation given by Eq. D.40, for a binary system the value for $\mathcal{M}_{xx}$ is given by the final expression :

$$\mathcal{M}_{xx} = \frac{x(1-x)}{V_m R} [(1-x)D_1 + xD_2] \tag{D.42}$$

Appendix E

Calculation of quantities using OpenCalphad

This appendix presents the expressions for the various thermodynamic quantities that are evaluated from CALPHAD database, to be used as inputs to the developed phase-field model in Chapter 4.

Recalling from the discussion on the CALPHAD method in Chapter 2, the calculation of various thermodynamic quantities required for modelling the corium system has been done by using the NUCLEA database in combination with the Gibbs energy minimizer incorporated in the OpenCalphad (OC) software. For each possible phase, OC provides with the Gibbs energy per mole of the constituent (*i.e.* species, denoted by y_i) for an n component, n constituent system, which is represented as:

$$\tilde{G}_M = \tilde{G}_M(y_1, ...y_n)$$

It should be noted that the tilde notation has been introduced above only to differentiate between a complete n component system from a reduced system composed of $n-1$ components. In order to obtain the Gibbs energy per mole of the component ($\tilde{G}_m$), the following relation can be used:

$$\tilde{G}_m = \frac{\tilde{G}_M}{\tilde{\mathcal{N}}}$$

where $\tilde{\mathcal{N}}$ is the number of mole of components (elements) per 1 mole of constituents (species).

For a system consisting of the same number of constituents as the number of components, (*i.e.* n elements that combine to form n species), it is possible to define a reduced system with $n-1$ independent constituents. Following $\sum_i^n y_i = 1$, y_n can be expressed as $y_n = 1 - \sum_j^{n-1} y_j$, the molar Gibbs energy for the reduced system G_M is defined as:

$$G_M = \tilde{G}_M(y_1, ...y_{n-1}, (1 - \sum_{j=1}^{n-1} y_j))$$

Similarly, the Gibbs energy per mole of components for the reduced system (G_m) is given by:

$$G_m = \frac{1}{\mathcal{N}} G_M \tag{E.1}$$

where $\mathcal{N}$ is the number of moles of elements per mole of species, for the reduced system. Using this expression, the thermodynamic quantities can then be obtained for the reduced system as follows:

E.1 Gibbs energy density per mole of component

By definition, g_m is expressed as:

$$g_m = \frac{G_m}{V_m} = \frac{G_M}{V_m \mathcal{N}} \tag{E.2}$$

Using Eq. E.2, the various quantities of interest can be extracted from the CALPHAD database, by making use of appropriate thermodynamic relations.

E.2 Chemical potential for Binary systems

For a binary system composed of components with mole fractions x_1 and x_2, the following holds true from conservation law:

$$x_1 + x_2 = 1 \tag{E.3}$$

$$x_2 = 1 - x_1 \tag{E.4}$$

Assuming that the system is composed of constituent species with mole fractions y_1 and y_2 and that species conservation holds, the state of the system can be completely

determined by a single variable. The reduced molar Gibbs energy for constituents G_M is defined for this system as :

$$G_M = \tilde{G}_M\left(y_1, (1-y_1)\right) \tag{E.5}$$

By definition, μ is given as :

$$\mu = \frac{\partial G_m}{\partial x_1} = \frac{\partial G_m}{\partial y_1}.\frac{\partial y_1}{\partial x_1} \tag{E.6}$$

Where y_1 corresponds to the molar fraction of the constituent 1. For a constant molar volume, the substitution of Eq. E.1 for G_m in the above equation gives:

$$\mu = \left[\frac{\partial}{\partial y_1}\left(\frac{G_M}{\mathcal{N}}\right)\right]\left(\frac{\partial y_1}{\partial x_1}\right) \tag{E.7}$$

$$= \left[\frac{1}{\mathcal{N}}\left(\frac{\partial G_M}{\partial y_1}\right) - \frac{G_M}{\mathcal{N}^2}\left(\frac{\partial \mathcal{N}}{\partial y_1}\right)\right]\left(\frac{\partial y_1}{\partial x_1}\right) \tag{E.8}$$

From the thermodynamic relation between ω_m and g_m give by Eq. C.16, it can be recalled that the quantity required in place of μ is μ/V_m, which can be expressed as:

$$\frac{\mu}{V_m} = \frac{1}{V_m}\left[\frac{1}{\mathcal{N}}\left(\frac{\partial G_M}{\partial y_1}\right) - \frac{G_M}{\mathcal{N}^2}\left(\frac{\partial \mathcal{N}}{\partial y_1}\right)\right]\left(\frac{\partial y_i}{\partial x_1}\right) \tag{E.9}$$

where the derivative $\frac{\partial G_M}{\partial y_1}$ can be written as:

$$\begin{aligned}\frac{\partial G_M}{\partial y_1} &= \left(\frac{\partial \tilde{G}_M}{\partial y_1}\right)_{y_2} + \left(\frac{\partial \tilde{G}_M}{\partial y_2}\right)_{y_1}\frac{\partial y_2}{\partial y_1} \\ &= \left(\frac{\partial \tilde{G}_M}{\partial y_1}\right)_{y_2} - \left(\frac{\partial \tilde{G}_M}{\partial y_2}\right)_{y_1}\end{aligned} \tag{E.10}$$

Similarly, $\mathcal{N}$ can be expressed in terms of y_1 as:

$$\mathcal{N} = \tilde{\mathcal{N}}(y_1, (1-y_1)) \tag{E.11}$$

$\therefore$ the derivative $\frac{\partial \mathcal{N}}{\partial y_1}$ can be obtained from the above relation as:

$$\begin{aligned}\frac{\partial \mathcal{N}}{\partial y_1} &= \left(\frac{\partial \tilde{\mathcal{N}}}{\partial y_1}\right)_{y_2} + \left(\frac{\partial \tilde{\mathcal{N}}}{\partial y_2}\right)_{y_1}\left(\frac{\partial y_2}{\partial y_1}\right) \\ &= \left(\frac{\partial \tilde{\mathcal{N}}}{\partial y_1}\right)_{y_2} - \left(\frac{\partial \tilde{\mathcal{N}}}{\partial y_2}\right)_{y_1}\end{aligned} \tag{E.12}$$

Eqs. E.10 and E.12 can be substituted in Eq. E.8 to obtain the final expression for μ:

$$\begin{aligned}\mu &= \left[\frac{1}{\mathcal{N}}\left(\frac{\partial G_M}{\partial y_1}\right) - \frac{G_M}{\mathcal{N}^2}\left(\frac{\partial \mathcal{N}}{\partial y_1}\right)\right] \\ &= \frac{1}{\tilde{\mathcal{N}}}\left[\left(\frac{\partial \tilde{G}_M}{\partial y_1}\right)_{y_2} - \left(\frac{\partial \tilde{G}_M}{\partial y_2}\right)_{y_1}\right] \\ &- \frac{\tilde{G}_M}{\tilde{\mathcal{N}}^2}\left[\left(\frac{\partial \tilde{\mathcal{N}}}{\partial y_1}\right)_{y_2} - \left(\frac{\partial \tilde{\mathcal{N}}}{\partial y_2}\right)_{y_1}\right]\end{aligned} \tag{E.13}$$

With the relation between y and x being known, the derivative $\frac{\partial y_1}{\partial x_1}$ can be obtained.

Case: U-Zr system

For the $U - Zr$ system, the constituents (also components) are U and Zr. The following hold true :

$$x_U = y_U \tag{E.14}$$

$$x_{Zr} = y_{Zr} \tag{E.15}$$

$$x_U + x_{Zr} = 1 \tag{E.16}$$

$$\tilde{\mathcal{N}} = y_U + y_{Zr} = 1 \tag{E.17}$$

G_M and $\mathcal{N}$ are defined as:

$$G_M = \tilde{G}_M(y_U, (1 - y_U)) \tag{E.18}$$

$$\mathcal{N} = y_U + (1 - y_U) \tag{E.19}$$

For $x_1 = x_U$, the chemical potential $\tilde{\mu}_U$ is expressed as:

$$\mu_U = \frac{\partial G_m}{\partial x_U} = \left(\frac{\partial G_m}{\partial y_U}\right).\left(\frac{\partial y_U}{\partial x_U}\right) \tag{E.20}$$

From Eq. E.14 it can be seen that $\frac{\partial y_U}{\partial x_U} = 1$. From this, the final expression for μ_U is obtained as :

$$\mu_U = \frac{1}{\tilde{\mathcal{N}}}\left[\left(\frac{\partial \tilde{G}_M}{\partial y_U}\right)_{y_{Zr}} - \left(\frac{\partial \tilde{G}_M}{\partial y_{Zr}}\right)_{y_U}\right] \tag{E.21}$$

Case: U-O system

This particular case corresponds to the type of systems where the number of components and constituents are no longer the same. In such cases, direct use of the associate model with species as its constituents to evaluate quantities is not possible.

In order to obtain the chemical potential, an additional hypothesis is required. The components and constituents of the U-O system include elements U and O and species U, UO_2 and O respectively. The relation between the element and species molar fractions is given as:

$$x_U + x_O = 1 \tag{E.22}$$

$$x_O = 1 - x_U \tag{E.23}$$

$$y_{UO_2} + y_O + y_U = 1 \tag{E.24}$$

$$\tilde{\mathcal{N}} = 3y_{UO_2} + y_O + y_U \tag{E.25}$$

The molar fractions of the components are dependent on the molar fractions of the constituents as:

$$x_U = \frac{1 - y_O}{1 + 2y_{UO_2}}$$

$$x_O = \frac{y_O + 2y_{UO_2}}{1 + 2y_{UO_2}}$$

Application of additional hypothesis: For the present system, an initial assumption of no free oxygen is made based on the equilibrium calculations performed for $T = 3200\ K$ (*i.e.* $y_O = 0$). The application of this assumption to the initial state of the system leads to the presence of equal number of constituents and components in the system, which ensures the direct use of the thermodynamic data from CALPHAD and so the molar fraction x_U can be expressed as $x_U = \frac{1}{1+2y_{UO_2}}$, within the range $\left[\frac{1}{3}, 1\right]$ and from Eq. E.24 we obtain $y_{UO_2} = 1 - y_U$. Moreover, with this initial assumption, it can also be ensured that the

system is devoid of y_O during the transient as well. Thus, x_U and x_O can be rewritten as:

$$\begin{aligned} x_U &= \frac{1}{3-2y_U} \\ x_O &= \frac{2(1-y_U)}{3-2y_U} \end{aligned}$$

The constituent fractions can be related to x_U as:

$$y_U = \frac{3x_U - 1}{2x_U} \tag{E.26}$$

$$y_{UO_2} = 1 - y_U = \frac{1 - x_U}{2x_U} \tag{E.27}$$

G_M and $\mathcal{N}$ are defined as:

$$G_M = \tilde{G}_M(y_U, y_O, (1 - y_U - y_O)) \tag{E.28}$$

$$\mathcal{N} = \tilde{\mathcal{N}}\left(y_U, y_O, (1 - y_U - y_O)\right) = y_U + y_O + 3(1 - y_U - y_O) \tag{E.29}$$

For $x_1 = x_U$, the chemical potential μ_U is expressed as:

$$\mu_U = \frac{\partial G_m}{\partial x_U} = \left(\frac{\partial G_m}{\partial y_U}\right).\left(\frac{\partial y_U}{\partial x_U}\right) \tag{E.30}$$

The derivative $\frac{\partial y_U}{\partial x_U}$ can be computed from Eq. E.26. From this, the final expression for μ_U can be obtained as:

$$\mu_U = \frac{1}{\tilde{\mathcal{N}}}\left[\left(\frac{\partial \tilde{G}_M}{\partial y_U}\right)_{y_O, y_{UO_2}} - \left(\frac{\partial \tilde{G}_M}{\partial y_{UO_2}}\right)_{y_U, y_O} + 2\frac{\tilde{G}_M}{\tilde{\mathcal{N}}}\right]\frac{1}{2(x_U)^2} \tag{E.31}$$

E.3 Grand potential density

It can be recalled from Eq. C.18, the grand potential density ω_m is given for the reduced system from the thermodynamic relation:

$$\omega_m = g_m - \hat{\mu} x_i \tag{E.32}$$

where $\hat{\mu} = \mu / V_m$. ω_m can be computed from CALPHAD by substitution of Eqs. E.2 and E.9 to Eq. E.32.

E.4 Entropy density

By definition, s can be obtained from Eq. C.26 of Appendix C as :

$$s = -\frac{\partial \omega_m}{\partial T} = -\frac{\partial g_m}{\partial T} \tag{E.33}$$

Substitution of Eq. E.2 for g_m in the above equation, entropy density can be evaluated from OC.

E.5 Second order derivatives of the Grand potential density

The generalized evolution equations for the variables T and μ given by Eqs. 4.38 and 4.40 require second order derivatives of the grand potential density with respect to T and μ : $\frac{\partial^2 \omega_m}{\partial T^2}$, $\frac{\partial^2 \omega_m}{\partial \hat{\mu}^2}$ and $\frac{\partial^2 \omega_m}{\partial \hat{\mu} \partial T}$. The general expressions for these quantities have been derived below.

It can be recalled from Eq. C.26 that the second derivative of grand potential density with respect to T can be expressed in terms of a partial derivative of Gibbs energy density with respect to T. Substitution of Eq. E.2 for g_m, the final expression for $\frac{\partial^2 \omega_m}{\partial T^2}$ can be obtained as:

$$\begin{aligned} \frac{\partial^2 \omega_m}{\partial T^2} &= \frac{\partial^2 g_m}{\partial T^2} \\ &= \frac{1}{V_m \mathcal{N}} \left(\frac{\partial^2 G_M}{\partial T^2} \right) \end{aligned} \tag{E.34}$$

Similarly, the second derivative of ω_m with respect to μ can be obtained from Eq. C.21 as:

$$\frac{\partial^2 \omega_m}{\partial \hat{\mu}^2} = -\frac{\partial x}{\partial \hat{\mu}} \tag{E.35}$$

Contrary to the other derivatives, $\frac{\partial^2 \omega_m}{\partial \hat{\mu}^2}$ cannot be directly obtained from OC through an analytical derivative. Hence, a numerical derivative is used to evaluate it, which is achieved by making use of the forward difference scheme for discretization of the derivative:

$$-\frac{\partial x}{\partial \hat{\mu}} = -\left[\frac{x(\hat{\mu}_i + \epsilon) - x(\hat{\mu}_i)}{\epsilon}\right] \tag{E.36}$$

where ϵ is an arbitrary value that is smaller than the difference between two consecutive values of $\hat{\mu}$ for the defined grid. Finally, for the partial derivative of ω_m with respect to T and μ, the expression can be obtained by using Eqs. E.33 and E.2:

$$\begin{aligned} \frac{\partial^2 \omega_m}{\partial \hat{\mu} \partial T} &= -\frac{\partial x}{\partial T} = -\frac{\partial s}{\partial \hat{\mu}} \\ &= \frac{\partial}{\partial \hat{\mu}} \left(\frac{1}{V_m \mathcal{N}} \left(\frac{\partial G_M}{\partial T} \right) \right) \end{aligned} \tag{E.37}$$

Appendix F

Non-dimensionalization of the evolution equations for the isothermal phase field model

The present appendix discusses the approaches followed for the non-dimensionalization of the evolution equations Eqs. 4.66 and 4.67 of the phase field model developed in Chapter 4. The dimensionless variables introduced in Section 4.3.2.2.2 of Chapter 4 can be recalled here:

$$t^* = \frac{t}{\tau} \tag{F.1}$$

$$z^* = \frac{z}{L} \tag{F.2}$$

$$\mu^* = \frac{\mu}{\mu_0} \tag{F.3}$$

$$\Omega^*{}_m = \frac{\Omega_m}{\Omega_0} \tag{F.4}$$

$$\Delta\Omega^*_m = \frac{\Omega^s_m - \Omega^l_m}{\Delta\Omega_0} \tag{F.5}$$

$$M^*_{xx} = \frac{M_{xx}}{M_0} \tag{F.6}$$

where:

- τ is the characteristic time associated the evolution of the variable μ, which represents the time taken for the diffusion process to occur in the system of a given length scale L, and;

- μ_0 , Ω_0, $\Delta\Omega_0$ are the characteristic values associated with the order of magnitudes of μ $(1.0 * 10^5)$, Ω_m $(1.0 * 10^5)$ and $\Omega_m^s - \Omega_m^l$ $(1.0 * 10^3)$, and M_0 is the characteristic value associated with the kinetic coefficient M_{xx}, which has been taken as the average value for M_{xx}, depending on the system under consideration in Chapter 4 (*i.e.* the binary U-Zr or U-O system) respectively.

Non-dimensionalization of the μ evolution equation and defining the characteristic time for diffusion

The evolution equation in μ (Eq. 4.66) is given as:

$$\left(\frac{\partial^2\Omega_m}{\partial\mu^2}\right)\dot{\mu} = -\frac{V_m}{T}\nabla(M_{xx}\nabla\mu) - \left(\frac{\partial^2\Omega_m}{\partial\mu\partial\phi}\right)\dot{\phi} \tag{F.7}$$

The dimensionless form for Eq. F.7 can be written as:

$$\left(\frac{\partial^2\Omega_m^*}{\partial\mu^{*2}}\right)\ \frac{d\mu^*}{dt^*} = -\left(\frac{V_m\mu_0^2 M_0\tau}{TL^2\Omega_0}\right)\frac{\partial}{\partial z^*}\left(M_{xx}^*\frac{\partial\mu^*}{\partial z^*}\right) - \left(\frac{\partial^2\Omega_m^*}{\partial\mu^*\partial\phi}\right)\frac{d\phi}{dt^*} \tag{F.8}$$

where we set:

$$\frac{V_m\mu_0^2\tau}{TL^2\Omega_0}M_0 = 1 \tag{F.9}$$

From Eq. F.9, an expression for the characteristic diffusion time τ can be obtained:

$$\tau = \frac{L^2}{V_m\mu_0^2 M_0/\Omega_0 T} = \frac{L^2}{D_x} \tag{F.10}$$

where $V_m\mu_0^2 M_0/\Omega_0 T$ has the same dimensions as that of the diffusion coefficient D_x.

Non-dimensionalization of the ϕ evolution equation and defining its characteristic time

The evolution equation for the non-conserved order paramter ϕ is given by Eq. 4.67 as:

$$\dot{\phi} = \left(\frac{M_\phi\kappa_\phi^2}{T}\right)\nabla^2\phi - \left(\frac{M_\phi}{aT}\right)f'_{dw}(\phi) - \left(\frac{M_\phi\left(\Omega_m^s - \Omega_m^l\right)}{V_m T}\right)p'(\phi) \tag{F.11}$$

From the discussion in Section 4.3.2.2.2 of Chapter 4, it can be recalled that the characteristic time of evolution for ϕ depends on the magnitudes of the three terms present in Eq. 4.67. The characteristic time associated with the evolution of ϕ can be recalled from

Eq. 4.74, which is expressed as:

$$\frac{1}{\tau_\phi} = \frac{M_\phi}{aT} \tag{F.12}$$

Multiplication of the evolution equation by τ_ϕ and its subsequent simplification gives:

$$\begin{aligned}
\tau_\phi \dot{\phi} &= \tau_\phi \left(\frac{M_\phi \kappa_\phi^2}{T} \right) \nabla^2 \phi - f'_{dw}(\phi) - \tau_\phi \left(\frac{M_\phi \left(\Omega_m^s - \Omega_m^l \right)}{V_m T} \right) p'(\phi) \\
&= \left(a \kappa_\phi^2 \right) \nabla^2 \phi - f'_{dw}(\phi) - \left(\frac{a \left(\Omega_m^s - \Omega_m^l \right)}{V_m} \right) p'(\phi) \\
\dot{\phi} &= \left(\frac{a \kappa_\phi^2}{\tau_\phi} \right) \nabla^2 \phi - \left(\frac{1}{\tau_\phi} \right) f'_{dw}(\phi) - \left(\frac{a(\Omega_m^s - \Omega_m^l)}{\tau_\phi V_m} \right) p'(\phi)
\end{aligned} \tag{F.13}$$

The term $a\kappa_\phi^2/\tau_\phi$ can be written as the phase field diffusion coefficient D_ϕ. Substituting for κ_ϕ^2 and a from Eqs. 4.57 and 4.58 :

$$D_\phi = \frac{\delta_\beta^2}{32\tau_\phi} = \frac{\delta_\beta^2 M_\phi}{32aT} \tag{F.14}$$

Non-dimensionalization of Eq. F.13 in space and time gives:

$$\frac{1}{\tau_\phi} \frac{d\phi}{dt^*} = \underbrace{\left(\frac{D_\phi}{L^2} \right)}_{=\frac{1}{\tau_1}} \frac{\partial^2 \phi}{\partial z^{*2}} - \left(\frac{1}{\tau_\phi} \right) f'_{dw}(\phi) - \underbrace{\left(\frac{a \Delta \Omega_0}{\tau_\phi V_m} \right)}_{=\frac{1}{\tau_3}} \Omega_m^* p'(\phi) \tag{F.15}$$

where:

$$\frac{1}{\tau_1} = \frac{D_\phi}{L^2} = \left(\frac{\delta_\beta^2}{32 L^2} \right) \frac{1}{\tau_\phi} \tag{F.16}$$

Hence, τ_1 and τ_ϕ are shown to be proportional. On the other hand, the characteristic time associated with the evolution of the third term (τ_3) can be recalled from Eq. 4.75 as:

$$\frac{1}{\tau_3} = \frac{M_\phi \Delta \Omega_0}{V_m T} \tag{F.17}$$

With the relations for τ, τ_ϕ and τ_3 known, Eqs. F.10, F.12 and F.17 can be substituted in the relations given by Eqs. 4.78 and 4.79, with t_{diff} defined by Eq. 4.76 to obtain the

inequalities for the mobility coefficient M_ϕ as :

$$\frac{aV_m\mu_0^2M_0}{\Omega_0 L^2} \ll M_\phi \ll \frac{aV_m\mu_0^2M_0}{\Omega_0\delta_\beta^2} \tag{F.18}$$

$$\frac{V_m^2\mu_0^2M_0}{L^2\Omega_0\Delta\Omega_0} \ll M_\phi \ll \frac{V_m^2\mu_0^2M_0}{\delta_\beta^2\Omega_0\Delta\Omega_0} \tag{F.19}$$

An alternate approach to the non-dimensionalization of the evolution equations for the choice of M_ϕ

From the thermodynamic relation between the component mass fraction and the grand potential density (Eq. 4.35), the second order derivative of ω with respect to μ and the derivative $\frac{\partial^2\mu}{\partial\mu\partial\phi}$ are given as:

$$\frac{\partial^2\omega_m}{\partial\mu^2} = p(\phi)\frac{\partial^2\omega_m^s}{\partial\mu^2} + (1-p(\phi))\frac{\partial^2\omega_m^l}{\partial\mu^2} \tag{F.20}$$

$$\frac{\partial^2\omega_m}{\partial\mu\partial\phi} = p'(\phi)\left[\frac{\partial\omega_m^s}{\partial\mu} - \frac{\partial\omega_m^l}{\partial\mu}\right] \tag{F.21}$$

From Eqs. 4.35 and F.20, the concentration ρ (mol^1m^{-3}) and the susceptibility χ ($J^{-1}mol^2m^{-3}$) respectively for solid and liquid phase are defined as:

$$\rho_s = \frac{x_s}{V_m} = -\left(\frac{\partial\omega_m^s}{\partial\mu}\right) \tag{F.22}$$

$$\rho_l = \frac{x_l}{V_m} = -\left(\frac{\partial\omega_m^l}{\partial\mu}\right) \tag{F.23}$$

$$\chi_s = \left(\frac{\partial\rho_s}{\partial\mu}\right) = -\left(\frac{\partial^2\omega_m^s}{\partial\mu^2}\right) \tag{F.24}$$

$$\chi_l = \left(\frac{\partial\rho_l}{\partial\mu}\right) = -\left(\frac{\partial^2\omega_m^l}{\partial\mu^2}\right) \tag{F.25}$$

where ρ and χ are functions of chemical potential μ. Since the absolute reference (*i.e.* the "zero") of the chemical potential is not uniquely defined (unlike temperature which has an absolute value proportional to the kinetic energy), there does not exist a value for μ

which is equivalent to the temperature T_β corresponding to the phase change. However, it is possible to find a range of chemical potential that is associated to the phase change, *i.e.* the chemical potential difference. For this, lets start from a reference value μ_{eq} and look for a value of μ at which the composition of the liquid phase is equal to the reference composition of the solid phase:

$$\rho_l(\mu) = \rho_s(\mu_{eq}) \tag{F.26}$$

ρ_l can expressed by the Taylor series expansion around the value μ_{eq} as:

$$\begin{aligned} \rho_l(\mu) &= \rho_l(\mu_{eq}) + \left(\frac{\partial \rho_s}{\partial \mu}\right)_{\mu_{eq}} (\mu - \mu_{eq}) && \text{(F.27)} \\ &= \rho_l^{eq} + \chi_l^{eq}(\mu - \mu_{eq}) && \text{(F.28)} \end{aligned}$$

Substitution of Eq. F.28 for ρ_l in Eq. F.26 gives:

$$(\mu_{eq} - \mu) = \mu^* = \frac{(\rho_l^{eq} - \rho_s^{eq})}{\chi_l^{eq}} = \frac{(x_l^{eq} - x_s^{eq})}{V_m \chi_l^{eq}} \tag{F.29}$$

A dimensionless chemical potential u for the difference $(\mu - \mu_{eq})$ (*i.e.* the chemical potential of the phase and the equilibrium chemical potential value) can be defined as:

$$u = \frac{(\mu - \mu_{eq})}{\mu^*} = \frac{(\mu - \mu_{eq}) V_m \chi_l^{eq}}{x_l - x_s} \tag{F.30}$$

The derivatives Eqs. 4.35, F.20 and F.21 can be re-written for the grand potential density expressed as a function of the intensive variables and the phase field order parameter (Eq. 4.33) in terms of ρ and χ as:

$$\begin{aligned} \frac{\partial \omega_m}{\partial \mu} &= -\rho_m(\mu, T, \phi) = -\left[p(\phi)\rho_s + (1 - p(\phi))\rho_l\right] && \text{(F.31)} \\ \frac{\partial^2 \omega_m}{\partial \mu^2} &= -\left[p(\phi)\frac{\partial \rho_s}{\partial \mu} + (1 - p(\phi))\frac{\partial \rho_l}{\partial \mu}\right] && \text{(F.32)} \\ &= \chi(\mu, T, \phi) = -\left[p(\phi)\chi_s + (1 - p(\phi))\chi_l\right] && \text{(F.33)} \\ \frac{\partial^2 \omega_m}{\partial \mu \partial \phi} &= -\frac{\partial \rho_m}{\partial \phi} = -p'(\phi)\left[\rho_s - \rho_l\right] && \text{(F.34)} \end{aligned}$$

Non-dimensionalization of the evolution equation for μ and defining the characteristic time for diffusion

The substitution of Eqs. F.33 and F.34 in Eq. 4.66 for the evolution μ gives:

$$-\chi\frac{d\mu}{dt} = -\nabla\left(\frac{M_{xx}}{T}\nabla\mu\right) + p'(\phi)\left[\rho_s - \rho_l\right]\frac{\partial\phi}{\partial t} \tag{F.35}$$

Close to equilibrium, ρ_l is given by Eq. F.28. Similarly, $\rho_s = \rho_s^{eq} + \chi_s^{eq}(\mu - \mu_{eq})$. A quantity $\Delta\rho_{eq} = \rho_l^{eq} - \rho_s^{eq}$ is defined, using which the difference $\rho_s - \rho_l$ can be expressed as:

$$\begin{aligned}
\rho_s - \rho_l &= (\rho_s^{eq} - \rho_l^{eq}) + (\mu - \mu_{eq})\left[\chi_s^{eq} - \chi_l^{eq}\right] && \text{(F.36)}\\
&= -\Delta\rho_{eq} - (\mu_{eq} - \mu)\left[\chi_l^{eq} - \chi_s^{eq}\right] && \text{(F.37)}\\
&= -\Delta\rho_{eq}\left[1 + u\left(1 - \frac{\chi_s^{eq}}{\chi_l^{eq}}\right)\right] && \text{(F.38)}
\end{aligned}$$

Similarly, the μ in the evolution equation corresponds to the difference $(\mu - \mu_{eq})$, which can be written as $u\Delta\rho_{eq}/\chi_l^{eq}$. Substitution of $(\mu - \mu_{eq})$ and Eq. F.38 for $\rho_s - \rho_l$, the Eq. F.35 modifies as:

$$\begin{aligned}
-\frac{\chi\Delta\rho_{eq}}{\chi_l^{eq}}\frac{du}{dt} &= -\Delta\rho_{eq}\left[\nabla\left(\frac{M_{xx}}{\chi_l^{eq}T}\nabla u\right) + p'(\phi)\left[1 + u\left(1 - \frac{\chi_s^{eq}}{\chi_l^{eq}}\right)\right]\frac{\partial\phi}{\partial t}\right] && \text{(F.39)}\\
\left(\frac{\chi}{\chi_l^{eq}}\right)\dot{u} &= \nabla\left(\frac{M_{xx}}{\chi_l^{eq}T}\nabla u\right) + p'(\phi)\left[1 + u\left(1 - \frac{\chi_s^{eq}}{\chi_l^{eq}}\right)\right]\frac{\partial\phi}{\partial t} && \text{(F.40)}
\end{aligned}$$

With the dimensionless variables z^*, M_{xx}^* and t^*, the above equation is non-dimensionalized to give:

$$\frac{du}{dt^*} = \left(\frac{M_0\tau}{\chi TL^2}\right)\frac{\partial}{\partial z^*}(M_{xx}^*\frac{\partial u}{\partial z^*}) + p'(\phi)\left[1 + u\left(1 - \frac{\chi_s^{eq}}{\chi_l^{eq}}\right)\right]\frac{\partial\phi}{\partial t^*} \tag{F.41}$$

where $\frac{M_0\tau}{\chi TL^2}$ is set to 1. Hence the characteristic diffusion time τ is expressed as:

$$\tau = \frac{\chi TL^2}{M_0} = \frac{L^2}{D_x} \tag{F.42}$$

where $D_x = M_0/\chi T$ and χ is given by Eq. F.33.

Non-dimensionalization of the evolution equation for ϕ and defining its characteristic time

With the characteristic time for ϕ defined as per Eq. F.12, Eq. 4.67 is re-written in terms of grand potential densities as:

$$\frac{d\phi}{dt} = \left(\frac{a\kappa_\phi^2}{\tau_\phi}\right)\nabla^2\phi - \left(\frac{1}{\tau_\phi}\right) f'_{dw}(\phi) - \left(\frac{a\left(\omega_m^s - \omega_m^l\right)}{\tau_\phi}\right) p'(\phi) \tag{F.43}$$

For an interface close to equilibrium, $\omega_m^s - \omega_m^l$ can be written from the Taylor series expansions as :

$$\begin{aligned}
\omega_m^s &= \omega_m^s(\mu_{eq}) + \left(\frac{\partial \omega_s}{\partial \mu}\right)_{\mu_{eq}} (\mu - \mu_{eq}) = \omega_m^s(\mu_{eq}) - \rho_s^{eq}(\mu - \mu_{eq}) \\
\omega_m^l &= \omega_m^l(\mu_{eq}) + \left(\frac{\partial \omega_l}{\partial \mu}\right)_{\mu_{eq}} (\mu - \mu_{eq}) = \omega_m^l(\mu_{eq}) - \rho_l^{eq}(\mu - \mu_{eq}) \\
\omega_m^s - \omega_m^l &= (\mu - \mu_{eq})\left[\rho_l^{eq} - \rho_s^{eq}\right] = \frac{u(\Delta\rho_{eq})^2}{\chi_l T}
\end{aligned}$$

Substitution of the above expression for $\omega_m^s - \omega_m^l$ in Eq. F.43:

$$\frac{d\phi}{dt} = \underbrace{\left(\frac{a\kappa_\phi^2}{\tau_\phi}\right)}_{=D_\phi}\nabla^2\phi - \left(\frac{1}{\tau_\phi}\right) f'_{dw}(\phi) - \left(\frac{au(\Delta\rho_{eq})^2}{\chi_l \tau_\phi}\right) p'(\phi) \tag{F.44}$$

Non-dimensionalization of the above equation and re-substitution for τ_ϕ gives :

$$\frac{d\phi}{dt^*} = \tau\left[\left(\frac{M_\phi \kappa_\phi^2}{TL^2}\right)\frac{d^2\phi}{dz^{*2}} - \left(\frac{M_\phi}{Ta}\right) f'_{dw}(\phi) - \left(\frac{M_\phi(\Delta\rho_{eq})^2}{\chi_l T}u\right) p'(\phi)\right] \tag{F.45}$$

with:

$$\frac{1}{\tau_3} = \frac{M_\phi \Delta\rho_{eq}^2 u}{\chi_l T} \tag{F.46}$$

and u is of the order of magnitude equal to 1. With the relations for τ, τ_ϕ and τ_3 known, Eqs. F.42, F.12 and F.46 can be substituted in the relations given by Eqs. 4.78 and 4.79,

with t_{diff} defined by Eq. 4.76 to obtain the inequalities for the mobility coefficient M_ϕ as:

$$\frac{aM_0}{\chi L^2} \ll M_\phi \ll \frac{aM_0}{\delta_\beta^2 \chi} \tag{F.47}$$

$$\frac{M_0 \chi_l}{\chi (\Delta\rho_{eq})^2 L^2} \ll M_\phi \ll \frac{M_0 \chi_l}{\chi (\Delta\rho_{eq})^2 \delta_\beta^2} \tag{F.48}$$

From the above two approaches of non-dimensionalization, if the inequality conditions for the characteristic diffusion times τ (*i.e.* Eqs. F.18 and F.47) and τ_3 (Eqs. F.19 and F.48 respectively) are compared, the order of magnitudes for χ and $\Delta\rho_{eq}$ can be obtained as:

$$\chi = \frac{\Omega_0}{\mu_0^2 V_m} \tag{F.49}$$

$$\Delta\rho_{eq} = (\chi_l \Delta\Omega_0)^{1/2} \tag{F.50}$$

where χ_l has the same order of magnitude as Eq. F.49.

It is evident that the two non-dimensionalization approaches can be made equivalent by an appropriate choice of $\Delta\Omega_0$. However, the constraint lies in making this appropriate choice of $\Delta\Omega_0$ which is an external parameter related to the choice of initial condition for the system (as mentioned in Section 4.3.2.2.2 of Chapter 4), that approaches to zero as the system tends to a state of equilibrium.

If the discussion in the Section 4.3.2.2.2 is recalled, based on the choice of order of magnitude for $\Delta\Omega_0$ as 10^3 and 10^{-1} for the two initial conditions (corresponding to Section 4.5.1.4.1 and Section 4.5.1.4.3, respectively for the binary U-Zr system), the upper and lower bounds for M_ϕ evaluated from Eqs. F.18 and F.19 were obtained as:

$$6.26 \times 10^{-8}\ J^{-1}K^1s^{-1}m^3 \ll M_\phi \ll 1.08 \times 10^{-5}\ J^{-1}K^1s^{-1}m^3 \tag{F.51}$$

$$1.18 \times 10^{-6}\ J^{-1}K^1s^{-1}m^3 \ll M_\phi \ll 6.80 \times 10^{-2}\ J^{-1}K^1s^{-1}m^3 \tag{F.52}$$

The large variation in the acceptable bounds for M_ϕ posed great difficulty in choosing an appropriate value of M_ϕ, making it dependent on the choice of initial state of the system. On the contrary, if the alternate non-dimensionalization approach is followed, since the value of $\Delta\rho_{eq}$ is independent of the choice of initial state, the bounds on M_ϕ value were evaluated to be the same, irrespective of the initial condition posed on the system. Furthermore,

for the two non-dimensionalization approaches to be equivalent, the appropriate choice of $\Delta\Omega_0$ corresponds to an order of magnitude of 2.7×10^{-1}, which is very small compared to the choice of $\Delta\Omega_0 = 10^3$ which was made for the first non-dimensionalization approach (for the initial system condition corresponding to Section 4.5.1.4.1).

Appendix G

Numerical discretization of the evolution equations

This appendix presents the 1-D numerical discretization of the coupled system of evolution equations that have been derived for the phase-filed model developed in Chapter 4. For the spatial discretization of the evolution equations, a finite difference scheme has been adopted, which has been taken from the discretization scheme described by Appendix B of [44]. The temporal discretization of the system of equations has been achieved by using a theta scheme.

Section G.1 presents the temporal discretization of the evolution equations that have been obtained by making use of the theta scheme, which is followed by a discussion on the conditions for the numerical stability of the Euler explicit time scheme in Section G.2.

G.1 The theta scheme for temporal discretization of the evolution equations in μ and ϕ under isothermal conditions

G.1.1 Evolution equation for ϕ

For μ value evaluated at time $t = t_n$, the ϕ evolution equation is written for 1-D situation from Eq. 4.67 as:

$$\frac{\partial \phi}{\partial t} = A\frac{\partial^2 \phi}{\partial z^2}\underbrace{-C\phi^4 + 2(C-B)\phi^3 + (3B-C)\phi^2 - B\phi}_{=H(\phi)} \tag{G.1}$$

By performing the Taylor series expansion, the source term represented by $H(\phi)$ in the above equation can be linearized as:

$$\begin{aligned} H = &\underbrace{\left[3C\phi_i^{*4} + (4B-4C)\phi_i^{*3} + (C-3B)\phi_i^{*2}\right]}_{=(D)} \\ &+ \underbrace{\left[-B + (6B-2C)\phi_i^{*} + (6C-6B)\phi_i^{*2} - 4C\phi_i^{*3}\right]}_{=(E)}\phi_i \end{aligned} \tag{G.2}$$

Thus, Eq. G.1 has the final form:

$$\frac{\partial \phi}{\partial t} = A\frac{\partial^2 \phi}{\partial z^2} + E\phi + D \tag{G.3}$$

Taking the term corresponding to coefficient D as a constant, *i.e.* $D^n = D^{n+1}$, the above equation is discretized in time using theta-scheme:

$$\frac{\phi^{n+1} - \phi^n}{\Delta t} = \theta\left[A\frac{\partial^2 \phi^n}{\partial z^2} + E\phi^n + D^n\right] + (1-\theta)\left[A\frac{\partial^2 \phi^{n+1}}{\partial z^2} + E\phi^{n+1} + D^{n+1}\right] \tag{G.4}$$

Upon regrouping the like terms together, the final form the equation is given as:

$$\left[1 - \Delta t(1-\theta)E - \Delta t(1-\theta)A\nabla^2\right]\phi^{n+1} = \left[1 + \theta\Delta tE + \theta\Delta tA\nabla^2\right]\phi^n + D\Delta t \tag{G.5}$$

G.1.2 Evolution equation for μ

The evolution equation in μ can be recalled from Eq. 4.66 as:

$$\left(\frac{\partial^2\Omega_m}{\partial\mu^2}\right)\frac{\partial\mu}{\partial t} = -\frac{V_m}{T}\nabla(M_{xx}\nabla\mu) - \left(\frac{\partial^2\Omega_m}{\partial\mu\partial\phi}\right)\frac{\partial\phi}{\partial t} \tag{G.6}$$

where M_{xx} is calculated for μ and ϕ values at $t = t_n$. Let us assign:

$$\left(\frac{\partial^2\Omega_m}{\partial\mu^2}\right) = A_1 \tag{G.7}$$

$$-\frac{V_m}{T} = A_2 \tag{G.8}$$

$$-\left(\frac{\partial^2\Omega_m}{\partial\mu\partial\phi}\right) = A_3 \tag{G.9}$$

then, Eq. G.6 can be re-written as:

$$A_1\frac{\partial\mu}{\partial t} = A_2\nabla(M_{xx}\nabla\mu) + A_3\frac{\partial\phi}{\partial t} \tag{G.10}$$

where $\dot{\phi_i}$ is treated as a constant, calculated by :

$$\frac{\partial\phi}{\partial t} = \frac{\phi_i^{n+1} - \phi_i^n}{\Delta t} \tag{G.11}$$

The discretization of Eq. G.10 in time by using the theta scheme gives us:

$$\begin{aligned} A_1\left[\frac{\mu^{n+1}-\mu^n}{\Delta t}\right] = \theta&\left[A_2\nabla(M_{xx}\nabla\mu^n) + A_3\frac{\partial\phi}{\partial t}\right] \\ &+ (1-\theta)\left[A_2\nabla(M_{xx}\nabla\mu^{n+1}) + A_3\frac{\partial\phi}{\partial t}\right] \end{aligned} \tag{G.12}$$

which, upon regrouping like terms together gives the final form:

$$\left[1 - \frac{A_2(1-\theta)\Delta t}{A_1}\nabla M_{xx}\nabla\right]\mu^{n+1} = \left[1 + \frac{A_2\theta\Delta t}{A_1}\nabla M_{xx}\nabla\right]\mu^n + \frac{A_3}{A_1}\Delta t\frac{\partial\phi}{\partial t} \tag{G.13}$$

Eqs. G.5 and G.13 are of the form $[\mathcal{A}]\,\vec{x} = \vec{b}$, which can be solved for the variable of interest (*i.e.* ϕ^{n+1} and μ^{n+1} for for Eqs. G.5 and G.13 respectively) by an inversion of the matrix $[\mathcal{A}]$ (represented by the respective expressions on the L.H.S. of these

equations). These equations represent a generalized form for discretization of the evolution equations, which can be reduced to the Implicit as well as the Explicit by choosing the appropriate value of θ:

$$\theta = \begin{cases} 0 & \text{implicit scheme} \\ 1 & \text{explicit scheme} \end{cases} \tag{G.14}$$

By substituting $\theta = 1$ in Eqs. G.5 and G.13, the discretized form of the evolution equations for the explicit scheme can be obtained as:

$$\phi^{n+1} = \left[1 + E\Delta t - \Delta t A \nabla^2\right] \phi^n + D\Delta t \tag{G.15}$$

$$\mu^{n+1} = \left[1 + \frac{A_2 \Delta t}{A_1} \nabla M_{xx} \nabla\right] \mu^n + \frac{A_3}{A_1} \Delta t \dot{\phi} \tag{G.16}$$

It should be noted that for the discretized equations Eqs. G.5 and G.13 obtained by substituting $\theta = 0$, since the terms D and M_{xx} (for Eqs. G.5 and G.13 respectively) the variation is not considered (*i.e.* they are calculated for $t = t_n$), the final discretized equations represent a semi-implicit scheme.

G.2 Criterion for the stability of the Explicit discretization scheme: the CFL condition

The stability of the explicit numerical scheme applied for solving the evolution equations, depends on an appropriate choice of the time-step and the spatial mesh size value. The following sections describe the steps to be followed for obtaining the maximum bound values for the choice of time-step value, to solve the discretized evolution equations for the case of a non-linear source term.

G.2.1 CFL condition for the ϕ evolution equation

The evolution equation for ϕ can be recalled from Eq. 4.67 as:

$$\frac{\partial \phi}{\partial t} = \underbrace{\left(\frac{M_\phi \kappa_\phi^2}{T}\right) \nabla^2 \phi}_{I} - \underbrace{\left(\frac{M_\phi}{aT}\right) f'_{dw}(\phi)}_{II} - \underbrace{\left(\frac{M_\phi \left(\Omega_m^s - \Omega_m^l\right)}{V_m T}\right) p'(\phi)}_{III} \tag{G.17}$$

Where :

$$f'_{dw}(\phi) = 0.5\left[\phi(1-\phi)(1-2\phi)\right] \quad \text{(G.18)}$$

$$= 0.5\phi - 1.5\phi^2 + \phi^3 \quad \text{(G.19)}$$

$$p'(\phi) = 30\phi^2(1-\phi)^2 \quad \text{(G.20)}$$

$$= 30\phi^2 - 60\phi^3 + 30\phi^4 \quad \text{(G.21)}$$

Eq. G.17 can be written as :

$$\frac{\partial\phi}{\partial t} = A\frac{\partial^2\phi}{\partial z^2} - Bf'_{dw}(\phi) - Cp'(\phi) \quad \text{(G.22)}$$

Lets assume:

$$A = \frac{M_\phi \kappa_\phi^2}{T} \quad \text{(G.23)}$$

$$B = \frac{M_\phi}{aT} \quad \text{(G.24)}$$

$$C = \frac{M_\phi}{V_m T}\left[\Omega_m^s - \Omega_m^l\right] \quad \text{(G.25)}$$

Case 1: When in a bulk region (*i.e.* a single phase, with $\phi = 0$ or 1), the terms II and III are zero beacuse $f'_{dw}(\phi) = 0$ and $p'(\phi) = 0$ for $\phi = 0, 1$. Hence, Eq. G.22 reduces to a simple diffusion equation:

$$\frac{\partial\phi}{\partial t} = A\frac{\partial^2\phi}{\partial z^2} \quad \text{(G.26)}$$

The solution to the above equation by the Euler Explicit method requires discretization of the equation in space and time. For this scheme, the numerical stability analysis of the scheme is given by the **Courant-Friedrichs-Lewy (or CFL) condition** as :

$$\Delta t \leq \frac{1}{\left[\frac{2A}{(\Delta z)^2}\right]} \quad \text{(G.27)}$$

Case 2: When inside the interface region, at equilibrium the term III is zero due to the condition $\Omega_m^s = \Omega_m^l$. With the presence of the interface, Eq. G.22 obtains the form :

$$\frac{\partial \phi}{\partial t} = A\frac{\partial^2 \phi}{\partial z^2} - \underbrace{Bf'_{dw}(\phi)}_{=H(\phi)} \tag{G.28}$$

Substitution of $f'_{dw}(\phi)$ in the above equation, the second term needs to be linearized in order to obtain the condition for numerical stability.

The source term linearization can be done by adopting Taylor series expansion of $H(\phi)$ *(Note: for the sake of simplicity, in the equations,* ϕ_i^n *is denoted by* ϕ_i *and* $(\phi_i^n)^*$ *by* ϕ_i^**)*:

$$H = H^* + \left(\frac{dH}{d\phi}\right)^* (\phi_i - \phi_i^*) \tag{G.29}$$

For the present case:

$$H(\phi) = -Bf'_{dw}(\phi) = -0.5B\left[\phi(1-\phi)(1-2\phi)\right] \tag{G.30}$$

$$\frac{dH}{d\phi} = -Bf''_{dw}(\phi) = -0.5B\left[1 - 6\phi + 6\phi^2\right] \tag{G.31}$$

$$\left(\frac{dH}{d\phi}\right)^* (\phi_i - \phi_i^*) = -0.5B\left[(1 - 6\phi_i^* + 6\phi_i^{*2})\phi_i - (\phi_i^* - 6\phi_i^{*2} + 6\phi_i^{*3})\right] \tag{G.32}$$

Thus, $H(\phi)$ can be expressed as:

$$\begin{aligned} H &= -0.5B[\phi_i^* - 3\phi_i^{*2} + 2\phi_i^{*3}] - 0.5B[(1 - 6\phi_i^* + 6\phi_i^{*2})\phi_i \\ &\quad - (\phi_i^* - 6\phi_i^{*2} + 6\phi_i^{*3})] \\ &= \underbrace{[-0.5B(3\phi_i^{*2} - 4\phi_i^{*3})]}_{=D} + \underbrace{[-0.5B(1 - 6\phi_i^* + 6\phi_i^{*2})]}_{=E}\phi_i \\ &= D + E\phi_i \end{aligned} \tag{G.33}$$

Upon the temporal discretization of Eq. G.28 by using the theta scheme, the CFL condition can be obtained by regrouping like terms together as:

$$\Delta t \leq \frac{1}{\left[\frac{2A}{(\Delta z)^2} - E\right]} \tag{G.34}$$

Case 3: For a point inside the interface, when the condition of thermodynamic

equilibrium is not achieved, all the terms of the Eq. G.17 play a role. Rewriting the equation:

$$\frac{\partial \phi}{\partial t} = A\frac{\partial^2 \phi}{\partial z^2} \underbrace{-Bf'_{dw}(\phi) - Cp'(\phi)}_{=H(\phi)} \tag{G.35}$$

$$= A\frac{\partial^2 \phi}{\partial z^2} + H(\phi) \tag{G.36}$$

In order to obtain the CFL condition for Eq. G.36, the source term $H(\phi)$ has to be linearized :

$$H(\phi) = -Bf'_{dw}(\phi) - Cp'(\phi) \tag{G.37}$$

$$\frac{dH}{d\phi} = -Bf''_{dw}(\phi) - Cp''(\phi) \tag{G.38}$$

$$H^* = -Bf'_{dw}(\phi_i^*) - Cp'(\phi_i^*) \tag{G.39}$$

$$\left(\frac{dH}{d\phi}\right)^* (\phi_i - \phi_i^*) = \left[-Bf''_{dw}(\phi_i^*) - Cp''(\phi_i^*)\right](\phi_i - \phi_i^*) \tag{G.40}$$

The above relations can be substituted in Eq. G.29 to give:

$$\begin{aligned} H &= \underbrace{H^* - \left(\frac{dH}{d\phi}\right)^* \phi_i^*}_{=(D)} + \underbrace{\left(\frac{dH}{d\phi}\right)^*}_{=(E)} \phi_i \\ &= \underbrace{\left[-Bf'_{dw}(\phi_i^*) - Cp'(\phi_i^*) + \left(Bf''_{dw}(\phi_i^*) + Cp''(\phi_i^*)\right)\phi_i^*\right]}_{=D} \\ &+ \underbrace{\left[-Bf''_{dw}(\phi_i^*) - Cp''(\phi_i^*)\right]}_{=E} \phi_i \\ &= D + E\phi_i \end{aligned} \tag{G.41}$$

where D and E are constant values calculated at the value of ϕ obtained from the previous iteration. Eq. G.36 can be discretized by using Finite Differences method:

$$\frac{\phi_i^{n+1} - \phi_i^n}{\Delta t} = A\left[\frac{\phi_{i+1}^n - 2\phi_i^n + \phi_{i-1}^n}{(\Delta z)^2}\right] + H(\phi_i^n) \tag{G.42}$$

$$= A\left[\frac{\phi_{i+1}^n - 2\phi_i^n + \phi_{i-1}^n}{(\Delta z)^2}\right] + D + E\phi_i^n \tag{G.43}$$

Upon regrouping the like terms together we obtain:

$$\phi_i^{n+1} = \underbrace{\left(\frac{A\Delta t}{(\Delta z)^2}\right)\phi_{i+1}}_{=a_{i+1}\phi_{i+1}} + \underbrace{\left(E\Delta t - \frac{2A\Delta t}{(\Delta z)^2} + 1\right)\phi_i}_{a_i\phi_i} + \underbrace{\left(\frac{A\Delta t}{(\Delta z)^2}\right)\phi_{i-1}}_{a_{i-1}\phi_{i-1}} + D\Delta t \tag{G.44}$$

From the above equation, the CFL condition can be calculated as:

$$E\Delta t - \frac{2A\Delta t}{(\Delta z)^2} + 1 \geq 0 \tag{G.45}$$

$$\Delta t \left[\frac{2A}{(\Delta z)^2} - E\right] \leq 1 \tag{G.46}$$

$$\Delta t \leq \frac{1}{\left[\frac{2A}{(\Delta z)^2} - E\right]} \tag{G.47}$$

At this point, it should be noted that the linearization of the source term carried out for the cases 2 and 3 may or may not lead to convergence of the Explicit scheme. The reason for this uncertainty lies in the fact that the coefficient of the linearized source function (*i.e.* value of E) must follow the condition $E \leq 0$ [107]. To be consistent with the condition, an alternative approach can be followed, wherein the source H is split into two parts based on the signs of the coefficients of ϕ. Out of these parts, the part with all positive coefficients of ϕ is kept as a constant at the value of previous iteration (*i.e.* at ϕ_i^*) and the second part (with negative coefficients) is linearized using Eq. G.29.

Whether this condition is followed at all times or not, depends on the sign of the value of E. For the systems under consideration in Chapter 4, based on the input values for the model parameters and the initial condition, it was observed that the order of magnitude for the coefficients depicted by Eqs. G.24 and G.25 have a huge difference, thus making the third term of the equation dominates the evolution of ϕ. In addition to it, from the initialization of the system, the value $\Omega_m^s - \Omega_m^l$ when plotted against spatial profile of μ (at $t = 0s$), showed an inversion of sign within the interface region (depicted by Figure G.1 for the case of binary U-Zr system), making it even more difficult to compute the CFL condition.

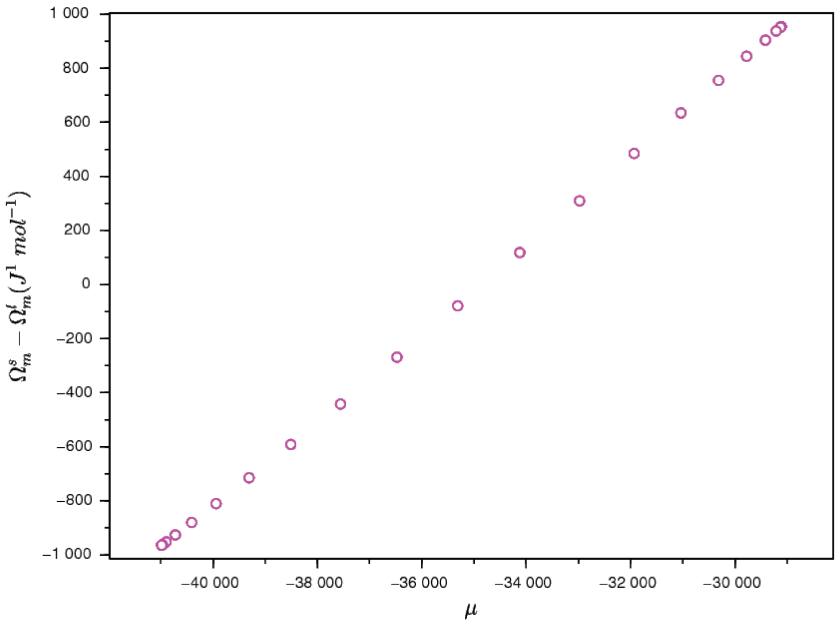

FIGURE G.1: Variation of $\Omega_m^s - \Omega_m^l$ with μ for the binary U-Zr system at $T = 1800$ K, evaluated at $t = 0$ s.

As a result, the third term of the ϕ evolution equation, which is otherwise 0 in the homogeneous phases, undergoes a change in the sign (shown by Figure G.2).

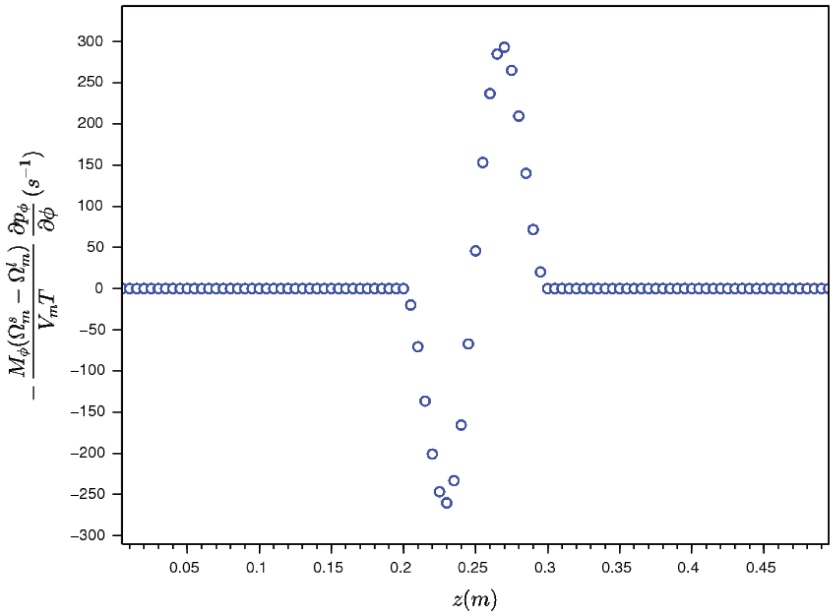

FIGURE G.2: Variation of $-\frac{M_\phi}{V_m T}\left[\Omega_m^s - \Omega_m^l\right] p'(\phi)$ with z for the binary U-Zr system at $T = 1800$ K, evaluated at $t = 0s$.

In such a case, at the end of each time-step, CFL condition is to be calculated based on the signs of the coefficients in Eq. G.37. Eq. G.37 is recalled at this point:

$$H(\phi) = -Bf'_{dw}(\phi) - Cp'(\phi) = [-30C]\,\phi^4 + [60C - B]\,\phi^3 + [1.5B - 30C]\,\phi^2 + [-0.5B]\,\phi \tag{G.48}$$

G.2.1.1 Case: $C < 0$

The expression for the non-linear term is re-written by grouping together the terms which have an odd valued exponents, which need to be linearized:

$$H(\phi) = \left[-30C\phi_i^{*4} + (1.5B - 30C)\phi_i^{*2}\right] + \underbrace{\left[(60C - B)\phi^3 - 0.5B\phi\right]}_{H_1(\phi)} \tag{G.49}$$

$$\begin{aligned} H_1(\phi) &= (60C - B)\phi^3 - 0.5B\phi \\ &= \left((60C - B)\phi_i^{*3} - 0.5B\phi_i^*\right) + \left(3(60C - B)\phi_i^{*2} - 0.5B\right)(\phi_i - \phi_i^*) \\ &= -2(60C - B)\phi_i^{*3} + \underbrace{\left(3(60C - B)\phi_i^{*2} - 0.5B\right)}_{<0}\phi_i \end{aligned} \tag{G.50}$$

The linearized source H is finally obtained as :

$$H = \left[-30C\phi_i^{*4} - 2(60C - B)\phi_i^{*3} + (1.5B - 30C)\phi_i^{*2}\right] + \left[3(60C - B)\phi_i^{*2} - 0.5B\right]\phi_i \tag{G.51}$$

Discretization of Eq. G.36 :

$$\begin{aligned} \frac{\phi_i^{n+1} - \phi_i^n}{\Delta t} &= A\left[\frac{\phi_{i+1}^n - 2\phi_i^n + \phi_{i-1}^n}{(\Delta z)^2}\right] + H(\phi_i^n) \\ &= A\left[\frac{\phi_{i+1}^n - 2\phi_i^n + \phi_{i-1}^n}{(\Delta z)^2}\right] + \left[3(60C - B)\phi_i^{*2} - 0.5B\right]\phi_i^n \\ &\quad + \left[-30C\phi_i^{*4} - 2(60C - B)\phi_i^{*3} + (1.5B - 30C)\phi_i^{*2}\right] \end{aligned} \tag{G.52}$$

Regrouping like terms together :

$$\begin{aligned} \phi_i^{n+1} = &\underbrace{\left[\frac{A\Delta t}{(\Delta z)^2}\right]\phi_{i+1}}_{=a_{i+1}\phi_{i+1}} + \underbrace{\left[(3(60C - B)\phi_i^{*2} - 0.5B)\Delta t - \frac{2A\Delta t}{(\Delta z)^2} + 1\right]\phi_i}_{a_i\phi_i} \\ &+ \underbrace{\left[\frac{A\Delta t}{(\Delta z)^2}\right]\phi_{i-1}}_{a_{i-1}\phi_{i-1}} + \underbrace{\left[-30C\phi_i^{*4} - 2(60C - B)\phi_i^{*3} + (1.5B - 30C)\phi_i^{*2}\right]\Delta t}_{constant} \end{aligned} \tag{G.53}$$

From the above equation, the CFL condition can be calculated as:

$$(3(60C - B)\phi_i^{*2} - 0.5B)\Delta t - \frac{2A\Delta t}{(\Delta z)^2} + 1 \geq 0 \tag{G.54}$$

$$\Delta t\left[\frac{2A}{(\Delta z)^2} - (3(60C - B)\phi_i^{*2} - 0.5B)\right] \leq 1 \tag{G.55}$$

$$\Delta t \leq \frac{1}{\left[\frac{2A}{(\Delta z)^2} + \left[0.5B - 3(60C - B)\phi_i^{*2}\right]\right]} \tag{G.56}$$

G.2.1.2 Case: $C = 0$

The expression for the non-linear term is re-written by grouping together the terms which have an odd valued exponents, which need to be linearized:

$$\begin{aligned} H(\phi) &= -Bf'_{dw}(\phi) && \text{(G.57)} \\ &= 1.5B\phi^2 + \underbrace{\left[-0.5B\phi - B\phi^3\right]}_{H_1(\phi)} && \text{(G.58)} \\ H_1(\phi) &= (-0.5B\phi_i^* - B\phi_i^{*3}) + (-0.5B - 3B\phi_i^{*2})(\phi_i - \phi_i^*) && \text{(G.59)} \\ &= 2B\phi_i^{*3} + \underbrace{\left[-3B\phi_i^{*2} - 0.5B\right]}_{<0}\phi_i && \text{(G.60)} \\ \therefore H(\phi) &= \left[1.5B\phi_i^{*2} + 2B\phi_i^{*3}\right] + \left[-3B\phi_i^{*2} - 0.5B\right]\phi_i && \text{(G.61)} \end{aligned}$$

Discretization of Eq. G.36 and rearrangement of like terms together gives :

$$\begin{aligned} \phi_i^{n+1} = &\underbrace{\left[\frac{A\Delta t}{(\Delta z)^2}\right]\phi_{i+1}}_{=a_{i+1}\phi_{i+1}} + \underbrace{\left[-(3B\phi_i^{*2} + 0.5B)\Delta t - \frac{2A\Delta t}{(\Delta z)^2} + 1\right]\phi_i}_{a_i\phi_i} \\ &+ \underbrace{\left[\frac{A\Delta t}{(\Delta z)^2}\right]\phi_{i-1}}_{a_{i-1}\phi_{i-1}} + \underbrace{\left[1.5B\phi_i^{*2} + 2B\phi_i^{*3}\right]\Delta t}_{constant} \end{aligned} \qquad \text{(G.62)}$$

$\therefore$ the CFL condition is given as :

$$\begin{aligned} -(3B\phi_i^{*2} + 0.5B)\Delta t - \frac{2A\Delta t}{(\Delta z)^2} + 1 \geq 0 && \text{(G.63)} \\ \Delta t\left[\frac{2A}{(\Delta z)^2} + (0.5B + 3B\phi_i^{*2})\right] \leq 1 && \text{(G.64)} \\ \Delta t \leq \frac{1}{\left[\frac{2A}{(\Delta z)^2} + \left[0.5B + 3B\phi_i^{*2}\right]\right]} && \text{(G.65)} \end{aligned}$$

G.2.1.3 Case: $C > 0$

The expression for the non-linear term is re-written by grouping together the terms which have an odd valued exponents, which need to be linearized:

$$H(\phi) = \left[1.5B\phi_i^{*2} + 60C\phi_i^{*3}\right] + \underbrace{\left[-0.5B\phi - 30C\phi^2 - B\phi^3 - 30C\phi^4\right]}_{H_1(\phi)} \qquad \text{(G.66)}$$

$$\begin{aligned} H_1(\phi) &= -0.5B\phi - 30C\phi^2 - B\phi^3 - 30C\phi^4 \\ &= \left(-0.5B\phi_i^* - 30C\phi_i^{*2} - B\phi_i^{*3} - 30C\phi_i^{*4}\right) \\ &+ \left(-0.5B - 60C\phi_i^* - 3B\phi_i^{*2} - 120C\phi_i^{*3}\right)(\phi_i - \phi_i^*) \\ &= \left(30C\phi_i^{*2} + 2B\phi_i^{*3} + 90C\phi_i^{*4}\right) + \underbrace{\left(-0.5B - 60C\phi_i^* - 3B\phi_i^{*2} - 120C\phi_i^{*3}\right)}_{<0}\phi_i \end{aligned} \tag{G.67}$$

The linearized source term is obtained as:

$$\begin{aligned} H(\phi) = &\left[(1.5B + 30C)\phi_i^{*2} + (2B + 60C)\phi_i^{*3} + 90C\phi_i^{*4}\right] \\ &+ \left[-0.5B - 60C\phi_i^* - 3B\phi_i^{*2} - 120C\phi_i^{*3}\right]\phi_i \end{aligned} \tag{G.68}$$

Discretization of Eq. G.36:

$$\begin{aligned} \frac{\phi_i^{n+1} - \phi_i^n}{\Delta t} &= A\left[\frac{\phi_{i+1}^n - 2\phi_i^n + \phi_{i-1}^n}{(\Delta z)^2}\right] + H(\phi_i^n) \\ &= A\left[\frac{\phi_{i+1}^n - 2\phi_i^n + \phi_{i-1}^n}{(\Delta z)^2}\right] + \left[-0.5B - 60C\phi_i^* - 3B\phi_i^{*2} - 120C\phi_i^{*3}\right]\phi_i^n \\ &+ \left[(1.5B + 30C)\phi_i^{*2} + (2B + 60C)\phi_i^{*3} + 90C\phi_i^{*4}\right] \end{aligned} \tag{G.69}$$

Upon regrouping the like terms together:

$$\begin{aligned} \phi_i^{n+1} = &\underbrace{\left[\frac{A\Delta t}{(\Delta z)^2}\right]\phi_{i+1}}_{=a_{i+1}\phi_{i+1}} + \underbrace{\left[(-0.5B - 60C\phi_i^* - 3B\phi_i^{*2} - 120C\phi_i^{*3})\Delta t - \frac{2A\Delta t}{(\Delta z)^2} + 1\right]\phi_i}_{a_i\phi_i} \\ &+ \underbrace{\left[\frac{A\Delta t}{(\Delta z)^2}\right]\phi_{i-1}}_{a_{i-1}\phi_{i-1}} + \underbrace{\left[(1.5B + 30C)\phi_i^{*2} + (2B + 60C)\phi_i^{*3} + 90C\phi_i^{*4}\right]\Delta t}_{constant} \end{aligned} \tag{G.70}$$

From the above equation, the CFL condition can be calculated as:

$$(-0.5B - 60C\phi_i^* - 3B\phi_i^{*2} - 120C\phi_i^{*3})\Delta t - \frac{2A\Delta t}{(\Delta z)^2} + 1 \geq 0 \tag{G.71}$$

$$\Delta t\left[\frac{2A}{(\Delta z)^2} - (-0.5B - 60C\phi_i^* - 3B\phi_i^{*2} - 120C\phi_i^{*3})\right] \leq 1 \tag{G.72}$$

$$\Delta t \leq \frac{1}{\left[\frac{2A}{(\Delta z)^2} + \left[0.5B + 60C\phi_i^* + 3B\phi_i^{*2} + 120C\phi_i^{*3}\right]\right]} \tag{G.73}$$

G.2.2 CFL condition for the μ evolution equation

The time evolution of μ under isothermal conditions can be recalled from Eq. 4.66 as:

$$\left(\frac{\partial^2\Omega_m}{\partial\mu^2}\right)\frac{\partial\mu}{\partial t} = -\frac{V_m}{T}\nabla(M_{xx}\nabla\mu) - \left(\frac{\partial^2\Omega_m}{\partial\mu\partial\phi}\right)\frac{\partial\phi}{\partial t} \tag{G.74}$$

$$A_1\frac{\partial\mu}{\partial t} = A_2\nabla(M_{xx}\nabla\mu) + \underbrace{A_3\frac{\partial\phi}{\partial t}}_{=S} \tag{G.75}$$

where:

$$A_1 = \left(\frac{\partial^2\Omega_m}{\partial\mu^2}\right) < 0 \tag{G.76}$$

$$A_2 = -\frac{V_m}{T} < 0 \tag{G.77}$$

$$A_3 = -\left(\frac{\partial^2\Omega_m}{\partial\mu\partial\phi}\right) > 0 \tag{G.78}$$

and M_{xx} (abbreviated as M in further equations) is calculated for values of μ and ϕ at $t = t_n$. Assuming the term including $\frac{\partial\phi}{\partial t}$ to be a constant source term, the discretization of Eq. G.75 gives:

$$\frac{\mu_i^{n+1} - \mu_i^n}{\Delta t} = \frac{A_2}{A_1}\left[\frac{2M^+\mu_{i+1}^n - 2(M^+ + M^-)\mu_i^n + 2M^-\mu_{i-1}^n}{(\Delta z)^2}\right] + \frac{S}{A_1} \tag{G.79}$$

$$\begin{aligned}\mu_i^{n+1} = {} & \underbrace{\left[\frac{A_2\Delta t}{A_1(\Delta z)^2}\left(2M^+\right)\right]\mu_{i+1}^n}_{=a_{i+1}\mu_{i+1}} + \underbrace{\left[1 - \frac{A_2\Delta t}{A_1(\Delta z)^2}2\left(M^+ + M^-\right)\right]\mu_i^n}_{=a_i\mu_i} \\ & + \underbrace{\left[\frac{A_2\Delta t}{A_1(\Delta z)^2}\left(2M^-\right)\right]\mu_{i-1}^n}_{=a_{i-1}\mu_{i-1}} + \underbrace{\left[\frac{S}{A_1}\right]}_{constant}\end{aligned} \tag{G.80}$$

The CFL condition can be obtained from the above equation as:

$$1 - \frac{A_2 \Delta t}{A_1 \left(\Delta z\right)^2} 2 \left(M^+ + M^-\right) \geq 0 \tag{G.81}$$

$$\frac{A_2 \Delta t}{A_1 \left(\Delta z\right)^2} 2 \left(M^+ + M^-\right) \leq 1 \tag{G.82}$$

$$\Delta t \leq \frac{A_1 \left(\Delta z\right)^2}{2 A_2 \left(M^+ + M^-\right)} \tag{G.83}$$

where M^+ and M^- are values of M_{xx} calculated for ϕ^+ and ϕ^- values respectively, with ϕ^+ and ϕ^- defined as:

$$\phi^+ = \frac{\phi^n_{i+1} + \phi^n_i}{2} \tag{G.84}$$

$$\phi^- = \frac{\phi^n_i + \phi^n_{i-1}}{2} \tag{G.85}$$

Appendix H

Résumé

Cette thèse de doctorat s'intéresse à la manière d'assurer une représentation thermodynamiquement consistante du corium en cuve (un mélange à haute température de matériaux fondus du cœur et des structures d'un réacteur nucléaire) dans les modèles couplés de thermohydraulique-thermochimie mis en jeu pour l'étude des Accidents Graves (AG) des Réacteurs refroidis à l'Eau Légère (RELs). En particulier, dans le contexte d'une stratégie de rétention de corium en fond de cuve (« In-Vessel Retention » - IVR), la connaissance du comportement de ce corium et du risque associé de percement "thermique" de la cuve sont des questions de premier ordre.

Le corium en fond de cuve est un système thermodynamique complexe (a minima quaternaire U-O-Zr-Fe) dont la modélisation du comportement transitoire nécessite un couplage de modèles décrivant les principaux phénomènes thermochimiques (ségrégation des phases : solidification à l'interface et lacune de miscibilité à l'état liquide) et thermohydrauliques (convection naturelle et instabilités de Rayleigh-Taylor pour les liquides, conduction dans le solide). Dans ce cadre, un point essentiel est lié aux entrées thermodynamiques et l'utilisation d'une base de données thermodynamiques obtenue par la méthode CALPHAD apparait pertinente pour l'obtention des fermetures et données d'entrée des modèles de thermohydraulique et de thermochimie respectivement. Ces bases de données décrivent des modèles relatifs aux fonctions d'énergie de Gibbs des différentes phases possibles d'un système. Elles peuvent être utilisées pour évaluer les conditions possibles d'équilibre thermodynamique d'un système ainsi que ses propriétés thermodynamiques dans des conditions hors-équilibre.

Dans ce travail, une approche systématique pour l'utilisation exhaustive de ces données CALPHAD dans les modèles couplés a été proposée. Les questions soulevées ont été traitées au travers de l'étude de modèles « maquettes » décrivant une partie des phénomènes relatifs au comportement du corium en cuve à des échelles macroscopique ou mésoscopique.

Dans une première partie, la faisabilité de l'utilisation des données CALPHAD pour un modèle intégral (échelle macroscopique) été testée. En considérant le système ternaire U-O-Zr, ce modèle décrit le processus de solidification en front plan à la frontière d'un bain de corium fondu. Ces modèles thermiques intégrés consistent en des équations de conservation de masse et d'énergie qui nécessitent des entrées liées aux propriétés thermochimiques des matériaux, qui sont étroitement liées aux variables d'état thermodynamique. En conservant une formulation générale des équations de conservation de l'énergie en termes d'enthalpies spécifiques des phases, les fonctions d'énergie de Gibbs d'une base CALPHAD peuvent être utilisées à la fois pour le calcul des conditions d'équilibre local à l'interface liquide/solide (température de changement de phase et composition de la phase solide se formant) mais aussi pour les fermetures des équations de conservation d'énergie (sous la forme de relations enthalpie-température dépendant de la composition). Des résultats numériques obtenus pour divers degrés d'oxydation initiaux du corium ont montré la viabilité d'une telle approche pour garantir une représentation thermodynamique cohérente des systèmes à travers le modèle.

Une seconde partie dans ce travail a été consacrée au développement d'une formulation générale pour des modèles à interface diffuse obtenus par une approche par champ de phase et s'adressant à la simulation de différents processus thermochimiques non-isothermes tels que la solidification ou la ségrégation des phases liquides. Pour cela, un modèle de champ de phase a été développé en adoptant une formulation générale en grand potentiel. Ce choix d'utiliser le grand potentiel est pertinent car les propriétés de volume et d'interface peuvent être ajustées indépendamment dans un tel modèle. Pour le cas de solidification non isotherme, l'incorporation de l'équation de conservation de l'énergie est nécessaire. Les fermetures thermodynamiques du modèle peuvent être obtenues à partir des bases de données CALPHAD. Les fermetures de ce modèle non isotherme ont été étudiées en détail, en particulier les contraintes liées à l'utilisation des données CALPHAD. De plus, l'effet de la « mise à l'échelle » de l'épaisseur d'interface sur

la cinétique du modèle de champ de phase a été étudié. En particulier, les contraintes liées au choix maximum de l'épaisseur d'interface et son impact sur le choix du paramètre de mobilité du champ de phase ont été quantifiés. Des résultats numériques pour les systèmes binaires U-Zr et U-O dans des conditions isothermes ont permis de vérifier cette paramétrisation du modèle.

Bibliography

[1] G.F. Hewitt and J.G. Collier. *Introduction to Nuclear Power, Second Edition.* Taylor & Francis, 2000.

[2] B.R. Sehgal, editor. *Nuclear Safety in Light Water Reactors: Severe Accident Phenomenology.* Academic Press publications, 2012.

[3] *In-Vessel Core Degradation Code Validation Matrix : Report by OECD/NEA Group of Experts.* 2000.

[4] D. Magallon, S. Basu, and M. Corradini. Implications of FARO and KROTOS experiments for FCI issues (FZKA–6475). In *Proc. of OECD workshop on ex-vessel debris coolability*, Germany, 1999.

[5] OECD Research programme on Fuel-Coolant Interaction Steam Explosion Resolution for Nuclear Applications – SERENA, final report [NEA/CSNI/R(2007)11]. Technical report, December, 2006.

[6] R.E. Henry and H.K. Fauske. External cooling of a reactor vessel under severe accident conditions. *Nuclear Engineering and Design*, 139:31–43, 1993.

[7] H. Tuomisto and T. G. Theofanous. A consistent approach to severe accident management. *Nuclear Engineering and Design*, 148, 1994.

[8] T. G. Theofanous, C. Liu, S. Addition, S. Angelini, O. Kymäläinen, and T. Salimassi. In-vessel coolability and retention of a core melt. *Nuclear Engineering and Design*, 169:1–48, 1997.

[9] H. Esmaili and M. Khatib-Rhabar. Analysis of in-vessel retention and ex-vessel fuel coolant interaction for AP-1000.

[10] O. Kymäläinen, H. Tuomisto, and T. G. Theofanous. In-vessel retention of corium at the loviisa plant. *Nuclear Engineering and Design*, 169, 1997.

[11] D.L. Knudson, J.L. Rempe, K.G. Condie, K.Y. Suh, F.-B. Cheung, and S.-B. Kim. Late-phase melt conditions affecting the potential for in-vessel retention in high power reactors. *Nuclear Engineering and Design*, 230, 2004.

[12] J.L. Rempe, D.L. Knudson, K.G. Condie, K.Y. Suh, F.-B. Cheung, and S.-B. Kim. Corium retention for high power reactors by an in-vessel core catcher in combination with external reactor vessel cooling. *Nuclear Engineering and Design*, 230, 2004.

[13] S. Whang, H.S. Park, K. Moriyama, K. Lim, Y.J Cho, and M.H. Kim. Uncertainty analysis of in-vessel retention in a high power reactor during severe accident. *Nuclear Engineering and Design*, 319, 2017.

[14] J. Xing, D. Song, and Y. Wu. HPR1000: Advanced pressurized water reactor with active and passive safety. *Engineering*, 2:79–87, 2016.

[15] V. Maurel. EPR, spearhead of the european nuclear renaissance. *Nuclear Engineering and Design*, 236:147–154, 2006.

[16] S.K. Agrawal, A. Chauhan, and A. Mishra. The VVERs at kudankulam. *Nuclear Science Design*, 236:812–835, 2006.

[17] M. Fischer, O. Herbst, and H. Schmidt. Demonstration of the heat removing capabilities of the EPR core catcher. *Nuclear Engineering and Design*, 235:1189–1200, 2005.

[18] L. Jungjae, K. Jihun, K. Taehoon, S.H. Young, K. Eunho, and C.Y. Ku. Overview of ex-vessel cooling strategies and perspectives. In *Proc. of Transactions of Korean Nuclear Society Spring Meeting*, Jeju, Korea, 2017.

[19] M. Fischer. The core melt stabilization concept of the EPR and its experimental validation. In *Proc. of ICONE-14*, Miami FL, USA, 2006.

[20] F. Fichot, L. Carénini, N. Bakouta, H. Esmaili, L. Humphries, T. Laato, R. Le Tellier, L. Saas, I. Melnikov, P. Pandazis, S. Weber, R.J. Park, A. Filippov, and V. Strizhov. Elaboration of a PIRT for the modelling of in-vessel retention. In *Proc. of ERMSAR-2019*, Prague, Czech Republic, 2019.

[21] T.G. Theofanous, M. Maguire, S. Angelini, and Salmassi T. The first results from the ACOPO experiments. In *Proc. of PSA'96-Int. Topical Meeting on Probabilistic Safety Assessment*, Park City, Utah, 1996.

[22] J. M. Seiler, A. Fouquet, K. Froment, and F. Defoort. Theoretical analysis for corium pool with miscibility gap. *Nuclear Technology*, 141:233–243, 2003.

[23] K. Froment and et al. Physico-chemistry and corium properties for in-vessel retention. In *Proc. of Workshop on In-Vessel Core Debris Retention and Coolability*, Germany, 1998.

[24] P. Hofmann. Reaktions-und schmelzverhalten der lwr-corekomponenten UO2, zircaloy ung stahe wahrend der abschmelzperiod, KFK 2220, juli. 1976.

[25] B. Cheynet and P.-Y. Chevalier. Thermosuit. *Calphad*, 26, 2002.

[26] B. Spindler, B. Tourniaire, and J.M. Seiler. Simulation of MCCI with the TOLBIAC-ICB code based on the phase segregation model. *Nuclear Engineering and Design*, 236, 2006.

[27] R. Le Tellier, L. Saas, and F. Payot. Phenomenological analyses of corium propagation in LWRs : the PROCOR software platform. In *Proc. of ERMSAR-2015*, Marseille, France, 2015.

[28] J.M. Seiler and B. Tourniaire. A phenomenological analysis of melt progression in the lower head of a pressurized water reactor. *Nuclear Engineering and Design*, 268:87–95, 2014.

[29] R. Le Tellier, L. Saas, and S. Bajard. Transient stratification modelling of a corium pool in a LWR vessel lower head. *Nuclear Engineering and Design*, 287:68–77, 2015.

[30] V.G. Asmolov, S.S. Abalin, Yu.A. Veselkin, V.Yu. Vishnevsky, V.V. Vlasov, B.L. Gershman, Yu.G. Degaltsev, Ye.K. Dyakov, J.F. Isaev, A.N. Kiselev, N.P. Kiselev, A.M. Kovalev, A.G. Ol'khovsky, K.V. Pechalin, L.M. Semenov, V.F. Strizhov, T.V. Trushkina, V.S. Uglov, Yu.M. Utkin, V.V. Chudanov, A.E. Aksenova, V.A. Pervichko, and I.M. Khazanivich. RCW post-test analysis results, 2003.

[31] G. Ratel, F. Defoort, K. Froment, B. Tourniaire, and J.M. Seiler. Considerations on mass transfer kinetics for layer inversion and layer oxidation: from MASCA program

to the reactor situation. In *Proc. of MASCA2 Seminar*, Aix-En-Provence, France, 2007.

[32] D.F. Tsurikov, V.F. Strizhov, S.V. Bechta, V.N. Zagriazkin, and N.P. Kiselev. Main results of MASCA-1 and 2 projects, 2007.

[33] F. Fichot and L. Carénini. Some consequences of material interactions for in-vessel melt retention. In *Proc. of ICAPP Conference*, Nice, France, 2015.

[34] L. Carénini and F. Fichot. The impact of transient behavior of corium in the lower head of a reactor vessel for in-vessel melt retention strategies. In *Proc. of ICONE24*, Charlotte North Carolina, 2016.

[35] O. Kymäläinen, H. Tuomisto, H. Hongisto, and T.G. Theofanous. Heat flux distribution from a volumetrically heated pool with high rayleigh number. In *Proc. of 6th Int. Topical Meeting on Nuclear Reactor Thermal Hydraulics, NURETH-6*, Grenoble, France, 1993.

[36] J.M. Bonnet, S. Rouge, and J.M. Seiler. *Large scale experiments for core melt retention: BALI: corium pool thermal hydraulics, SULTAN: boiling under natural convection*. Nuclear Energy Agency of the OECD (NEA), 1994.

[37] B.R. Sehgal, T.N. Dinh, V.A. Bui, J.A. Green, and G. Kolb. SIMECO experiments on in-vessel melt pool formation and heat transfer with and without a metallic layer. In *Proc. of OECD/CSNI Workshop on 'In-Vessel Core Debris Retention and Coolability'*, Garching, Germany, 1998.

[38] V.I. Almjashev, V.S. Granovsky, V.B. Khabensky, S.Yu. Kotova, E.V. Krushinov, A.A. Sulatsky, S.A. Vitol, V.V. Gusarov, F. Fichot, B. Michel, P. Piluso, R. Le Tellier, C. Fischer, M. Le Guennic, and N. Bakouta. Experimental study of transient phenomena in the three-liquid oxidic-metallic corium pool. *Nuclear Engineering and Design*, 332:31–37, 2018.

[39] A. Pivano, P. Piluso, N. Chikhi, J. Delacroix, P Fouquart, and R. Le Tellier. In-vessel retention: Molten stainless steel - corium crust interaction. *submitted to Nuclear Engineering and Design*.

[40] P. Chatelard, N. Reinke, S. Arndt, S. Belon, L. Cantrel, L. Carenini, K. Chevalier-Jabet, F. Cousin, J. Eckel, F. Jacq, C. Marchetto, C. Mun, and L. Piar. ASTEC

V2 severe accident integral code main features, current V2.0 modelling status, perspectives. *Nuclear Engineering and Design*, 272:119–135, 2014.

[41] L. Li, T.W. Kim, Y. Zhang, S.T. Revankar, W. Tian, G.H. Su, and S. Qiu. MELCOR severe accident analysis for a natural circulation small modular reactor. *Progress in Nuclear Energy*, 100:197–208, 2017.

[42] Fauske & Associates Inc. MAAP5 – modular accident analysis program for LWR power plants. In *in : Code Structure and Theory, Vol. 2*, 2008.

[43] L. Carénini, F. Fichot, N. Bakouta, R. Le Tellier, L. Viot, I. Melnikov, P. Pandazis, and A. Filippov. Main outcomes from the IVR code benchmark performed in the IVMR project. In *Proc. of ERMSAR-2019*, Prague, Czech Republic, 2019.

[44] C. Cardon. *Modélisation de la diffusion multi-composants dans un bain de corium diphasique oxyde-métal par une méthode d'interface diffuse, Ph.D. thesis*. Université Paris-Saclay, 2016.

[45] L. Viot, R. Le Tellier, and M. Peybernes. Modelling of the corium crust of a stratified corium pool during severe accidents in light water reactors. *submitted to Nuclear Engineering and Design*.

[46] A. Kroupa. Modelling of phase diagrams and thermodynamic properties using Calphad method – development of thermodynamic databases. *Computational Materials Science*, 66:3–13, 2013.

[47] H.L. Lukas, S.G. Fries, and B. Sundman. *Computational Thermodynamics: The Calphad Method*. Cambridge University Press, 2007.

[48] M. Hillert. The compound energy formalism. *Journal of Alloys and Compounds*, 320:161–176, 2001.

[49] G. Cacciamani. An introduction to the CALPHAD method and the Compound Energy Formalism (CEF). *Tecnologia em Metalurgia, Materiais e Mineração*, 13:16–24, 2016.

[50] B. Sundman, U.R. Kattner, M. Palumbo, and S.G. Fries. OpenCalphad - a free thermodynamic software. *Integrating Materials and Manufacturing Innovation*, 4:1–15, 2015.

[51] S. Bakardjieva, M. Barrachin, S. Bechta, D. Bottomley, L. Brissoneau, B. Cheynet, E. Fischer, C. Journeau, M. Kiselove, L. Mezentseva, P. Piluso, and T. Wiss. Improvement of the european thermodynamic database NUCLEA. *Progress in Nuclear Energy*, 52, 2010.

[52] C. Guéneau, S. Gossé, A. Quaini, N. Dupin, B. Sundman, M. Kurata, T. Besmann, P. Turchi, J. Dumas, E. Corcoran, M. Piro, T. Ogata, R. Hania, B. Lee, Kennedy R., and S. Massara. FUELBASE, TAF-ID databases and OC software : Advanced computational tools to perform thermodynamic calculations on nuclear fuel materials. In *In Proc. of ERMSAR-2015*, 2015.

[53] B. Sundman, X.-G. Lu, and H. Ohtani. The implementation of an algorithm to calculate thermodynamic equilibria for multi-component systems with non-ideal phases in a free software. *Computational Materials Science*, 101:127–137, 2015.

[54] R. Le Tellier, E. Skrzypek, and L. Saas. On the treatment of plane fusion front in lumped parameter thermal models with convection. *Applied Thermal Engineering*, 120, 2017.

[55] M.C. Schneider and C. Beckermann. Effects of simplified enthalpy relations on the prediction of heat transfer during solidification of a lead-tin alloy. *Applied Mathematical Modelling*, 15(11-12):596–605, November 1991.

[56] R. N. Hills and P. H. Roberts. On the motion of a fluid that is incompressible in a generalized sense and its relationship to the boussinesq approximation. *Stability and Applied Analysis of Continuous Media*, 1(3):205–212, 1991.

[57] M. Fukusawa, S. Hayakawa, and M. Saito. Thermal-hydraulic analysis for inversely stratified molten corium in lower vessel. *Journal of Nuclear Science and Technology*, 45:873–888, 2008.

[58] C. Le Guennic, E. Skrzypek, L. Vyskocil, M. Skrzypek, A. Shams, and L. Saas. Analysis of in-vessel corium pool behaviour using CFD tools. In *Prco. of NURETH-17*, Xi'an, China, 2017.

[59] C. Le Guinnec, L. Saas, R. Le Tellier, Y. Wu, M. Guingo, and J. Laviéville. Contribution of CFD studies to IVR assessment. In *Proc. of ERMSAR-2017*, Warsaw, Poland, 2017.

[60] N. Mechitoua, M. Guingo, and P. Montarnal. *"Presentation of the Multi-Phase CFD Solver NEPTUNE_CFD"*. Springer, 2016.

[61] Peybernes. M, R. Le Tellier, L. Saas, and C. Dang. Thermalhydraulic DNS of a thin metallic layer : application to the evaluation of nuclear reactor severe accident mitigation strategy. In *Proc. of ERMSAR-2019*, Czech Republic, Prague, 2019.

[62] J. Rowlinson. Translation of j. d. van der waals : The thermodynamik theory of capillarity under the hypothesis of a continuous variation of density. *Journal of Statistical Physics*, 20, 1978.

[63] V. Ginzburg and L. Landau. On the theory of superconductivity, zh. eksp. teor. fiz. 20 (1950) 1064–1082. In *Translation in Collected papers of L.D. Landau*, Pergamon, Oxford, 1965.

[64] Nikolas Provatas and Ken Elder. *Phase-Field Methods in Materials Science and Engineering*. Wiley-VCH, 1st edition, 2010.

[65] N. Moelans, B. Blanpain, and P. Wollants. An introduction to phase-field modeling in microstructure evolution. *Computer Coupling of Phase Diagrams and Thermochemistry*, 32:268–294, 2008.

[66] I. Singer-Loginova and h.M. Singer. The phase field technique for modeling multiphase materials. *Reports on Progress in Physics*, 71(10):106501, 2008.

[67] M. Plapp. Phase-field modelling of solidification microstructures. *Journal of the Indian Institute of Science*, 96:179–198, 2016.

[68] W.J. Boettinger, J.A. Warren, C. Beckermann, and A. Karma. Phase-field simulation of solidification. *Annual Review of Materials Research*, 23, 2002.

[69] L.Q. Chen. Phase-field models for microstructure evolution. *Annual Review of Materials Research*, 32, 2002.

[70] Y. Jin, Y. Wang, and A. Khachaturyan. Three-dimensional phase field microelasticity theory and modelling of multiple cracks and voids. *Applied Physics Letters*, 2001.

[71] S. Hu and L. Chen. Solute segregation and coherent nucleation and growth near a dislocation — a phase-field model integrating defect and phase microstructures. *Acta Materialia*, 49, 2001.

[72] J. Cahn and J. Hilliard. Spinodal decomposition : A reprise. *Acta Metallurgica*, 19, 1971.

[73] P. Hohenberg and B. Halperin. Theory of dynamic critical phenomena. *Reviews of Modern Physics*, 49, 1977.

[74] S.M. Allen and J. Cahn. A microscopic theory for antiphase boundary motion and its application to antiphase domain coarsening. *Acta Metallurgica*, 27, 1979.

[75] O. Penrose and P.C. Fife. Thermodynamically consistent models of phase-field type for the kinetic of phase transitions. *Physica D: Nonlinear Phenomena*, 43(1):44 – 62, 1990.

[76] N. Bakouta, R. Le Tellier, and L. Saas. Assessment of advanced corium-in-lower-head models in MAAP and PROCOR codes. In *Proc. of the 7th European Review Meeting on Severe Accident Research ERMSAR*, Marseille (France), 2015.

[77] R. Le Tellier, L. Saas, and S. Bajard. Transient stratification modelling of a corium pool in a LWR vessel lower head. *Nuclear Engineering and Design*, 287:68–77, 2015.

[78] P. Despret, J.-L. Dulong, and P. Villon. The heat equation strictly written in enthalpy. In *Proc. of CSMA 2015 (12ème Colloque National en Calcul des Structures)*, 2015.

[79] V.R. Voller. Modeling microsegregation in metal alloys. *Materials Science Forum*, 508:349–360, 2006.

[80] Q. Du, D.G. Eskin, and L. Katgerman. Modeling macrosegregation during direct-chill casting of multicomponent aluminum alloys. *Metallurgical and Materials Transactions A*, 38:180–189, 2007.

[81] R. Le Tellier, B. Habert, and V. Tiwari. Consistent use of CALPHAD data for in-vessel corium pool modelling: so;e analytical and practical considerations. In *Proc. of ERMSAR-2019*, Prague, Czech Republic, 2019.

[82] V. Tiwari and R. Le Tellier. On the use of CALPHAD-based enthalpy-temperature relations in suboxidized corium plane front solidification modelling. *Annals of Nuclear Energy*, 117:175–182, 2018.

[83] H. E. Huppert and M. G. Worster. Dynamic solidification of a binary melt. *Nature*, 314(6013):703–707, April 1985.

[84] Q. T. Pham, J. M. Seiler, H. Combeau, X. Gaus-Liu, F. Kretzschmar, and A. Miassoedov. Modeling of heat transfer and solidification in LIVE L3a experiment. *International Journal of Heat and Mass Transfer*, 58(1-2):691–701, March 2013.

[85] X. Gaus-Liu, B. Fluhrer, A. Miassoedov, T. Cron, J. Foit, S. Schmidt-Stiefel, and T. Wenz. Results of the LIVE-L3A experiment. (KIT Scientific Reports 7542). Technical report, Institut für Kern- und Energietechnik, 2010.

[86] L. Zhang, Y. Zhou, Y. Zhang, W. Tian, S. Qiu, and G. Su. Natural convection heat transfer in corium pools: A review work of experimental studies. *Progress in Nuclear Energy*, 79:167–181, March 2015.

[87] J. M. Bonnet and J. M. Seiler. Thermohydraulic phenomena in corium pool: the bali experiment. In *Proc. of ICONE 7*, Tokyo, Japan, 1999.

[88] C. Cardon, R. Le Tellier, and M. Plapp. Modelling of liquid phase segregation in the uranium-oxygen binary system. *CALPHAD: Computer Coupling of Phase Diagrams and Thermochemistry*, 52:47–56, 2016.

[89] Nikolay Ivanov Kolev. *Thermo-physical properties for severe accident analysis*, pages 617–807. Springer Berlin Heidelberg, Berlin, Heidelberg, 2012.

[90] IAEA, editor. *Thermophysical Properties of Materials for Nuclear Engineering: A Tutorial and Collection of Data*. IAEA, 2008.

[91] C. Guéneau. private communication. CEA Saclay, DEN/DANS/DPC/SCCME, October 2016.

[92] J. M. Seiler, K. Froment, and J. P. Garandet. Equations for solidification of corium without sparging gas - scaling criteria. In *Proc. of OECD Workshop on Ex-Vessel Debris Coolability*, Karlsruhe, Germany, 1999. OECD.

[93] J.M. Seiler and H. Combeau. Transient interface temperature on a vertical surface in multi-component solid-liquid systems with volume heating. application to various severe accident situations. *Nuclear Engineering and Design*, 278:199–208, 2014.

[94] R. Taylor and R. Krishna. *Multicomponent Mass Transfer*. John Wiley and Sons, Inc., 1993.

[95] R.F. Sekerka. Irreversible thermodynamic basis of phase field models. *Philosophical Magazine*, 91(1):3–23, 2011.

[96] B. Zhiqiang and R.F. Sekerka. Phase-field model for solidification of a binary alloy. *Physica A*, 261:95–106, 1998.

[97] R. S. Qin and H. K. Bhadeshia. Phase field method. *Materials Science and Technology*, 26(7):803–811, 2010.

[98] A. A. Wheeler, W.J. Boettinger, and G.B. McFadden. Phase-field model for isothermal phase transitions in binary alloys. *Physical Review A*, 45:7424–7439, 1992.

[99] S.G. Kim, W.T. Kim, and T. Suzuki. Phase-field model for binary alloys. *Physical Review E*, 60:7186–7197, 1999.

[100] M. Plapp. Unified derivation of phase-field models for alloy solidification from a grand-potential functional. *Physical Review E*, 84, 2011.

[101] D.A. Danilov, V.G. Lebedev, and P.K. Galenko. A grand potential approach to phase-field modeling of rapid solidification. *Journal of Non Equilibrium Thermodynamics*, 39:93–111, 2014.

[102] G. Kaptay. On the solid/liquid interfacial energies of metals and alloys. *Journal of Materials Science*, 53:3767–3784, 2018.

[103] M. Kavinay. *Essentials of Heat Transfer*. Cambridge University Press, 2011.

[104] A. Prosperetti. Boundary conditions at a liquid-vapor interface. *Meccanica*, 14, 1979.

[105] J. O. Andersson and J. Agren. Models for numerical treatment of multicomponent diffusion in simple phases. *Journal of Applied Physics*, 72(4), 1992.

[106] H.J.V. Tyrrell and K. R. Harris. *Diffusion in Liquids: A Theoretical and Experimental Study*.

[107] S.V. Patankar. *Numerical Heat Transfer and Fluid flow*. Taylor & Francis, 1980.

université PARIS-SACLAY

ÉCOLE DOCTORALE
INTERFACES
Approches Interdisciplinaires : Fondements, Applications et Innovation

Titre : Une approche consistante pour le couplage aux bases thermodynamiques de modèles intégraux et de champ de phase dédiés au comportement du corium en cuve.

Mots clés : Accidents graves, corium en cuve, CALPHAD, méthode du champ de phase, modèles intégraux

Résumé : Cette thèse s'intéresse à la consistance de la description thermodynamique du corium (un mélange à haute température de matériaux fondus du cœur et des structures d'un réacteur nucléaire) dans les modèles couplés de thermohydraulique-thermochimie mis en jeu pour l'étude des accidents graves des réacteurs refroidis à l'eau légère. Dans ce contexte, l'utilisation d'une base de données thermodynamiques apparait pertinente pour l'obtention des fermetures et données d'entrée des modèles de thermohydraulique et de thermochimie respectivement. Une approche systématique visant à l'utilisation exhaustive d'une telle base de données thermodynamiques dans les modèles couplés a été suivie et les questions relatives à ce couplage ont été traitées pour des modèles ≪ maquettes ≫ décrivant une partie des phénomènes relatifs au comportement du corium à des échelles macroscopique (modèle intégral) ou mésoscopique (modèle de champ de phase).

Title : A consistent approach for coupling lumped-parameter and phase-field models for in-vessel corium to thermodynamic databases.

Keywords : Severe accidents, in-vessel corium, CALPHAD, phase-field, lumped-parameter models

Abstract : This thesis focuses on the consistent thermodynamic representation of corium (a high-temperature mixture of molten core and structural materials from a nuclear reactor) for thermohydraulic-thermochemical models used for performing Severe Accident analysis of Light Water Nuclear Reactors. In this context, the use of a thermodynamic database for ensuring consistency of the coupling by providing closures and inputs to the thermohydraulic and thermochemical models respectively is relevant. Following a systematic approach for ensuring extensive utilization of the thermodynamic database in the coupled models, the questions associated to such a coupling have been answered for 'mock-up' macroscopic and mesoscopic models (describing some of the phenomena pertaining to corium behaviour) developed under lumped-parameter and phase-field approaches respectively.

Université Paris-Saclay
Espace Technologique / Immeuble Discovery
Route de l'Orme aux Merisiers RD 128 / 91190 Saint-Aubin, France